UNIVERSITÀ DEGLI STUDI DI TRIESTE

XXIV CICLO DEL DOTTORATO DI RICERCA IN SCIENZE E TECNOLOGIE CHIMICHE E FARMACEUTICHE

PHOTOCATALYTIC PROCESSES FOR SUSTAINABLE HYDROGEN PRODUCTION FROM RENEWABLE SOURCES

(settore scientifico disciplinare: CHIM/03)

DOTTORANDA
Valentina Gombac

COORDINATORE DEL COLLEGIO DEI DOCENTI
Chiar.mo Prof. Enzo Alessio
Università degli Studi di Trieste

SUPERVISORE/RELATORE
Chiar.mo Prof. Paolo Fornasiero
Università degli Studi di Trieste

A.A. 2010/2011

Contents

Abstract v

Chapter 1. Introduction and aim of the thesis 1

Chapter 2. Experimental techniques 35

Chapter 3. Embedding systems 67

Chapter 4. Photodeposited systems 91

Chapter 5. Supported systems

Part1: systems based on copper oxides 107

Part 2: systems based on cobalt oxides 129

Part 3: systems based on zinc oxide 151

Chapter 6 Conclusions 169

Acknowledgements 173

Abstract

The importance of hydrogen as an appealing energy vector, due to its high efficiency and environment-friendly use in Fuel Cells, is nowadays well recognized and documented. Nevertheless, in spite of several research activities in this field, the large-scale production of H_2 is still a challenging issue in view of the possible transition to an H_2-based economy. In this context, the development of materials capable of acting as multi-functional platforms for the sustainable generation, though representing a strategic target, is still far from being completely satisfied. In order to make feasible the dream of utilizing sunlight for sustainable energy production, it is of paramount importance to develop catalytic systems that are not affected by leaching or poisoning phenomena and possess a high photonic efficiency, in particular upon visible activation. Heterogeneous catalysis is a key area that can help solving this issue. Using the tools offered by nanotechnology, the tailored preparation of nanoarchitectures can lead to the obtainment of photocatalytic materials that show remarkably better performance than that currently achievable even with state-of-the-art materials. The main focus of this thesis is the preparation of such tailored photoactive materials and their characterization in order to obtain catalysts that are active and stable for the sustainable photocatalytic hydrogen production by photoreforming of biomass derived compounds as raw materials.

Different synthetic approaches are developed in this work to achieve the above mentioned scopes. The materials were prepared either in the form of nanopowders with controlled morphology or of supported nanostructures. Embedding approach, in which preformed metal nanoparticles are encapsulated in porous titania, and photodeposition of metal nanoparticles over preformed tailored supporting titania were investigated for nanopowder materials. Different oxide-based materials were synthesized by Chemical Vapor Deposition (CVD) and Plasma enhanced-CVD for the supported systems. The CVD route is compatible with large-scale production, to prepare metal oxide nanostructures on Si (100), enabling the resulting metal oxide phase composition and nanoscale organization to be controlled by simple variation of the growth temperature. In addition, and more interestingly, the photocatalytic production of hydrogen on the supported catalysts upon irradiation with UV and even visible light proved that the control of the system morphogenesis is crucial to obtain good performances even in the absence of TiO_2.

The results obtained represent an important step forward in the exploration of new active nanosystems for the conversion of solar light into storable chemical energy. All the findings significantly contributed to the development of photocatalytic materials for hydrogen production.

Chapter 1

INTRODUCTION

Over the last decade, the interest in the production of hydrogen, a key reactant for a variety of purposes, has registered a remarkable increase. Beside being widely used in various industrial processes,[1, 2] hydrogen has emerged as a strategic energy vector to overcome the finite supply of fossil fuels, ensuring a limited environmental pollution. In fact, its conversion in fuel cells efficiently generates energy producing only water as a byproduct.[3-5] However, despite hydrogen being the most abundant element in the Universe, it is not freely present on Earth and one of the main challenges is the viable H_2 production in appreciable amounts.

Nowadays, nearly 95 % of hydrogen is produced from fossil fuels, mainly by methane steam reforming, an unsustainable process on a long term scale. As a consequence, great efforts are currently devoted to its production starting from renewable resources,[4] for instance by biomass catalytic steam reforming/gasification and photoelectrochemical or enzymatic approaches.[6-14] Nevertheless, these methods suffer from severe limitations associated to low efficiency/high energy demand, since they require the use of harsh operating conditions. On the other hand, photoactivated

routes, though far from large-scale industrial application, are extremely promising as alternative hydrogen preparation strategies. In fact, they can ultimately enable to exploit sunlight, an infinite energy source, to obtain hydrogen from natural products, such as water or biomasses.

Photocatalytic reactions can be classified into "down-hill" and "up-hill" processes (Figure 1.1), the former category comprising photooxidation of organic compounds at expenses of oxygen.[15]

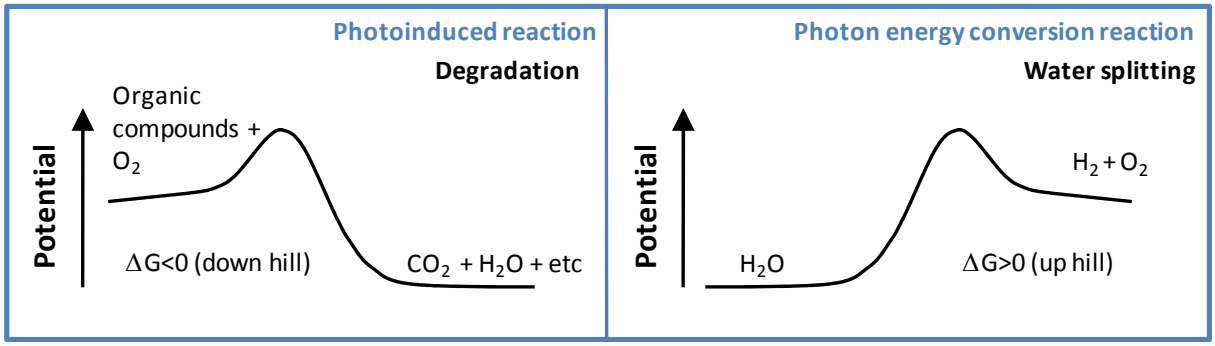

Figure 1.1: *Types of photocatalytic reactions. Adapted from Ref.[16]*

In these irreversible reactions, a photocatalyst triggers the production of various active species ($O_2^{\bullet-}$, $OH^{\bullet}$, $HO_2^{\bullet}$, … and H^+) initiating the oxidation process. On the other hand, the "up-hill" water splitting into H_2 and O_2 is accompanied by a large positive change in the Gibbs free energy (ΔG_0 = 237 kJ×mol^{-1}).[16] In this reaction, photon energy is converted into chemical energy as in photosynthesis by green plants, so that it is also termed *artificial photosynthesis*.[2]

The key feature of a photocatalytic process is the presence of a semiconductor material with a band gap E_g,[17] in which, upon illumination with radiation having an energy E_g, the promotion of an electron (e^-) from the valence band (VB) to the conduction band (CB) takes place. Concomitantly, the formation of a positive hole (h^+) in the VB occurs. Photogenerated electrons and holes can either undergo undesired recombination or migrate to the system surface, where they can initiate reactions with adsorbed species. Whereas holes in the VB are powerful oxidizing species that can produce hydroxyl radicals ($OH^{\bullet}$) from the reaction with H_2O, photogenerated electrons in the CB are directly involved in H_2 production. For this process to occur, the semiconductor CB edge must be more negative than the $H^+ \rightarrow H_2$ reduction potential [$E(H^+/H_2)$ = 0.00 V with respect to normal hydrogen electrode (NHE) at pH = 0]. In

addition, oxygen evolution from water requires a VB edge more positive than the H_2O oxidation potential [$E(O_2/H_2O)$ = 1.23 V with respect to NHE at pH = 0]. Figure 1.2 summarizes the band-edge positions for the most commonly employed semiconductors.

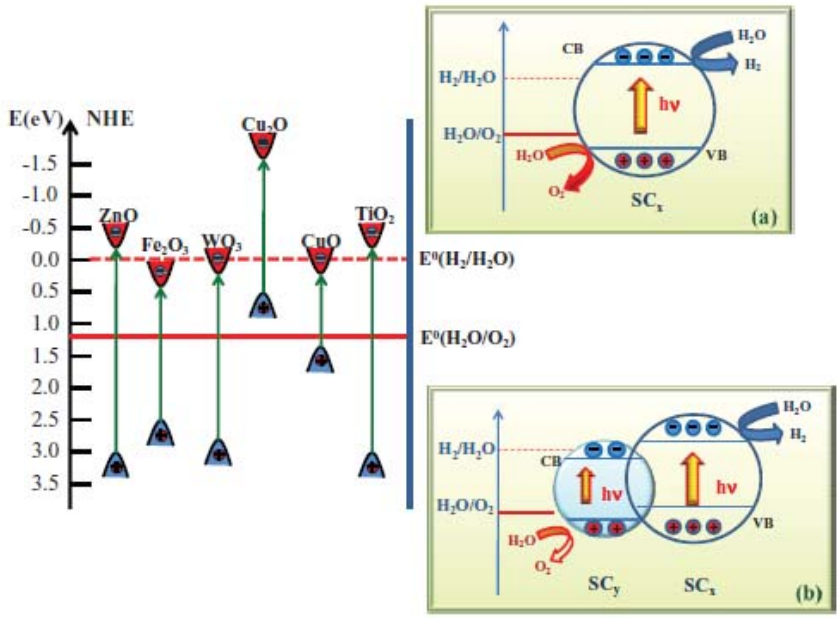

***Figure 1.2**:. Sketch of band edge positions for the main oxide semiconductors examined in the present work with respect to the standard H_2O redox potentials. The bottom edge of the conduction band (in red) and the top edge of the valence band (in blue) are reported on an eV scale with respect to the normal hydrogen electrode (NHE).[18-22] Photoactivated water splitting mechanism in the case of: a) a one-step photoexcitation process; b) a two-step mechanism involving the use of a composite system based on a junction between two semiconductors SC_x and SC_y.[23]*

It is worth pointing out that the plotted data refer to bulk SC systems and must hence be considered as guidance only. In fact, as new nanomaterials are explored, the presence of size effects, inducing an upward/downward shift of the CB/VB edges, complicate the prediction of the exact band positions.[24-26] It is worth recalling that, apart from the system nanostructure, photoconversion performances are also directly influenced by the crystal phase (i.e., *anatase* <u>*vs*</u> *rutile* in TiO_2), surface area, and defect content.[27]

Since the pioneering work of Fujishima and Honda,[28] who first demonstrated water splitting into H_2 and O_2 by a photoinduced process, enormous research efforts have been devoted to the design of active and stable photocatalysts capable of producing hydrogen under UV and, ultimately, Vis activation.[21] To this regard, various semiconducting systems, such as sulfides, oxysulfides, oxynitrides, have been considered.[21, 23, 29] Nevertheless, metal oxide semiconductors show superior long-term

stability and corrosion resistance, and, as a result, they have been much more investigated.[21, 30] Among them, the most popular is undoubtedly titania (TiO_2), that has been the object of intensive studies.[31]

An open problem for such systems is related to the fact that they generally absorb in the UV spectral range, accounting only for 3-4 % of the incident solar radiation. As a consequence, a great attention has been devoted to the development of suitable semiconducting systems adsorbing light in the Vis range, in view of a really sustainable H_2 production.[32, 33]

In spite of the intense research activities registered in the last decades, pure water splitting is still far from any technological application[34, 35] due to the complexity of the process and its inherent drawbacks.[16, 36] In particular, the main ones are the fast recombination between H_2 and O_2 (inverse reaction, thermodynamically favorable) or between photogenerated electrons and holes. In order to minimize the former, the production of the two gases in separate chambers, connected through photocatalyst thin films, has been proposed (Figure 1.2).[37, 38]

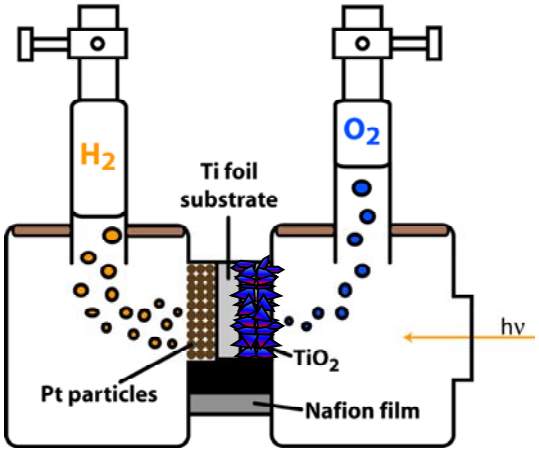

***Figure 1.3**: Schematic representation of a two-compartment photoelectrochemical cell to produce hydrogen and electricity from oxygenates aqueous solutions. In this device, the compartments are separated by a proton-transfer membrane (e.g., Nafion), whereas TiO_2 and Pt are used as photoanode and photocathode, respectively. Adapted from Ref.[21].*

To prevent e^-/h^+ recombination processes, the use of cocatalysts, such as noble metals (NM; Pt, Pd, Au,…), transition metal oxides (RuO_2, IrO_2, NiO, …), sulphides (MoS_2,….), able to act as electron or hole traps, has been proposed.[33] The presence of supported metal nanoparticles that have surface plasmon resonance bands can further enhance the photoreactivity under visible irradiation as a result of increased light

absorption.[39-41] Nishijima et al.[39] reported surface-plasmon-assisted photocurrent generation by near-infrared radiation with use of Au nanorods and TiO_2 systems. Similarly, photosensitization of titania by small gold nanoparticles was reported by Corma et al.[40] An alternative attractive approach is the addition to water of sacrificial agents.[37] In particular, the latter can irreversibly react with photogenerated holes (or $OH^{\bullet}$ radicals derived from h^+ reaction with H_2O), undergoing an easier oxidation than water, with a concomitant H_2 production by photogenerated e^- much higher than for pure water splitting.

To date, many sacrificial reactants, both inorganic, such as H_2S, S^{2-}/SO_3^{2-}, Br^-, I^-, CN^-, Fe^{2+}, Ce^{3+}, … and organic, such as alcohols, acids, aldehydes, sugars, have been proposed for hydrogen generation.[33, 42] In particular, when oxygenate molecules (ethanol, glucose, glycerol …) are used as sustainable sacrificial agents, photoreforming processes can accompany water splitting (Figure 1.4), and, depending on the adopted experimental conditions, the identification/separation of the two processes can be rather tricky, since they take place concomitantly.

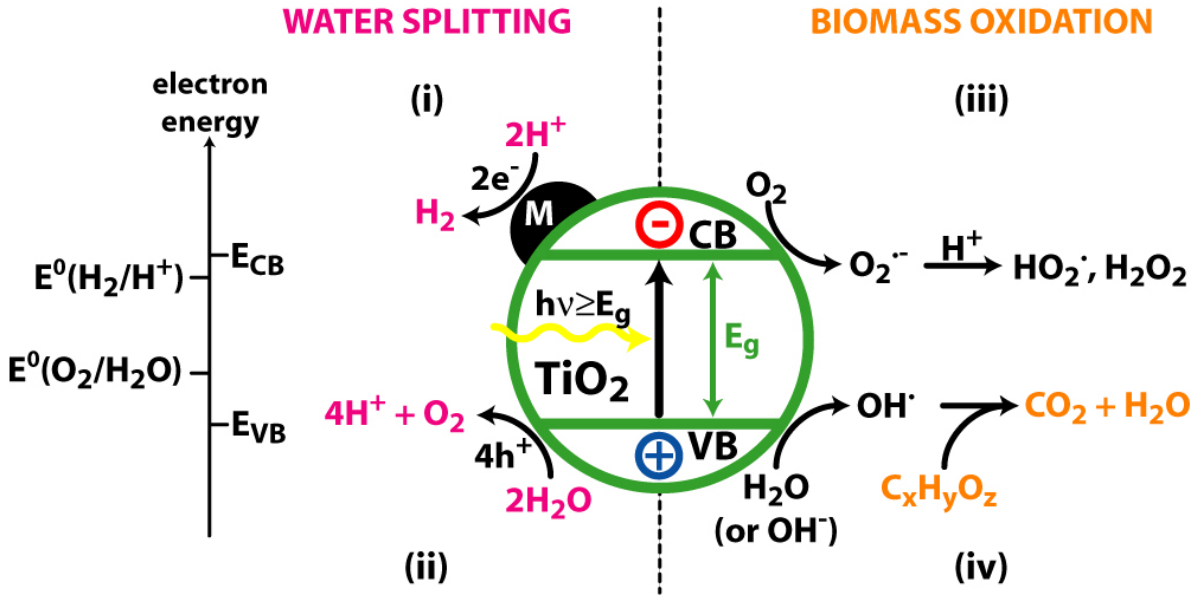

***Figure 1.4**:. Schematic representation of water splitting, biomass ($C_xH_yO_z$) oxidation and photoreforming reactions over an irradiated M-TiO_2 photocatalyst. Production of hydrogen (i) and oxygen (ii) from water cleavage is triggered by photogenerated electrons and holes, respectively. Oxidation of organic compounds takes place in the presence of oxygen (air) with the participation of photogenerated holes, and ultimately leads to the production of CO_2 and H_2O (iv). This process is accompanied by consumption of photogenerated electrons by chemisorbed oxygen (iii). The overall photoreforming process combines photoinduced hydrogen production (i) and oxidation of organic derivatives (iv). Adapted from Ref.[43]*

Such routes, which is another example of an "up-hill" process" (Figure 1.5), can be expressed by the following general equation:[44]

$$C_xH_yO_z + (2x - z)\ H_2O \rightarrow x\ CO_2 + (2x + y/2 - z)\ H_2$$

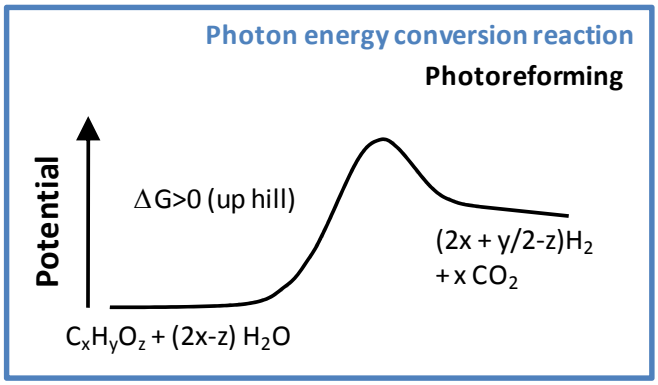

***Figure 1.5**: "Up-hill" process representing the photoreforming of biomass-derived feedstock.*

The latter route combines the photocatalytic splitting of water with the light-induced oxidation of organic substrates into a single process that takes place at ambient conditions.[45] Photoreforming is a much less explored route for obtaining H_2 from oxygenates, such as alcohols, or from biomass extracts and wastes.[46, 47] Nevertheless, it presents significant and attractive advantages in terms of photoenergy conversion. In fact, conventional reforming routes to produce hydrogen typically require high reaction temperatures and harsh conditions, being endothermal processes.[47-49] As a consequence, a more efficient and sustainable hydrogen production is highly desirable, and photoreforming constitutes a promising alternative for H_2 production in both liquid and gas phases.[50]

Many oxygenate molecules, mostly derived from biomasses (sugar, starch, vegetable oils, lignocellulosic crops, algae fuels,…), have been tested for H_2 production by these routes.[21] Among them, the species obtained by the hydrolysis of lignocellulosic materials are particularly important. In these cases, a significant fraction of the generated CO_2 can be taken up by plants during their growth. One additional key advantage is the possibility to interrupt the process at the desired stage, with the selective production of important chemicals through clean and sustainable routes.[51-53]

An aspect of great importance for technological applications, which has not been adequately considered in the scientific literature up to date, concerns photocatalyst

deactivation. At variance with traditional heterogeneous catalysts operating under conditions of medium to high temperature, photocatalysts work close to room temperature, making sintering phenomena generally negligible. On the other hand, surface poisoning is a frequent reason for the observed deactivation. In particular, photocatalysts that do not completely oxidize sacrificial agents to CO_2 can lead to the production of non-volatile intermediates that accumulate on the active sites, thus causing detrimental poisoning phenomena. In addition, undesired leaching effects of the active phase can be favored by a progressive pH variation during the process and by the capability of reaction intermediates (e.g., carboxylic acids) to coordinate metal ions on the catalyst surface.

For photocatalytic processes, a set of key parameters is usually employed to quantitatively characterize the efficiency in substrate conversion.[54] Such efficiency, defined in photochemistry by the quantum yield Φ, is based on the knowledge of the number of photons with a particular wavelength absorbed by the system. Whereas this quantity can be measured with great accuracy in homogeneous processes,[55] in heterogeneous ones only the number of photons incident onto the photocatalyst surface, representing the upper limit of the absorbed ones, can be estimated. As a consequence, the concept of photonic yield, defined as the amount of incident photons arriving at the internal surface of the irradiation window, has been introduced in heterogeneous photocatalysis. In addition, whereas the term yield can be only used for excitation with monochromatic photons (i.e., with energy in the wavelength range between λ and $\lambda + d\lambda$), it is convenient to adopt the generalized definition of efficiency when a polychromatic source is used.

In general, the following considerations on the evaluation of quantum yields for heterogeneous photocatalysis must be taken into proper account.

(i) It is of fundamental importance to monitor the initial rate of reactant consumption/product formation. Under these conditions, products do not interfere with the measurements and the possible catalyst deactivation is minimized. In fact, the quantum yield of substrate consumption, as well as that of product formation, generally varies with the irradiation time, especially upon prolonged illumination.

(ii) The catalyst concentration should not affect the reaction rate.

(iii) Non-uniform catalyst distribution and mass transfer limitations must be carefully avoided by effective stirring.

(iv) The reactant adsorption on the catalyst surface must have reached a steady-state regime before starting irradiation.

(v) The reaction rate should linearly depend on the spectral radiance, a requisite which is rigorously fulfilled only at moderate radiation intensities.

(vi) The emission spectrum of the adopted polychromatic source and the absorption spectrum of the substrate must be taken into account. In addition, the absorbed radiation contribution should be properly determined.

Hereafter, the following general definitions will be used, in accordance with IUPAC rules. [54]

Photocatalytic efficiency: amount of formed product (alternatively, of consumed reactant) divided by the number of photons incident on the system.

Quantum efficiency: rate of a given photophysical/photochemical process divided by the total absorbed photon flux. In heterogeneous photocatalysis, the photonic efficiency is commonly used.

Photonic efficiency: ratio of the photoreaction rate measured for a specified time interval to the rate of incident photons within a defined wavelength interval inside the reactor irradiation window.

Quantum yield, Φ: number of defined events occurring per photon absorbed by the system at a specified wavelength. The integral quantum yield is:

$$\Phi(\lambda) = \frac{\text{number of events}}{\text{number of photons absorbed}}$$

For a photochemical reaction:

$$\Phi(\lambda) = \frac{\text{amount of reactant consumed or product formed}}{\text{amount of photons absorbed}}$$

Although, these values are independent of the angle of irradiation, a correlation between the quantum or photocatalytic efficiency and the specific solar irradiation

conditions (such as the standard Air Mass 1.5 or Air Mass 0) might offer additional interesting information on the performances of the most promising materials.

As a matter of fact, methanol is largely used as sacrificial agent in photocatalysis, being an attractive model compound for its high reactivity, structural simplicity and absence of C-C bonds. These aspects enable an easier investigation of reaction pathways and limit photocatalyst deactivation phenomena due to surface adsorption of partial oxidation byproducts. Nevertheless, methanol is not a preferred choice in terms of sustainability. In fact, despite that methanol can be obtained from bio-syngas, produced for instance during biomass gasification, its production is still largely accomplished from fossil fuels, in particular methane. As a consequence, the attention will be also dedicated to other compounds, which are already largely produced from biomasses. For instance, ethanol can be obtained from sugars fermentation, as well as enzymatic or thermochemical degradation of cellulose.[56, 57] Similarly, glycerol is nowadays the major byproduct in the trans-esterification of vegetable oils to biodiesel.[58] Finally, degradation of cellulose-derived compounds and lignin can lead to large quantities of sugars.[59]

General mechanisms for hydrogen production from oxygenates

In spite of extensive studies involving the design of active oxide photocatalysts, a limited attention has been dedicated to photodegradation mechanisms of oxygenates over oxide semiconductors, which are still the object of debates. In the case of TiO_2, the most studied semiconductor, the main oxidizing species are reported to be free or trapped holes, $OH^{\bullet}$ radicals, $O_2^{\bullet-}$ and $^1O_2$, as well as H_2O_2 and O_2.[31, 60] While in some cases the reaction pathway involves the direct oxidation by holes, in others the process is reported to be mediated by highly oxidizing species. Among them, $OH^{\bullet}$ radicals, deriving by the reaction of photogenerated holes with water molecules, are generally considered responsible for initiating oxidation processes.[60, 61]

Several studies revealed that both shallowly and deeply trapped holes exist on the photocatalyst surface,[62, 63] despite their exact chemical nature is still an open question and their mutual content directly depends both on the catalyst nature and the adopted experimental conditions. Shallowly trapped holes can show reactivity and mobility comparable to free ones, reacting thus very rapidly with chemisorbed species.

In this case, oxidation processes might even be competitive with ultrafast charge trapping events. Vice versa, deeply trapped holes, that exhibit lower oxidizing potentials, preferentially react with more mobile physisorbed substances, and the corresponding reaction rates are lower.[62-64]

For a given molecule, the predominance of physisorption vs. chemisorption is significantly affected by the environment and, in particular, by the presence of water or oxidation byproducts. To this regard, Nosaka et al. demonstrated the competitive adsorption between CH_3CH_2OH and H_2O on TiO_2 photocatalysts by NMR analyses.[65] In a similar way, Wang et al. investigated the interaction of methanol and water with TiO_2 by means of in-situ sum frequency generation (SFG), a highly sensitive surface characterization technique.[66] Upon using pure methanol vapor in contact with TiO_2, both molecular methanol and methoxide were detected. The former one was still present after water addition, whereas chemisorbed methoxide signals disappeared and were reversibly recovered upon H_2O removal. These data indicate that methanol oxidation pathway is directly dependent on the H_2O/CH_3OH ratio. In addition, the predominance of physisorption/chemisorption influences the oxidation rate. For instance, NMR studies showed that during the oxidation of ethanol and 2-propanol, the chemisorbed species, i.e., ethoxide or propoxide, are oxidized much more rapidly than the corresponding H-bonded ones.[66, 67]

In spite of the extensive use of methanol as electron donor for photocatalytic H_2 production, only few studies have discussed in detail the underlying process. Chen et al. investigated the photoelectrochemical oxidation of alcohols and organochlorides on the surfaces of Pt- or Pd-loaded TiO_2[68] and proposed a mechanism for the oxidation of both methanol and ethanol. Specifically, in the case of suspended powders, the organic compound oxidation and the concomitant reduction (of oxygen or protons in aerated or de-aerated systems, respectively) take place on different areas of the photocatalyst surface. In particular, two mechanisms were proposed for the anodic methanol oxidation. The first one consists in the direct oxidation by holes of adsorbed methanol, up to its complete conversion into CO_2. The second one involves an indirect oxidation mediated by $OH^{\bullet}$ species (either adsorbed or in solution). In these situations, both CH_3OH and its oxidation products are adsorbed on the photocatalyst surface. Alternatively, methanol can be oxidized without being adsorbed on the catalyst surface,

and, correspondingly, its partial oxidation intermediates, such as formaldehyde or formic acid, can be identified and isolated in the reaction medium.

Notably, whereas some reports describe the photocatalytic H_2 production from aqueous solutions as water splitting,[69-73] others classify the process as CH_3OH dehydrogenation to formaldehyde, or CH_3OH reforming to CO_2.[74, 75]

The mechanism for hydrogen evolution using metal oxide semiconductors and alcohols includes the release of H^+ from the sacrificial agent and the formation of different oxygenated radicals, which are powerful oxidizing species. The result is the reduction of protons to H_2 and the concomitant full oxidation of the organic compounds to CO_2 through various intermediates, including aldehydes and carboxylates.[33]

A direct correlation between H_2 yield and the polarity of different alcohols (methanol, ethanol, propanol and butanol) used as sacrificial agents was evidenced over TiO_2-based photocatalysts taking in consideration the first reaction step, i.e. dissociative alcohol adsorption on TiO_2 surface to form alkoxide and surface OH groups. Nevertheless, the limited process efficiency (< 10%) under UV light makes this approach still far from practical technological application.[76]

Bowker and co-workers[46] highlighted that the presence of hydroxyl groups in the sacrificial agent was essential for the photoreforming process to occur, since chemicals like alkanes and alkenes revealed to be inactive under the same experimental conditions. Bahruji et al. studied hydrogen production using Pd-TiO_2 photocatalysts,[77] obtaining similar H_2 evolution rates from primary/secondary alcohols and observing the formation of the alkane derivatives of the parent alcohols (e.g. propane and butane from 1-propanol and 1-butanol, respectively). This phenomenon suggested that metal particles dehydrogenate alcohols, and the obtained alkenes are subsequently hydrogenated by the photocatalytically produced H_2. In the case of methanol, the dehydrogenation step is accompanied by the formation of CO, which, in turn, is oxidized by titania. The authors also found that, in general, a higher number of hydrogen atoms in the α-position with respect to the OH group led to improved catalyst activity in H_2 generation. The use of compounds with different chain lengths (methanol, ethanol, propanol, butanol, glycerol, sugars) resulted in similar hydrogen production rates, which was related to the inability of the catalyst to promote the process after the first dehydrogenation steps, even if C–C bond breaking occurred. Different mechanisms for

H_2 production were thus proposed, α-hydrogen dissociation and β-hydride elimination to a ketone intermediate being suggested as the rate-determining steps for primary and secondary alcohols, respectively. In the case of tertiary alcohols, where no α-hydrogen atoms are present, H_2 production was not observed.

The presence of hydroxy groups in the structure of the sacrificial agent is therefore a significant benefit for increased hydrogen production.[78] It is also worthwhile noting that, when photocatalysts yield a modest amount of H_2 and CO_2, the selective preparation of added-value intermediate oxidation products can be fruitfully exploited.

Methanol is one of the most popular sacrificial agents used in the photocatalytic evolution of H_2 from water, since its hydroxy group captures photogenerated holes and minimizes the probability of e^-/h^+ recombination. Yet, CH_3OH can only be partially considered as a renewable source (see Section 1), and bio-methanol obtained from biomass gasification might be of higher interest as a sustainable sacrificial agent in photoreforming.

In this context, systems based on Pt-TiO_2 were extensively investigated since 1980, when Kawai and Sakata[79] reported on the efficient production of hydrogen from liquid CH_3OH and H_2O at room temperature under Xe-lamp irradiation. In general, the NM-TiO_2 system (NM = Rh, Pd, Pt) can be regarded as a photoelectrochemical cell in which a TiO_2 semiconductor electrode and a metal counter-electrode are brought into contact. In fact, well-dispersed metal nanoparticles act as mini-photocathodes, trapping electrons, which, in turn, reduce water to hydrogen. In this regard, Chiarello et al.[80] studied methanol photoreforming over metal-containing TiO_2 both in aqueous solution and in the vapor phase, observing a 30-fold enhancement of the H_2 production rate upon the addition of 1% gold to TiO_2. Thanks to the absence of mass transfer limitations, a further rate increase was obtained in a vapor-phase photoreactor (up to a hydrogen yield greater than 10 μmol $h^{-1}g_{cat}^{-1}$ or 70 mmol $h^{-1}m^{-2}$ corresponding to an apparent photon efficiency higher than 6%). Identification of the main reaction products demonstrated that the first step of methanol photoreforming on Au-TiO_2 consisted of its photocatalytic dehydrogenation to formaldehyde, the only intermediate species detected in the gas phase. Moreover, isotope exchange photocatalytic tests

demonstrated that a complex network of steps is involved in the photoreforming of methanol, comprising (1) an indirect pathway mediated by the OH·radical; (2) a direct path, implying the reaction of valence band holes with adsorbed methanol at the titania–NM interface; (3) a water-assisted direct path, involving the reaction of valence band holes with methanol molecules adsorbed far from the interface between titania and the noble metal.[81] A general scheme of the reaction involved in the gas-phase photoreforming of methanol over TiO_2 is presented in Figure 1.6.

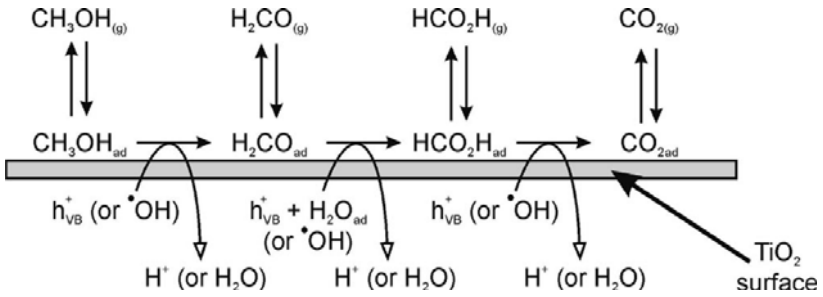

Figure 1.6. *Reaction scheme of the photocatalytic gas-phase oxidation of methanol on the TiO_2 surface. Adapted from ref. [81]*

A similar reaction pathway can be proposed for the liquid-phase photoreforming of methanol. In this case, multiple equilibria are established, leading to a repartition of each oxidation intermediate between the surface of the catalyst, the liquid, and the gaseous phases. Subsequently, the photocatalytic reforming of methanol over a series of NM-based (NM = Rh, Pt, Ag, Au, and so on) TiO_2 photocatalysts was attempted; this resulted in a high yield of hydrogen, thanks to the reduced NM particle size and the high dispersion of NM on a high-surface-area oxide (Figure 1.7). [47]

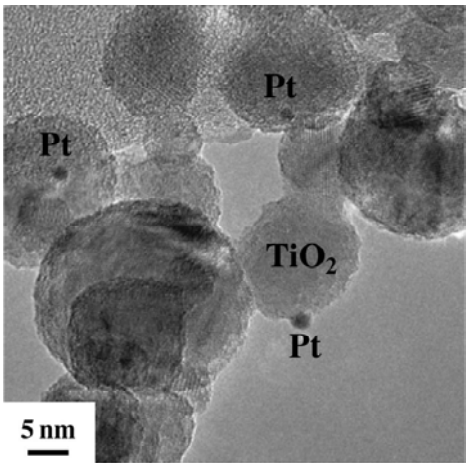

Figure 1.7. *HRTEM micrograph of a 0.5% Pt-TiO_2 photocatalyst prepared by flame spray pyrolysis (surface area = 70 m^2 g^{-1}). Adapted from ref.[47]*

In another study by Bahnemann et al.,[82] H_2 production with ultra-low CO concentration (10 ppm) was achieved via photoreforming of aqueous CH_3OH solutions on Pt-TiO_2 catalysts containing adsorbed sulfate/phosphate ions. The role of Pt nanoparticles was reported to be twofold, that is, enhancement of H_2 generation and suppression of CO formation. Sulfate and phosphate ions adsorbed on TiO_2 were found to further inhibit CO production, without appreciably decreasing H_2 evolution.[83]

Further interesting results were achieved by tailoring TiO_2 morphology, focusing in particular on titania nanowires obtained by a hydrothermal route. Upon annealing at suitable temperatures, photocatalytic H_2 evolution from CH_3OH/H_2O solutions over such systems was even higher than that exhibited by Degussa P-25, the benchmark TiO_2 standard for powdered materials.[71]

Recent attempts to increase H_2 production from methanol solutions under visible light irradiation included N-doping of titania by using urea[84] or co-doping with Ce and N.[85] In the same context, a series of Pt- and Au-TiO_2 photocatalysts were also employed, examining different TiO_2 materials with variable anatase/rutile contents. Under optimized conditions, a significant H_2 production efficiency (120 μmol min^{-1}) was obtained with very low amounts of methanol over days of irradiation, without any significant deactivation.[72]

Finally, the research efforts devoted to materials different from TiO_2 are also worth mentioning. Recently, a tin(II) tungstosilicate derivative, $K_{11}H[Sn_4(SiW_9O_{34})_2]\cdot 25H_2O$, with four sandwiched Sn^{2+} cations, was prepared by reaction of $SnCl_2$, KCl, and $Na_{10}[\alpha\text{-}SiW_9O_{34}]\cdot xH_2O$. Good visible-light photocatalytic H_2 evolution was observed with Pt nanoparticles as cocatalysts and methanol as sacrificial agent.[86]

Ethanol is an attractive renewable source for hydrogen production via photoreforming, since it can be obtained in large amounts by fermentation processes starting from second-generation biomass, as well as from steam reforming of cellulose and lignocellulose.[87]

As with methanol, various studies on H_2 photoproduction with ethanol have been devoted to NM-TiO_2 systems, such as that of Mizukoshi et al. reporting on the use of a sonochemical synthesis.[88] In this case, among Pd, Pt, and Au, Pt was found to be the

best choice in terms of functional performance, because of the lower dimensions of the nanoparticles obtained.

Yang et al. studied hydrogen production from CH_3CH_2OH over TiO_2 doped with Pd, Pt, or Rh obtained by flame spray pyrolysis.[76] They found a good H_2 yield under UV light for 1 wt.-% Pd/Pt-TiO_2 samples, whereas the use of Rh led to an inferior activity due to Rh oxidation, as confirmed by ex situ X-ray photoelectron spectroscopy (XPS) analyses. The process was mainly governed by the formation of surface ethoxide and OH groups by dissociative adsorption at the interface between metal particles and TiO_2:

$$CH_3CH_2O–H(a) + Ti(s)–O(s)\ CH_3CH_2O–Ti(s) + H–O(s)$$

where (a) and (s) stand for adsorbed and surface, respectively (see Figure 1.8 for Pt). Upon illumination with UV light, at the Pt-TiO_2 interface hydrogen atoms of hydroxyl groups are readily reduced by electrons from Pt particles, whereas chemisorbed ethoxide species act as hole traps.

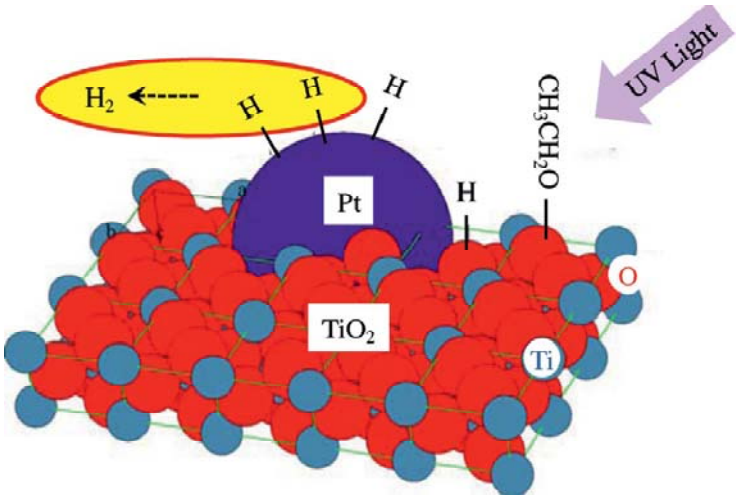

Figure 1.8. *Schematic representation of ethanol photodecomposition on Pt-TiO_2 photocatalysts. Adapted from ref.[76]*

Kondarides et al. performed various studies on photocatalytic hydrogen production, mainly using Pt-TiO_2 materials, from biomass-derived sacrificial molecules, such as acids, aldehydes, and alcohols.[44] Among the latter, ethanol was one of the easiest to be fully converted into CO_2 as a result of its simpler structure, leading to the limited formation of intermediate C-containing products. Interestingly, with acetaldehyde the hydrogen yield was lower than the predicted stoichiometric one, an unexpected phenomenon, considering that acetaldehyde is an intermediate product of

ethanol oxidation. In all cases, photocatalyst deactivation was observed and attributed to the formation of photogenerated species poisoning the Pt surface.

Another work reported on the use of metal-doped nanocrystalline titania for ethanol photoreforming.[89] Under the best conditions, over Pt-TiO_2, an overall quantum efficiency as high as 74% was obtained. These systems were used to assemble a two-compartment chemically biased photoelectrochemical cell to produce H_2 and/or electricity from aqueous CH_3CH_2OH.[90, 91] Yet, the measured cell activity showed a marked deactivation after 20 h due to the formation of several by-products, including acetaldehyde, acetone, and 2-butenal, produced by the partial oxidation and UV decomposition of ethanol.

Yu et al. prepared TiO_2 nanosheets with exposed (001) facets by a hydrothermal process involving the use of HF and resulting in F-doped titania.[92] The material showed very good hydrogen production rates from ethanol solutions after deposition of 2 wt.-% Pt. The same photocatalyst was also appreciably active when more complex oxygenates, such as glycerol or glucose, were used.

Recently, Pt/CdS/TiO_2 nanocomposites[42] were used under simulated solar light for photoelectrochemical H_2 production from ethanol. High hydrogen yields were obtained when the CdS/TiO_2 photoanode was separated, but shortcircuited, from a Pt cathode. The effect of spatial separation on the effectiveness of the sacrificial agent as hole scavenger was explained through a favorable cascade of energy states, enabling electron accumulation on Pt and favoring hydrogen production. The presence of OH^- ions, acting as hole traps at the CdS/TiO_2 anode, was also found to play a key role for the observed activity. This study highlights how the matching of component energy states in composite systems is of great importance to optimize hydrogen production.

Due to the high cost and toxicity of Pt and noble metals, recent efforts have been devoted to the development of systems alternative to the widely investigated NM-TiO_2 ones.

Another interesting alternative to TiO_2-based materials has been proposed by Wang et al.,[93] who prepared VO_2 nanorods in a novel body-centered cubic phase. This phase was found to have a much larger band gap (2.7 eV) with respect to the previously known monoclinic one (0.7 eV). When these materials were used for H_2 production

from water/ethanol solutions, a production rate of 800 μmol $h^{-1}m^{-2}$ was observed, with a quantum efficiency as high as approximately 40% even in the absence of noble metals.

To date, some studies on more complex photocatalysts for CH_3CH_2OH photoreforming are also available. Various factors yielding improved functional performance in H_2 generation were considered, though their nature and impact depended both on the target systems and on the adopted processing conditions. Dubey and co-workers[94] incorporated titania, phosphomolybdic acid, and cobalt into zeolite-Y, and the resulting composites showed good H_2 generation rates, though long-term stability tests were not reported. Hoffmann et al. showed that Ni/NiO/$KNbO_3$/CdS composites were active in hydrogen production from ethanol, though the use of 2-propanol yielded improved results.[95] The same group also used CdS/zeolite and CdS/silica nanosystems for the same reaction under simple visible irradiation, an important technological issue.[96]

Other studies were devoted to perovskite-like materials. Mesoporous $SrTiO_3$ with the addition of small amounts of Pt demonstrated good UV or visible H_2 photoproduction from both ethanol and methanol,[97] a result that was directly related to the peculiar system morphology. In a different way, in the case of S-doped $La_{0.8}Ga_{0.2}InO_3$, a significant synergistic effect between photocatalytic performance and ultrasonic irradiation was reported.[98] The promise of mixed perovskites in this field was also evidenced by results obtained on $CaTi_{1-x}Zr_xO_3$ materials (x = 0–0.15) prepared by a polymerized complex method.[99] In this case, the substitution of small amounts of Ti^{IV} with Zr^{IV} resulted in larger surface areas, reduced crystallite sizes and enhanced H_2 production from aqueous CH_3CH_2OH solutions, after addition of small quantities of Pt. A maximum of approximately 9000 μmol $g^{-1}h^{-1}$ of H_2 under UV irradiation (500W high-pressure Hg lamp) was obtained for x= 0.07, corresponding to a quantum yield higher than 13%.

Finally, it is worth mentioning a study by Liu et al. on the preparation of mixed lanthanum–tantalum oxynitrides as visible-active photocatalysts for hydrogen production from water/ethanol solutions.[100] A synergistic effect of small amounts of Pt and Ru added as co-catalysts was observed, producing up to approximately 130 μmol $g^{-1}h^{-1}$ of H_2.

Glycerol is an attractive candidate for hydrogen production for different reasons. In addition to being renewable, it is a biodegradable, nontoxic, nonflammable molecule, which, despite having poor properties as a fuel, does not swell the Nafion in proton exchange membrane (PEM) fuel cells used for electricity production from hydrogen.[101] Glycerol can be prepared in a variety of processes, such as sorbitol hydrogenolysis or glucose fermentation, but one of its most important sources is biodiesel. In fact, in biodiesel plants, around 10% of the vegetable oil or animal fat is converted to glycerol, thus contributing to approximately 100 kg for every ton of biodiesel obtained.[58] The huge overproduction of glycerol has a negative impact on the global biodiesel economy, since the processes for the economical valorization of glycerol are still limited.[102, 103] In addition, glycerol as a by-product comprises a mixture of several other constituents, such as methanol, water, inorganic salts, free fatty acids, triglycerides, and methyl esters. This mixture as such has a low commercial value and further refining processes are not economically viable. As a consequence, great efforts are being devoted to the search of more convenient alternatives for the utilization of glycerol. Though conventional steam reforming routes for its conversion to hydrogen and CO_2 are available, for example, with Ni, Pt, or Ru catalysts,[104-106] the high temperatures (800 °C) required and problems related to catalyst poisoning make the process hardly sustainable. Recently, aqueous-phase reforming of glycerol was proposed as an alternative less energy-demanding technology.[9] In a different way, glycerol photoreforming is an appealing route for its conversion not only into H_2, but also into other added-value chemicals.

Kondarides et al.[43] described the photoreforming of glycerol to H_2 and CO_2 (and other biomass-derived compounds, such as saccharides and organic acids) over Pt(0.5%)-TiO_2 materials under non-aerated conditions and with UV irradiation (Figure 1.9). The presence of glycerol in aqueous solution resulted in an initial enhancement of the H_2 production rate of one order of magnitude with respect to pure water. The extra amount of hydrogen produced upon the introduction of glycerol into pure H_2O can be estimated from the difference in area under the corresponding H_2 evolution curves shown in Figure 1.9 and equals 156 μmol under the adopted conditions. Production of hydrogen is also accompanied by the evolution of CO_2, the rate of which goes through a maximum at 70 min of illumination and subsequently decreases, reaching a value of zero after approximately 1300 min of irradiation. The photocatalysts used were very

active even for cellulose-derived materials, but their main disadvantages were progressive deactivation and the requirement of UV excitation. In comparison, Bowker and co-workers used Pd and Au-TiO_2 systems for the same process.[46] They found that a Pd(0.5%)-TiO_2 catalyst was as active as Pt under similar conditions, whereas a Au(2 %)-TiO_2 catalyst presented an inferior hydrogen yield with respect to the Pd-containing catalyst, in spite of the higher metal loading. Yet, the main limitation was the use of UV light also in this case.

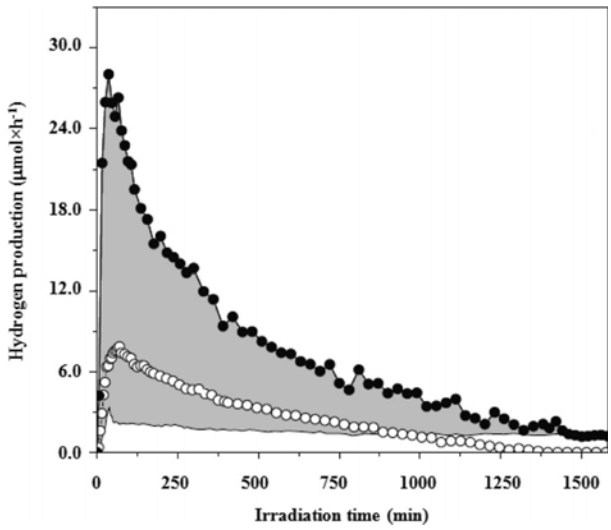

Figure 1.9. *H_2 (filled circles and solid line) and CO_2 (open circles) production rates vs. irradiation time for Pt-TiO_2 photocatalysts. Filled and open circles show data obtained with a 0.368 mM glycerol solution, whereas the solid line represents data obtained with pure water. The area marked in gray highlights the extra hydrogen produced thanks to the presence of glycerol in solution. Incident light intensity: $3.8x10^{-7}$ Einstein s^{-1}. Adapted from Ref. [43]*

In an attempt to move towards the use of activation by visible light, Fu and Lu[107] employed heteropolytungstate-sensitized TiO_2 materials. Upon UV illumination in the presence of an electron donor, heteropolytungstate yields dark blue heteropoly blue (HPB), which absorbs light in the visible spectral range. The authors prepared a Pt(0.5%)-TiO_2 catalysts and deposited heteropoly blue on its surface by UV irradiation in the presence of glycerol as electron donor. HPB was capable of absorbing energy in the visible range and, subsequently, to activate an interfacial electron transfer to TiO_2. Interestingly, the composite was effective for H_2 production under visible light, but a dramatic system deactivation, mainly due to the light-induced decomposition of HPB, took place.

Another interesting attempt to use visible light was proposed by Luo et al.[108] on B,N-codoped TiO_2 systems. After Pt deposition, the materials showed good results in hydrogen photoproduction. In a similar way, Lalitha and coworkers demonstrated the activity of mixed copper and titanium oxide photocatalysts under visible light.[109] After Cu deposition by impregnation, the materials were calcined ex situ at different temperatures, resulting in the copresence of CuO/Cu_2O species. A continuous and stable photocatalytic hydrogen production under visible light was observed for Cu^I-containing samples.

Glucose and other sugars can be obtained from the degradation of cellulosic materials, and they are therefore very promising feedstock for hydrogen production under solar irradiation. In addition, sugars are also studied for H_2 generation from biological sources.[110] The feasibility of hydrogen evolution from carbohydrates, such as sugars, starches, and/or cellulose, on $RuO_2/TiO_2/Pt$ materials under light irradiation was demonstrated in 1980 in a pioneering work by Kawai and Sakata.[111] As previously mentioned, the presence of many hydroxy groups in sugars enables their easy activation on semiconductor surfaces, though the complex skeleton is responsible for a lower H_2 yield than that from simpler alcohols. The photoreforming of glucose and sucrose over B,N-codoped TiO_2 has been reported to occur even with visible light. [108] A possible mechanism for H_2 production from glucose, proposed in a detailed work by Fu et al. in 2008 for a Pt-TiO_2 photocatalyst, is sketched in Figure 1.10.[112] The initial step was suggested to be the coordination of one glucose OH group to an under-coordinated Ti^{IV} surface site. Subsequently, H^+ and an alkoxide anion (RCH_2O^-) are formed, and the latter reacts with a photogenerated hole to give the RCH_2O radical as oxidation product (process a). Subsequently, this species attacks another glucose molecule, transferring the electron to yield an R'C$^\bullet$HOH radical. The latter undergoes process a again to give rise to aldehyde (process b) and carboxylic acid derivatives, which are ultimately converted to CO_2 (process c). Before being oxidized to CO_2, these products can undergo other deprotonation/decarboxylation cycles, whereas the obtained H^+ can be reduced to hydrogen on Pt sites by using photogenerated electrons. Although this scheme is

complex, it provides only a rough picture of the occurring process, and the exact chemical identification of reaction intermediates is still an open challenge.

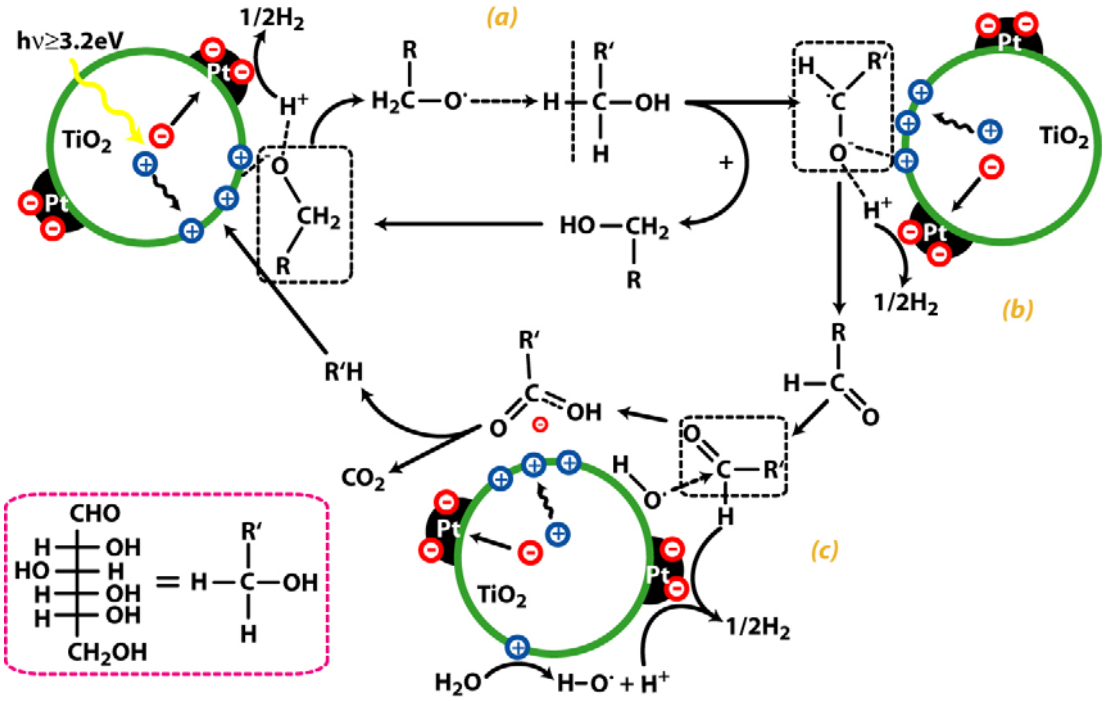

Figure 1.10. *Reaction scheme illustrating the possible mechanism for glucose photooxidation over Pt-TiO2 catalysts. Adapted from ref.[112]*

The same authors then studied the reactivity of NM-loaded TiO_2 catalysts for the photoreforming of glucose, sucrose, and starch.[112] An increased hydrogen production over Pt-TiO_2 was found in the order starch < sucrose < glucose, which is clearly related with the progressively decreasing complexity of the carbon skeleton. A further synergistic contribution to this activity is the faster diffusion of smaller molecules to the active sites of the photocatalyst.

The dependence of the activity on glucose concentration provided evidence for a Langmuir-type catalytic behavior, and the photocatalytic performance followed the order Ag, Ru < Pd, Au, Rh < Pt. The latter effect can be explained in terms of the interaction between the titania energy levels and the metal work functions (WFs), Pt showing the highest WF and, hence, an improved possibility of storing photogenerated electrons.

Also for glucose and sugars, research efforts have been devoted to photocatalysts different from TiO_2. Among the various systems, it is worth citing the case of $Bi_xY_{1-x}VO_4$ materials prepared by solid-state synthesis. The as-prepared particles had a relative

uniform shape and were aggregated into large bundles with lengths in the μm range (Figure 1.11a).

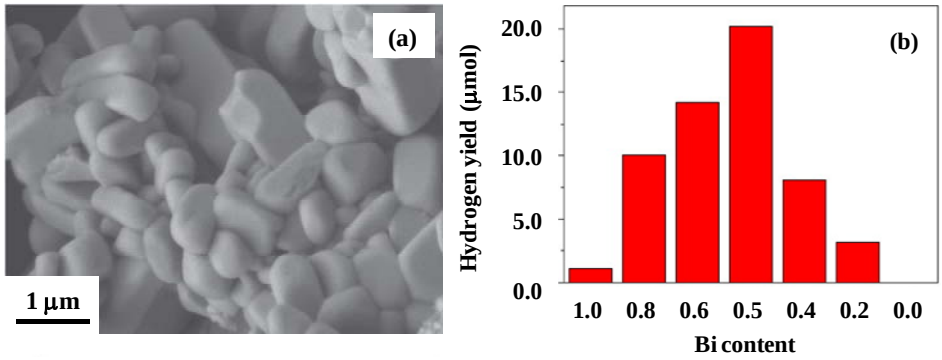

Figure 1.11. *(a) Representative SEM image of $Bi_{0.5}Y_{0.5}VO_4$ photocatalysts. (b) Amount of H_2 produced after 2 h of illumination at pH=3. Samples were loaded with 1% Pt. Illumination: Xe lamp (350 W) with a 430 nm cut-off filter for the removal of UV light. Adapted from ref.[113]*

These materials were reported to be active under visible light for the photoreforming of glucose to H_2.[113] The highest H_2 production rate was obtained for a Bi/Y ratio of 1:1 (Figure 1.11b). In fact, this ratio influences the photocatalyst band positions, and at such a particular value, the resulting solid solution has a beneficial effect on charge transport and separation phenomena. Nevertheless, the maintenance of the observed activity required the photodeposition of Pt and the removal of gaseous products. These observations highlight that material properties useful for preparing active photocatalysts must be well tuned in terms of band positions, solid phases, and operational conditions.

Other biomass-derived oxygenates or organic wastewater pollutants have been investigated as sustainable sacrificial agents for photocatalytic hydrogen production.[43] These include various alcohols, for example, 2-propanol,[114] acids, including oxalic, formic, and acetic,[114-120] and aldehydes, such as formaldehyde and acetaldehyde.[121, 122]

Very recently, reforming of 2-propanol over Pt(1%)-TiO_2 photocatalysts was investigated by means of FTIR spectroscopy.[123] The results indicated that both chemisorbed and physisorbed propanol were present on the catalyst surface. Under UV irradiation, an initial rapid deprotonation of chemisorbed 2-propoxide occurs (Figure 1.12, step 1). Acetone is subsequently produced on the surface of the catalyst and can either be desorbed into the gas phase or slowly oxidized by holes or hydroxy radicals to carboxylates (mainly acetate and formate species, step 2). Finally, these intermediates are decarboxylated over Pt nanoparticles, resulting in the evolution of CO_2 and CH_4

(step 3). The OH groups of 2-propanol and its intermediates serve as anchoring sites for the adsorption and are involved in charge transport processes, facilitating oxidation by valence band holes.

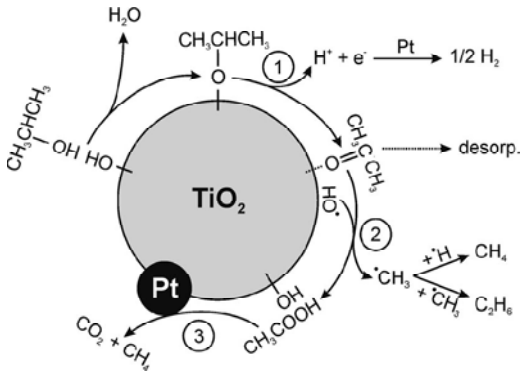

Figure 1.12. *Schematic representation of the mechanism proposed for the photoreforming of 2-propanol over Pt-TiO_2. Adapted from ref.[123]*

Notably, some of the above-mentioned aldehydes and acids are the products of the partial mineralization of the already discussed oxygenates (methanol, ethanol, glycerol). Interesting results were obtained on $LaNiO_3$-based catalysts by simple visible-light activation, with formaldehyde as sacrificial agent (Figure 1.13). The rate of H_2 evolution in the second and subsequent runs was almost constant, indicating that the photocatalyst had a good reproducibility and could be used repeatedly in practical technological applications.

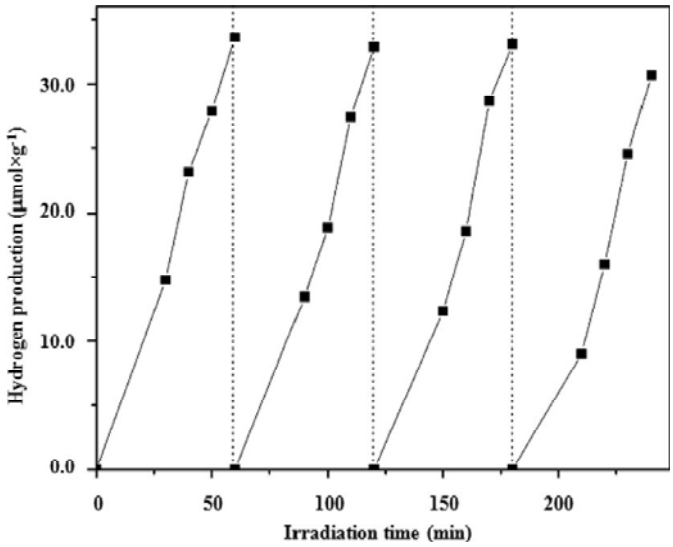

Figure 1.13. *Effect of consecutive photocatalyst recycling: hydrogen production from aqueous formaldehyde solution under visible irradiation on Ni/$LaNiO_3$-based photocatalysts. Illumination: Xe lamp (125 W) with a 400 nm cut-off filter for the removal of UV light. Vertical dotted lines mark the evacuation of the reaction system. Adapted from ref.[122]*

Notably, some of the above studies were aimed at developing efficient and sustainable technologies for wastewater purification with the concomitant production of hydrogen.[44] This latter "green" approach was also proposed for the degradation of azo dyes, with the simultaneous generation of H_2 from irradiated Pt-TiO_2 suspensions.[124] Further studies in this direction are needed to extend the validity of this methodology and to evaluate the actual sustainability of the process.

Although the large majority of reports focuses on the use of powdered materials,[21, 125-127] very attractive results can be achieved with supported oxide nanosystems (e.g., thin films, nanoplatelets, nanowires (NWs), …), which offer a broader perspective for property tailoring and a lower tendency to sintering and/or deactivation upon operation. In fact, nanotechnology has undoubtedly opened new scenarios in the development of highly active systems, where functional performances dependent directly on particle size, microstructure, and morphological organization.[18, 22, 23, 127-130] These characteristics, in turn, concur in determining a minimized carrier-transport distance and an increased surface area available for charge-transfer processes, minimizing recombination losses.[21, 25, 131-134] Beside offering a high catalytic activity,[22] nanomaterials can provide enhanced performances thanks to a suppression of ohmic losses, usually occurring in bulk SCs.[135, 136] In addition, the magnitude of E_g in SC nanosystems can, in principle, be tuned as a function of particle size, in order to increase light absorption in the solar spectrum.[25] Finally, the utilization of supported nanosystems eliminates the necessity of inconvenient filtration processes required by powdered catalysts, opening attractive perspectives for onsite technological utilization.[22] There are many reasons to believe that further improvements in tailoring supported oxide nanostructures will lead to unprecedented performances for H_2 preparation. Nevertheless, the development of eco-friendly strategies for controlling the nano-organization–activity correlations in such nanomaterials still remains a challenge.

It is important to highlight that, in spite of extensive research activities on various powdered photocatalysts, only few reports on the use of supported oxide nanosystems are available. In addition, most of the so called "water-splitting" studies have been conducted in the presence of sacrificial agents (alcohols in particular).[21, 47, 48, 92, 125, 128, 131, 137-145] Under such conditions, the process could be rigorously categorized as

H_2O photosplitting only if a simultaneous and stoichiometric (2:1) evolution of hydrogen and oxygen occurs, indicating thus H_2 production only from water reduction.

Recently, visible-light-responsive TiO_2 thin films have been produced on titanium substrates at 200–600°C by radio-frequency (RF) magnetron sputtering from a TiO_2 target under a pure Ar atmosphere, using an RF-power of 300 W.[146, 147] These layers consisted of columnar nanocrystals grown perpendicularly to the substrate surface and characterized by O defects [i.e., Ti(III) centres], responsible for a considerable absorption at $\lambda > 400$ nm. As a matter of fact, these materials possessed an appreciable activity in H_2 photoproduction from methanol–aqueous solutions. The adopted setup enabled a physical separation of the produced hydrogen and oxygen. Consistently, the observation of nearly stechiometric H_2 and O_2 evolution clearly demonstrates the occurrence of water splitting. The results are extremely promising, also upon visible-light activation, especially in the presence of platinum particles. It is generally recognized that the tailored introduction of metal nanoparticles (NP) in SCs has a beneficial influence on their photoactivated performances, thanks to several advantages.[143] First, the Schottky barrier character of metal-oxide junctions results in an electron drawing effect by metal NPs, favouring charge-carrier separation.[49, 93, 128, 146, 148] In addition, the introduction of metal NPs promotes the absorption in the visible range thanks to the surface plasmon resonance (SPR) phenomenon,[47, 80, 128, 149] a key point in view of the eventual hydrogen production by means of solar radiation. Last but not least, the unique catalytic activity of nanometer-sized metal particles on oxide matrices synergistically contributes to the above-mentioned effects.[47, 80, 128, 142, 150] In this scenario, Pt-TiO_2 is undoubtedly one of the most studied metal-oxide nanosystems for photocatalytic applications.[21, 26, 48, 50, 74, 92, 125, 127, 131, 135, 138, 142, 146, 151] Nevertheless, the high cost and environmental impact of platinum have stimulated intensive research efforts towards alternative metals, from palladium to copper, silver and gold NPs.[46, 48, 49, 128, 130, 141, 144, 152]

Forefront and advanced research trends are actually directed towards supported oxide materials different from titania. An interesting example showing the influence of the system nanostructure on H_2 photogeneration are ordered arrays of VO_2 NWs, obtained by V evaporation at 5×10^{-2} mbar on Si(100) substrates at temperatures <350°C.[93] The obtained 1D arrays, composed of a body-centered cubic VO_2 phase were

≈ 6 μ m long and ≈ 150 nm in diameter and were characterized by a sharp conical tip (Figure 1.14). The formation of such peculiar 1D structures was attributed to the fast evaporation and oxidation of V atoms and their subsequent deposition on the substrate at relatively low temperatures. Such systems were utilized as photocatalysts for H_2 generation through H_2O photosplitting (Figure 1.14d), revealing no appreciable degradation within the first 4 h of UV exposure. However, the use of a ≈ 17% vol/vol ethanol/water mixture leaves open questions of the role of the sacrificial agent. Interestingly, hydrogen production depended not only on the illumination time but also on the adopted incidence angle and reached a maximum when irradiation was performed along the NW axis (see Figure 1.14d, inset).

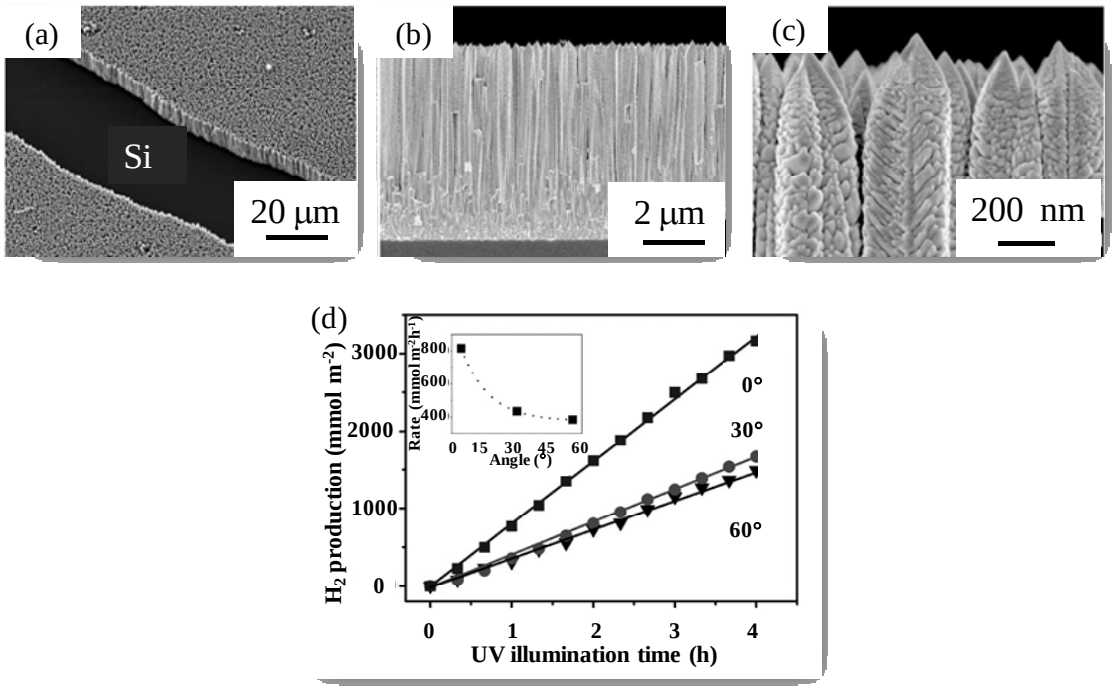

Figure 1.14. *Representative scanning electron microscopy (SEM) images of VO 2 NWs grown on Si(100): a) Low magnifi cation image; b,c) cross-sectional views; d) hydrogen production from an aqueous ethanolic solution catalyzed by vanadium oxide nanostructures upon UV irradiation (as a function of the radiation incidence angle, as shown in the inset). [93]*

This effect could be interpreted with a smaller amount of light being absorbed when the radiation direction was not parallel to the NW axis, resulting in less H_2 formation.[93] These results may be of great interest for technical applications of the obtained arrays in photoactivated hydrogen generators with prescribed performances.

A very recent study concerns the use of TiO_2 nanotube arrays prepared by anodic oxidation of Ti foils.[50] Figure 1.15a shows a representative SEM image of the nanotube systems obtained under optimized conditions. As can be observed, bamboo-shaped hollow tubes with very straight walls (average internal diameter = 40 nm, length up to ≈15 μm) could be obtained. These high density arrays were subsequently used for H_2 generation through H_2O/CH_3CH_2OH photoreforming, both in the liquid and in the gas phase (Figure 1.15b). A significant increase in hydrogen production rate was observed in the gas phase, thanks to the reduced light scattering and the enhanced desorption of interfering adsorbed species.[50] As expected, the introduction of 8-nm Pt NPs resulted in an appreciable performance increase.

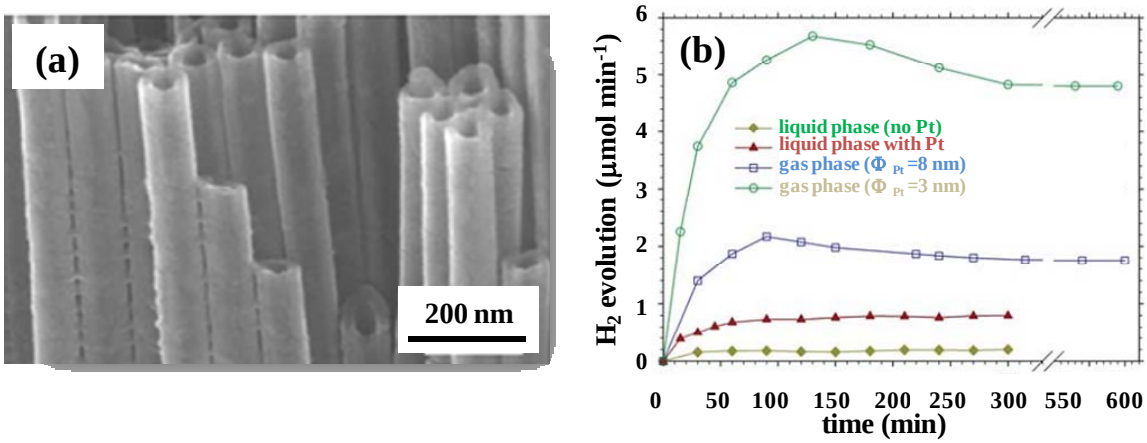

Figure 1.15. *a) Cross-sectional SEM image of a TiO_2 nanotube array synthesized by oxidation of Ti foils in ethylene glycol containing 0.3 wt% NH_4F and 2vol% H_2O (pH=7; anodizing voltage=50V; duration=6h). Low-sized Pt particles (diameter=3nm) were deposited by photoreduction, whereas in the other cases Pt functionalization was performed by wet impregnation. b) H_2 evolution rate for TiO_2 and TiO_2–Pt nanosystems in the case of liquid- and gas-phase photoreforming. Adapted from ref.[50]*

Interestingly, smaller Pt particles (≈3 nm) characterized by a minor density and a more homogeneous dispersion resulted in an almost doubled H_2 evolution rate, highlighting thus the impact of the preparation conditions and nanostructural control on the resulting system activity.

As can be observed, particularly upon operation in the gas phase, the rate of H_2 evolution exhibited a maximum and subsequently reached a mean value ≈ 20% below the maximum. This phenomenon was mainly attributed to the progressive deactivation of TiO_2 nanotube arrays, a critical issue in view of large-scale solar fuel production that requires further investigation.

Aim of the thesis

Photocatalytic water splitting is an extremely promising and environmentally friendly route for the conversion of water and radiation into oxygen and hydrogen. This latter compound is indicated as one of the emerging energy vector that in combination with Fuel Cells can guarantee high conversion efficiency, avoiding the emission of undesired pollutants typically of the fossil fuel based internal combustion engine. However, the efficiency of this process is still far from reaching industrial viability. Conversely, light-induced reforming (photoreforming) of organic compounds, such as biomass-derived carbohydrates, into H_2 is a significantly less explored method. Photoreforming can be particularly attractive when polluted wastewater is used as a feedstock, offering the possibility for the simultaneous production of H_2 and abatement of organic pollutants. Recently research activities have provided some encouraging results for hydrogen generation. However, various technical and cost problems still hinder commercial viability. In particular, a key target is the availability of catalysts endowed both with a high efficiency under visible light and an appreciable durability.

TiO_2 , the most investigates photocatalyst, can only be excited by ultraviolet light, i.e., with wavelengths shorter than ca. 400 nm. Therefore, only a very small portion of solar irradiation (3-5%) can be utilized to drive chemical reactions. Thus extension of its absorption wavelength range to visible region (vis) is an key issue. Noble metals, platinum in particular, have been used as surface modifiers, primly because they possibly inhibit charge recombination by accelerating transfer of photoexcited electrons from titania to substrates. The high cost and environmental impact of platinum have stimulated intensive research efforts towards alternative metals, ranging from palladium to copper, from silver to gold, or alloys.

The aim of this PhD thesis was to contribute to identify and optimize efficient and stable photocatalytic nanosystems based on oxides and transition metals to be used in advanced technologies for photocatalytic production of hydrogen. Two approaches were adopted, the first consisted in the design, characterization and evaluation of the photocatalytic performances of metal-metal oxides based materials, while the second one focuses the attention on innovative metal oxide only. In the first case, various metals were investigated, such Au, Ag, Cu that were supported or embedded in

semiconductors such as TiO_2 and/or ZnO. These materials were prepared either in the form of nanopowders with controlled morphology or of supported nanostructures. Many efforts were also directed to use oxide-based photocatalysts as attractive alternative to TiO_2-based systems. Specifically, Cu_2O, CuO and Co_3O_4 were deeply investigated. The systems were fully characterized and their activity was tested in the photoreforming of oxygenates derived from renewable sources for sustainable hydrogen production. Remarkably, promising photocatalytic activity was observed on nanostructured thin films of F-doped Co_3O_4.

References

[1] N. Armaroli, V. Balzani. *ChemSusChem* **2011**, *4*(1), 21-36.
[2] E. Reisner. *European Journal of Inorganic Chemistry* **2011**, (7), 1005-1016.
[3] A. Paracchino, V. Laporte, K. Sivula, M. Grätzel, E. Thimsen. *Nature Materials* **2011**, *10*(6), 456-461.
[4] S. K. Singh, Z. H. Lu, Q. Xu. *European Journal of Inorganic Chemistry* **2011**, (14), 2232-2237.
[5] J. Tollefson. *Nature* **2010**, *464*(7293), 1262-1264.
[6] R. D. Cortright, R. R. Davda, J. A. Dumesic. *Nature* **2002**, *418*(6901), 964-967.
[7] C. N. Dasgupta, J. Jose Gilbert, P. Lindblad, T. Heidorn, S. A. Borgvang, K. Skjanes, D. Das. *International Journal of Hydrogen Energy* **2010**, *35*(19), 10218-10238.
[8] J. D. Holladay, J. Hu, D. L. King, Y. Wang. *Catalysis Today* **2009**, *139*(4), 244-260.
[9] G. W. Huber, J. W. Shabaker, J. A. Dumesic. *Science* **2003**, *300*(5628), 2075-2077.
[10] G. W. Huber, S. Iborra, A. Corma. *Chemical Reviews* **2006**, *106*(9), 4044-4098.
[11] H. S. Lee, W. F. J. Vermaas, B. E. Rittmann. *Trends in Biotechnology* **2010**, *28*(5), 262-271.
[12] D. B. Levin, R. Chahine. *International Journal of Hydrogen Energy* **2010**, *35*(10), 4962-4969.
[13] R. M. Navarro, M. A. Peña, J. L. G. Fierro. *Chemical Reviews* **2007**, *107*(10), 3952-3991.
[14] S. Zinoviev, F. Müller-Langer, P. Das, N. Bertero, P. Fornasiero, M. Kaltschmitt, G. Centi, S. Miertus. *ChemSusChem* **2010**, *3*(10), 1106-1133.
[15] A. Kudo. *Catalysis Surveys from Asia* **2003**, *7*(1), 31-38.
[16] D. G. Nocera. *Inorganic Chemistry* **2009**, *48*(21), 10001-10017.
[17] O. Carp, C. L. Huisman, A. Reller. *Progress in Solid State Chemistry* **2004**, *32*(1-2), 33-177.
[18] Y. Bessekhouad, D. Robert, J. V. Weber. *Catalysis Today* **2005**, *101*(3-4 SPEC. ISS.), 315-321.
[19] P. E. De Jongh, D. Vanmaekelbergh, J. J. Kelly. *Chemical Communications* **1999**, (12), 1069-1070.
[20] M. Grätzel. *Nature* **2001**, *414*(6861), 338-344.
[21] A. Kudo, Y. Miseki. *Chemical Society Reviews* **2009**, *38*(1), 253-278.
[22] R. Van De Krol, Y. Liang, J. Schoonman. *Journal of Materials Chemistry* **2008**, *18*(20), 2311-2320.
[23] J. Zhu, M. Zäch. *Current Opinion in Colloid and Interface Science* **2009**, *14*(4), 260-269.
[24] M. D. Archer, A. J. Nozik. *Nanostructured and Photoelectrochemical Systems for Solar Photon Conversion* **2008**.
[25] Y. Li, J. Z. Zhang. *Laser and Photonics Reviews* **2010**, *4*(4), 517-528.
[26] M. K. I. Senevirathna, P. K. D. D. Pitigala, K. Tennakone. *Journal of Photochemistry and Photobiology A: Chemistry* **2005**, *171*(3), 257-259.
[27] A. Testino, I. R. Bellobono, V. Buscaglia, C. Canevali, M. D'Arienzo, S. Polizzi, R. Scotti, F. Morazzoni. *Journal of the American Chemical Society* **2007**, *129*(12), 3564-3575.
[28] A. Fujishima, K. Honda. *Nature* **1972**, *238*(5358), 37-38.
[29] A. J. Esswein, D. G. Nocera. *Chemical Reviews* **2007**, *107*(10), 4022-4047.
[30] L. M. Torres-Martínez, R. Gómez, O. Vázquez-Cuchillo, I. Juárez-Ramírez, A. Cruz-López, F. J. Alejandre-Sandoval. *Catalysis Communications* **2010**, *12*(4), 268-272.
[31] A. Fujishima, T. N. Rao, D. A. Tryk. *Journal of Photochemistry and Photobiology C: Photochemistry Reviews* **2000**, *1*(1), 1-21.
[32] R. Abe. *Journal of Photochemistry and Photobiology C: Photochemistry Reviews* **2010**, *11*(4), 179-209.
[33] X. Chen, S. Shen, L. Guo, S. S. Mao. *Chemical Reviews* **2010**, *110*(11), 6503-6570.
[34] K. Maeda, K. Domen. *Journal of Physical Chemistry Letters* **2010**, *1*(18), 2655-2661.
[35] F. E. Osterloh. *Chemistry of Materials* **2008**, *20*(1), 35-54.
[36] F. M. Toma, A. Sartorel, M. Iurlo, M. Carraro, P. Parisse, C. MacCato, S. Rapino, B. R. Gonzalez, H. Amenitsch, T. Da Ros, L. Casalis, A. Goldoni, M. Marcaccio, G. Scorrano, G. Scoles, F. Paolucci, M. Prato, M. Bonchio. *Nature Chemistry* **2010**, *2*(10), 826-831.
[37] M. Kitano, K. Tsujimaru, M. Anpo. *Topics in Catalysis* **2008**, *49*(1-2), 4-17.
[38] E. Selli, G. L. Chiarello, E. Quartarone, P. Mustarelli, I. Rossetti, L. Forni. *Chemical Communications* **2007**, (47), 5022-5024.
[39] Y. Nishijima, K. Ueno, Y. Yokota, K. Murakoshi, H. Misawa. *Journal of Physical Chemistry Letters* **2010**, *1*(13), 2031-2036.
[40] A. Primo, A. Corma, H. García. *Physical Chemistry Chemical Physics* **2011**, *13*(3), 886-910.
[41] A. Primo, T. Marino, A. Corma, R. Molinari, H. García. *Journal of the American Chemical Society* **2011**, *133*(18), 6930-6933.
[42] V. M. Daskalaki, M. Antoniadou, G. Li Puma, D. I. Kondarides, P. Lianos. *Environmental Science and Technology* **2010**, *44*(19), 7200-7205.
[43] D. I. Kondarides, V. M. Daskalaki, A. Patsoura, X. E. Verykios. *Catalysis Letters* **2008**, *122*(1-2), 26-32.
[44] A. Patsoura, D. I. Kondarides, X. E. Verykios. *Catalysis Today* **2007**, *124*(3-4), 94-102.
[45] V. M. Daskalaki, D. I. Kondarides. *Catalysis Today* **2009**, *144*(1-2), 75-80.
[46] M. Bowker, P. R. Davies, L. S. Al-Mazroai. *Catal. Lett.* **2009**, *128*(3-4), 253-255.
[47] G. L. Chiarello, M. H. Aguirre, E. Selli. *Journal of Catalysis* **2010**, *273*(2), 182-190.

[48] Y. Ichihashi, M. Yamaguchi, Y. H. Nishikawa, K. Taniya, S. Tsuruya, S. Nishiyama. *Research on Chemical Intermediates* **2010**, *36*(5), 463-472.
[49] G. Wu, T. Chen, W. Su, G. Zhou, X. Zong, Z. Lei, C. Li. *International Journal of Hydrogen Energy* **2008**, *33*(4), 1243-1251.
[50] C. Ampelli, G. Centi, R. Passalacqua, S. Perathoner. *Energy and Environmental Science* **2010**, *3*(3), 292-301.
[51] G. Palmisano, V. Augugliaro, M. Pagliaro, L. Palmisano. *Chemical Communications* **2007**, (33), 3425-3437.
[52] S. Protti, M. Fagnoni. *Photochemical and Photobiological Sciences* **2009**, *8*(11), 1499-1516.
[53] Y. Shiraishi, T. Hirai. *Journal of Photochemistry and Photobiology C: Photochemistry Reviews* **2008**, *9*(4), 157-170.
[54] S. E. Braslavsky, A. M. Braun, A. E. Cassano, A. V. Emeline, M. I. Litter, L. Palmisano, V. N. Parmon, N. Serpone. *Pure and Applied Chemistry* **2011**, *83*(4), 931-1014.
[55] H. J. Kuhn, S. E. Braslavsky, R. Schmidt. *Pure and Applied Chemistry* **2004**, *76*(12), 2105-2146.
[56] P. Alvira, E. Tomás-Pejó, M. Ballesteros, M. J. Negro. *Bioresource Technology* **2010**, *101*(13), 4851-4861.
[57] A. Demirbas. *Energy Conversion and Management* **2001**, *42*(11), 1357-1378.
[58] A. Sivasamy, K. Y. Cheah, P. Fornasiero, F. Kemausuor, S. Zinoviev, S. Miertus. *ChemSusChem* **2009**, *2*(4), 278-300.
[59] N. Gil, S. Ferreira, M. E. Amaral, F. C. Domingues, A. P. Duarte. *Industrial Crops and Products* **2010**, *32*(1), 29-35.
[60] M. R. Hoffmann, S. T. Martin, W. Choi, D. W. Bahnemann. *Chemical Reviews* **1995**, *95*(1), 69-96.
[61] J. Marugán, D. Hufschmidt, M. J. López-Muñoz, V. Selzer, D. Bahnemann. *Applied Catalysis B: Environmental* **2006**, *62*(3-4), 201-207.
[62] D. W. Bahnemann, M. Hilgendorff, R. Memming. *Journal of Physical Chemistry B* **1997**, *101*(21), 4265-4275.
[63] N. Serpone, D. Lawless, R. Khairutdinov. *Journal of Physical Chemistry* **1995**, *99*(45), 16646-16654.
[64] Y. Tamaki, A. Furube, M. Murai, K. Hara, R. Katoh, M. Tachiya. *Journal of the American Chemical Society* **2006**, *128*(2), 416-417.
[65] A. Y. Nosaka, T. Fujiwara, H. Yagi, H. Akutsu, Y. Nosaka. *Langmuir* **2003**, *19*(6), 1935-1937.
[66] S. Pilkenton, S. J. Hwang, D. Raftery. *Journal of Physical Chemistry B* **1999**, *103*(50), 11152-11160.
[67] W. Xu, D. Raftery. *Journal of Physical Chemistry B* **2001**, *105*(19), 4343-4349.
[68] J. Chen, D. F. Ollis, W. H. Rulkens, H. Bruning. *Water Research* **1999**, *33*(3), 661-668.
[69] S. Ekambaram. *Journal of Alloys and Compounds* **2008**, *448*(1-2), 238-245.
[70] J. Jitputti, S. Pavasupree, Y. Suzuki, S. Yoshikawa. *Journal of Solid State Chemistry* **2007**, *180*(5), 1743-1749.
[71] J. Jitputti, Y. Suzuki, S. Yoshikawa. *Catalysis Communications* **2008**, *9*(6), 1265-1271.
[72] O. Rosseler, M. V. Shankar, M. K. L. Du, L. Schmidlin, N. Keller, V. Keller. *Journal of Catalysis* **2010**, *269*(1), 179-190.
[73] J. Tang, H. Quan, J. Ye. *Chemistry of Materials* **2007**, *19*(1), 116-122.
[74] J. G. Highfield, M. H. Chen, P. T. Nguyen, Z. Chen. *Energy and Environmental Science* **2009**, *2*(9), 991-1002.
[75] C. Y. Wang, R. Pagel, D. W. Bahnemann, J. K. Dohrmann. *Journal of Physical Chemistry B* **2004**, *108*(37), 14082-14092.
[76] Y. Z. Yang, C. H. Chang, H. Idriss. *Applied Catalysis B: Environmental* **2006**, *67*(3-4), 217-222.
[77] H. Bahruji, M. Bowker, P. R. Davies, L. S. Al-Mazroai, A. Dickinson, J. Greaves, D. James, L. Millard, F. Pedrono. *Journal of Photochemistry and Photobiology A: Chemistry* **2010**, *216*(2-4), 115-118.
[78] H. Tran, K. Chiang, J. Scott, R. Amal. *Photochemical and Photobiological Sciences* **2005**, *4*(8), 565-567.
[79] T. Kawai, T. Sakata. *Journal of the Chemical Society, Chemical Communications* **1980**, (15), 694-695.
[80] G. L. Chiarello, L. Forni, E. Selli. *Catalysis Today* **2009**, *144*(1-2), 69-74.
[81] G. L. Chiarello, D. Ferri, E. Selli. *Journal of Catalysis* **2011**, *280*(2), 168-177.
[82] T. A. Kandiel, R. Dillert, L. Robben, D. W. Bahnemann. *Catalysis Today* **2011**, *161*(1), 196-201.
[83] G. Wu, T. Chen, X. Zong, H. Yan, G. Ma, X. Wang, Q. Xu, D. Wang, Z. Lei, C. Li. *Journal of Catalysis* **2008**, *253*(1), 225-227.
[84] T. Sreethawong, S. Laehsalee, S. Chavadej. *Catalysis Communications* **2009**, *10*(5), 538-543.
[85] X. Sun, H. Liu, J. Dong, J. Wei, Y. Zhang. *Catalysis Letters* **2010**, *135*(3-4), 219-225.
[86] Z. Zhang, Q. Lin, S. T. Zheng, X. Bu, P. Feng. *Chemical Communications* **2011**, *47*(13), 3918-3920.
[87] P. Binod, R. Sindhu, R. R. Singhania, S. Vikram, L. Devi, S. Nagalakshmi, N. Kurien, R. K. Sukumaran, A. Pandey. *Bioresource Technology* **2010**, *101*(13), 4767-4774.
[88] Y. Mizukoshi, Y. Makise, T. Shuto, J. Hu, A. Tominaga, S. Shironita, S. Tanabe. *Ultrasonics Sonochemistry* **2007**, *14*(3), 387-392.
[89] N. Strataki, V. Bekiari, D. I. Kondarides, P. Lianos. *Applied Catalysis B: Environmental* **2007**, *77*(1-2), 184-189.
[90] M. Antoniadou, D. I. Kondarides, P. Lianos. *Catalysis Letters* **2009**, *129*(3-4), 344-349.
[91] M. Kaneko, J. Nemoto, H. Ueno, N. Gokan, K. Ohnuki, M. Horikawa, R. Saito, T. Shibata. *Electrochemistry Communications* **2006**, *8*(2), 336-340.
[92] J. Yu, L. Qi, M. Jaroniec. *Journal of Physical Chemistry C* **2010**, *114*(30), 13118-13125.
[93] Y. Wang, Z. Zhang, Y. Zhu, Z. Li, R. Vajtai, L. Ci, P. M. Ajayan. *ACS Nano* **2008**, *2*(7), 1492-1496.
[94] N. Dubey, N. K. Labhsetwar, S. Devotta, S. S. Rayalu. *Catalysis Today* **2007**, *129*(3-4), 428-434.

[95] S. Y. Ryu, J. Choi, W. Balcerski, T. K. Lee, M. R. Hoffmann. *Industrial and Engineering Chemistry Research* **2007**, *46*(23), 7476-7488.
[96] S. Y. Ryu, W. Balcerski, T. K. Lee, M. R. Hoffmann. *Journal of Physical Chemistry C* **2007**, *111*(49), 18195-18203.
[97] T. Puangpetch, T. Sreethawong, S. Yoshikawa, S. Chavadej. *Journal of Molecular Catalysis A: Chemical* **2009**, *312*(1-2), 97-106.
[98] P. L. Gentili, M. Penconi, F. Ortica, F. Cotana, F. Rossi, F. Elisei. *International Journal of Hydrogen Energy* **2009**, *34*(22), 9042-9049.
[99] W. Sun, S. Zhang, C. Wang, Z. Liu, Z. Mao. *Catalysis Letters* **2007**, *119*(1-2), 148-153.
[100] M. Liu, W. You, Z. Lei, T. Takata, K. Domen, C. Li. *Chinese Journal of Catalysis* **2006**, *27*(7), 556-558.
[101] R. L. Arechederra, B. L. Treu, S. D. Minteer. *Journal of Power Sources* **2007**, *173*(1), 156-161.
[102] M. Aresta, A. Dibenedetto, F. Nocito, C. Ferragina. *Journal of Catalysis* **2009**, *268*(1), 106-114.
[103] A. Behr, J. Eilting, K. Irawadi, J. Leschinski, F. Lindner. *Green Chemistry* **2008**, *10*(1), 13-30.
[104] A. M. D. Douette, S. Q. Turn, W. Wang, V. I. Keffer. *Energy and Fuels* **2007**, *21*(6), 3499-3504.
[105] P. R. D. L. Piscina, N. Homs. *Chemical Society Reviews* **2008**, *37*(11), 2459-2467.
[106] P. D. Vaidya, A. E. Rodrigues. *Chemical Engineering and Technology* **2009**, *32*(10), 1463-1469.
[107] N. Fu, G. Lu. *Catalysis Letters* **2009**, *127*(3-4), 319-322.
[108] N. Luo, Z. Jiang, H. Shi, F. Cao, T. Xiao, P. P. Edwards. *International Journal of Hydrogen Energy* **2009**, *34*(1), 125-129.
[109] K. Lalitha, G. Sadanandam, V. D. Kumari, M. Subrahmanyam, B. Sreedhar, N. Y. Hebalkar. *Journal of Physical Chemistry C* **2010**, *114*(50), 22181-22189.
[110] Y. H. P. Zhang. *Energy and Environmental Science* **2009**, *2*(3), 272-282.
[111] T. Kawai, T. Sakata. *Nature* **1980**, *286*(5772), 474-476.
[112] X. Fu, J. Long, X. Wang, D. Y. C. Leung, Z. Ding, L. Wu, Z. Zhang, Z. Li, X. Fu. *International Journal of Hydrogen Energy* **2008**, *33*(22), 6484-6491.
[113] D. Jing, M. Liu, J. Shi, W. Tang, L. Guo. *Catalysis Communications* **2010**, *12*(4), 264-267.
[114] B. Zieliñska, E. Borowiak-Palen, R. J. Kalenczuk. *International Journal of Hydrogen Energy* **2008**, *33*(7), 1797-1802.
[115] T. Chen, G. Wu, Z. FENG, G. HU, W. Su, P. YING, C. Li. *Chinese Journal of Catalysis* **2008**, *29*(2), 105-107.
[116] Y. Li, G. Lu, S. Li. *Chemosphere* **2003**, *52*(5), 843-850.
[117] B. Ohtani, M. Kakimoto, S. Nishimoto, T. Kagiya. *Journal of Photochemistry and Photobiology, A: Chemistry* **1993**, *70*(3), 265-272.
[118] S. Shen, L. Guo. *Catalysis Today* **2007**, *129*(3-4), 414-420.
[119] Y. J. Zhang, L. Zhang. *Desalination* **2009**, *249*(3), 1017-1021.
[120] X. J. Zheng, L. F. Wei, Z. H. Zhang, Q. J. Jiang, Y. J. Wei, B. Xie, M. B. Wei. *International Journal of Hydrogen Energy* **2009**, *34*(22), 9033-9041.
[121] A. Patsoura, D. I. Kondarides, X. E. Verykios. *Catalysis Today* **2007**, *124*(3-4), 94-102.
[122] L. Jia, J. Li, W. Fang. *Journal of Alloys and Compounds* **2010**, *489*(2), L13-L16.
[123] Q. Gu, X. Fu, X. Wang, S. Chen, D. Y. C. Leung, X. Xie. *Applied Catalysis B: Environmental* **2011**, *106*(3-4), 689-696.
[124] A. Patsoura, D. I. Kondarides, X. E. Verykios. *Applied Catalysis B: Environmental* **2006**, *64*(3-4), 171-179.
[125] H. Yoshida, K. Hirao, J. I. Nishimoto, K. Shimura, S. Kato, H. Itoh, T. Hattori. *Journal of Physical Chemistry C* **2008**, *112*(14), 5542-5551.
[126] K. Maeda, K. Domen. *Chemistry of Materials* **2010**, *22*(3), 612-623.
[127] Y. K. Kho, A. Iwase, W. Y. Teoh, L. Mädler, A. Kudo, R. Amal. *Journal of Physical Chemistry C* **2010**, *114*(6), 2821-2829.
[128] G. L. Chiarello, E. Selli, L. Forni. *Appl. Catal. B: Environ.* **2008**, *84*, 332-339.
[129] M. Tripathi, K. Pandey, S. D. Kumar. *Solar Energy Materials and Solar Cells* **2007**, *91*(18), 1663-1668.
[130] M. A. Khan, O. B. Yang. *Catalysis Today* **2009**, *146*(1-2), 177-182.
[131] W. C. Lin, W. D. Yang, I. L. Huang, T. S. Wu, Z. J. Chung. *Energy and Fuels* **2009**, *23*(4), 2192-2196.
[132] M. Cornuz, M. Grätzel, K. Sivula. *Chemical Vapor Deposition* **2010**, *16*(10-12), 291-295.
[133] M. Frites, Y. A. Shaban, S. U. M. Khan. *International Journal of Hydrogen Energy* **2010**, *35*(10), 4944-4948.
[134] S. Kumari, A. P. Singh, Sonal, D. Deva, R. Shrivastav, S. Dass, V. R. Satsangi. *International Journal of Hydrogen Energy* **2010**, *35*(9), 3985-3990.
[135] N. T. Hahn, H. Ye, D. W. Flaherty, A. J. Bard, C. B. Mullins. *ACS Nano* **2010**, *4*(4), 1977-1986.
[136] V. M. Arakelyan, V. M. Aroutiounian, G. E. Shahnazaryan, E. A. Khachaturyan. *Renewable Energy* **2008**, *33*(2), 299-303.
[137] L. Armelao, D. Barreca, G. Bottaro, A. Gasparotto, C. MacCato, C. Maragno, E. Tondello, U. L. Štangar, M. Bergant, D. Mahne. *Nanotechnology* **2007**, *18*(37).
[138] J. Bandara, C. P. K. Udawatta, C. S. K. Rajapakse. *Photochemical and Photobiological Sciences* **2005**, *4*(11), 857-861.
[139] J. Gong, Y. Lai, C. Lin. *Electrochimica Acta* **2010**, *55*(16), 4776-4782.
[140] C. C. Hu, J. N. Nian, H. Teng. *Solar Energy Materials and Solar Cells* **2008**, *92*(9), 1071-1076.

[141] C. M. Janet, S. Navaladian, B. Viswanathan, T. K. Varadarajan, R. P. Viswanath. *Journal of Physical Chemistry C* **2010**, *114*(6), 2622-2632.
[142] D. I. Kondarides, A. Patsoura, X. E. Verykios. *Journal of Advanced Oxidation Technologies* **2010**, *13*(1), 116-123.
[143] S. Xu, D. D. Sun. *International Journal of Hydrogen Energy* **2009**, *34*(15), 6096-6104.
[144] L. S. Yoong, F. K. Chong, B. K. Dutta. *Energy* **2009**, *34*(10), 1652-1661.
[145] F. Gärtner, B. Sundararaju, A. E. Surkus, A. Boddien, B. Loges, H. Junge, P. H. Dixneuf, M. Beller. *Angewandte Chemie - International Edition* **2009**, *48*(52), 9962-9965+9771.
[146] M. Matsuoka, M. Kitano, M. Takeuchi, K. Tsujimaru, M. Anpo, J. M. Thomas. *Catalysis Today* **2007**, *122*(1-2), 51-61.
[147] M. Kitano, K. Iyatani, K. Tsujimaru, M. Matsuoka, M. Takeuchi, M. Ueshima, J. M. Thomas, M. Anpo. *Topics in Catalysis* **2008**, *49*(1-2), 24-31.
[148] R. Brahimi, Y. Bessekhouad, A. Bouguelia, M. Trari. *Journal of Photochemistry and Photobiology A: Chemistry* **2007**, *186*(2-3), 242-247.
[149] G. L. Chiarello, L. Forni, E. Selli. *Catalysis Today* **2009**, *144*(1-2), 69-74.
[150] D. Barreca, A. Gasparotto, E. Tondello. *Journal of Materials Chemistry* **2011**, *21*(6), 1648-1654.
[151] M. Grandcolas, M. Karkmaz-Le Du, F. Bosc, A. Louvet, N. Keller, V. Keller. *Catalysis Letters* **2008**, *123*(1-2), 65-71.
[152] J. Graciani, A. Nanbu, J. Evans, J. A. Rodriguez, J. F. Sanz. *J. Am. Chem. Soc.* **2008**, *130*, 2056.

Chapter 2

CHARACTERIZATION TECHNIQUES

In this chapter, an overview of the main characterization techniques used in this work to study the reactivity and the morphological and chemical properties of the samples is reported. The aim of the present chapter is not that of providing exhaustive information about all the techniques. Rather, it is expected to furnish to the reader the main elements to better appreciate the results obtained and described in the following chapters of this thesis.

Characterization of the textural properties: physisorption of N_2

The catalytic activity of a solid material is strictly related to the morphology and the extension of its surface. The dimension and the texture of pores also play a crucial role since they can have a strong influence on the reaction selectivity: in fact they influence the diffusion processes of both reagents and products, in some cases inducing the selective formation of only a one product ("shape selectivity"). Key examples are some cracking[1-3] and isomerization catalysts.[4, 5] Moreover, an adequate texture of the support is of fundamental importance to obtain catalysts resistant to the sinterization, especially when subjected to high temperature treatments. The ability to measure the surface area of a catalyst and the dimension and distribution of its pores is therefore essential in order to better understand the performance of a catalyst.

The common method used to determine the textural characteristics of a solid material is based on the physisorption of a gas (reversible adsorption) because of the following advantages [6]

- it is accompanied by low adsorption heat. In fact the adsorption process is determined by weak and reversible interactions (ion-dipole, ion-induct dipole, dipole-dipole, dipole-induct dipole, quadrupole interactions). This implies that the process does not modify the surface of the sample;
- many molecular layers of adsorbate can be formed, leading to a completely filling of the pores allowing to measure the pore volume;
- it occurs at low temperatures;
- physisorption equilibrium is quickly reached since the process energy is zero (except in the case of adsorption into small pores, where there are diffusion limitations);
- physical adsorption is a reversible process and this permits the study of both the adsorption and desorption processes;
- it allows to estimate the total surface area of a solid since physisorbed molecules are not restricted to specific sites but they are free to completely cover the surface.

Brunauer, Emmet and Teller have developed a method (commonly regarded as BET) which allows the experimental determination of the number of adsorbate molecules needed for the formation of the theoretical monolayer. If the area effectively occupied by a single adsorbed molecule is known, it is possible to determine the total surface area. BET model starts from the assumption that adsorption process is an equilibrium with the formation of a series of layers, where the most external one is formed by adsorbate molecule directly in contact with the vapour phase.

The surface area can be determined by directly applying the BET equation:

$$\frac{p}{n(p^0-p)} = \frac{1}{n_m C} + \frac{C-1}{n_m C} \times \frac{p}{p^0} \qquad \text{Eq. 2.5}$$

where: p gas pressure;

p^0 saturation gas pressure;

n adsorbed gas at the pressure p (grams);

n_m adsorbed gas corresponding to the monolayer formation (grams);

C BET constant (dependent on the interaction type between adsorbent and adsorbate).

In the range $0.05 < \frac{p}{p^0} < 0.30$, the plot of $\frac{p}{n(p^0-p)}$ versus $\frac{p}{p^0}$ is generally a straight line. The slope s and the intercept i are:

$$s = \frac{C-1}{n_m C} \quad \text{and} \quad i = \frac{1}{n_m C} \qquad \text{Eqs. 2.6-2.7}$$

Therefore it is possible to obtain the values of n_m and C. Then, the surface area can be calculated as follow:

$$S_t = \frac{n_m N_A a_m}{M_w} \qquad \text{Eq. 2.8}$$

where: N_A Avogadro's constant;

M_W adsorbate molecular weight;

a_m area occupied by an adsorbate molecule (at -196°C, for N_2 a_m = 0.162 nm^2).

The major part of the materials having high surface areas, useful for catalysis, shows a porous structure. It is thus usual to distinguish between external and internal area, indicating with the latter term the contribution to the surface area due to the

pores of the system. It is worth noting that pores accessibility, and therefore the volume and the relative surface area, depends on the shape and the dimension of gas molecule used in the analysis.

Pores can vary in dimensions and shapes in a wide range even in the same material. Based on dimensions, they can be divided into three groups:

- *micropores*, with diameters less than 2 nm;
- *mesopores*, with diameters in the range 2-50 nm, typical of not crystalline materials;
- *macropores*, with diameters larger than 50 nm.

The porous system of a material can be first classified from the shape of the physisorption isotherm. The International Union for Pure and Applied Chemistry (IUPAC) have stabilised rules to classify the most common isotherms into six types (Figure 2.3).

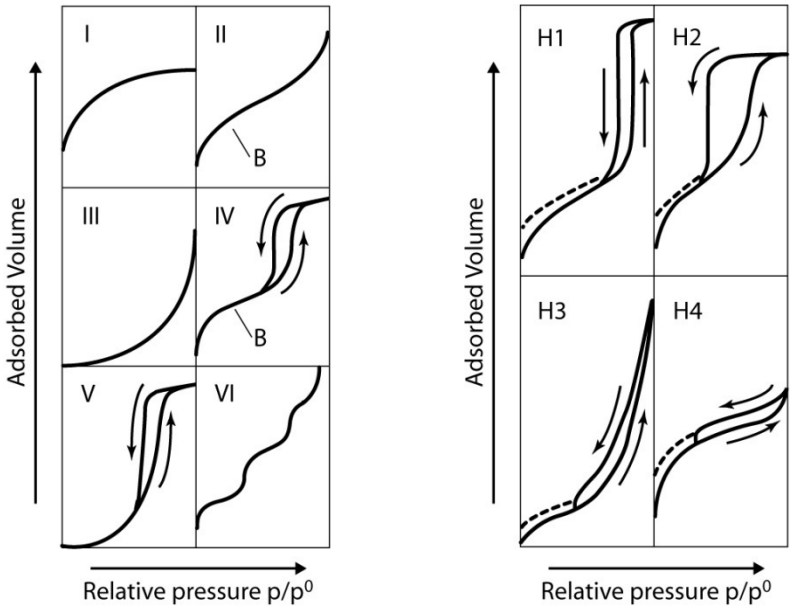

Figure 2.3: type of isotherms (left) and hysteresis (right).

Type I isotherm is typical of microporous systems, in which the external surface area is small while the internal contribute is relevant.

Type II isotherm is generally observed in non-porous or macroporous systems and represents a multi-layer adsorption. The B point (at the inflection point) is generally considered as the point of monolayer formation.

Type III and V isotherms are not common and indicate a very weak interaction between adsorbent and adsorbate. This problem can be solved using a different adsorbate in order to obtain a physisorption curve easier to analyze.

Type IV isotherm is the most common one and it is typical of mesoporous systems. The initial part of the isotherm is similar to that of type II one while, at higher relative pressures, it shows the typical hysteresis associated to capillary condensation that takes place into the mesopores. The hysteresis shape can change to a great extent according to pores geometry. IUPAC has classified the hysteresis shapes into four main groups, denoted as H1, H2, H3 and H4 (Figure 2.3). Type H1 and H4 hysteresis represent two opposite and extreme situations: the first is often find in compact agglomerates of spherical particles with uniform dimensions. The latter one is obtained in the case of materials with pores formed by the aggregation of bidimensional particles. Type H2 and H3 hysteresis represents intermediate situations between those two extremes. However, hysteresis can not be easily classified as most of the materials show heterogeneous distributions in shapes and dimensions of pores.

Type VI isotherm represents a multilayer adsorption which occurs by subsequent passages onto a non-porous surface.

Many methods have been developed to estimate pores distribution. The difference along them arises from the pores dimension range in which they can be applied. According to the objectives of the present research work, it has been decided to focus the attention to the mesopores. In fact, while some micropores can be present in the fresh materials, they are not thermally stable as they can easily collapse even under mild conditions.

The method commonly used to describe mesopores (and smaller macropores) distribution is that developed by Barret, Joyner and Halenda (BJH method). It describes adsorption and capillary condensation processes which take place inside the mesopores. In the capillary condensation range ($0.40 < p/p^0 < 0.98$), an increase of the relative pressure corresponds to an increase of the thickness of the layer adsorbed on the pores walls. The capillary condensation in cylindrical pores is described by the Kelvin equation:

$$\ln \frac{p}{p^0} = - \frac{\gamma \, 2V_m \, \cos\theta}{RTr_c} \qquad \text{Eq. 2.9}$$

where: p pressure of the gas;

p^0 saturation pressure of the gas;

γ surface tension of the liquid;

V_m liquid molar volume;

R gas constant;

T absolute temperature;

r_c pore radius where capillary condensation occurs;

θ contact angle between adsorbed molecules and thin layer adsorbed onto the walls; for simplicity, in the normal applications it is equal to 0.

Analyzing the physisorption isotherm in the $0.40 < \frac{p}{p^0} < 0.98$ range (region comprised between the formation of the monolayer and the saturation of the system, equivalent to a complete emptiness of pores) it is possible to obtain the mesoporous volume and pores distribution.

Characterization of the accessibility of the metal phase: chemisorption

Chemisorption is based on a specific interaction between a probe molecule and the active phase of a catalyst (generally a metal). The method consists in the adsorption of a probe molecule that is able to chemically react with the metal, generating a single layer of chemisorbed molecules. The measure of the volume of adsorbed gas could allow the calculation of the metal dispersion of the sample. The most common gases used for chemisorption studies are hydrogen and carbon monoxide, but also nitrogen oxides or oxygen are used as probe molecules.

The number of surface metal atoms $N_{(s)M}$ and the active metal surface S_M can be obtained from the following equations:

$$N_{(s)M} = n \frac{V}{V_m} N_A \qquad \text{Eq. 2.10}$$

$$S_M = N_{(s)M}\, a_M \qquad \text{Eq. 2.11}$$

where: V adsorbed gas volume until single layer formed;

V_m gas molar volume;

a_m surface covered by a single metal atom;

n number of metal atoms needed to adsorb a single hydrogen molecule (also commonly referred as "chemisorption reaction stoichiometry");

N_A Avogadro's constant.

Generally, the chemisorption stoichiometry with hydrogen is assumed to be 2. In fact, H_2 can be activated by the metal and subsequently each metal atom can form a bond with a hydrogen atom. However, this is not always true for noble metals which form hydride species or when the active phase is extremely dispersed, leading to particles lower than 1 nm.[7] Moreover, reducible oxides or active carbon can show spillover effects which should be taken into account.[7]

In the case of dissociative adsorption (as is the case of hydrogen) the Langmuir isotherm equation can be applied, assuming a constant chemisorption energy:

$$n^s = \frac{n_m^S\, bp^{\frac{1}{2}}}{1 + bp^{\frac{1}{2}}} \qquad \text{Eq. 2.12}$$

where: p gas pressure;

n^s quantity of gas adsorbed at pressure p;

n_m^s quantity of gas needed for single layer formation;

b constant.

In the high pressure region, isotherm should be horizontal, corresponding to the saturation limit. However, this is not usual because, in most of the experiments, this region shows a straight positive trend due to the formation of subsequent layers due to the physical adsorption of H_2. The hydrogen volume corresponding to the formation of the monolayer can be calculated by extrapolating the linear part of the isotherm to zero pressure. This procedure is used to well correct the values for the physisorption. Other more complex methods are based on the subtraction of the physisorption contribute.

From the chemisorbed H_2 volume it is possible to obtain the metal dispersion D_M and the average metal particle diameter d_M, assuming a geometrical shape of the particles:

$$D_M = \frac{N_{(s)M}}{N_{(tot)M}} \qquad \text{Eq. 2.13}$$

$$d_M = 6\,\frac{S_i V_i}{S_i A_i} = 6\,\frac{V_M}{a_m}\,\frac{N_{(tot)M}}{N_{(s)M}} = 6\,\frac{V_M}{a_m}\,\frac{1}{D_M} \qquad \text{Eq. 2.14}$$

where: $N_{(s)M}$ surface metal atoms;

$N_{(tot)M}$ total metal atoms;

6 geometrical factor.

V_M is the volume of a bulk metal atom. It can be calculated from the equation 2.15:

$$V_M = \frac{M_w}{\rho\, N_A} \qquad \text{Eq. 2.15}$$

where: M_w atomic weight of the metal;

ρ density of the metal.

In the present thesis, chemisorption experiments were performed on a Micromeritics ASAP 2020C. The samples, placed in an U-shaped quartz reactor with an internal diameter of 1 cm, were subjected to thermal and/or chemical treatments by using the automatic valve apparatus. Usually, samples are cleaned by a treatment under

O_2/Ar, the metallic phase is reduced under H_2/Ar at the desired temperature and the sample is then evacuated at 350°C for at least 4 hours. These treatments are essential to clean and reduce the sample and finally to eliminate the hydrogen gas from the surface of the catalyst.

Powder X-ray diffraction

X-ray crystallography is a well established method to explore the structure of a material. This technique is based on the diffraction principle of a x-ray beam by a family of planes of a crystalline lattice. The intensity of the diffracted beam is not zero only when all the diffracted rays give constructive interference. In these conditions, the Bragg's equation is satisfied:

$$\lambda = 2d\text{sen}\theta \qquad \text{Eq. 2.16}$$

where: λ wavelength of the incident radiation;

d interplanar spacing;

θ incident angle of X-ray beam.

In this thesis, powder XRD was used to identify the composition of the phases and to estimate the average dimension of the crystallites.

Most of the powder XRD patterns were recorded with a computer-controlled Philips X'Pert diffractometer using CuK_α radiation (λ=0.154 nm). The data were collected at 0.02 ° in the 2θ range from 10 ° to 100 °.

The experimental XRD peak amplitude (B_{obs}) is composed of two contributions: the first is due to the finite crystallites dimension (B_d) while the second is typical of the instrument (B_{instr}). These three parameters are related by the equation:

$$B_{obs}^2 = B_d^2 + B_{instr}^2 \qquad \text{Eq. 2.17}$$

Taking into account the same instrumental contribution, the larger the XRD peaks (Full Width at Half Maximum, FWHM), the lower the crystallites dimension. In order to know the B_d value it is necessary to know the instrument contribution (B_{instr}) to peak broadening. This contribute is generally quantified using reference materials, with large crystals (100-1000 nm) and with good crystallinity. The assumption is that this type of material does not significantly contribute to peak broadening; therefore, it is possible to gain the diffractometer contribute.

XRD peaks broadening, even for the reference material, is dependent on the angle which characterise reflections in the spectrum. For the calculation of B_d it is

necessary to consider the amplitude of a peak of the reference material which is near to that considered in the sample spectrum.

The mean crystallites dimension $\bar{d}$ (in nm) can be determined from the value of the peak broadening (B_d) according to Scherrer's equation:

$$\overline{d} = \frac{K}{B_d \cos\theta} \qquad \text{Eq. 2.18}$$

where: λ wavelength of the radiation used (in this work, Cu K_α 0.1541 nm);

K Scherrer's constant (0.90 if the width is measured at half maximum; 1.05 if the width is obtained dividing peak area by its height);

θ Bragg's angle.

The peak broadening allows the crystallites dimension to be measured in the direction perpendicular to the considered reflection plane. In this way, $\bar{d}$ values obtained from different diffraction peaks would be equal only if reflection planes are randomly orientated with respect of external shape of the crystallites.

Transmission Electron Microscopy techniques

Catalyst characterization is the cornerstone of the science of catalysis. Not only we need to know the electronic and geometric structure of the active components in a heterogeneous catalyst but also we need to understand how the reactant molecules interact with or modify these components during a catalytic reaction.

Among many characterization techniques, advanced electron microscopy is the only technique that can provide information on the individual components of heterogeneous catalysts. All the other techniques (e.g. X-ray diffraction, X-ray absorption spectroscopy, IR spectroscopy, nuclear magnetic resonance spectroscopy, X-ray photoelectron spectroscopy, etc.) provide information either averaged over millions to trillions of nanocomponents or they (e.g., scanning probe microscopy techniques) require stringent conditions on the samples to be examined. Moreover, some techniques are not useful when the dimension of crystallites are smaller than 3 nm. On the other hand, small particles, clusters or even single atoms can be directly observed in the modern electron microscopes. Therefore, advanced electron microscopy techniques are indispensable to understand the properties of heterogeneous catalysts and to provide useful information for the development of nanostructured catalysts.

The transmission electron microscopy (TEM) technique was initially conceived as a response to the limitation of light microscopes for imaging very small objects shortly after de Broglie's discovery that electrons could be treated theoretically as waves. The resolution of a microscope is the minimum distance at which two objects may be distinguished. The maximum theoretical resolution (δ) is proportional to the wavelength of the radiation used (λ). Basing on the classical Rayleigh criterion for light microscopy:

$$\delta = 0.61\,\theta \qquad \text{Eq. 2.19}$$

for green light in the middle of the visible spectrum λ is about 550 nm, hence the maximum theoretical resolution (δ) of a good light microscope is of the order of 300 nm. It is clear that this resolution is not low enough to characterize the nanocomponents typical of a heterogeneous catalyst.

Instead, starting from the de Broglie's equation we can calculate the maximum resolution for a microscope which uses electrons. Based on de Broglie's ideas of the wave-particle duality, we can relate the particle momentum p (and thus, the electron mass m_0 and its velocity v) to its wavelength λ through Planck's constant (h):

$$\lambda = \frac{h}{p} = \frac{h}{m_0 v} \qquad \text{Eq. 2.20}$$

In the TEM a momentum is imparted to the electrons accelerating them by a potential drop, V. This gives them a kinetic energy eV. This potential energy must equal the kinetic energy of the electrons at the end of the accelerating section of the instrument:

$$m_0 eV = \frac{(m_0 v)^2}{2} \qquad \text{Eq. 2.21}$$

The momentum p can be written also as a function of the kinetic energy eV as follow:

$$p = (2m_0 eV)^{1/2} = m_0 v \qquad \text{Eq. 2.22}$$

Thus it is possible to obtain the relationship between the electron wavelength λ and the accelerating voltage of the electron microscope, V:

$$\lambda = \frac{h}{(2m_0 eV)^{1/2}} \qquad \text{Eq. 2.17}$$

An electron accelerated to 100 keV has a wavelength (which more or less corresponds to the maximum theoretical resolution of a microscope) of about 0.004 nm, and is 100 times smaller than the diameter of an atom. Moreover, by increasing the accelerating voltage the wavelength of the electrons decrease. It is noteworthy that equations 2.14-2.17 does not take into account relativistic effects. These can not be ignored at 100-keV energies and above because the velocity of the electrons becomes greater than half the speed of light. This is the first reason that not allow the potentiality of the electron microscope to attain such sub-atomic resolution to be fulfilled. In addition to this intrinsic limitation, considerable practical limitations involved in the microscope construction must be taken into account (especially for the homogeneity of the magnetic fields used as lenses). However, atomic scale resolution is attainable using modern instruments.

The Transmission Electron Microscope (TEM) consists of a vertical column in which the electron beam passes from an electron source at the top, through the specimen and down to the bottom of the column where the image is formed and revealed (Figure 2.6).

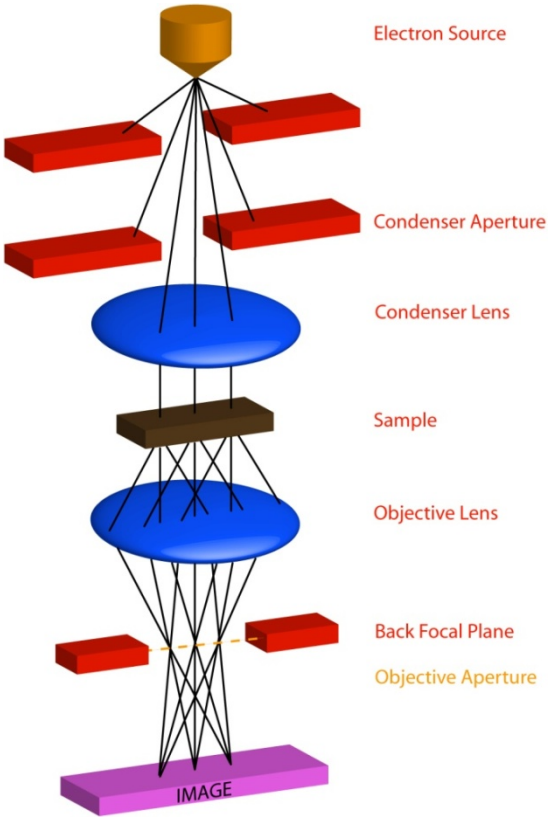

Figure 2.6: schematic representation of the TEM column.

The column is held under ultra high vacuum conditions by a system of high performance pumps in order to reduce the scattering of the electron beam by gas atoms. Electromagnetic coils, known as lenses, are positioned around the column along its length and are used to modify the trajectories of the electrons in the beam, either concentrating or spreading the beam as required (in an analogous way to the optical lenses in a light microscope). Apertures of different diameters can be inserted into the electron beam at several positions along the column. This is done to select part of the beam and exclude the contribution of the rest.

Two types of electron sources exist and they are characterized by the way in which the electron beam is generated. The most common source involves the thermionic emission of electrons from a filament of tungsten or LaB_6 heated by an

electric current to about 2500°C and 1500°C, respectively. At these temperatures, a significant number of electrons obtain energy equal or greater than the work function of the material and are able to leave the filament passing into the vacuum. The produced electrons are focused and accelerated by an electrostatic field and they enter into the TEM column. The strength of this field determines the kinetic energy of the electron beam (Eq. 2.15). In practice, an applied potential of at least 100 kV is advisable for High-Resolution TEM (HRTEM). The electron beam may also be generated in a Field Emission Gun (FEG). It works at much lower temperatures, about 300°C, and contains two successive electrostatic fields. The tungsten filament in a FEG has an extremely fine tip. The first electrostatic potential extracts electrons from the filament through this tip. The second potential is used, as above, to accelerate the electrons and form the high energy beam. Because the filament area of the emission of electrons is very low, the beam produced by a FEG is much more intense and much more spatially coherent than the beam from a thermionic filament. Furthermore, the variation in energy within the beam is very small. This allows to obtain more resolved images which is particularly useful for HRTEM measures.

After electrons are produced, they are selected by the Condenser Apertures and the electrons are formed in a parallel beam by the Condenser Lens system. Moreover, this system allows the set of the beam diameter to a desired value. Then, electron beam passes through the specimen, which is mounted on the specimen holder. The incident beam interact with the internal crystal structure of the sample and emerges as a set of diffracted and non-diffracted (transmitted) beams. These beams are again focused by the Objective Lens. It is clear that beams diffracted at the same angle are brought to a focus in a plane that lies after or “behind” the lens and so this is called the Back Focal Plane (BFP). In this plane, the diffraction pattern is formed. Considering the rules for diffraction, each spot is related to one family of crystal planes at one particular orientation in a similar way of the formation of the diffraction pattern in single crystal X-ray diffraction. The Objective Lens performs a Fourier Tranform on the exit wave to form the diffraction pattern; the image is an inverse Fourier Transform of this diffraction pattern and is closely related to the internal structure of the sample.

Images and diffraction patterns are visualised on a fluorescent screen and may be digitally recorded using a camera positioned below the fluorescent screen. To record

a diffraction pattern, the strength of the Objective Lens is changed in order to throw the diffraction pattern onto the image plane. Further electromagnetic lenses are incorporated between the BFP and the image plane in commercial TEM instruments to allow the operator to focus and adjust the magnification of the final image.

The diffraction pattern contains electrons from the whole area of the specimen illuminated by the beam. Such a pattern is not very useful because the specimen will often be buckled. Furthermore, the direct beam is often so intense that it will damage the camera. Therefore there are basic TEM operations that allow both to select a specific area of the specimen to contribute to the diffraction pattern and to reduce the intensity of the diffraction pattern reaching the screen. There are two ways to perform this operation:

- make the beam smaller;
- insert an aperture above the specimen which would only permit electrons that pass through it to hit the specimen.

The standard way is the second solution. This operation is called Selected-Area Diffraction (SAD). It is clear that it is not possible to insert an aperture at the specimen plane. Therefore the aperture is inserted in one of the image planes, then it creates a virtual aperture at the plane of the specimen. Then any electron that hits the sample outside the area defined by the virtual aperture will be excluded from contributing to the diffraction pattern that is projected on the viewing screen.

Independently from the sample, SAD pattern will show a bright central spot (the Transmitted Beam) which contains the direct electrons and some scattered electrons (Figure 2.7). After the diffraction pattern area is selected, it is possible to perform the two most basic imaging operations in the TEM. It is possible to form the image in the TEM by using the central spot or some or all of the scattered electrons. To do this last operation, an aperture is inserted into the Back Focal Plane of the Objective Lens, blocking most of the diffraction pattern except that which is visible through the aperture. If the direct beam is selected, the resultant image is called bright-field (BF) image. On the contrary, if scattered electrons of any form are selected, the resultant image is called dark-field (DF) image. The BF detector is therefore put directly down to the direction of the beam in the TEM column. For the DF images, rather than using the

BF detector, it is usually used an annular detector, which surround the BF detector. This is called Annular Dark-Field (ADF) imaging.

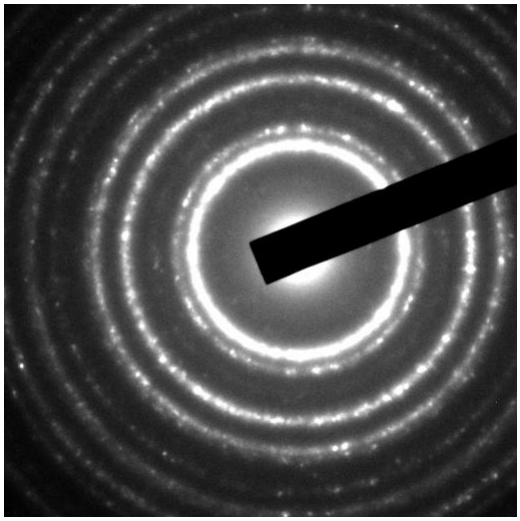

Figure 2.7: a SAD pattern which illustrates the presence of the direct electrons (bright central spot) and scattered electrons (rings more or less intense).

There is another way to perform the analysis of the specimen. Instead of directing a parallel beam onto the sample it is possible, trough optics system, to deliberately create a focused convergent beam. Any useful image is not formed immediately. It is needed to scan the beam; this operation mode is standard for the Scanning Transmission Electron Microscopy (STEM) technique. To do this it is necessary to use more lenses than in the TEM mode. Nowadays, this auxiliary lens for operating in the STEM mode is standard on TEMs that also operate as STEMs. One of the best advantages of the use of the STEM technique is that the sample does not move. Moreover, the combination of the STEM mode with the ADF detector leads to the obtainment of images less noisy than TEM DF. However, ADF detector collect also some Bragg electrons instead of only scattered particles. If, instead, the system is set up to avoid that Braggs's electrons hit the detector, the image is formed only from the very high angle, incoherently scattered electrons. This type of detector is called a High-Angle ADF (HAADF). The images are sometimes called Z-contrast images because this technique is particularly indicated for samples in which atoms present high values of Z. The complete HAADF detector set-up for Z-contrast imaging in a STEM is depicted in the Figure 2.8.

With this detector the species with high values of Z appear bright, on the contrary with light elements which appear dark. As in general the signal strength of the high-angle scattered electrons is proportional to approximately Z^2, this technique is particularly advantageous for detecting supported heavy-metal particles such as Bi, Au, Pt, Ir, Re, W, Pd, Rh, Ru, Ag, etc.. Under optimum conditions, single atoms, dimers, trimers, and small nanoclusters can be observed.

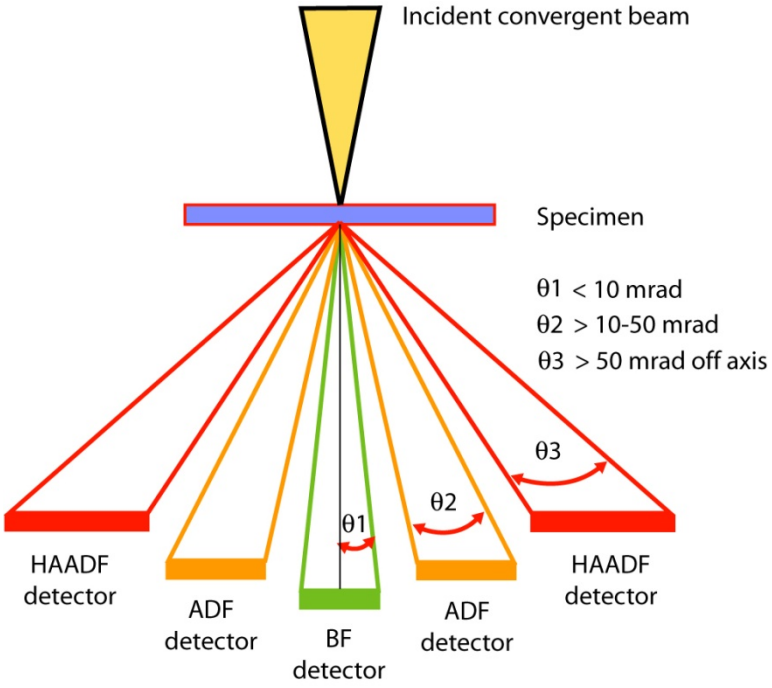

Figure 2.8: schematic representation of the HAADF detector set-up for Z-contrast imaging in a STEM. The conventional ADF and BF detectors are also shown along with the range of electron scattering angles gathered by each detector.

The ability to quantify the size of individual nanostructures in the STEM is primarily determined by the size of the electron beam (probe) and the stability of the nanoclusters under the intense electron irradiation of the beam. The recent development of aberration correctors for STEM has largely improved the spatial resolution allowed by these instruments, taking the resolution to less than 0.1 nm. However, this advance does not automatically improve sensitivity/accuracy when the size measurement is limited by electron irradiation effects such as chemical changes and the movement of the nanoclusters on the support surface.[8]

As well as the elastic interactions of electrons with the specimen which give rise to the image and the diffraction pattern, their inelastic interactions, in which energy is

transferred, also provide useful complimentary information and several analytical techniques have grown up around the TEM to exploit this.[9] An incoming high energy electron may transfer energy to one of the core electrons of an atom such that it is ejected from the atom. An electron at a higher energy level in the atom may then fall into the resulting electron hole releasing its excess energy as an X-ray photon. The frequency of these photons is determined by the difference between the two electron energy levels and will therefore be characteristic of the nature of the atom from which it was emitted. In X-ray Energy Dispersive Spectroscopy (XEDS or EDX), these X-ray photons are collected and number of counts plotted against their energy to give a spectrum. This technique allows quantitative measurement of the elemental composition of the area of the sample illuminated by the beam. This technique provides information which is not available from HRTEM in itself.[10] For this reason, XEDS spectrometer is commonly fitted to the modern TEM.

HRTEM presents also several limitations which must be remembered. Since it is a transmission technique, the samples must be electron transparent and, in addition, must be thin enough to minimise multiple diffraction of the electrons. Specimens below 100 nm should be used wherever possible and, in extreme cases, specimen thicknesses <50 nm are essential. The high energy electron beam may alter and damage the specimen by heating it or by reducing susceptible materials such as some oxides. Moreover, for a correct interpretation of the images, it must be taken into account that HRTEM images are 2-D representation of a 3-D set of objects viewed by transmission rather than reflection.

X-ray Absorption Spectroscopies (XANES and EXAFS)

X-ray Absorption Spectroscopy (XAS) is based on the measurement of the x-ray absorption coefficient of an atomic species in a sample. It is commonly divided into two parts: X-ray Absorption Near Edge Structure (XANES) and Extended X-ray Absorption Fine Structure (EXAFS). This technique is particularly sensitive to the chemical environment of the atomic species in terms of number and type of neighbouring atoms, interatomic distances and level of static and/or thermic disorder. Since X-rays are highly energetic and penetrating, the samples can be studied under all the aggregation states (solids, liquids or gases). The sensitivity is however limited to 4-8 Å in length from the atomic species under investigation. Nevertheless, its main advantage is that the sample does not need to possess long-range order, unlike X-ray diffraction-based techniques that require strictly crystalline samples. Furthermore, it is possible to obtain distinct information regarding all the species present in the sample.

The X-ray absorption coefficient (indicated with μ) of an atomic species is a function that varies smoothly with the energy of the incident X-ray photons (indicated as X photons), but with some sharp discontinuities (absorption edges) that correspond to core electrons that are ejected as photoelectrons. This phenomenon occurs only when the energy of the incident photons is equal or greater than the bonding energy for a certain electron with respect to the nucleus (indicated as E_0).

The ejection probability of a photoelectron decreases with increasing the energy of the X photons with respect to the E_0 of a certain electron. Figure 2.9 schematically reports the trend of μ against the energy of the X photons with the edges due to K, L_I, L_{II}, L_{III} transitions.

Every atoms presents edges at different values of energy of the X photons thus implying that if a scan of the absorption coefficient μ is done varying the energy, it is possible to collect the edges for every atomic species in the sample at the respective energy edges.

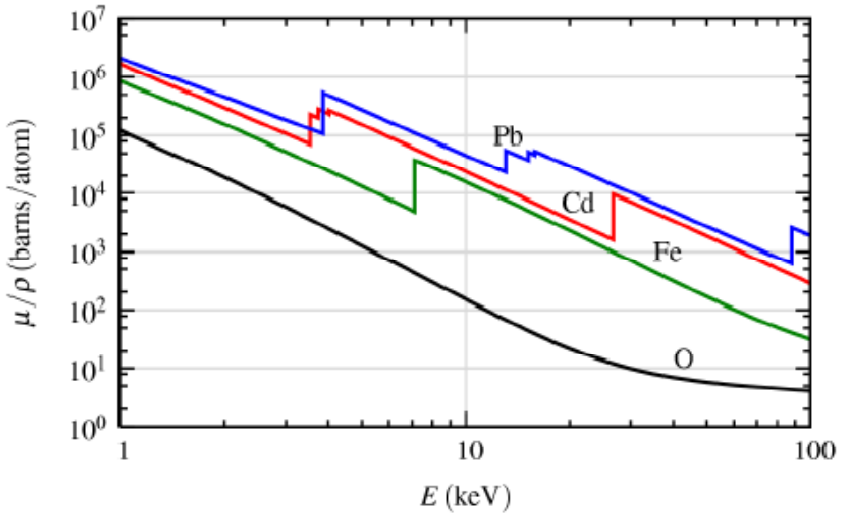

Figure 2.9: *The absorption cross-section μ/ρ for several elements over the x-ray energy range of 1 to 100 keV. Notice that there are at least 5 orders of magnitude in variation in μ/ρ, and that in addition to the strong energy dependence, there are also sharp rises corresponding to the core-level binding energies of the atoms. ρ represents the density of the sample. Reproduced from Matthew Newville, Fundamentals of XAFS, Consortium for Advanced Radiation Sources University of Chicago, Chicago, IL.*

If we suppose to invest a sample of thickness x (cm) with a beam of X photons with a certain energy E_X and intensity I_0, the intensity of the beam I transmitted by the sample can be derived using the Lambert-Beer equation:

$$ln\frac{I_0}{I} = \mu\, x$$

The absorption coefficient μ between two edges always monotonically decreases at increasing the energy of X photons only in the case of a monoatomic gas. In all other situations, μ decreases but not monotonically: it is observed the presence of oscillations in the signal that extend up to 1000 eV after the edge and these oscillations are called EXAFS signal. It is possible to clearly distinguish the different oscillation pattern in the spectra of gaseous and solid samples, for example. In this case, the ejected electrons come in both cases from the same, internal level. Its initial state is the same, and therefore it is not influenced by the aggregation state of the sample. The difference in the EXAFS signal therefore is not due to this reason. Instead, the final states of the ejected electrons are very different. The energy with which the electron leaves the atom is given by:

$$E = E_x - E_0$$

In the case of an isolated atom (as is the situation of a monoatomic gas) the excitation is followed by an ejected electronic wave that propagates isotropically in the space with no perturbation. On the contrary, if the absorbing atom is surrounded by other atoms (as is the situation of a solid sample), these atoms act as scattering centres giving interferences between the ejected electronic wave and those back-scattered by the neighbouring atoms (Figure 2.10). The interference can be either constructive, with an increase of the μ compared to the isolated atom, or destructive, with the decrease of μ.

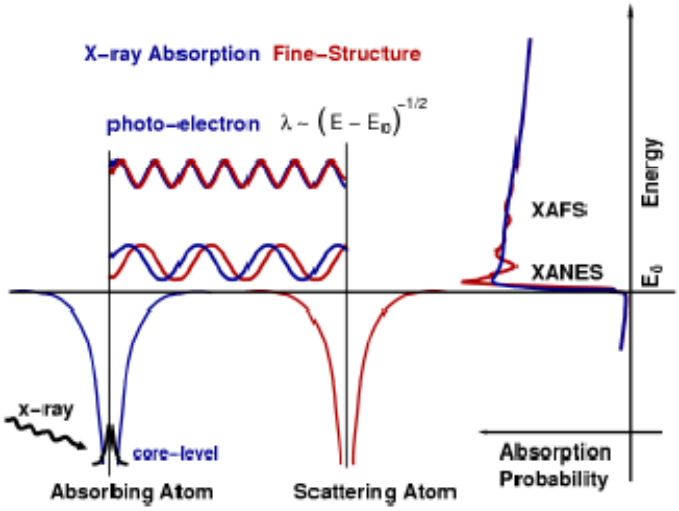

Figure 2.10: *XAFS occurs because the photo-electron can scatter from a neighboring atom. The scattered photo-electron can return to the absorbing atom, modulating the amplitude of the photo-electron wave-function at the absorbing atom. This in turn modulates the absorption coefficient μ(E), causing the EXAFS.*

The amplitude of the oscillation is a linear function of the number of neighbouring atoms. It is therefore possible to correlate the amplitude with the type and number of neighbouring atoms, thus reconstructing the chemical environment around the absorbing atom.

For a given energy of the ejected photoelectron, the type of interference between the exiting wave and those back-scattered depends on the path followed by the photoelectron and therefore by the interatomic distances. Furthermore, the type of generated wave is dependent upon the type of neighbouring atoms.

XANES spectra instead are those extending very close to the absorption edge, generally in the first 50 eV after the edge. Their shape is strictly related with the geometry of the absorbing site and it is also very sensitive to the valence state of the atom, being the energy of the ejected photoelectron sensitive to the oxidation state of

the atom (presence or absence of electrons in the investigated atom). It is therefore possible to extract useful data about the oxidation state of the atom under investigation.

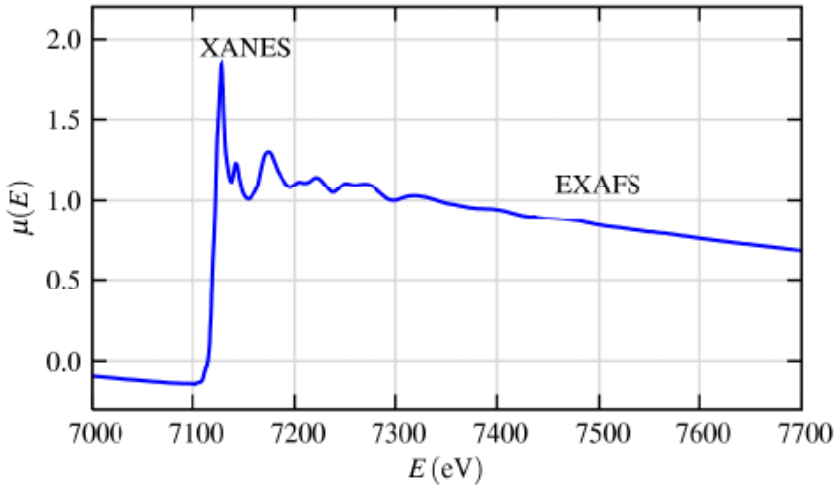

Figure 2.11: *XAFS signal for FeO. The two regions in which XAFS is usually divided, XANES and EXAFS, are highlighted. Reproduced from Matthew Newville, Fundamentals of XAFS, Consortium for Advanced Radiation Sources University of Chicago, Chicago, IL.*

Photocatalysis and photocatalytic activity measurements

The word "*photocatalysis*" derived from the combination of two Greek words: the prefix "photo" (*phos*: light) and the word "catalysis" (*katalyo*: brake apart, decompose). The term can be generally used to describe a process in which light is used to activate a substance, the photocatalyst, which modifies the rate of a chemical reaction without being involved itself in the chemical transformation.

Heterogeneous photocatalysis is by far more intensively studied in recent years even though photocatalytic reaction may occur homogeneously or heterogeneously. This is probably due to its possible use in a variety of environmental and energy-related application as well as in organic syntheses. In heterogeneous photocatalysis, the reaction scheme implies the previous formation of an interface between a solid photocatalyst (metal or semiconductor) and a fluid containing the reactants and products of the reaction. Processes involving illuminated adsorbate-metal interfaces are commonly categorized in the branch of *photochemistry*. Therefore, the term "heterogeneous photocatalysis" is mainly used in cases where light-absorbing semiconductor photocatalyst is utilized, which is in contact with either a liquid or a gas phase.

Semiconductors are particularly useful as photocatlyst because of a positive combination of electronic structure, light absorption properties, charge transport characteristics and excited-state lifetimes.

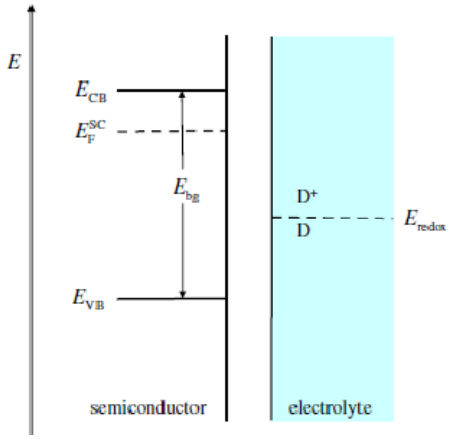

Figure 2.12: *Energy diagram for a n-type semiconductor and a solution with redox couple D/D⁺*

When a semiconductor and a liquid solution come into contact, charge transfer occurs at the interface, until the Fermi level of the two phases reach the same energy

(Figure 2.12). The driving force of this charge transfer is the difference in the tendency of the two phases to gain or to lose electrons. When the Fermi level of the semiconductor is higher of E_{redox} of the solution, electrons will flow downhill in electrochemical potential from the high energy *n*-type semiconductor into the low energy redox species in solution.

Semiconductor can absorb light provided that the incident photon energy is sufficient to overcome the band gap ($h\nu > E_{bg}$) (Figure 2.13). Thus they can only absorb light below a threshold wavelength λ_{th}. The photon energy stored by e^--h^+ pair is equivalent to E_{bg}.

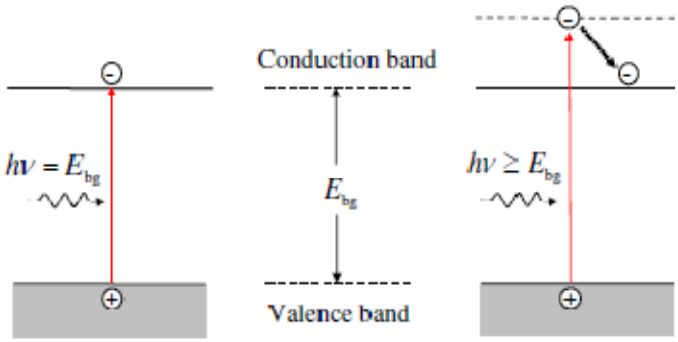

$$\lambda\ (nm) = \frac{1240}{E_{bg}}\ (eV)$$

Figure 2.13: *Photogeneration of electron-hole pairs in an optically excited semiconductor*

As for every heterogeneous catalytic process occurring at a solid-fluid interface, the sequence for converting reactants to products comprises the following independent steps:

1. Transfer of reactant(s) from the bulk fluid to the photocatalyst surface
2. Adsorption oa at least one of reactants
3. Chemical transformation of adsorbed reactants to adsorbed products
4. Desorption of product(s)
5. Transport of products from the fluid-solid interface to the bulk fluid

The main difference with conventional catalysis is the mode of activation of the catalyst, in which thermal activation is replaced by photonic activation.

All photo-induced reaction processes are contained in step 3, in fact:

3a. *Excitation* of the semiconductor by absorption of photons of appropriate energy ($h\nu \geq E_{bg}$)

3b. *Separation* of photogenerated species into quasi-free conduction band electrons and valence band holes.

3c. *Interfacial electron transfer* to adsorbed species and initiation of surface redox reactions.

The ability to photogenerated carriers (electrons or holes) to initiate a specific redox reaction depends on the relative position of E_{CB} or E_{VB} with respect to redox potential of the adsorbed species. As shown in figure 2.14, for reduction of species A, E_{CB} has to be positioned above the energy level of A/A^- couple and for oxidation of species D, E_{VB} has to be positioned below the energy level of D/D^+ couple.

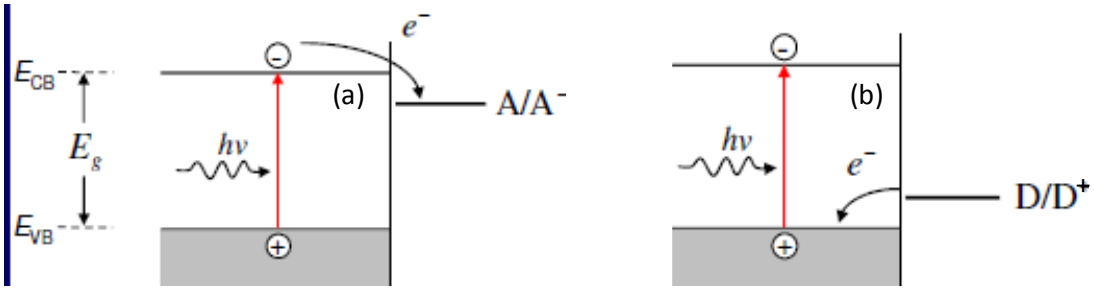

Figure 2.14: *Interfacial charge transfer by capture of (a) a photogenerated electron by an electron acceptor and (b) a photogenerated hole by an electron donor*

The efficiency of semiconductors in promoting photocatalytic areaction is greatly determinated by the extent of the major deactivation processes, which involves electron-hole recombination.

$$\text{recombination: } e_{CB}^- + h_{VB}^+ \rightarrow \text{energy}$$

The rate of charge carrier recombination can be reduced by trapping either the CB-electrons or the VB-holes by suitable surface-adsorbed electron acceptors or donors, respectively. Even when this is the case, a prerequisite for the occurrence of the photocatalytic process is that the surface electron transfer competes kinetically with the electron-hole recombination processes.

The efficiency of a photocatalytic reaction is usually expressed in terms of its quantum yield. For a more complete treatment of this subject the reader should refer to Chapter 1.

The potential applications of heterogeneous photocatalysis depends strongly on the development of reactor designs with increased efficiency. The major challenge in the design of a photocatalytic reactor is the efficient illumination of the catalyst.

Otherwise, photoreactor design is not significantly different than that of conventional catalytic reactors, and can be of any type (batch reactors, plug flow reactors, continuous stirred tank reactors, etc.). A major issue in photoreactor design is whether to use a suspended or a supported photocatalyst.

Figure 2.15 shows a schematic representation of the apparatus for the evaluation of the photocatalytic activity in the near-UV- visible range.

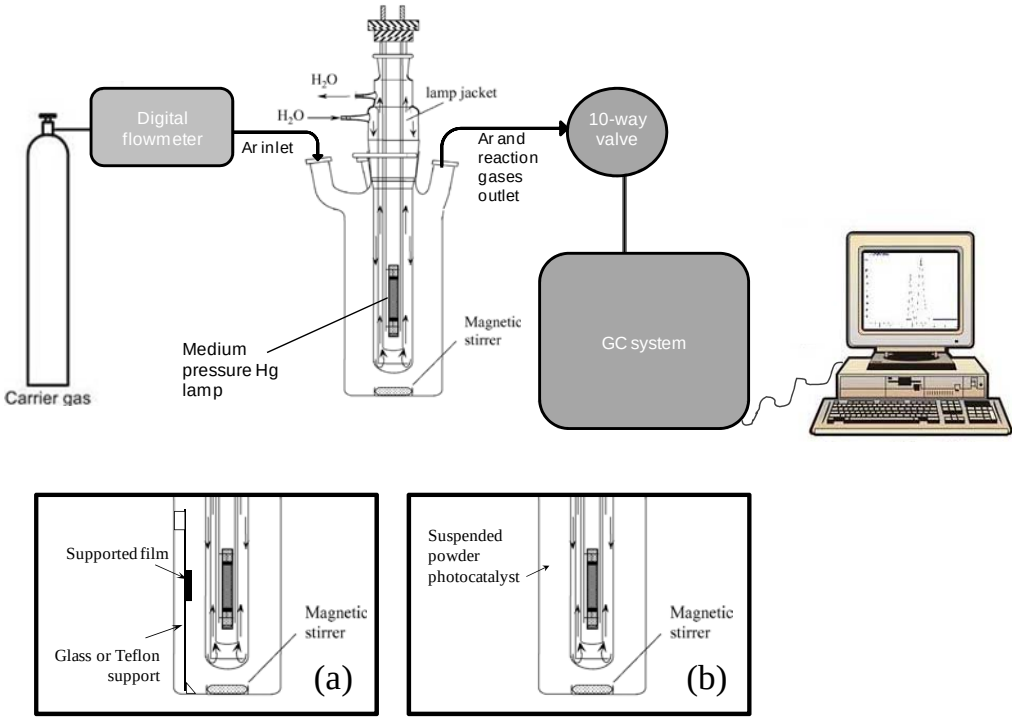

Figure 2.15: *Schematic representation of the reactivity line used for testing the photocatalytic activity of the catalysts (a) configuration for testing the activity of supported systems and (b) for suspended powder systems.*

Medium-pressure mercury lamps operate at vapor pressures greater than 1 bar, but are commonly called high-pressure lamps, especially in Europe. The spectral distribution consists of lines, together with a very weak continuum background. The 253.7 nm line is in most cases absent, owing to the self-absorption by the high concentration of mercury atoms near the bulb walls. Among the commercial lamps differences exist in design and operating conditions, such us temperature and pressure, which lead to small differences in spectral output (Figure 2.16).

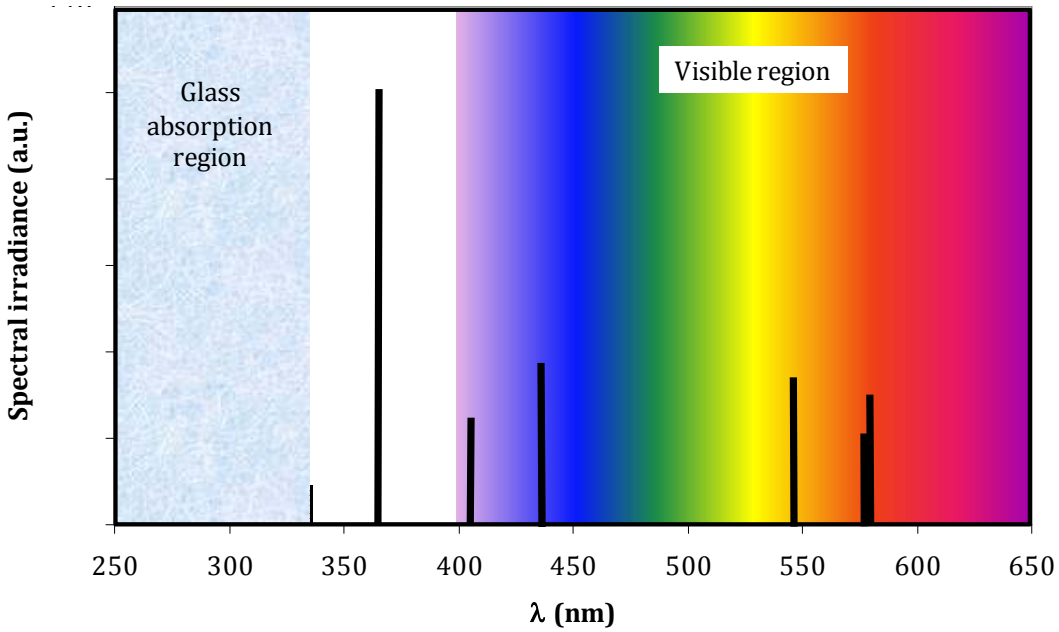

Figure 2.16: *Typical spectral irradiance of medium pressure mercury lamp*

Where an optical source of small size and of very high radiance is required a high pressure arc lamp may be used. These have a filling gas of mercury vapour, mercury vapour plus xenon gas or xenon gas. Metal halide types are also available. The spectral emission of xenon lamps, which at wavelengths shorter than infra-red, closely matches that of a black-body radiator at about 6000 K. This enables their use in photography and as solar radiation simulators. The spectral emission of xenon lamps, which at wavelengths shorter than infrared closely matches that of a black body radiator at about 6000 K, enables their use as solar radiation simulators. Their emission spectrum is continuous from the UV through to the IR regions. The luminance of compact xenon arcs may approach that of the sun and in some lamps with greater than 10 kW rating the luminance may exceed that of the sun. The xenon lamp spectrum differs from all solar spectra because of the intense line output in the 800 - 1100 nm region, with the use of an AM 0 filter is possible to reduce the mismatch. An example of the emission spectra of such a lamp are reported in figure 2.17 for the 150W Solar Simulator.

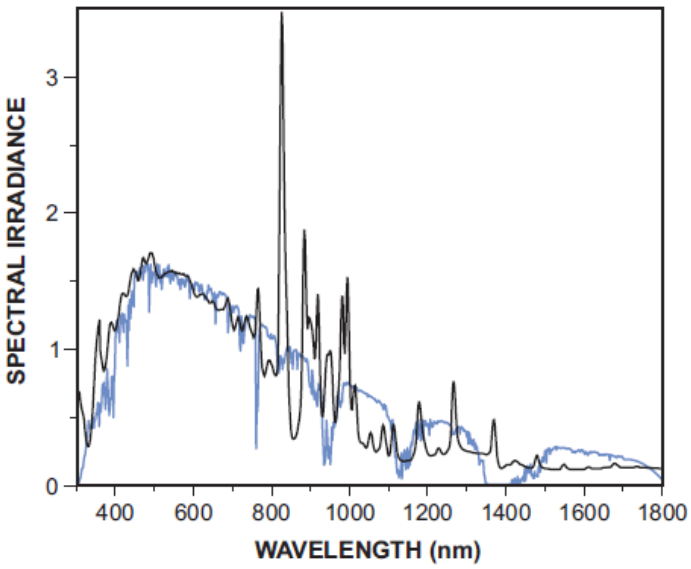

Figure 2.17: *Typical spectral output (black) of a solar simulator shown in Fig.2.18 (there is negligible output from 250-300 nm) and standard AM1.5G spectrum(blue).*

Figure 2.18 shows a schematic representation of the apparatus for the evaluation of the photocatalytic activity under sunlight simulated irradiation.

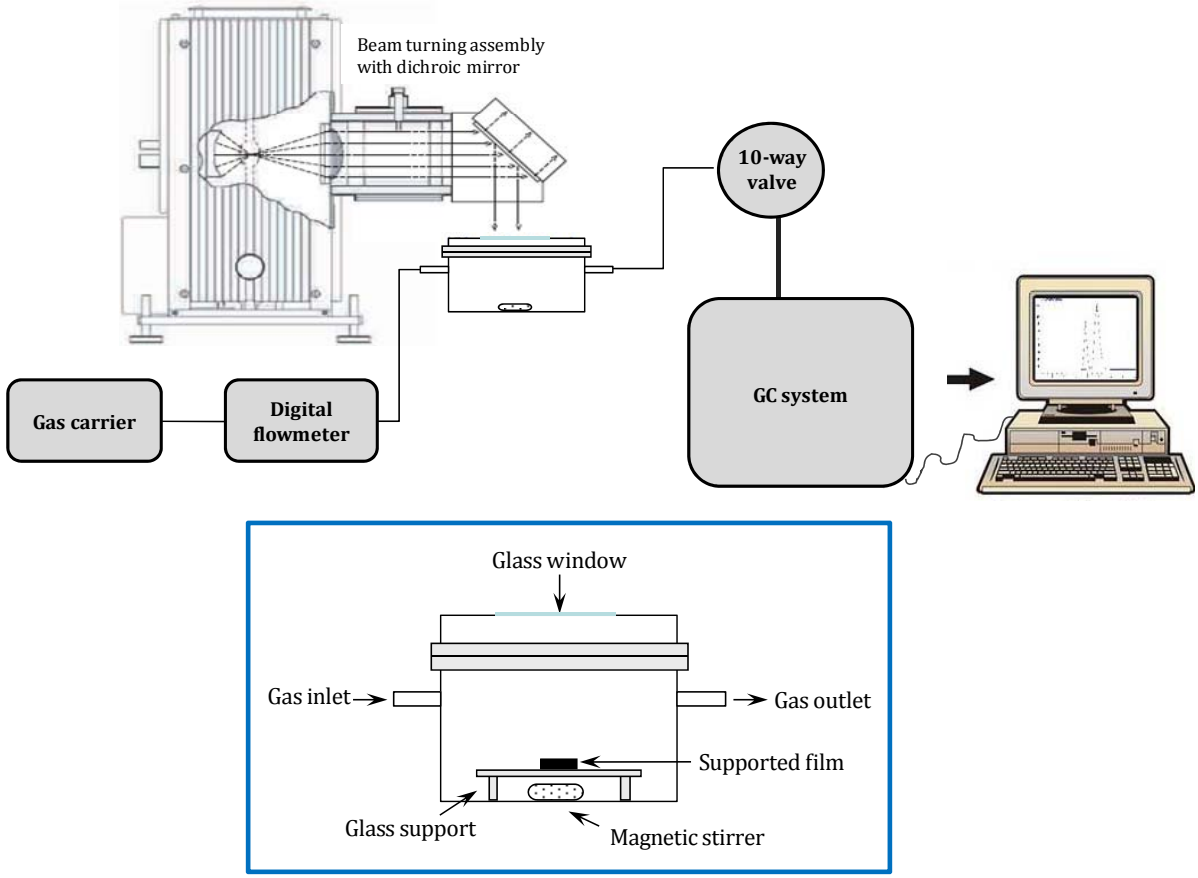

Figure 2.18: *In the upper side schematic representation of the reactivity line used for testing the photocatalytic activity of the catalysts under sunlight simulated irradiation, in the lower side a particular of photoreactor configuration for testing the activity of supported systems.*

The quantum efficiency was evaluated using a small photoreactor and a 4W low pressure mercury lamp (PenRay), with the emission of the single Hg line at 365 nm with a configuration of the equipment analogous to that reported for the near UV-visible tests. In this case, 100 mg of photocatalyst and 18 mL of the aqueous solutions were loaded into the photoreactor while 15 mL/min of Ar were used as transport gas. To have a comparison with literature data on similar systems, the apparent quantum efficiency φ was calculated accordingly to refs [11] and [12] using the formula:

$$\varphi = \frac{n_e}{n_p} = \frac{2 \times n_{H_2}}{n_p}$$

where n_p is the flux of photons emitted by the lamp ($4.57 * 10^{16}$ photons/s), n_e is the flux of photogenerated electrons useful for H_2 production, and n_{H2} is the flux of H_2 calculated from the H_2 flow measured by the analytic system.

The amount of gases produced by the photocatalytic reaction was evaluated as described above.

References

[1] A. Corma, F. V. Melo, L. Sauvanaud, F. Ortega. *Catalysis Today* **2005**, *107-108*, 699-706.
[2] H. B. Mostad, T. U. Riis, O. H. Ellestad. *Applied Catalysis* **1990**, *58*(1), 105-117.
[3] M. W. Anderson, J. Klinowski. *Journal of the American Chemical Society* **1990**, *112*(1), 10-16.
[4] G. D. Yadav, J. J. Nair. *Langmuir* **2000**, *16*(9), 4072-4079.
[5] M. Guisnet, P. Andy, N. S. Gnep, E. Benazzi, C. Travers. *Journal of Catalysis* **1996**, *158*(2), 551-560.
[6] S. J. Gregg, and K. S. W. Sing. *Adsorption, Surface Area and Porosity*. **1981**. Academic Press, New York.
[7] J. M. Gatica, R. T. Baker, P. Fornasiero, S. Bernal, J. Kaspar. *Journal of Physical Chemistry B* **2001**, *105*(6), 1191-1199.
[8] P. E. Batson, N. Dellby, O. L. Krivanek. *Nature* **2002**, *418*(6898), 617-620.
[9] D. Bazin, L. Guczi, J. Lynch. *Applied Catalysis A: General* **2002**, *226*(1-2), 87-113.
[10] D. C. Bazin, D. A. Sayers, J. J. Rehr. *Journal of Physical Chemistry B* **1997**, *101*(51), 11040-11050.
[11] M. L. Satuf, R. J. Brandi, A. E. Cassano, O. M. Alfano. *Industrial and Engineering Chemistry Research* **2007**, *46*(1), 43-51.
[12] N. Strataki, V. Bekiari, D. I. Kondarides, P. Lianos. *Applied Catalysis B: Environmental* **2007**, *77*(1-2), 184-189.

Chapter 3

EMBEDDED SYSTEMS

To enhance the photocatalytic H_2 production, different approaches have been proposed[1] such as the modification of the photocatalyst by metal doping, semiconductor coupling or dye sensitization.[2] Indeed, the presence of metal particles, such as Pt, Au, Pd, Rh, Ni, Cu, or Ag, on the TiO_2 surface has been demonstrated to inhibit charge recombination. Furthermore, as the Fermi levels of these metals are lower than that of TiO_2, photoexcited electrons can be transferred from conduction band (CB) to metal particles on the surface of TiO_2, while photogenerated valence band (VB) holes remain on the TiO_2. Therefore, the possibility of electron-hole recombination is reduced, resulting in efficient separation and more favorite photocatalytic reactions. Pt-TiO_2 systems have shown promising results for H_2 production from water-ethanol or water-glycerol solution.[3-6]

The high cost of platinum and its relatively low availability are strong limitations for its large scale application in photocatalytic systems. This has stimulated increasing attention to largely available and cheap transition metals. In this context, the

appropriate conduction band edges of both CuO and Cu_2O, i.e., -0.96 and -0.22 V, respectively, make Cu a suitable candidate for TiO_2 doping to enhance hydrogen production.[7, 8] Kang et al.[9, 10] discussed the role of CuO_x species in promoting the photocatalyic H_2 production. Their data suggest that the surface CuO_x species are more active with respect to the bulk ones. Korzhak et al.[11] investigated the relationships between the quantum efficiencies of the photocatalytic hydrogen production and the textural characteristics of a mesoporous Cu based TiO_2 system. In particular, the good activity was correlated with the Cu nanostructure obtained by in situ photoreduction of copper(II) chlorides and with the mesoporous structure of the TiO_2 prepared using a structure-directing template method.

Catalysts Preparation

CuO nanoparticles embedded into TiO_2 were prepared by water-in-oil microemulsion (ME) synthesis in the presence of protected Cu nanoparticles and compared with two similar systems obtained by classical "wet impregnation" of preformed TiO_2. In all materials, the nominal Cu loading was 2.5% by weight. The embedded catalyst, denoted in the following as CuO_x@TiO_2, was prepared in a two-step procedure at 25°C. In the first step an aqueous solution of copper nitrate (1.0 M) was added into a cyclohexane solution containing the surfactant t-octylphenoxypolyethoxyethanol (Triton X-100). Afterwards, hydrazine (Cu/hydrazine molar ratio 0.08) was added to the microemulsion system to reduce copper ions, leading to the formation of Cu-based nanoparticles.[12] In the second step, hydrolysis and polycondensation of tetraisopropyl orthotitanate ($Ti(i\text{-}PrO)_4$) were performed by addition a cyclohexane solution of $Ti(i\text{-}PrO)_4$ into the microemulsion system, leading to the formation of the Cu-containing particles embedded in TiO_2. After 16 h, the precipitate was filtered, washed, dried and calcined in air at 450°C for 6 h. The calcination procedure, while transforming the titanium hydroxide into the desired TiO_2, inevitably leads to Cu oxidation.

To highlight the importance of the embedding procedure in the photocatalytic activity, two different Cu-impregnated TiO_2 catalyst reference materials (denoted as CuO_x/TiO_2 hereafter) were prepared by standard impregnation with a copper nitrate

solution in ethanol. Two TiO_2 materials with different phase composition (see below) were used as supports. The first one was obtained using the above-described microemulsion (ME) method, but in the absence of Cu nanoparticles, whereas the second one was prepared by a sol-gel (SG) method. Briefly, TiO_2-SG were prepared by hydrolysis of titanium butoxide in ethanol in presence of HNO_3 as a catalyst.[13] The gel was aged at room temperature for 24h, dried at 80°C overnight and finally calcined at 450°C for 6h. Hereafter, these supports are denoted as TiO_2-ME and TiO_2-SG, where the suffix indicates the preparation procedure. After the support was stirred in the copper nitrate solution for 16 h, the solvent was removed at reduced pressure, and the materials were dried and calcined in air at 450 °C for 1 h.

Catalysts characterization

Table 3.1 summarizes the main textural and structural characteristics of the Cu-containing samples, compared with those of the two bare TiO_2 used for the preparation of the impregnated samples. All the materials present high and very similar total surface area, pore volume and pore size distributions. Consistently with the fact that the wet impregnation techniques requires an additional calcinations step and that the Cu containing phase(s) may block some of the smallest pores, the impregnated Cu/TiO_2 samples show a surface area slightly lower as compared to that of the corresponding bare TiO_2.

Table 3.1. *Textural and structural characterization of TiO_2 and Cu-doped TiO_2 samples.*

Samples	XRD		N_2 physisorption			CO chemisorption
	Composition[a] (%)	Mean CS (nm)	BET SA (m^2/g)	Total V_p (mL/g) [c]	r_p (nm)	CO/Cu[d]
TiO_2-SG	A (64) R (8) B (28)	A (11) R (32) B (11)	71	0.17	8.1[c]-7.1[b]	-
CuO_x/TiO_2-SG	A (64) R (17) B (19)	A (11) R (34) B (14)	65	0.16	8.2[c]-7.3[b]	0.43
TiO_2-ME	A (92) R (3) B (5)	A (14) R (9) B (13)	67	0.11	5.4[c]-4.3[b]	-
CuO_x/TiO_2-ME	A (92) R (3) B (5)	A (14) R (9) B (13)	64	0.10	5.5[c]-4.3[b]	0.21
CuO_x@TiO_2-ME	A (91) R (6) B (3)	A (13) R (9) B (11)	69	0.15	7.9[c] -6.8[b]	0.48

[a]The labels A, B and R refer to *anatase*, *brookite* and *rutile* polymorphs, respectively. [b]Calculated from the desorption branch. [c]Calculated from the adsorption branch. [d]CO/Cu ratio obtained from CO chemisorption at −90 °C.

XRD patterns (Figure 3.1) reveal the presence of the *anatase*, *rutile* and *brookite* polymorphs in all samples, but with a very different relative amount for the SG and the ME samples. The relative TiO_2 phase contents were calculated by the integrated intensity of the *anatase* (101) and of the *rutile* (110) peaks, in accordance with the literature[14]:

$$W_A = \frac{0.884\,A_A}{0.884\,A_A + A_R + 2.721\,A_B}$$

$$W_R = \frac{A_R}{0.884\,A_A + A_R + 2.721\,A_B}$$

$$W_B = \frac{2.721\,A_B}{0.884\,A_A + A_R + 2.721\,A_B}$$

where W_A, W_R and W_B represent the weight fraction of *anatase*, *rutile* and *brookite*, respectively. A_A represents the integrated intensity of the *anatase* (101) peak, A_R the integrated intensity of *rutile* (110) peak and A_B is the integrated intensity of the *brookite* (121) peak

The low metal loading and a very small size of the particles preclude the possibility of univocal determination of the presence of Cu related species.

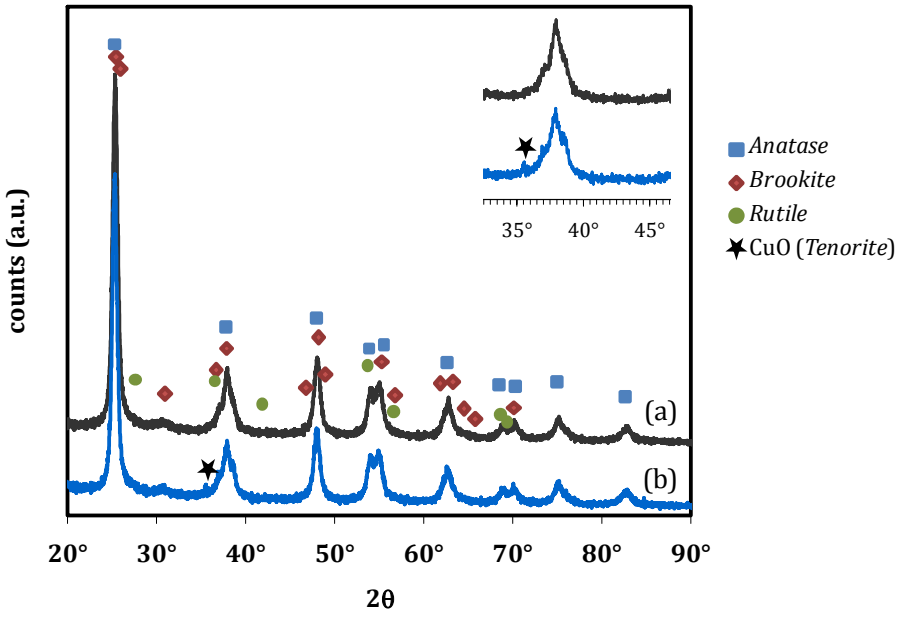

Figure 3.1: *Powder XRD patterns of CuO_x@TiO_2-ME (a) and CuO_x/TiO_2-ME (b)*

Only in the Cu/TiO_2-ME sample weak evidences for CuO (presence of reflection at 35.5) were observable (data not shown), consistently with the lower CO

chemisorption (see below). In the Cu/TiO_2-SG sample, the comparison with the bare TiO_2 sample shows that the presence of Cu induced the transformation of some *brookite* crystals into the *rutile* phase, probably during the calcinations step. The ME synthesis strongly favored the formation of the *anatase* phase compared to *rutile* or *brookite* phases.

Despite the fact that CO weakly adsorb on oxidized and reduced Cu surfaces, IR investigation proved that, under optimized conditions, CO can be used as probe for the oxidation state and the accessibility of the various Cu species.[15] For example CO chemisorption at −80°C has been used to estimate the Cu dispersion due to Cu(II), Cu(I) and Cu(0) in $Cu/CeO_2/Al_2O_3$ catalysts.[16] CO chemisorption data (Table 3.1) indicates that Cu/TiO_2-SG and $Cu@TiO_2$-ME possess high and similar ability to adsorb CO at low temperature. From these data is not possible to discriminate the relative amount of the various Cu species. However, these chemisorption data suggest that, in both Cu/TiO_2-SG and $Cu@TiO_2$-ME, the Cu species are highly accessible. On the other hand, the Cu/TiO_2-ME sample is characterized by a significantly lower CO/Cu ratio, suggesting a corresponding larger average particle size. Since the two impregnated samples were obtained by the same procedure, the only difference between the two samples must lay on the phase variation of the two bare TiO_2 used. This suggests that the interaction of the Cu ions/complexes with the *anatase* phase is significantly different with respect to that with *rutile* and *brookite*.

Figure 3.2 shows a representative image of the impregnated TiO_2 sample, where few larger *rutile* crystals are visible among *anatase* and *brookite*, as indicated by the XRD data. The SAED pattern (Fig. 3.2(b)) reflects this situation by showing well defined rings of the *anatase* phase and, to a minor degree, for the *brookite* phase, whereas only few spots are visible for the *rutile* phase. Similar images were obtained for the other two samples. The localization of copper nanoparticles was challenging both in the images and in the SAED pattern due to the presence of titania nanoparticles of the size comparable to that expected for the copper and reliable discrimination of the lattice planes of the possible copper phases (Cu, CuO and Cu_2O) from those of the three titania phases. In the SAD pattern two possible spots due to copper phases are suggested.

The copper catalysts have been characterized by means of HAADF-STEM and HRTEM techniques. As is known,[17]

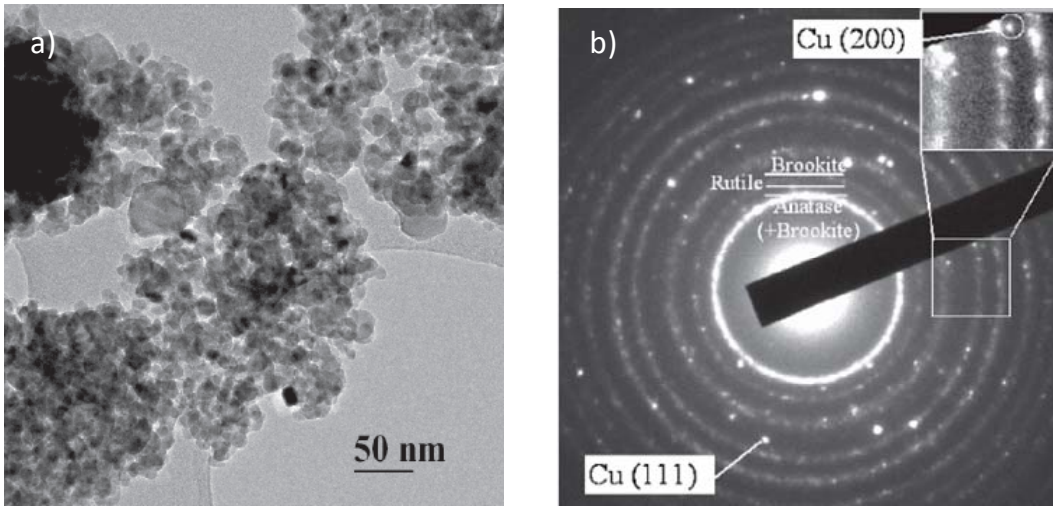

Figure 3.2: *(a) TEM image of sample Cu-TiO_2-SG and (b) relevant selected area diffraction (SAD).*

HAADF-STEM image contrasts are related to the Z^2 (Z: atomic number) of the elements present in the investigated material. Accordingly, this technique has proved to be particularly useful in metal dispersion studies of supported catalysts.[18-21] Metal particles appear in the images as characteristic brighter spots. Figure 3.3 summarizes the HAADF-STEM study carried out on the three copper catalysts. As may be deduced from the images reported in Figure 3.3e,f, CuO_x/TiO_2-ME shows a very poor copper dispersion, its particle size typically ranging from 5 to 10 nm (Figure 3.3e). Occasionally, particles as large as 150 nm (Figure 3.3f) could also be found. In contrast, $CuO_x@TiO_2$, Figure 3.3a, and CuO_x/TiO_2-SG, Figure 3.3c, samples show much smaller copper particle size. Accordingly, meaningful, much narrower, particle size distribution could be determined for the latter catalysts. The corresponding results are reported in Figure 3.3b for $CuO_x@TiO_2$, and Figure 3.3d for CuO_x/TiO_2-SG. The mean Cu particle sizes associated to the recorded distributions could also be determined; they were found to be 2.9 nm for $CuO_x@TiO_2$, and 4.0 nm for CuO_x/TiO_2-SG. Therefore, $CuO_x@TiO_2$ is the catalyst showing the best metal dispersion among those investigated here. These results are consistent with those obtained from the XRD study, in accordance with which CuO_x/TiO_2-ME is the only catalyst for which diffraction peaks due to a copper-containing phase could be detected.

HRTEM studies have also provided some relevant information. Parts A and B of Figure 3.4 show representative images recorded for $CuO_x@TiO_2$ and CuO_x/TiO_2-SG catalysts, respectively. In both cases the copper-containing nanoparticles look similar in both size and morphology.

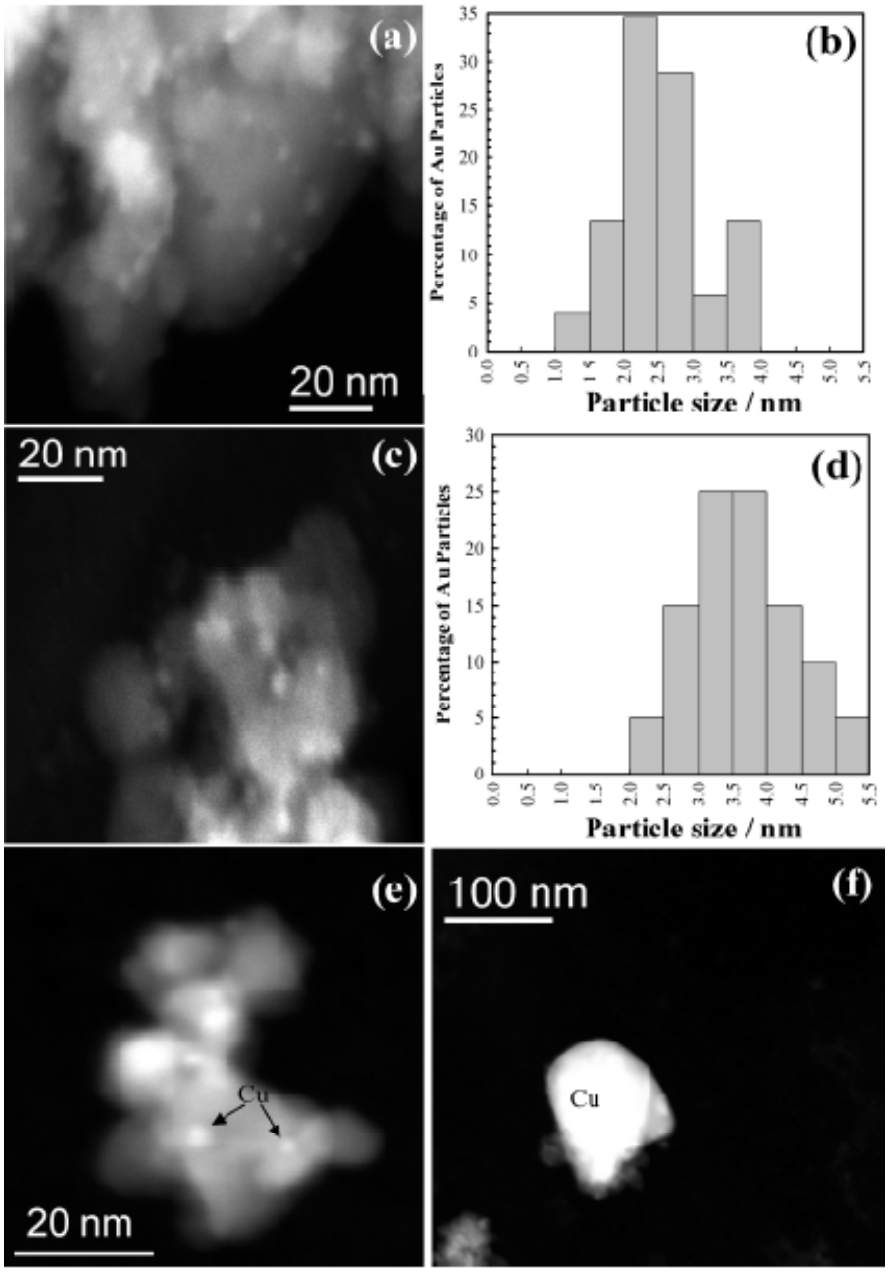

Figure 3.3: *Representative HAADF-STEM images of (a) CuO_x@TiO_2, (c) CuO_x/TiO_2-SG, and (e, f) CuO_x/TiO_2-ME samples. The particle size distribution of the CuO_x@TiO_2 and CuO_x/TiO_2-SG samples are reported in (b) and (d), respectively.*

However, the analysis of the computer generated diffraction patterns (DDP: *digital diffraction patterns*) for each of the catalyst samples shows a significant difference between them. In effect, the DDP included as an inset in Figure 3.4B (CuO_x/TiO_2-SG) can only be interpreted as due to a copper oxide phase (either CuO or Cu_2O). This result is consistent with the procedure applied in the preparation of this sample, consisting of the calcination of a copper nitrate precursor supported on the

TiO_2-SG sample. In contrast, the DDP recorded for the nanoparticle shown in Figure 3.4A may be assigned to metallic copper.

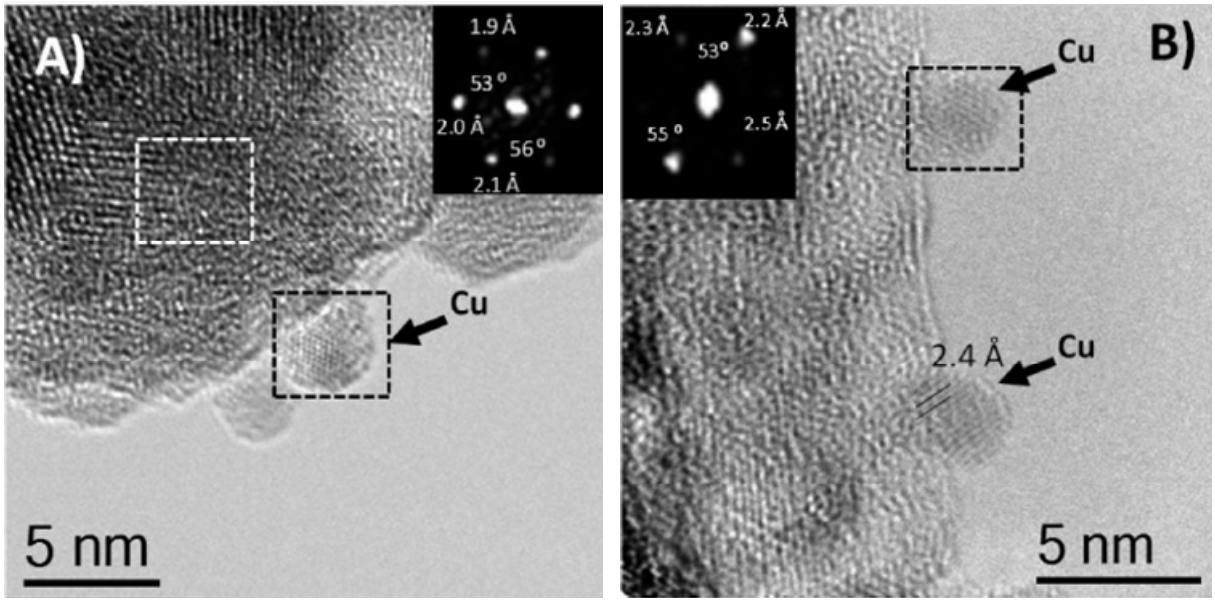

Figure 3.4: *Representative HREM images of the samples CuO_x@TiO_2 (A) and CuO_x/TiO_2-SG (B). The digital diffraction patterns (DDP) of the particles in the squares are shown in the insets.*

This observation is in good agreement with the CuO_x@TiO_2 preparation procedure, the first step of which consisting of the generation of a colloidal dispersion of reduced copper, whose nanoparticles were further embedded in the titania matrix. Regarding the nature of the thin amorphous layer covering the Cu nanoparticle, marked in Figure 3.4A with a black square, it may consist of either titania or an oxidized copper phase resulting from the partial oxidation of the metallic particle occurred during the calcination step of the preparation of the CuO_x@TiO_2 catalyst.

Figure 3.5 shows representative X-EDS data corresponding to Cu nanoparticles located in the outer border of CuO_x@TiO_2 and CuO_x/TiO_2-SG samples. The analysis was performed in the HAADF mode, by using an electron probe of 0.5 nm. As deduced from the reported spectra, in the case of the CuO_x@TiO_2 catalyst, both copper and titanium signals are observed. In contrast, for CuO_x/TiO_2-SG, the X-EDS spectrum mainly consists of Cu signal, with a negligible contribution due to titanium. This indicates, in good agreement with the HRTEM images, that, as expected from the different preparation procedure, the CuO_x@TiO_2 sample mainly consists of copper nanoparticles covered by the titania support, whereas in the case of the CuO_x/TiO_2-SG, Cu nanoparticles look like free from a large decoration of the support.

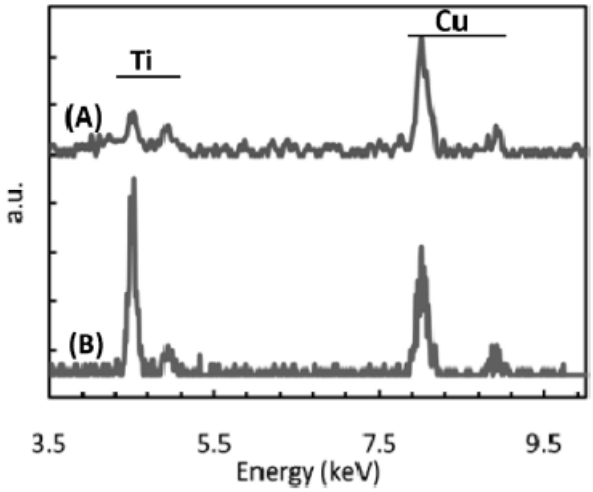

Figure 3.5: *EDX spectra of the samples CuO_x/TiO_2-S G (A) and CuO_x@TiO_2 (B).*

XANES/EXAFS spectroscopies were employed to analyze the Cu phases present in the samples and to evidence the modifications of the metal phase during irradiation under UV-Vis light. Figure 3.6 shows the XANES spectra obtained for the samples after calcination and after irradiation in the glycerol solution for 2 h.

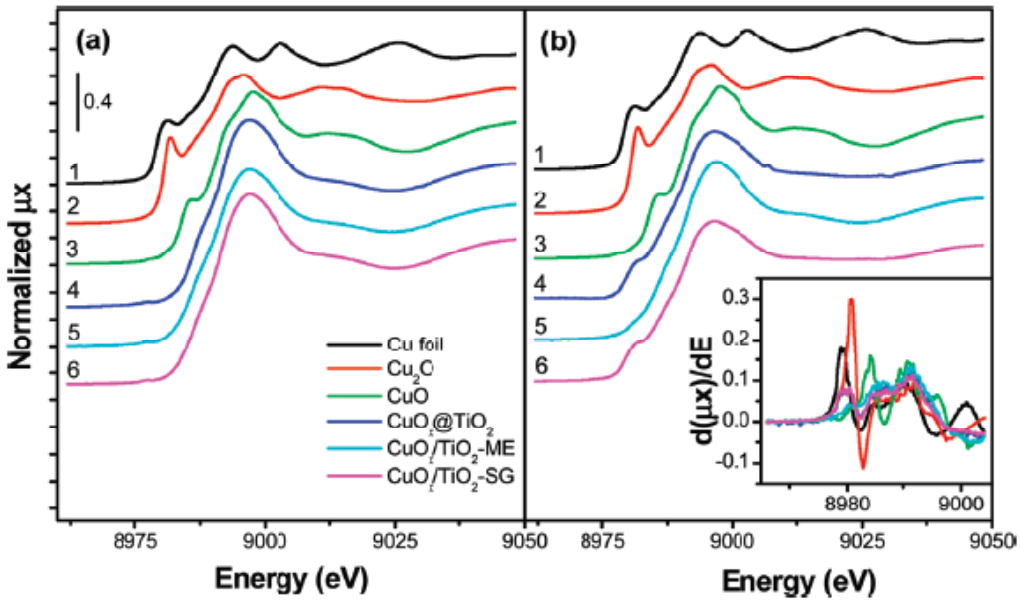

Figure 3.6: *Cu K-edge XANES spectra recorded for (a) fresh samples and (b) irradiated in the glycerol solution for 2 h. For comparison, the spectra of the standard materials are reported. The derivative XANES spectra of the irradiated samples are reported in the inset. Trace: (1) Cu foil, (2) Cu_2O, (3) CuO, (4) CuO_x@TiO_2, (5) CuO_x/TiO_2-ME, and (6) CuO_x/TiO_2-SG*

In Figure 3.7 are reported the Fourier-transformed EXAFS spectra of the extracted $k^3\chi(k)$ signals (not phase corrected) for the three samples after calcination and after irradiation, compared with the reference standards, depicting the radial

distribution of the neighbor scattering atoms around the absorbing Cu atoms. The best fit results of the back-transformed filtered peaks of the Fourier Transformed spectra (typical R range 0.1-0.4 nm) are reported in Table 3.2, together with the structural parameters refined for the standard materials. The XANES spectra of the calcined materials evidenced the presence of Cu(II) in all the samples, suggesting the formation of CuO during the calcination treatment. This was already confirmed by XRD for the CuO_x/TiO_2-ME sample but this verification was missing for the $CuO_x@TiO_2$ and CuO_x/TiO_2-SG materials. The Cu-O coordination number is near 4 (as in the bulk CuO) for CuO_x/TiO_2-ME while it is significantly lower for $CuO_x@TiO_2$ and CuO_x/TiO_2-SG, suggesting a high dispersion of CuO phase in the last materials in agreement with the absence of CuO reflection in the XRD patterns.

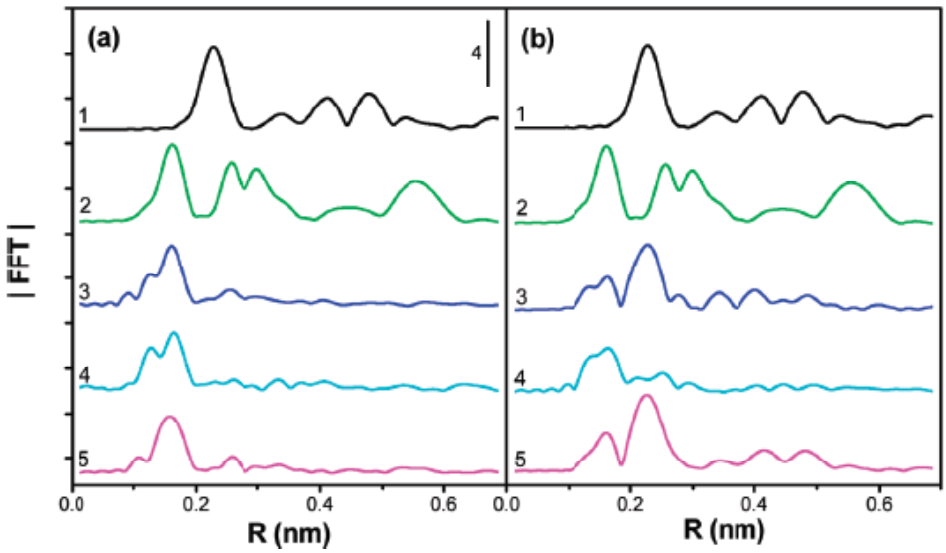

Figure 3.7: *Fourier transformed Cu K-edge EXAFS spectra (not phase corrected) of (a) fresh samples and (b) irradiated in the glycerol solution for 2 h. For comparison, the spectra of the standard materials are reported (Cu foil not in scale). Trace: (1) Cu foil, (2) CuO, (3) $CuO_x@TiO_2$, (4) CuO_x/TiO_2-ME, and (5) CuO_x/TiO_2-SG.*

After irradiation in the glycerol solution for 2 h, significant modifications of the Cu-related phases are observed. For both $CuO_x@TiO_2$ and CuO_x/TiO_2-SG materials, a significant shift to lower energy of the edge position is observed in the XANES spectra, whose first derivative analysis evidence also the presence of Cu(0) and Cu(I) contributions, although the major part is still present as Cu(II). In agreement, in the corresponding EXAFS spectra, both the contribution of a Cu-O shell at the distance characteristic of bulk CuO and of a Cu-Cu shell at the distance characteristic of bulk Cu

metal are observed. From the coordination number of the Cu-Cu shell (N_{Cu} = 2.2 for irradiated CuO_x@TiO_2 and 2.7 for irradiated CuO_x/TiO_2-SG), the average diameters of the Cu nanoparticles were estimated at 0.7 and 0.8 nm for CuO_x@TiO_2 and CuO_x/TiO_2-SG, respectively. In the case of CuO_x/TiO_2-ME, only marginal changes in the XANES spectra are observed, suggesting only a partial reduction of Cu(II) to Cu(I) and the complete absence of Cu(0) phase. In agreement, no Cu-Cu neighbor contribution is observed in the EXAFS signal.

Table 3.2. *Results of the EXAFS fittings at the Cu K-edge*

Sample	Shell	C.N.	Distance (nm)
CuO [a]	Cu-O	4	0.195
	Cu-O	2	0.276
	Cu-Cu	4	0.290
	Cu-Cu	4	0.309
Cu_2O [a]	Cu-O	2	0.184
	Cu-Cu	12	0.302
Cu foil [a]	Cu-Cu	12	0.2556
	Cu-Cu	6	0.3615
	Cu-Cu	24	0.4427
	Cu-Cu	12	0.5112
CuO_x@TiO_2 calcined	Cu-O	3.8	0.1962
	Cu-Cu	---	---
CuO_x@TiO_2 irradiated [b]	Cu-O	4.0	0.1975
	Cu-Cu	2.2	0.2572
CuO_x/TiO_2-ME calcined	Cu-O	3.5	0.1989
	Cu-Cu	---	---
CuO_x/TiO_2-ME irradiated [b]	Cu-O	3.1	0.1959
	Cu-Cu	---	---
CuO_x/TiO_2-SG calcined	Cu-O	3.9	0.1959
	Cu-Cu	----	----
CuO_x/TiO_2-SG irradiated [b]	Cu-O	3.6	0.1967
	Cu-Cu	2.7	0.2574

[a] Standard material, [b] After irradiation in the glycerol solution for 2h.

Independently from XANES, the presence of oxidized copper centers was confirmed by EPR in the case of CuO_x@TiO_2 sample as well as in both cases of the reference CuO_x/TiO_2-SG and CuO_x/TiO_2-ME samples before photo-reforming tests. The spectra shown in Figure 3.8 are axial and characteristic of paramagnetic Cu(II) ($3d^9$, S=1/2) ions in oxygen environment of distorted octahedral geometry. As mentioned earlier, calcinations of all investigated samples at 450°C for 6 h caused at least partial oxidation of copper particles. The absence of a signal from Ti(III) ($3d^1$, S = 1/2) ions can

be a versatile proof that any reduction of titania did not occur in the studied materials at the preparation step.

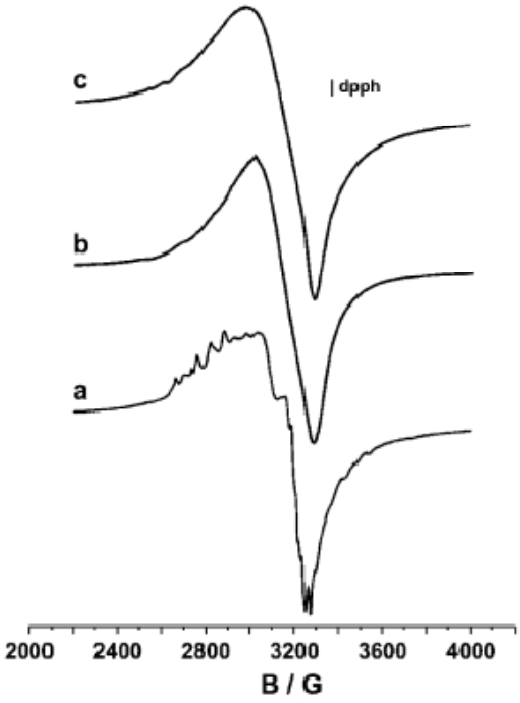

Figure 3.8: *EPR spectra of (a) CuO_x@TiO_2, (b) CuO_x/TiO_2-SG, and (c) CuO_x/TiO_2-ME samples, recorded at liquid nitrogen temperature (-196 °C).*

Differences in the shapes of the spectral lines clearly observed in the case of CuO_x@TiO_2 sample (Figure 3.8a) compared to those obtained for the reference samples (Figure 3.8b,c), reflected distinct changes in copper speciation induced by various preparation procedures. Well-resolved hyperfine structure (hfs), originating from interaction of an unpaired electron with ^{63}Cu (natural abundance 69.09%) and ^{65}Cu (natural abundance 30.91%) nuclei of spins I = 3/2, can be observed only for the CuO_x@TiO_2 sample, prepared by the embedding method, for which line broadening is lower (ΔB_{pp} ≈ 204 G) in comparison with those manifested in the EPR spectra of the reference samples. For CuO_x/TiO_2-SG and CuO_x/TiO_2-ME samples spectral lines were strongly broadened (ΔB_{pp} ≈ 263-312 G) by dipole-dipole interaction occurring between neighboring Cu(II) sites within oxide clusters.[22] As a consequence, the hyperfine structure was practically unresolved. The differences in ΔB_{pp} can indicate that copper ions stabilized in CuO_x@TiO_2 structure are magnetically more isolated than those in the two remaining systems. Even if dispersion of Cu(II) ions is higher for the embedded sample than for the reference samples, a surprisingly small value of $|A_{||}^1|$ ≈ 59G,

determined for one component of the spectrum recorded for CuO_x@TiO_2, suggests a delocalization of electron moiety on a few vicinal copper nuclei. For comparison, typical values of $|A_{||}|$ of fully isolated Cu(II) ions range from 130 to 185 G.[23, 24] Most probably Cu(II) sites are located within small clusters, where magnetic properties of an odd electron basically localized on Cu(II) cation can easily be influenced by magnetic fields of the neighboring nuclei of diamagnetic copper centers. There is more than one such localization of Cu(II) ions within CuO_x@TiO_2 structure, as can be inferred from the appearance of more than one set of the 4-fold hfs lines in the corresponding spectrum (Figure 3.8a). Copper ions can thus be stabilized in at least two inequivalent positions of slightly different geometry, having g-tensor components equal to $g_{||}^1$ = 2.419, $g_{\perp}^1$ = 2.067, and $g_{||}^2$ = 2.425, $g_{\perp}^2$ = 2.070. EPR parameters determined for CuO_x/TiO_2-SG and CuO_x/TiO_2-ME samples are quite similar: $g_{||}$ = 2.439, $g_{\perp}$ = 2.054 and $g_{||}$ = 2.440, $g_{\perp}$ = 2.052, respectively. For all the investigated samples the main g-tensor components follow the same trend $g_{||} > g_{\perp} > g_e$ (where g_e is the g value for a free electron equal 2.0023), indicating the same $|B_{1g}\rangle$ ground state with an unpaired electron described by the b_{1g} antibonding molecular orbital, being a linear combination of $d_{x^2-y^2}$ orbital of copper center and φ_{b1g} ligand (oxygen) orbitals of appropriate symmetries.[25]

A strong effect of adsorbed water on the status of copper ions, manifested itself in the ca. 1.5-2.5 times increase of the spectral intensity after outgassing of the samples, which was particularly pronounced in the case of CuO_x/TiO_2-SG and CuO_x/TiO_2-ME samples. This can be an additional evidence for preferential stabilization of copper ions mainly in oxide-like clusters over the catalyst surface. Contrary to this, because of better dispersion, coordination of Cu(II) ions in CuO_x@TiO_2 did not undergo modification by water molecules so easily.

Photocatalytic activity

The comparison of photocatalytic hydrogen production from methanol on the investigated systems is presented in Figure 3.9. It is important to mention here that, under our experimental conditions, both pure TiO_2 showed complete inability to produce hydrogen.

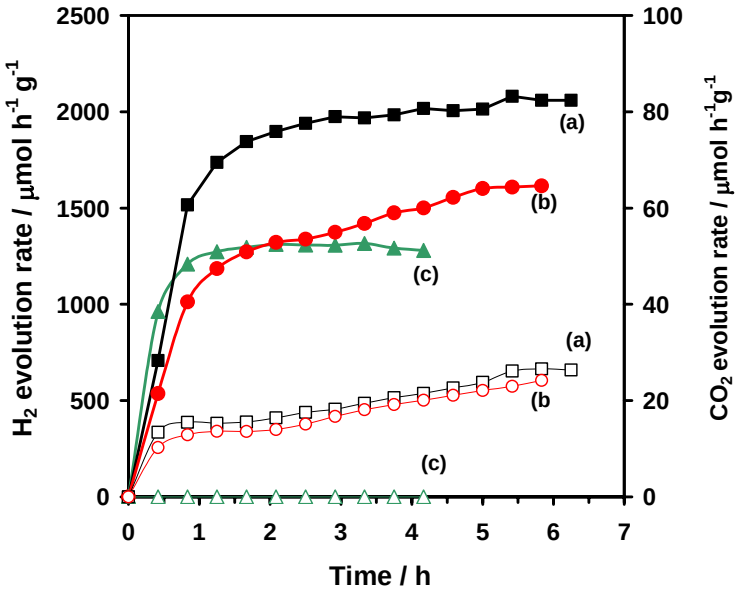

Figure 3.9: *Hydrogen (filled symbols) and CO_2 (empty symbols) evolution rate for photocatalytic treatment of mixtures containing 50% water-50% MeOH with (a) impregnated Cu/TiO_2-SG, (b) impregnated Cu/TiO_2-ME and (c) embedded Cu@TiO_2-ME*

Notably, despite identical metal loading and similar accessibility to Cu/CuO_x species (CO chemisorption data), the embedded system exhibited a nearly double yield of hydrogen with respect to the Cu/TiO_2-SG. However, it is known that the *anatase* phase is more active with respect to the *rutile* ones.[26-28] The reactivity of the impregnated Cu/TiO_2-ME, which has a TiO_2 phase composition almost identical to that of the embedded system, is slightly superior with respect to that of the Cu/TiO_2-SG. The rather modest improvement could be related to the presence of larger Cu-containing particles (XRD and CO chemisorption) in the Cu/TiO_2-ME with respect to Cu/TiO_2-SG. Therefore, the expected improvement due to the higher *anatase* content could have been compensated by the lower Cu/CuO_x accessibility. Notably, in the case of Cu/TiO_2-ME, a small activation effect could be appreciated after 3 h of reaction (Fig. 3.9). This might be related to the result of small leaching phenomena which can occur due to the lowering of the pH induced by formation of acids as intermediates of the methanol conversion. Cu ions can be subsequently photo-deposited leading to higher Cu dispersion and improved activity. The same process could be operative in the impregnated SG samples. However, in this case, as the starting material has already high metal dispersion, the resultant effect would be probably much more modest. Finally, in

the case of the embedded material the protecting surrounding TiO_2 could significantly prevent the Cu from photocorrosion.

Careful analysis of the gas phase indicates the presence of very small amount of CO_2 (Fig. 3.9) and only traces of formaldehyde, for the Cu@TiO_2 and Cu/TiO_2-ME. In the case of Cu/TiO_2-SG, the evolution of CO_2 is even lower and of the same order of the detection limits. Therefore, the data suggests that methanol, besides preventing hole-electron recombination pathway, is partially involved in dehydrogenation to formaldehyde, which can be further oxidized to formic acid and subsequently decomposed to CO_2 and water.[29, 30] Notably, no other byproducts were detected in the liquid phase. The extremely low CO_2/formaldehyde evolutions suggest that, under the present experimental conditions, most of the hydrogen comes from water splitting.

Figure 3.10 shows the H_2 evolution from a concentrated ethanol/water mixture during UV-vis irradiation in presence of the different CuO_x-TiO_2 nanocomposites. A significant difference in the activity of the three samples was observed.

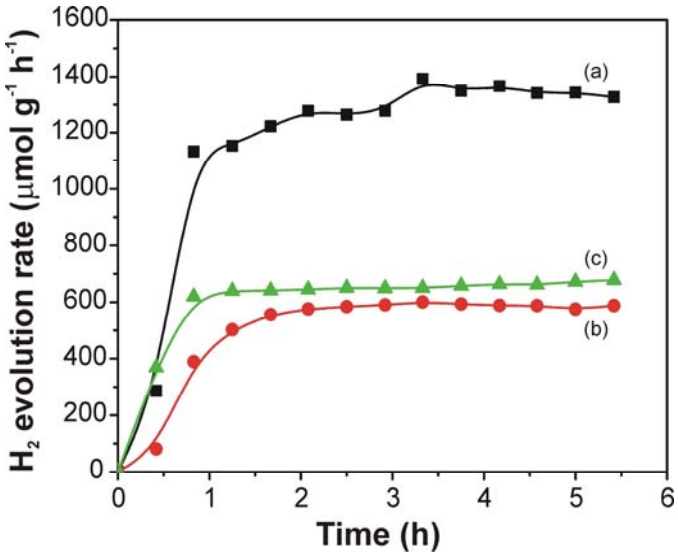

Figure 3.10: *Rate of H_2 evolution during UV-vis irradiation of a suspension of (a) CuO_x@TiO_2, (b) CuO_x/TiO_2-ME, or (c) CuO_x/ TiO_2-SG in a mixture containing ethanol/water 1:1 by volume.*

The CuO_x@TiO_2 catalyst, prepared by the embedding procedure, showed the best performances, the H_2 production rate being almost double with respect to that of the other photocatalysts. The activity of the two impregnated samples is rather similar, the CuO_x/TiO_2-SG sample having slightly better activity than CuO_x/TiO_2-ME. During all these experiments, no evolution of CO, CO_2, or CH4 was observed. GC analysis of the liquid phase after 6 h of reaction did not evidence the presence of any of the expected

reaction intermediates (acetaldehyde, acetic acid, etc.).[31-33] Traces of acetaldehyde were, however, present in the gas phase indicating that under our experimental conditions (20°C and in flow of Ar), the acetaldehyde could be preferentially eliminated from the reaction media before it can be further oxidized to acetic acid. Consistently no appreciable variation of pH was observed. Notably, no deactivation was observed for CuO_x@TiO_2 over 30 h of reaction (data not shown).

The evolution of H_2 and CO_2 during the photocatalytic tests using a 1.0 M glycerol solution are reported in Figure 3.11. In this case, the irradiation was performed up to 50 h, to check the stability of the catalysts, as the reaction proceeded to fully degrade some glycerol forming aldehydes and organic acids as intermediates. The extent of H_2 and CO_2 evolution depends on the type of photocatalyst, suggesting the presence of different population of active sites for the adsorption and conversion of glycerol and of its degradation products. In addition, traces of CO were observed for all the catalysts, being slightly higher than the amount observed for the embedded system.

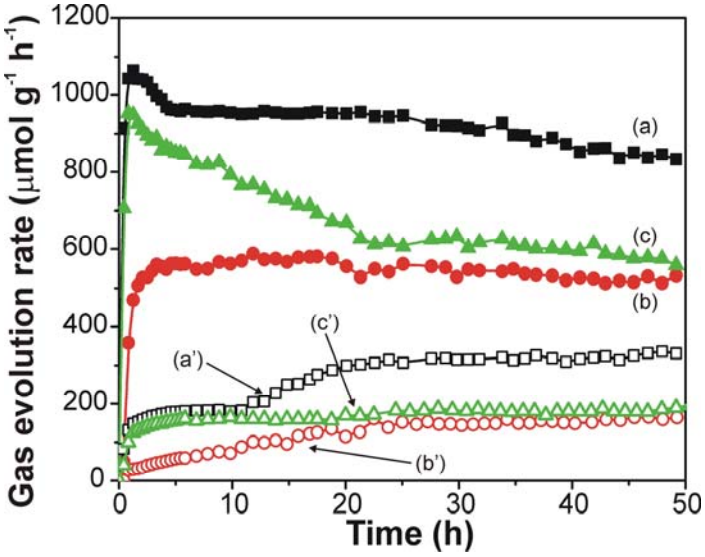

Figure 3.11: *Rates of H_2 (filled symbols) and CO_2 (empty symbols) evolution during UV-vis irradiation of a suspension of (a) CuO_x@TiO_2, (b) CuO_x/TiO_2-ME, or (c) CuO_x/TiO_2-SG in an aqueous solution of glycerol 1 M.*

Also in the case of glycerol, the highest hydrogen production rate was obtained using the embedded CuO_x@TiO_2. During prolonged irradiation, an almost linear decrease of the H_2 production rate (~10%) was observed in the first 6 h of reaction. After that, the activity decreased very slowly, being reduced by a further 10% after 50 h. At the same time, the rate of CO_2 evolution initially increased with a step raise after 10 h reaching a stationary level after 25 h. As a consequence, the H_2/CO_2 ratio progressively

decreased from the initial value of ~11 after 1 h to 2.5 after 50 h, approaching the theoretical value of 2.33 expected for the complete glycerol reforming according to the equation:

$$C_3H_8O_3 + 3H_2O \rightarrow 3CO_2 + 7H_2$$

The initial H_2 production rate of the CuO_x/TiO_2-SG catalyst was slightly lower with respect to that of the embedded catalyst. Furthermore, a more pronounced deactivation was observed during the overall duration of the experiment. In fact, an almost linear decrease of rate of H_2 evolution occurred in the first 20 h of reaction leading to 40% loss of the initial activity. In the subsequent 30 h of reaction, only minor deactivation was observed. On the other hand, the CO_2 evolution stabilized already during the first few hours of reaction, with a minor step at 20 h. The H_2/CO_2 ratio decreased from the initial value of ~17 to 2.9 after 50 h. CuO_x/TiO_2-ME is the less active catalyst, where a constant rate of H_2 production of 580 μmol g^{-1} h^{-1} is obtained after 4 h of reaction. In this case, the rate of CO_2 evolution slowly increased reaching a stationary value after 20 h. The H_2/CO_2 ratio decreased from the initial value of ~13 to 3.2 after 50h.

To allow the comparison of experimental results obtained under different experimental conditions, it is necessary to use commonly accepted efficiency parameters, such as (i) quantum yield (QY), defined as the number of radicals produced on the catalyst surface during the primary reaction processes per photon absorbed, and (ii) quantum efficiency (ϕ), defined as the ratio of the number of molecules of product formed to the total number of photons absorbed.[34] When photocatalytic experiments are performed in slurry reactors, two simultaneous phenomena occur: the photons are both absorbed and scattered in the reacting medium. Therefore, the exact determination of the quantity of absorbed photons is rather complex and still matter of debate. The direct comparison with the literature is still difficult, mainly because in many cases the description of the experimental conditions is poor. Indeed, several parameters such as (i) reactor geometry, (ii) catalyst concentration, (iii) particle agglomerate size, (iv) pH, (v) recycle flow rate, and (vi) radiation wavelength can influence the absorbed photons and thus the QY.[35] Table 3.3 reports the apparent QY

calculated accordingly to the experimental session procedure and in particular using a black light-monochromatic Hg lamp.

Table 3.3. *Apparent quantum yield measured for the different CuO_x-TiO_2 photocatalysts using methanol, ethanol and glycerol aqueous solutions*

Sample	Methanol	Ethanol	Glycerol
CuO_x@TiO_2	33%	27%	29%
CuO_x/TiO_2-ME	19%	23%	28%
CuO_x/TiO_2-SG	15%	24%	29%

Recently, Kondarides et al.[5] reported rather high apparent QY for a Pt-TiO_2 photocatalyst under experimental conditions rather similar to ours. In fact, using glycerol and ethanol, they estimated QY of 70 and 50, respectively. Using the same experimental procedure, our systems show apparent QY that are significantly lower. However, H_2 production from the photocatalytic re-forming of biomass on CuO_x@TiO_2 catalyst could be still promising on the bases of the lower copper cost with respect to that of platinum.

Figure 3.12 shows the results from thermogravimetric analysis (TGA) measurements on the aged catalysts after the 50 h of photo-reforming of the glycerol solution. All the samples present a weight loss of ~2% below 350 °C. This can be reasonably related to the desorption of carbonates from the surface of the aged samples. Notably, the amounts of carbonates removed from the catalysts are very similar, in agreement with the comparable surface area of these materials. The decrease of weight observed above 350 °C can be interpreted as the oxidation of reaction intermediate adsorbed on the catalyst surface. The weight loss is very low (~0.5%) in the case of the CuO_x@TiO_2 while the amount of residues is significantly higher on the two impregnated samples (weight loss of 5.8% for CuO_x/TiO_2-ME and 6.1% for CuO_x/TiO_2-SG). The TGA data can account for the different activity of the samples. In fact, the CuO_x@TiO_2 catalyst presents the highest H_2 and CO_2 production and the best stability, indicating that the material is more prompt to oxidize the organic sacrificial agent to CO_2.

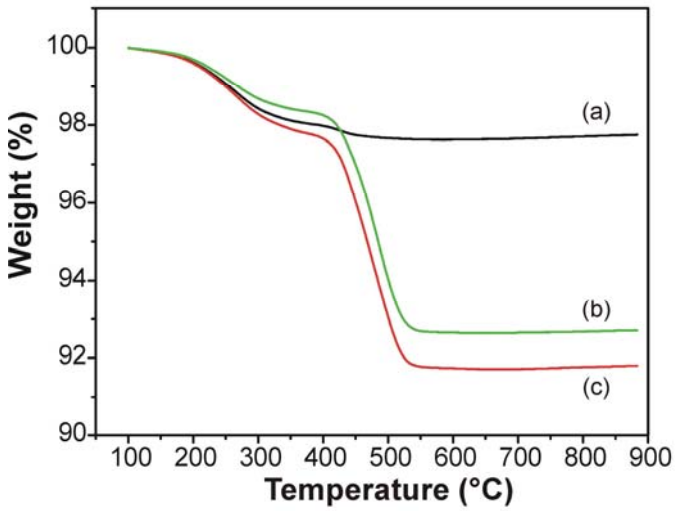

Figure 3.12: *Thermogravimetric analysis of the aged (a) CuO_x@TiO_2, (b) CuO_x/TiO_2-ME, and (c) CuO_x/TiO_2-SG. Sample recovered after the experiment of Figure 2.*

On the other hand, the aged CuO_x/TiO_2-SG and CuO_x/TiO_2-ME present similar amounts of organic residues, in agreement with the similar activity observed after 50 h of reaction. Moreover, the loss of activity evidenced by the CuO_x/TiO_2-SG can be related with the gradual buildup of organic intermediates on the surface of the photocatalyst. Figure 3.13 shows the extent of copper leaching for CuO_x@TiO_2, CuO_x/TiO_2-ME, and CuO_x/TiO_2-SG during 4 h of reaction under UV-vis irradiation and the subsequent 50 h in the absence of both irradiation and inert gas flow.

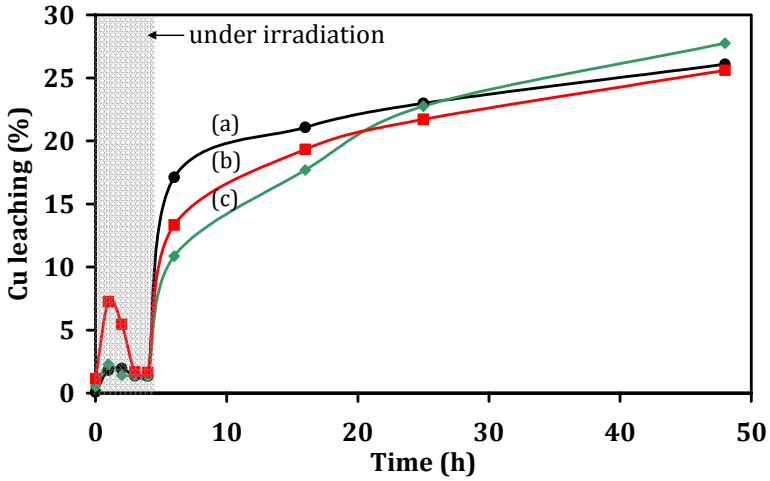

Figure 3.13: *Evaluation of the Cu leaching during 4 h of reaction (glycerol 1 M, UV-vis irradiation, flow of Ar) and in the subsequent 48 h (no irradiation and suspension exposed to air). Trace (a) CuO_x@TiO_2, trace (b) CuO_x/TiO_2-ME, and trace (c) CuO_x/TiO_2-SG*

The concentration of copper ions in solution was rather low (below 1% of the Cu was present in solution after 4 h) and almost the same for all the catalysts. This is consistent with the fact that the concomitant presence of the sacrificial agent, the TiO_2 and UV irradiation can guarantee the photodeposition of the small fraction of copper oxide which could possibly be leached out during the initial stage of reaction. An exception was observed for the CuO_x/TiO_2-ME sample, for which a transient appreciable leaching was detected even under UV-vis irradiation. This evidence could be justified by the fact that this sample presents large CuO particles that are rather difficult to be reduced. Consistently, under UV-vis irradiation only, a small fraction of the copper was present in the metallic form (see EXAFS data). Therefore, during the reaction, the formation of organic acids can favor a partial dissolution of the copper oxides. Subsequently, the occurrence of copper photodeposition can decrease the copper concentration in the solution.

Cu concentration significantly increases when the environment becomes oxidizing and acidic at the same time. Cu(II) ions are simply more easily formed under such conditions and subsequently can undergo stepwise leaching. In fact, around 25% of the copper is lost in all cases, when the sample is left in air in the presence of the reaction intermediate and products formed during 4 h of irradiation.

Discussion

The production of H_2 by photocatalysis in presence of an organic sacrificial agent (such as methanol, ethanol, glycerol, or sugars) has been extensively studied on Pt/TiO_2 photocatalysts.[4, 5, 36-38] It has been proposed that the process starts with the production of an electron/hole pair as a result of the absorption of a photon by TiO_2. The electron/hole recombination probability is reduced by the presence of platinum able to collect/accept electrons and by the interaction of the organic sacrificial molecules with the holes. The electrons stored in the metal phase can then reduce H^+ to H_2 while the holes can oxidize the sacrificial agent more easily than water.

The present CuO_x-TiO_2 samples show an initial rate of H_2 evolution, which strongly depends on the sacrificial molecule. The embedded $CuO_x@TiO_2$ showed superior performances using methanol (Figure 3.9), ethanol (Figure 3.10), or glycerol

(Figure 3.11) with respect to the impregnated samples. However, the two impregnated CuO_x/TiO_2-ME and CuO_x/TiO_2-SG systems have similar initial activity on ethanol reforming (Figure 3.10), while in the case of glycerol, CuO_x/TiO_2-SG has higher hydrogen and CO_2 production rates in comparison with that of CuO_x/TiO_2-ME. Despite this, after a long time the activities of the two impregnated systems are similar due to the progressive deactivation of the CuO_x/TiO_2-SG photocatalyst in the presence of glycerol. Notably, while the hydrogen production over CuO_x/TiO_2-SG dramatically decreases, suggesting a modification of the Cu phase, the rate of CO_2 production appears almost constant during the experiment, indicating that the titania remains able to interact with glycerol and its reaction intermediate. The reaction pathway is certainly very complex,[39] and far from being fully understood. The proposed main reaction intermediate for glycerol photo-reforming is methanol.[4] Nevertheless, our CuO_x/TiO_2-SG showed negligible ability to produce CO_2 from methanol degradation, while our $CuO_x@TiO_2$ and CuO_x/TiO_2-ME have this capability. Therefore, formaldehyde and/or formic acid obtained during the degradation of methanol over the CuO_x/TiO_2-SG can remain adsorbed on the catalyst and also on the Cu, progressively reducing the activity of the system. The low initial activity of the CuO_x/TiO_2-ME in the glycerol reforming can be interpreted as a combination of various aspects. First, its large CuO particles are difficult to be reduced under reaction conditions (EXAFS results) and therefore they are less efficient in electron trapping. Consequently, the electron-hole recombination should be favored in this system. Furthermore, the number of exposed copper sites for H+ reduction is significantly lower with respect to the other two samples, which show better copper dispersion. To better understand the difference in the reactivity of these systems with respect to the sacrificial agent, it is necessary to compare also the data obtained using monochromatic black light irradiation (Table 3.3) and with polychromatic irradiation (Figures 3.10 and 3.11). The H_2 production from degradation of ethanol of the $CuO_x@TiO_2$ is twice with respect to the other two samples (Figure 3.10) but the apparent QY for the three samples are very similar (Table 3.3). Analogously, significant differences of activity are observed in the case of glycerol (Figure 3.11) while similar apparent QY were obtained under irradiation at 365 nm (Table 3.3). A possible explanation of this apparent contradiction could be based on small structural differences of the samples which might influence their energy band

gap. In fact, it has been shown that the presence of copper in substitutional position in the lattice of TiO_2 can induce a change in the band gap energy of TiO_2 with a consequent extension of light absorption in the visible region.[40] Additionally, copper can be differently stabilized within various TiO_2 polymorphs. Cu doping may occur even in samples prepared by wet impregnation of preformed titania and heated in air for 24 h at 500°C. Since our impregnated samples were heated only for 1 h and at 450°C, the effect of Cu structural doping should be minimal. Vice versa, in the case of CuO_x@TiO_2 this possibility is significantly higher as the TiO_2 is produced during the calcination step (6 h) from a soft titanium oxyhydroxide in the presence of Cu nanoparticles. Therefore, the band gap of the CuO_x@TiO_2 could be slightly reduced with respect to that of the CuO_x/TiO_2-ME. In the case of CuO_x/TiO_2-SG, the presence of a larger amount of *brookite* (3.4 eV) with respect to the other *anatase* (3.2 eV) based samples, could lead to a slightly higher band gap. Unfortunately, the low metal dispersion of CuO_x/TiO_2-ME can minimize the possible advantage of a better visible-light response of this sample.

Conclusions

The present study indicates appreciable advantages in preparing embedded CuO_x@TiO_2 photocatalyst for hydrogen production by photo-reforming of ethanol and glycerol water solutions with respect to conventional impregnated materials. The superior activity of the Cu@TiO_2-ME system can be interpreted on the bases of combination of positive effects:

(i) high dispersion of the active Cu/CuO_x species,

(ii) large presence of *anatase* phase and

(iii) efficient metal-support interaction.

The fact that embedded Cu particles serve as the “core” for the electron transfer processes, initiated in the surrounding TiO_2 particles with the absorption of light (E > Eg), for hydrogen production along with the centre for charge carrier recombination inhibition process. Secondly, in the case of embedded system, the Cu phase, being deeply surrounded by the porous TiO_2, is protected against the adsorption of poisoning species, generated by photocatalytic oxidation of alcohols and water in the aqueous alcohol environment. In the Cu/TiO_2 system, the Cu particles are essentially localized at

the surface, in a weaker interaction with TiO_2 with respect to the embedded one and exposed to incoming light radiation and other oxidizing species produced as a result of the photocatalytic water splitting process. The effective light absorption of the CuO_x nanoparticles on the surface significantly reduces their capability as electron scavenger and co-catalyst, leading to lower hydrogen yields compared to the embedded system. An initial increase followed by steady production of hydrogen (Fig. 3.9, Fig. 3.10 and Fig. 3.11), with the time, predicts the equilibrium between hydrogen radicals (H•), precursor for H_2 formation, production and consumption reactions occurring in the bulk or at the surface of the catalyst.

In conclusion, combination of preformed Cu nanoparticles with ME synthesis of TiO_2, owing to the core arrangement of CuO_x nanoparticles with an optimal interfacial contact with the surrounding TiO_2 particles, embedded Cu nanoparticles exemplifies

(i) Better synergic compatibility with TiO_2 particles due to high dispersion.

(ii) Enhanced light harvesting, charge partitioning and disbursing ability.

(iii) Efficient metal-support interaction compared to impregnation.

(iv) Protection against photocorrosion.

The Cu nanoparticles embedded TiO_2 has proved to be valuable addition to the catalyst bank for enhanced hydrogen production from aqueous methanol or ethanol or glycerol solutions. This study also demonstrated that the proper tailoring of a photocatalyst with a suitable alteration technique and deep insight of the lattice structure promotes a better interfacial contact between the bulk (TiO_2) and doping agent (Cu nanoparticles) leading to enhanced product yield and open avenues for further exploration in this area.

References

[1] M. Li, S. Zhou, Y. Zhang, G. Chen, Z. Hong. *Applied Surface Science* **2008**, *254*(13), 3762-3766.
[2] M. Ni, M. K. H. Leung, D. Y. C. Leung, K. Sumathy. *Renewable and Sustainable Energy Reviews* **2007**, *11*(3), 401-425.
[3] G. R. Bamwenda, S. Tsubota, T. Nakamura, M. Haruta. *Journal of Photochemistry and Photobiology, A: Chemistry* **1995**, *89*(2), 177-189.
[4] V. M. Daskalaki, D. I. Kondarides. *Catalysis Today* **2009**, *144*(1-2), 75-80.
[5] D. I. Kondarides, V. M. Daskalaki, A. Patsoura, X. E. Verykios. *Catalysis Letters* **2008**, *122*(1-2), 26-32.
[6] Y. Z. Yang, C. H. Chang, H. Idriss. *Applied Catalysis B: Environmental* **2006**, *67*(3-4), 217-222.
[7] Y. Sakata, T. Yamamoto, T. Okazaki, H. Imamura, S. Tsuchiya. *Chem. Lett.* **1998**, *1253*.
[8] N. L. Wu, M. S. Lee. *International Journal of Hydrogen Energy* **2004**, *29*(15), 1601-1605.
[9] H. J. Choi, M. Kang. *International Journal of Hydrogen Energy* **2007**, *32*(16), 3841-3848.
[10] M. K. Jeon, J. W. Park, M. Kang. *Journal of Industrial and Engineering Chemistry* **2007**, *13*(1), 84-91.
[11] A. V. Korzhak, N. I. Ermokhina, A. L. Stroyuk, V. K. Bukhtiyarov, A. E. Raevskaya, V. I. Litvin, S. Ya. Kuchmiy, V. G. Ilyin, P. A. Manorik. *Journal of Photochemistry and Photobiology A: Chemistry* **2008**, *198*(2-3), 126-134.
[12] S. Takenaka, H. Umebayashi, E. Tanabe, H. Matsune, M. Kishida. *J. Catal.* **2007**, *245*(2), 392-400.
[13] L. Q. Jing, X. J. Sun, B. F. Xin, B. Q. Wang, W. M. Cai, H. G. Fu. *J. Solid State Chem.* **2004**, *177*(10), 3375-3382.
[14] H. Z. Zhang, J. F. Banfield. *J Phys Chem B* **2000**, *104*(15), 3481-3487.
[15] A. Dandekar, M. A. Vannice. *J. Catal.* **1998**, *178*(2), 621-639.
[16] S. Patel, K. K. Pant. *Fuel Process Technol* **2007**, *88*(8), 825-832.
[17] S. J. Pennycook, D. E. Jesson. *Ultramicroscopy* **1991**, *37*(1-4), 14-38.
[18] S. E. Collins, J. M. Cíes, E. Del Río, M. López-Haro, S. Trasobares, J. J. Calvino, J. M. Pintado, S. Bernal. *Journal of Physical Chemistry C* **2007**, *111*(39), 14371-14379.
[19] J. C. González, J. C. Hernández, M. López-Haro, E. Del Río, J. J. Delgado, A. B. Hungría, S. Trasobares, S. Bernal, P. A. Midgley, J. J. Calvino. *Angewandte Chemie - International Edition* **2009**, *48*(29), 5313-5315.
[20] A. H. Janssen, C. M. Yang, Y. Wang, F. Schüth, A. J. Koster, K. P. De Jong. *J Phys Chem B* **2003**, *107*(38), 10552-10556.
[21] J. M. Thomas, P. A. Midgley, T. J. V. Yates, J. S. Barnard, R. Raja, I. Arslan, M. Weyland. *Angewandte Chemie - International Edition* **2004**, *43*(48), 6745-6747.
[22] G. Li, N. M. Dimitrijevic, L. Chen, T. Rajh, K. A. Gray. *Journal of Physical Chemistry C* **2008**, *112*(48), 19040-19044.
[23] H. Tominaga, Y. Ono, T. Keii. *J. Catal.* **1975**, *40*(2), 197-202.
[24] C. O. Kowenje, B. R. Jones, D. C. Doetschman, S. W. Yang, C. W. Kanyi. *Chemical Physics* **2006**, *330*(3), 401-409.
[25] K. Bahranowski, R. Dula, M. Labanowska, E. M. Serwicka. *Applied Spectroscopy* **1996**, *50*(11), 1439-1445.
[26] J. Augustynski. *Electrochim Acta* **1993**, *38*(1), 43-46.
[27] O. Carp, C. L. Huisman, A. Reller. *Prog Solid State Chem* **2004**, *32*(1-2), 33-177.
[28] K. Yanagisawa, J. Ovenstone. *J Phys Chem B* **1999**, *103*(37), 7781-7787.
[29] H. J. Choi, M. Kang. *Int J Hydrogen Energy* **2007**, *32*(16), 3841-3848.
[30] N. L. Wu, M. S. Lee. *Int J Hydrogen Energy* **2004**, *29*(15), 1601-1605.
[31] S. Klosek, D. Raftery. *J Phys Chem B* **2001**, *105*(14), 2815-2819.
[32] S. Pilkenton, S. J. Hwang, D. Raftery. *J Phys Chem B* **1999**, *103*(50), 11152-11160.
[33] U. Diebold. *Surface Science Reports* **2003**, *48*(5-8), 53-229.
[34] M. Salaices, B. Serrano, H. I. De Lasa. *Chemical Engineering Journal* **2002**, *90*(3), 219-229.
[35] R. J. Brandi, M. A. Citroni, O. M. Alfano, A. E. Cassano. *Chemical Engineering Science* **2003**, *58*(3-6), 979-985.
[36] N. Strataki, V. Bekiari, D. I. Kondarides, P. Lianos. *Applied Catalysis B: Environmental* **2007**, *77*(1-2), 184-189.
[37] X. Fu, J. Long, X. Wang, D. Y. C. Leung, Z. Ding, L. Wu, Z. Zhang, Z. Li, X. Fu. *International Journal of Hydrogen Energy* **2008**, *33*(22), 6484-6491.
[38] L. S. Al-Mazroai, M. Bowker, P. Davies, A. Dickinson, J. Greaves, D. James, L. Millard. *Catalysis Today* **2007**, *122*(1-2), 46-50.
[39] V. Maurino, A. Bedini, M. Minella, F. Rubertelli, E. Pelizzetti, C. Minero. *Journal of Advanced Oxidation Technologies* **2008**, *11*(2), 184-192.
[40] A. Di Paola, G. Marcì, L. Palmisano, M. Schiavello, K. Uosaki, S. Ikeda, B. Ohtani. *J Phys Chem B* **2002**, *106*(3), 637-645.

Chapter 4

PHOTODEPOSITED SYSTEMS

In the previous chapter the embedding methodology to prepare Cu@TiO_2 photocatalyst and the investigation of their peculiar properties was described. Herein, a cheap and active photocatalysts based on Cu nanoparticles dispersed on TiO_2 supports, which are capable of operating under solar radiation, are investigated for the production of hydrogen from ethanol and glycerol. Second generation ethanol and sugars, extracted from lignocellulosic parts of vegetables, and glycerol, produced as a by-product of bio-diesel, are attractive and largely available sacrificial agents.[1, 2]

Catalysts synthesis and characterization

TiO_2 supports were synthesized by sol-gel (SG) and precipitation from titanyl sulphate (PS). Briefly, TiO_2-SG were prepared by hydrolysis of titanium butoxide in ethanol in presence of HNO_3 as a catalyst.[3] The gel were aged at room temperature for 24h, dried at 80°C overnight and finally calcined at 450°C for 6h. TiO_2-PS were prepared

by precipitation of an aqueous solution of $TiOSO_4$ with NaOH 0.15M until pH = 5.5 is reached.[4] After aging at room temperature for 24h, the precipitate was filtered, it was washed carefully to remove sulphate and sodium ions, dried at 80°C overnight and finally calcined at 450°C for 6h. Cu were loaded on the supports by photodeposition technique. Usually 1g of TiO_2 (SG or PS) was suspended in a water/methanol 1:1 by volume solution containing copper nitrate. The amount of $Cu(NO_3)_2 \bullet 3H_2O$ was changed in order to obtain the desired Cu loading (1.0 of 2.5 wt%). After stirring for 30min, the suspension was irradiated with a 125W medium pressure Hg lamp for 2h. The samples were finally filtered and dried. In the presence of light, a rapid change from green to black in the color of the suspension is observed, indicating that the copper is easily reduced to Cu(0) and deposited on the support. All the samples showed a stable evolution of H_2 during the catalysts preparation. The nature of TiO_2 and the loading of Cu affect the H_2 evolution rate. Despite the lower surface area, the samples Cu/TiO_2-SG show a higher H_2 evolution with respect to Cu/TiO_2-PS (see below). The effect of the Cu loading depends on the nature of the support. On TiO_2-SG, comparable H_2 productions are obtained independently from the Cu loading, except for an initial higher activity of $Cu(2.5\%)/TiO_2$-SG. On the other hand, higher hydrogen production is observed on $Cu(2.5\%)/TiO_2$-PS with respect to the $Cu(1.0\%)/TiO_2$-PS.

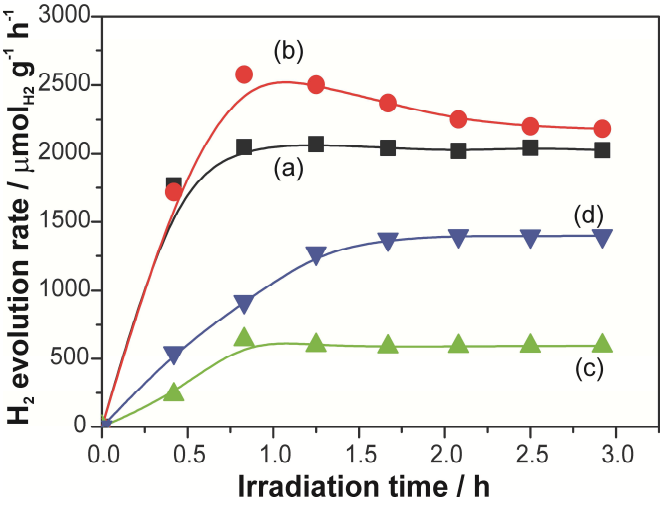

Figure 4.1: *H_2 evolution rates during photodepostion process in MeOH/H_2O 1:1 solution for the preparation of Cu(1.0%)/TiO_2-SG (a), Cu(2.5%)/TiO_2-SG (b), Cu(1.0%)/TiO_2-PS (c) and Cu(2.5%)/TiO_2-PS (d).*

The photocatalytic activity was evaluated for the hydrogen production from aqueous solutions of renewable oxygenates (ethanol 1:1 by volume or 1M glycerol). For UV-vis experiments, 500 mg of catalyst were suspended in 240 mL of solution and the

suspension was irradiated with a 125W medium pressure Hg lamp. For visible experiments, 100 mg of catalyst were suspended into 80 mL of solution and the suspension was irradiated using a Solar Simulator equipped with a 150W Xe lamp filtered with an Atmospheric Filter to reduce the fraction of UV photons. Ar flow (15 mL/min) was employed to remove air from the reactor and as carrier for the reaction products. As the hydrogen production can depend on the sacrificial agent concentration,[5] the duration of the long term experiments has been optimized to prevent significant alteration of the concentration of the oxygenates due to either the conversion and evaporation. Gaseous products were analyzed by GC analysis using a TCD for the quantification of H_2 and a FID, couple with a methanator, for the quantification of the C-containing compounds (CO, CO_2, CH_4 etc.). The by-products present in the liquid phases after catalytic activity were analyzed by GC/MS using a HP 7890 GC equipped with a DB-225ms column (J&W) and a HP 5975C mass spectrometer.

Specific surface areas of the samples were measured by N_2 physisorption at the liquid nitrogen temperature using a Micromeritics ASAP 2020 instrument. Usually, 250 mg of the samples were degassed overnight before the measurements.

Powder XRD patterns were collected using a Philips X-Pert instrument using Cu K_α sources. Mean crystallite sizes were calculated applying the Scherrer's equation to the main reflection of each phase.

EXAFS (Extended X-ray Absorption Fine Structure Spectroscopy) and XANES (Near Edge X-ray Absorption Spectroscopy) spectra have been recorded at the XAFS beamline of ELETTRA synchrotron (Trieste, Italy). Measurements were performed in the transmission mode using a double-crystal Si(111) monochromator and beam intensity was measured before and after samples and reference foils by ionization chambers. Harmonic rejection was obtained by an appropriate choice of the gaseous mixture in the ionization chambers and by a 10% de-tuning of the crystal. Three spectra have been acquired and averaged for each sample. Spectra were recorded at the Cu K-edge (8978.9 eV) working at a sampling step of 0.2 eV around the edge and of 2 eV over a range of 1.5 keV above the edge. An integration time of 2 sec was used for all the points. The XANES and EXAFS spectra were recorded at room temperature and at the liquid nitrogen temperature, respectively. For the preparation of the samples, the photoreactor was brought at the beamline and the photodeposition procedure were

repeated. After switching off the lamp, an adequate amount of the suspension was filtered on a PVDF membrane under N_2 in a glove-bag (in order to avoid any un-wanted oxidation process in air), washed with 2-propanol, dried with N_2 flow and sealed between kapton films. To avoid modifications during the spectra recording, the samples were measured immediately after the irradiation, preventing the air contact by evacuation inside the sample holder of the cryostat. Cu foil, Cu_2O and CuO samples were also measured as reference materials.

Data analysis has been performed with the FEFF8 software package.[6] Theoretical phase and amplitude functions for each pair were calculated with the FEFF8 potential modulus and were checked from the back-Fourier-transformed filtered peaks of the references sample spectra, getting a good agreement. The spectra have been extracted up to 20 $Å^{-1}$ with a good signal-to-noise ratio and analyzed in the typical k range from 2.5 to 15.5 $Å^{-1}$. The best fits of the extracted $k3\chi(k)$ signals were determined by a least-squares spherical curve fitting procedure. The parameter error bars were calculated from the experimental standard deviation derived from the averaging of the extracted $\chi(k)$ function. The F test was applied when necessary to distinguish between fits of similar quality. Average diameter size of the Cu nanoparticles has been estimated from the fitted Cu nearest neighbours value, in hypothesis of fcc packing and cuboctahedral geometry.[7]

Transmission Electron Microscopy (TEM) measurements were performed on a JEOL2010F instrument, with 0.21 nm spatial resolution at Scherzer defocus conditions.

High Angle Annular Dark Field-Scanning Transmission Electron Microscopy (HAADFSTEM) images were recorded on the same microscope by using an electron probe of 0.5 nm of diameter and a diffraction camera length of 12 cm. The use of STEM mode in combination with X-EDS detectors (Oxford Instrument) allows the possibility to corroborate the nature of the particles by perform chemical analysis with a spatial resolution better than 1 nm. To avoid any contact with solvents, samples were deposited by deeping the holeycarbon coated Mo grids into the fresh powder catalysts. The grids were previously pretreated at 200 °C under pure hydrogen flow to clean them and prevent the desorption of volatile carbon base molecules during the quasi in situ experiments. The sample pretreatment were performed in a homemade reaction cell which is coupled to a vacuum transfer holder (VTST4006, GATAN ltd.). This special

holder was used to transfer the sample to the microscope under anaerobic conditions. A standard analytical single tilt holder was used to study the oxidized samples.

The amount of total Cu released in the solution during and after the photocatalytic activity was determined by inductively coupled plasma-atomic emission spectroscopy (ICP-AES). After the photocatalytic activity, an aliquot of the suspension was filtered using a 0.45 μm membrane (Millipore) and the mother liquor was subjected to the analysis for the Cu determination. All solutions were analyzed by ICP-AES using a Spectroflame Modula E Optical Plasma Interface (OPI) instrument by SpectroTM. The total copper concentration was evaluated using calibration curves obtained by dilution of SpectrascanTM copper standard solutions for ICP-AES analysis (Teknolab A/S, Norway). All standards (range: 0.1-50.0 mg L^{-1}) were prepared using a EtOH/H_2O 1:1 solution or a 1.0 M glycerol solution to compensate the matrix effect. The used emission wavelength was 324.754 nm, the limit of detection 0.03 mg L^{-1} and the repeatability of measurements expressed as relative standard deviations (RSD%) and calculated on six replicates of various samples was lower than 4%. Calibration curves obtained by means of five standard solutions had correlation coefficients higher than 0.998.

Results and discussion

TiO_2-SG (surface area 69 m^2 g^{-1}) was composed of a mixture of polymorphs (Figure 4.2a). The analysis of its XRD pattern, following the work of Zhang et al.,[8] evidenced the presence of anatase (64 wt%), rutile (8 wt%) and brookite (28 wt%). Mean crystallite sizes of 11, 32, and 11 nm were calculated for *anatase*, *rutile*, and *brookite*, respectively. TiO_2-PS possessed a slightly higher surface area (104 m^2 g^{-1}). Its powder XRD pattern showed the presence of a pure *anatase* phase (Figure 4.2b), with a mean crystallite size of 8 nm.

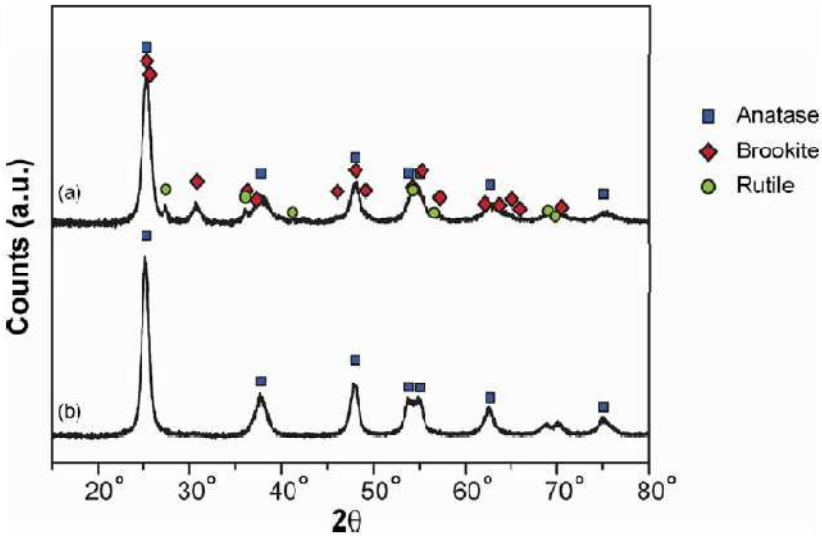

Figure 4.2: *Powder XRD patterns of TiO_2-SG (a) and TiO_2-PS (b)*

XRD analysis of the Cu/TiO_2 nanocomposites did not allow the identification of Cu-related phases probably because of their low amount and/or high dispersion. Therefore, the Cu phases photodeposited on TiO_2 supports were characterized by using X-ray absorption near-edge structure (XANES) or extended X-ray absorption fine structure (EXAFS) spectroscopy. Immediately after photodeposition, XANES spectra at the Cu K edge was in good agreement with that of Cu foil used as reference standard (Figure 4.3), thus indicating that copper is deposited in the form of zero-valent copper. The results of the analysis of the EXAFS spectra are summarized in Table 4.1.

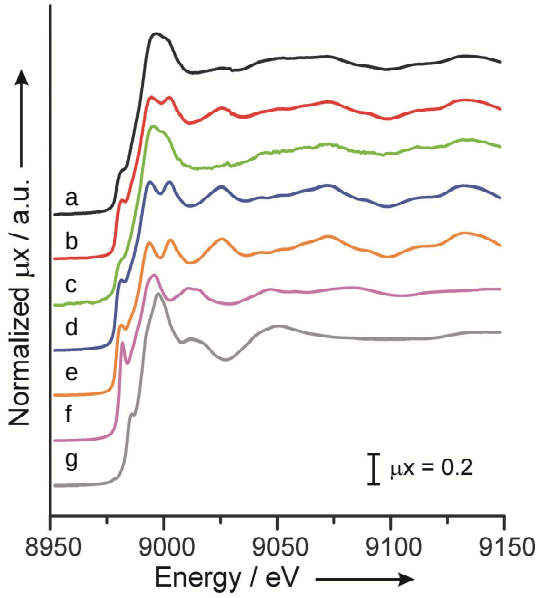

Figure 4.3: *Normalized XANES spectra at the Cu K-edge of photodeposited samples (after photodeposition by irradiation in CH_3OH/H_2O solution for 2h and exposure to air for 24h): Cu(1.0%)/TiO_2-SG (a), Cu(2.5%)/TiO_2-SG (b), Cu(1.0%)/TiO_2-PS (c), Cu(2.5%)/TiO_2-SG (d), Cu foil (e), Cu_2O (f) and CuO (g).*

The Cu-Cu bond lengths are in good accordance with the value observed for metal Cu (0.2556 nm). Cu-O contributions were also observed in the EXAFS signals of the samples with 1.0 wt% Cu loading. These contributions are likely to have originated from the interaction of the Cu atoms with the TiO_2 support, as the Cu-O bond lengths do not match those of standard materials, such as Cu_2O (0.184 and 0.302 nm) and CuO (0.195, 0.276, 0.290, and 0.309 nm). Assuming a cubooctahedral geometry, the average dimensions of the Cu nanoparticles were calculated,[9] evidencing a very high dispersion of the metal on the surface of TiO_2.

Table 4.1. Results from EXAFS analysis at the Cu K-edge of photodeposited samples.

Sample	Shell	N [a]	R (nm) [b]	D_M (nm) [c]
PD-Cu(1.0%)/TiO_2-SG	Cu-O Cu-Cu	2.1 5.1	0.2070 0.2576	1.2
PD-Cu(2.5%)/TiO_2-SG	Cu-O Cu-Cu	- 7.0	- 0.2548	1.5
PD-Cu(1.0%)/TiO_2-PS	Cu-O Cu-Cu	3.1 3.8	0.1984 0.2582	1.0
PD-Cu(2.5%)/TiO_2-PS	Cu-O Cu-Cu	- 10.5	- 0.2852	4.0

Cu nanoparticles of about 1 nm were observed for the samples with low metal loading. An increase in the amount of Cu, lead to a moderate increase in the size of metal nanoparticles for the sample supported on TiO_2-SG. Conversely, a significant increase in the particle size was observed for the samples prepared from TiO_2-PS (Table 4.1). Assuming that the nucleation of Cu occurs by reduction of metal ions by photogenerated electrons and that the subsequent growth of metal nanoparticles takes place around defects on the surface of the support,[10] the mean dimensions of Cu nanoparticles would suggest that in TiO_2-SG a higher number of growth centers are actually present with respect to TiO_2-PS. Indeed, multi-phasic TiO_2 materials show a lower rate for electron-hole recombination, as electrons and holes can be trapped in different and, therefore, separated phases.[11-13] In this way, the lifetime of surface defects is increased, favoring a better dispersion of Cu nanoparticles on the surface of TiO_2-SG.

After exposure to air, all the samples showed a rapid oxidation of Cu nanoparticles, as revealed by the change in color from black to green and by an analysis

of the XANES spectra of the samples. After exposure to the air for 24 h (Figure 4.4) only Cu(2.5 %)/TiO_2-PS still maintains a residual fraction of zerovalent Cu.

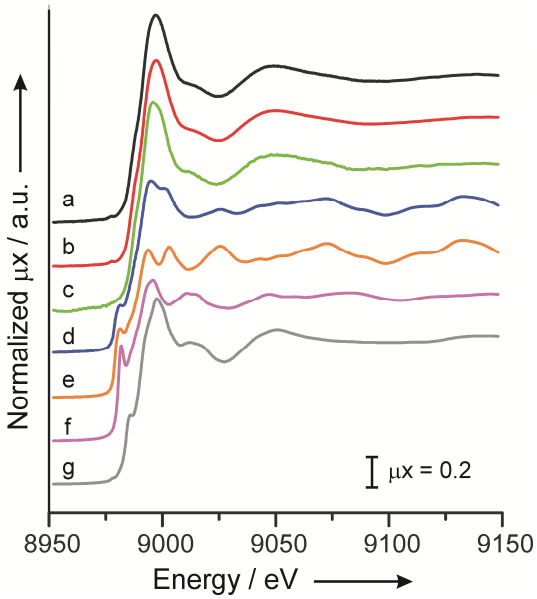

Figure 4.4: *Normalized XANES spectra at the Cu K-edge of photodeposited samples (after photodeposition by irradiation in CH_3OH/H_2O solution for 2h and exposure to air for 24h): Cu(1.0%)/TiO_2-SG (a), Cu(2.5%)/TiO_2-SG (b), Cu(1.0%)/TiO_2-PS (c), Cu(2.5%)/TiO_2-SG (d), Cu foil (e), Cu_2O (f) and CuO (g).*

Furthermore, EXAFS analysis revealed, for the samples supported on TiO_2-SG, CuO-like species without crystallographic order, as supported by the absence of next nearest Cu neighbor contributions. On the other hand, Cu(1.0 %)/TiO_2-PS formed small CuO aggregates, whereas Cu(2.5 %)/TiO_2-PS showed the same shell structure as that of a freshly irradiated sample. This latter behavior would suggest that around the metal core only an amorphous layer of oxide was formed, which can entirely preserve the metal particle structure, with only a negligible reduction in size.

To determinate the Cu particle size distribution and corroborate the EXASF results, high angle annular dark field scanning transmission electron microscopy (HAADF-STEM) was used in combination with X-ray energy dispersive spectrometry (XEDS) chemical analysis. Shown in Figure 4.5 are typical HAADF images of the Cu(2.5 %)/TiO_2-SG and Cu(2.5 %)/TiO_2-PS samples after exposure to the air.

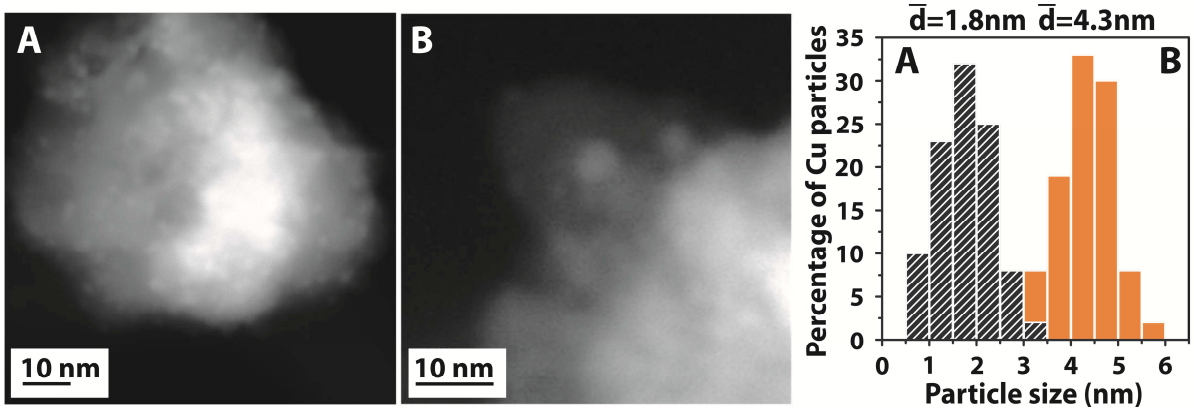

Figure 4.5: *Representative HAADF images and copper particle size distribution of the a) Cu(2.5 %)/TiO2-SG and b) Cu(2.5 %)/TiO2-PS. About 60 copper particles were measured for each sample.*

The average particle sizes were 1.8 and 4.3, respectively. To obtain reliable particle-size distributions of the reduced copper samples, that is, simulating the active state of the copper during photoreaction, the materials were also mildly pre-reduced (pure hydrogen at 70°C) in a quasi in situ equipment and subsequently transferred to the TEM under anaerobic conditions. This approach prevented particle re-oxidation under atmospheric pressure. The particle size distribution and representative STEM images are included in the Figure 4.6. In this case, the mean particle size of the Cu(2.5 %)/TiO_2-SG and Cu(2.5 %)/TiO_2-PS samples were 1.6 and 4.2 nm, respectively. The TEM data were in good agreement with the EXAFS results. The small differences between the fresh and reduced samples can be attributed to the reduction of the CuO_x nanoparticles.

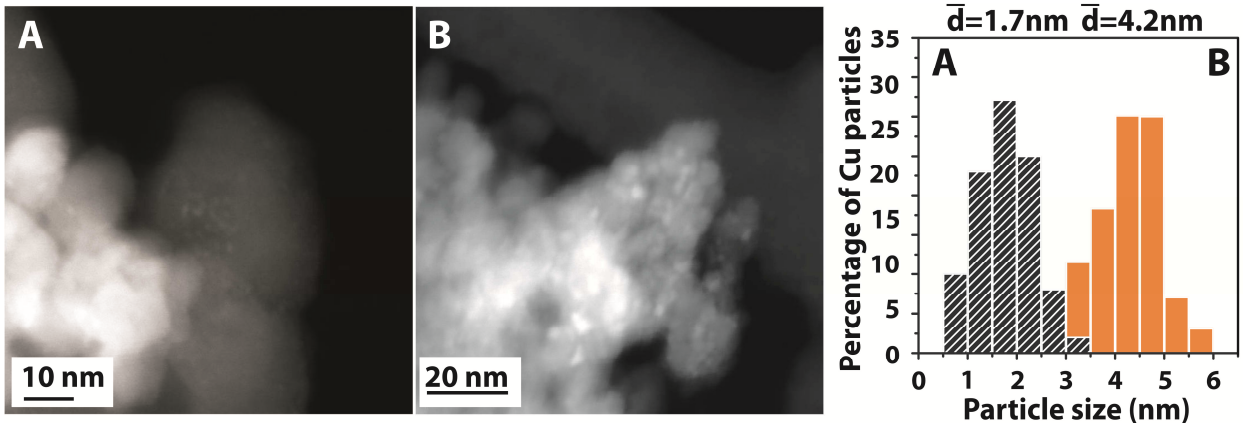

Figure 4.6: *Representative HAADF images and copper particle size distribution of the (A) Cu(2.5%)/TiO_2-SG and (B) Cu(2.5%)/TiO_2-PS, pre-reduced in pure hydrogen at 70°C in a "quasi in situ equipment" and subsequently transfer to the TEM under anaerobic conditions. Total particles about 65 per sample.*

Shown in Figure 4.7 is the H_2 evolution from aqueous solution of ethanol and glycerol, both of which used a UV/Vis light irradiation or a Solar Simulator. Other by-

products were detected in the gas stream: CH_4, CO_2, ethylene, and acetaldehyde in the case of ethanol, CO_2 in the case of glycerol.

Samples prepared from TiO_2-SG demonstrated better performance with respect to those prepared from TiO_2-PS. This could be ascribed to the longer lifetime of the electron/hole pair of multiphasic TiO_2 materials.[11-13] Comparing samples with the same support, higher H_2 productions were observed with a Cu loading of 1.0 wt% under UV/Vis irradiation and in the presence of ethanol, whereas for the glycerol solutions, a Cu loading of 2.5 wt% produced better results.

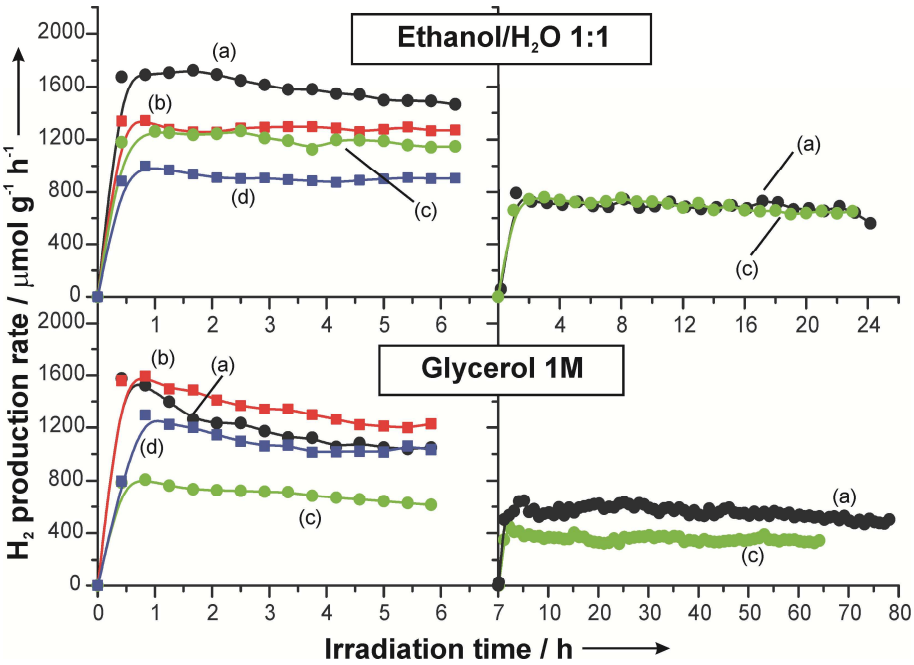

Figure 4.7: *H_2 production rates on photodeposited Cu/TiO_2 nanocomposites from ethanol or glycerol aqueous solutions by irradiation in the UV/Vis region (left side) or by Solar Simulator (right side): a) Cu(1.0 %)/TiO_2-SG; b) Cu(2.5 %)/TiO_2-SG; c) Cu(1.0 %)/TiO_2-PS; d) Cu(2.5 %)/TiO_2-PS. Please note the different time scale*

Using irradiation produced by the Solar Simulator produced a lower photocatalytic activity than if the UV/Vis source was used. This might be ascribed to the lower contribution of the TiO_2 support, which adsorbs only UV photons, scarcely present (≈4%) in the Solar Simulator source. Therefore, these materials possess an appreciable activity even using visible light. After an initial activation period, the H_2 production is rather stable. Ethanol dehydrogenation results in the production of large quantities of acetaldehyde, whose concentration continuously increased in the gas stream (Fig. 4.8), due to the equilibration with the products in the liquid phase.

Although no acetic acid or its esters are detected by GC/MS analysis (Fig. 4.9a), its intermediacy could be suggested by the presence of equimolar amounts of CO_2 and CH_4 (Fig. 4.8).

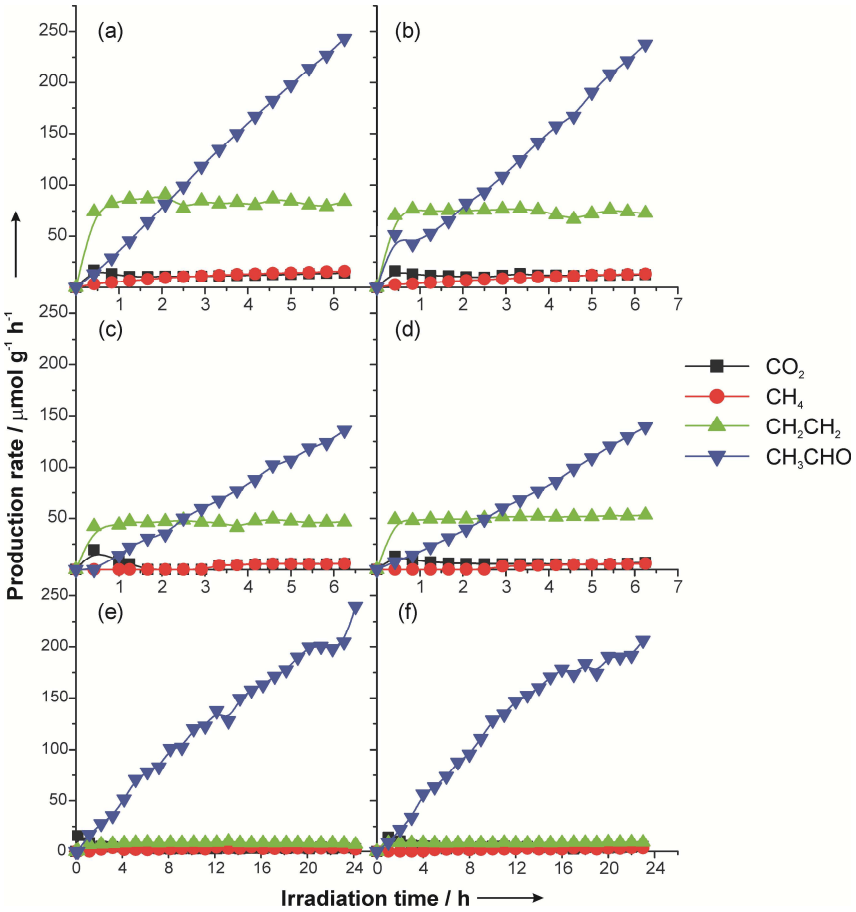

Figure 4.8: *By-products detected in the gas stream during H_2 production from EtOH/H_2O 1:1 solution under UV-vis irradiation of Cu(1.0%)/TiO_2-SG (a), Cu(2.5%)/TiO_2-SG (b), Cu(1.0%)/TiO_2-PS (c) and Cu(2.5%)/TiO_2-SG (d) and under irradiation with a Solar Simulator for Cu(1.0%)/TiO_2-SG (e) and Cu(1.0%)/TiO_2-PS (f). Please, note the different time scales.*

The mechanism of significant adsorption of acetic acid on TiO_2 polymorphs was recently discussed in details.[14] Alternatively, CH_3CHO could decompose to CH_4 and CO, followed by WGSR promoted by light.[15] Since CH_3CHO accumulates in solution, it is evident that its transformation is slower than its formation. As a consequence, owing to the presence of both ethanol and surface acidic sites on the TiO_2 support, formation of the corresponding acetaldehyde diethoxy acetal was also observed. The same acidic sites might be considered responsible for the formation of ethylene by dehydration of ethanol. (Fig. 4.9b)

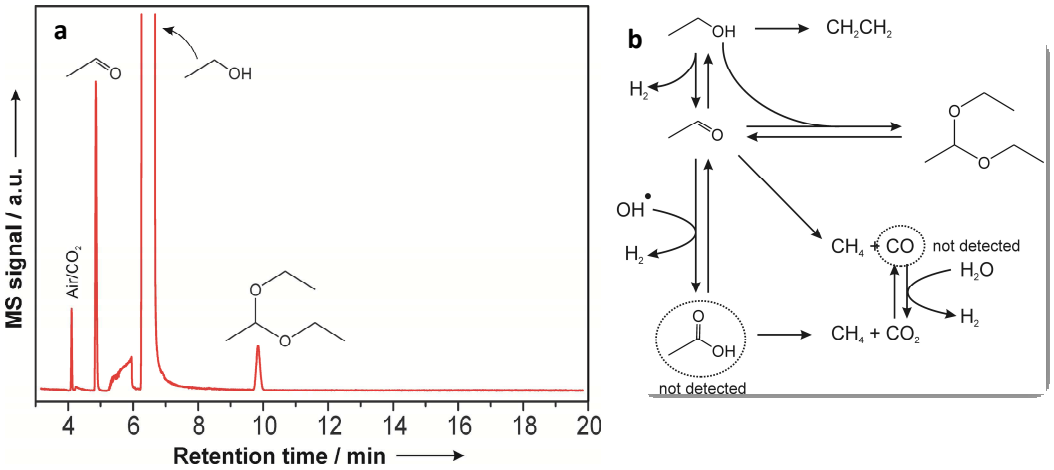

Figure 4.9: *a) GC/MS analysis of the liquid phase after photocatalytic H_2 production from EtOH/H_2O 1:1 solution using Cu(1.0%)/TiO_2-SG under irradiation with the Solar Simulator for 24h; b) possible reaction pathway involved in the photocatalytic H_2 production over Cu/TiO_2 nanocomposites from aqueous ethanol solution.*

In the case of glycerol, only CO_2 was detected in the gas stream (Fig. 4.10), while in the liquid phase the main by-products detected have been 1,3-dihydroxypropanone and hydroxyacetaldehyde.

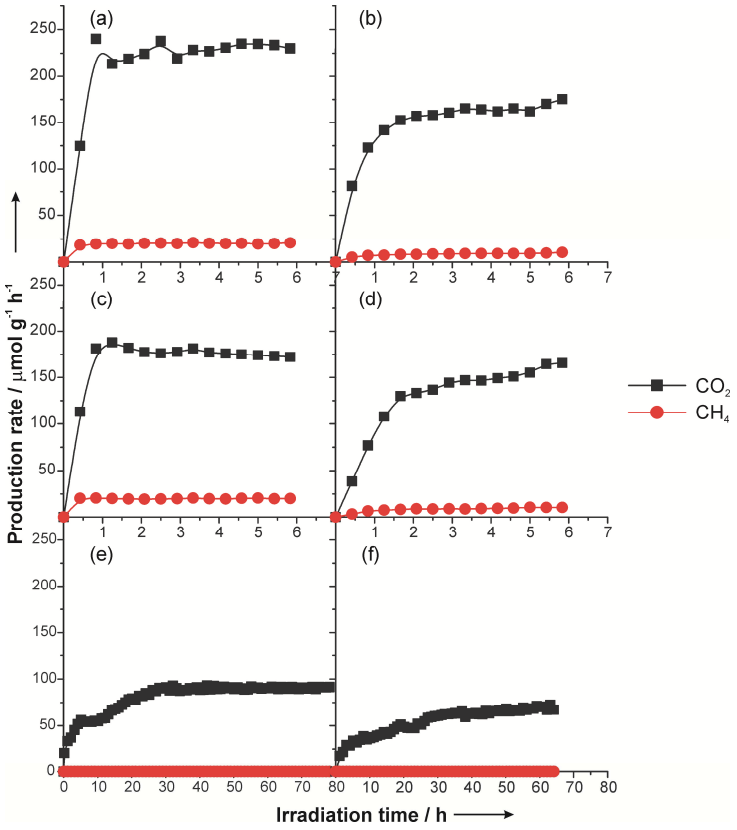

Figure 4.10: *By-products detected in the gas stream during H_2 production from glycerol 1M solution under UV-vis irradiation of Cu(1.0%)/TiO_2-SG (a), Cu(2.5%)/TiO_2-SG (b), Cu(1.0%)/TiO_2-PS (c) and Cu(2.5%)/TiO_2-SG (d) and under irradation with a Solar Simulator for Cu(1.0%)/TiO_2-SG (e) and Cu(1.0%)/TiO_2-PS (f). Please, note the different time scales.*

Minor amounts of 2,3-dihydroxypropanal, 1,2-ethanediol, hydroxyacetone, as well as two isomers of dimethyl-1,4-dioxane were also detected (Fig. 4.11a). Notably, no traces of either carboxylic acids or their ethyl esters were ever detected. The minor compounds derive from partial transformations occurring on the main products (Fig. 4.11b).

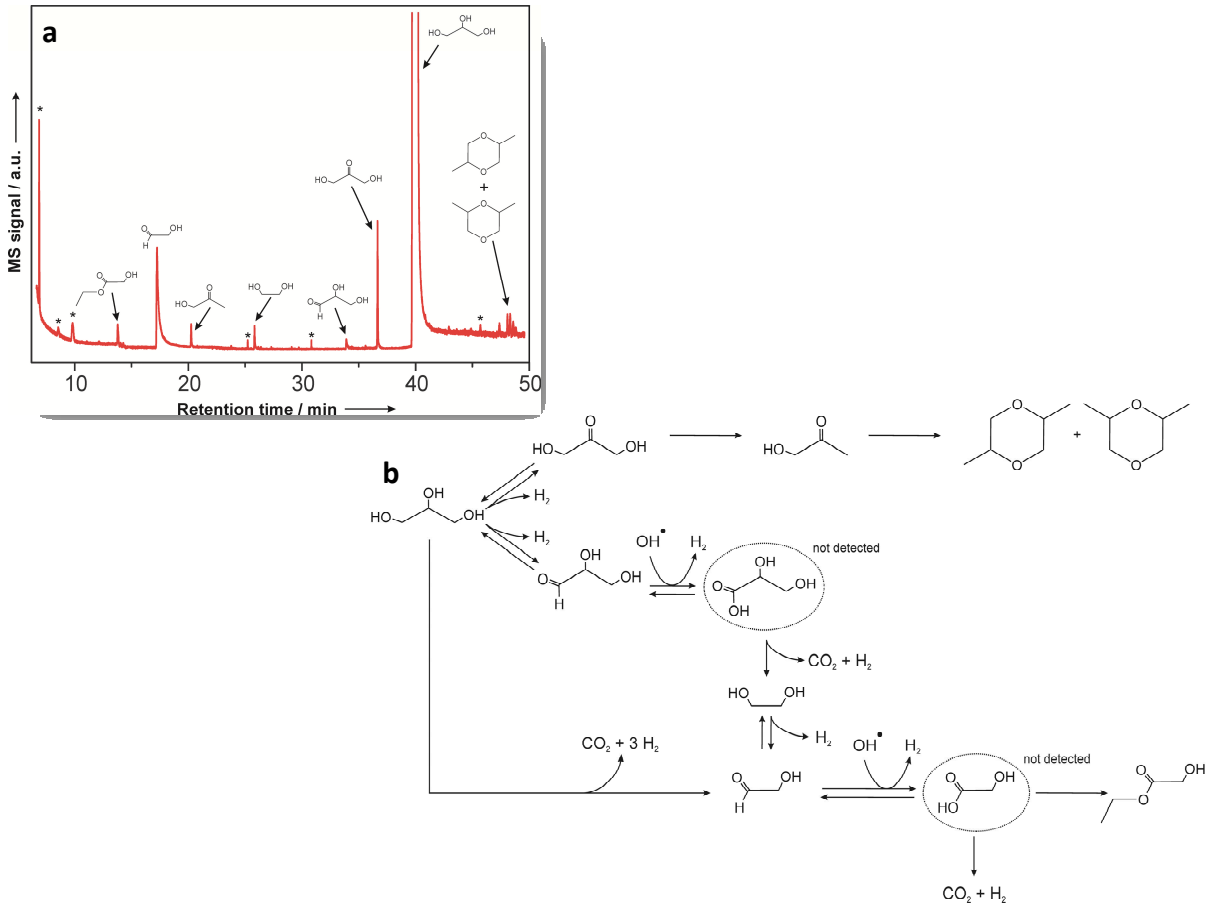

Figure 4.11: *a) GC/MS analysis of the liquid phase after photocatalytic H_2 production from glycerol 1M solution using Cu(1.0%)/TiO_2-SG under irradiation with the Solar Simulator for 24h. Asterisks mark impurities present in MeOH used for dilution of the samples before GC/MS analysis.; b) Possible reaction pathway involved in the photocatalytic H_2 production over Cu/TiO_2 nanocomposites from aqueous glycerol solution.*

For instance, conversion of 1,3-dihydroxypropanone into 1-hydroxy-2-propanone was very limited, which lead to the eventual accumulation of 1,3-dihydroxypropanone in solution. This makes possible the sustainable production of 1,3-dihydroxypropanone, an interesting compound used for preparation of skincare products and also as a building block for the synthesis of biodegradable polymers.[16] On the other hand, formation of 2,3-dihydroxypropanal opens the way to the full

degradation of glycerol to H_2 and CO_2 through a sequence of intermediate including alcohols, aldehydes and carboxylic acids.

After the photocatalytic experiments, the resulting liquid phases were analysed by ICP-AES to check a possible leach of Cu during irradiation. When irradiation was performed with a UV-vis, source, very small amounts of Cu (2 – 3 % of total) were detected in the liquid phase in both cases. This result is consistent with that reported in the previous chapter, indicating that some amount of Cu can be oxidized and leached out from the catalyst during the reaction. However, at the same time it can be re-photodeposited, owing to the constant presence of UV photons, of the TiO_2 semiconductor and the sacrificial agent. On the contrary, when irradiation was performed with the Solar Simulator (Fig. 3), the amount of Cu detected in the liquid phases were much higher (about 16% and 9% for the samples supported on TiO_2-SG and TiO_2-PS respectively). These values are independent of both the sacrificial agent (ethanol or glycerol) and the experiment time (24 or 80 h) suggesting that an equilibrium between the Cu ions in solution and the Cu photodeposited on the TiO_2 is established. In this case, the fraction of UV photons is quite low (~4%), not sufficient to re-photodeposite Cu efficiently. Despite this, only minor deactivation was observed in all the experiments performed using the Solar Simulator (Fig. 4.7).

Conclusions

Summarizing, active and cheap nanocomposites can be obtained by photodeposition of Cu on the surface of TiO_2 supports. The activity of TiO_2 is strongly influenced by its structural characteristics: when a multi-phasic support is used, the high number of defects (electron/hole pairs) produced results in a very high dispersion of the metal and in a higher activity in H_2 production, by an increase in the oxidation rate of the sacrificial agents. Minor leaching is observed under UV irradiation, while under solar like irradiation a considerable fraction of Cu is oxidized and subjected to photocorrosion. After a few hours, the amount of Cu ions becomes constant suggesting the establishment of an equilibrium between the Cu photodeposition process, induced by the small fraction of UV (~ 4%), and the leaching phenomena. Remarkably, the

negative effect on the hydrogen production is not dramatic. Regeneration process based on the use of short UV irradiation steps can overcome progressive and serious deactivation. Besides the production of hydrogen, photocatalysis could open the way to the synthesis of building blocks of interest for chemical industry, since the oxidation of carbonyl compounds is the limiting step of the degradation reaction occurring on the sacrificial agent.

References

[1] S. Fernando, S. Adhikari, C. Chandrapal, N. Murali. *Energy and Fuels* **2006**, *20*(4), 1727-1737.
[2] M. Kleinert, T. Barth. *Energy and Fuels* **2008**, *22*(2), 1371-1379.
[3] V. Gombac, L. De Rogatis, A. Gasparotto, G. Vicario, T. Montini, D. Barreca, G. Balducci, P. Fornasiero, E. Tondello, M. Graziani. *Chem. Phys.* **2007**, *339*(1-3), 111-123.
[4] S. Sakthivel, M. C. Hidalgo, D. W. Bahnemann, S. U. Geissen, V. Murugesan, A. Vogelpohl. *Applied Catalysis B-Environmental* **2006**, *63*(1-2), 31-40.
[5] D. I. Kondarides, A. Patsoura, X. E. Verykios. *J. Adv. Oxid. Technol.* **2010**, *13*(1), 116-123.
[6] A. L. Ankudinov, B. Ravel, J. J. Rehr, S. D. Conradson. *Phys. Rev. B Condens. Matter Mater. Phys.* **1998**, *58*(12), 7565-7576.
[7] A. Jentys. *Phys. Chem. Chem. Phys.* **1999**, *1*(17), 4059-4063.
[8] H. Zhang, J. F. Banfield. *J Phys Chem B* **2000**, *104*(15), 3481-3487.
[9] A. Jentys. *Phys. Chem. Chem. Phys.* **1999**, *1*(17), 4059-4063.
[10] R. Kydd, J. Scott, W. Y. Teoh, K. Chiang, R. Amal. *Langmuir* **2010**, *26*(3), 2099-2106.
[11] B. Sun, A. V. Vorontsov, P. G. Smirniotis. *Langmuir* **2003**, *19*(8), 3151-3156.
[12] C. A. Emilio, M. I. Litter, M. Kunst, M. Bouchard, C. Colbeau-Justin. *Langmuir* **2006**, *22*(8), 3606-3613.
[13] M. C. Hidalgo, M. Maicu, J. A. Navío, G. Colón. *Catalysis Today* **2007**, *129*(1-2 SPEC. ISS.), 43-49.
[14] A. Mattsson, L. Osterlund. *Journal of Physical Chemistry C* **2010**, *114*(33), 14121-14132.
[15] L. Millard, M. Bowker. *Journal of Photochemistry and Photobiology A: Chemistry* **2002**, *148*(1-3), 91-95.
[16] C. H. Zhou, J. N. Beltramini, Y. X. Fan, G. Q. Lu. *Chemical Society Reviews* **2008**, *37*(3), 527-549.

Chapter 5

SUPPORTED SYSTEMS

Part 1:
Supported systems based on copper oxides

Over the last decade, owing to their possible applications in various areas, p-type semiconducting Cu_2O- and CuO-based nanostructures have been the focus of a great interest. Cubic Cu_2O (Eg≈2.1 eV) and the monoclinic CuO (Eg≈1.2 eV) both have a broad perspective of attractive utilizations as active components in superconductors, electrode materials, field emitters, solar cells, and photocatalysts.[1-5] In the latter context, a challenging and strategic concern is actually the use of copper oxide based nanosystems for the direct photocatalytic splitting of water, an attractive solution to provide clean and recyclable H_2 energy in view of increased environmental concerns.[4, 6-10] To date, most of the investigations have focused on the use of nanocomposite Cu_xO-TiO_2 (x=1,2) systems,[4, 9-12] whereas the properties of pure copper oxides in these fields, especially as a function of their nanoscale organization, have been scarcely addressed despite their extensive use in solar cell devices.[1, 2, 13] In particular, pure Cu_2O and CuO thin films have been reported to be inactive in H_2O photocatalytic splitting,[8, 11] as a

result of very fast recombination phenomena and the position of the conduction band edge, respectively. Nevertheless, the design of supported nanostructured photocatalytic films can enhance performances and eliminate the necessity of filtration processes for recovery of the powdered catalyst. In fact, the development of effective and low-cost preparation routes for these materials is still an ongoing challenge.[14]

Catalysts preparation

The systems were grown under O_2-based atmospheres on HF etched Si (100) substrates at different temperatures starting from a Cu^{II} precursor, $Cu(hfa)_2$·TMEDA (hfa=1,1,1,5,5,5-hexafluoro-2,4-pentanedionate, TMEDA=N,N,N',N'-tetramethylethylenediamine), which has not been adopted to date in CVD routes to copper oxides. The precursor was synthesized following a modification of a reported procedure.[15] The custom-built CVD reaction system used for copper oxide depositions[16, 17] consisted of a horizontal quartz tube cold-wall reactor equipped with a resistively heated susceptor and an external glass vessel for precursor vaporization. Depositions were carried out in O_2-based reaction atmospheres at growth temperatures between 350 and 550°C on p-type Si(100) wafers (MEMC, Merano, Italy; size: 1cm x 1cm x 1mm), preliminarily subjected to etching treatment in 2% aqueous HF to remove the native SiO_2 layer from their surface. The precursor was vaporized at 70°C and transported into the reactor tube by means of an oxygen flow rate of 100 sccm, in the presence of a further 100 sccm O_2-based gas flow. Gas lines and valves between the precursor reservoir and the reaction chamber were maintained at a temperature of 120°C in order to avoid undesired precursor losses by condensation phenomena. The total pressure during the depositions, carried out for 120 min, was set at 10.0 mbar. Once the precursor supply was stopped, the deposits were cooled to room temperature under reduced pressure (10.0 mbar).

Catalysts characterization

Glancing Incidence X-ray Diffraction (GIXRD) patterns were recorded using a Bruker D8 Advance instrument equipped with a Göbel mirror and a CuK_α source (40 kV,

40 mA), at a constant incidence angle of 0.5°. The average crystallite dimensions were estimated by means of the Scherrer equation.

Field Emission-Scanning Electron Microscopy (FE-SEM) were performed by a Zeiss SUPRA 40VP instrument, operated at acceleration voltages between 10 and 20 kV. No sample pretreatment was performed prior to analyses.

X-ray Photoelectron and X-ray Excited Auger Electron Spectroscopy (XPS and XE-AES) analyses were performed on a Perkin Elmer Φ 5600ci spectrometer with a non-monochromatized AlK_α source, at a working pressure lower than 10-9 mbar. The Binding Energy (BE) shifts were corrected assigning to the C*1s* line of adventitious carbon a value of 284.8 eV.6 The atomic compositions were evaluated using sensitivity factors provided by Φ V5.4A software. Sputtering was carried out by an Ar^+ ion beam accelerated at 3.0 kV, with an argon partial pressure of $5x10^{-8}$ mbar.

Photocatalytic experiments were carried out in a 250-mL pyrex discontinuous batch reactor with an external cooling jacket and equipped with connections for inlet/outlet of argon gas (15 mL/min), which served for the collection and transfer of gaseous products to the analysis system. The reactor was filled with a 1:1 water-alcohol mixture. The supported Cu_xO (x=1,2) nanosystems were located on the internal walls of the photoreactor, that was externally covered by an aluminum foil. All the experiments were carried out at 20°C.

A 125 W medium pressure mercury lamp (Helios Italquartz) with pyrex walls was used for UV-visible excitation, while a 125 W low pressure mercury lamp (Hanovia) with quartz wall was employed for UV irradiation. The photon flux was measured by using a DeltaOHM radiometer HD2302.0. Accordingly to Lianos et al.,[18] the approximate average incident radiation power on the photocatalyst was 129 and 254 mW for UV-visible and UV excitation, respectively.

On-line gas detection was performed by mean of an Agilent 6890 GC system, equipped with a 10 way - two loop injection valve. A molecular sieve 5A column and a Thermal Conductivity Detector (TCD) were used for H_2 analysis, while a Poraplot Q connected to a methanator and to a Flame Ionization Detector (FID) was employed for CO, CO_2 and volatile organic compounds analysis. Ar (99.999 %) was used as carrier gas. Reference experiments (blank) were performed in the absence of photocatalysts.

Results and discussion

For a substrate temperature of 350°C (Fig. 5.1a), the presence of copper(I) oxide as the sole detectable crystalline phase of the Cu-O system was confirmed by the signals peaked at 2ϑ=29.5°, 36.4° and 42.2°, which were ascribed to the [110], [111] and [200] reflections of cubic Cu_2O (*cuprite*)[1]. In a different way, an increase in the substrate temperature resulted in the progressive $Cu_2O \rightarrow CuO$ transformation, and finally only CuO (*tenorite*)[2] was present for T≥400°C.

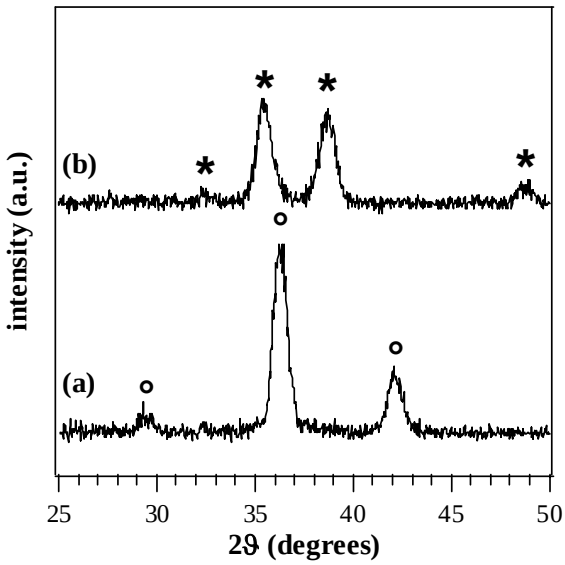

Figure 5.1: *GIXRD patterns of the copper oxide nanodeposits: (a) Cu_2O (o); (b) CuO (*).*

This phenomenon was unambiguously confirmed at 550°C (Fig. 5.1b) by the reflections located at 2ϑ=32.5°, 35.5°, 38.7° and 48.7°, assigned respectively to the [$\bar{1}$10], [002]/[$\bar{1}$11], [111] and [$\bar{2}$02] planes of monoclinic copper(II) oxide. In both cases, no appreciable orientations were detected and the average crystallite sizes were close to 20 nm, indicating that the obtained deposits were nanostructured.

Representative field emission scanning electron microscopy (FE-SEM) images (Figure 5.2) revealed the formation of nano-architectures as opposed to conventional thin films, the usual target of CVD processes.

[1] Pattern N° 5-667, *Joint Committee on Powder Diffraction Standards* (JCPDS**), 2000**.
[2] Pattern N° 45-937, *Joint Committee on Powder Diffraction Standards* (JCPDS), **2000**

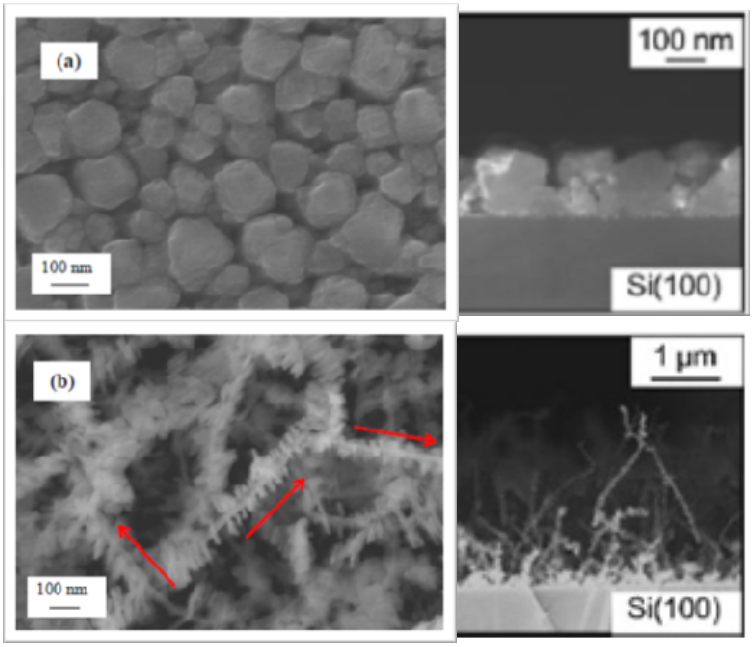

Figure 5.2: *Plane-view (left) and cross-sectional (right) FE-SEM images for a) Cu_2O and b) CuO nanosystems supported on Si(100). In the case of the CuO sample, the main growth axis for some nanowires is evidenced by arrows.*

Deposition temperatures of 350°C resulted in the formation of Cu_2O globular nanostructures (Figure 5.2a), characterized by evenly distributed faceted agglomerates (150 nm) typical of a three-dimensional growth mode, with an appreciable presence of voids.

The surface of each grain was highly nanostructured, with domains smaller that 20 nm (Fig. 5.3).

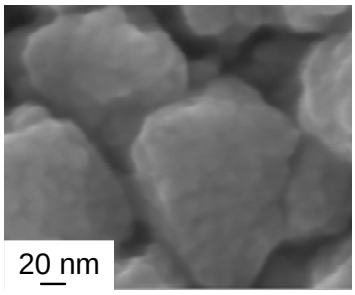

Figure 5.3: *High magnification FE-SEM image of a Cu_2O sample supported on Si(100).*

In contrast, higher temperatures led to the production of pure CuO nanodeposits (Figure 5.2b), characterized by the presence of uniformly distributed branched nanowires with lengths higher than 2 µm, protruding from the substrate surface and resembling nanosized saws with teeths distributed on both sides, were observed, resulting in the formation of a highly porous structure. The mean wire lateral size could

be evaluated as 100 nm. It is worthwhile highlighting that only marginal variations in the system morphology could be detected after the photocatalytic tests. The formation of these peculiar wires could be explained by assuming that, on increasing the growth temperature, the adsorbed species might progressively acquire a higher surface mobility, resulting ultimately in the observed anisotropic structures. The formation of side branches took place owing to the tendency of the system to reduce the lattice stress generated during the initial formation of 1D-like structures.[3]

In order to clarify the CuO growth mechanism, a valuable support was provided by a statistical TEM analysis evidencing two major families of 1D architectures (fig. 5.4). In particular, the growth direction indicated by arrows in fig. 5.2b is related to the presence of long wires with a lateral size of ≈20 nm (fig. 5.4a). Such nanostructures are characterized by a high content of stacking faults (marked by arrows in fig. 5.4b) and mainly grow either along the [001] or the [11$\bar{1}$] direction. In agreement with FESEM analyses, a second family of smaller nanorods (average length ≈90 nm; lateral size ≈8 nm) is observed and correlated to the tooth of the combs revealed in fig. 5.2b. TEM analyses evidenced that the latter branches preferentially grow with a [100] and [$\bar{1}$10] orientation and present a structural relation to the parent 1D nanorods that can be explained in terms of an oriented attachment mechanism (fig. 5.4c,d).[19] As a matter of fact, after the first nucleation stages, an anisotropic CuO growth of the largest nanowires takes place along the [001] and [11$\bar{1}$] directions. During this process, the generation of extensive defects is accommodated through the formation of smaller lateral branches, reducing thus the overall system energy and resulting in the observed peculiar morphology.

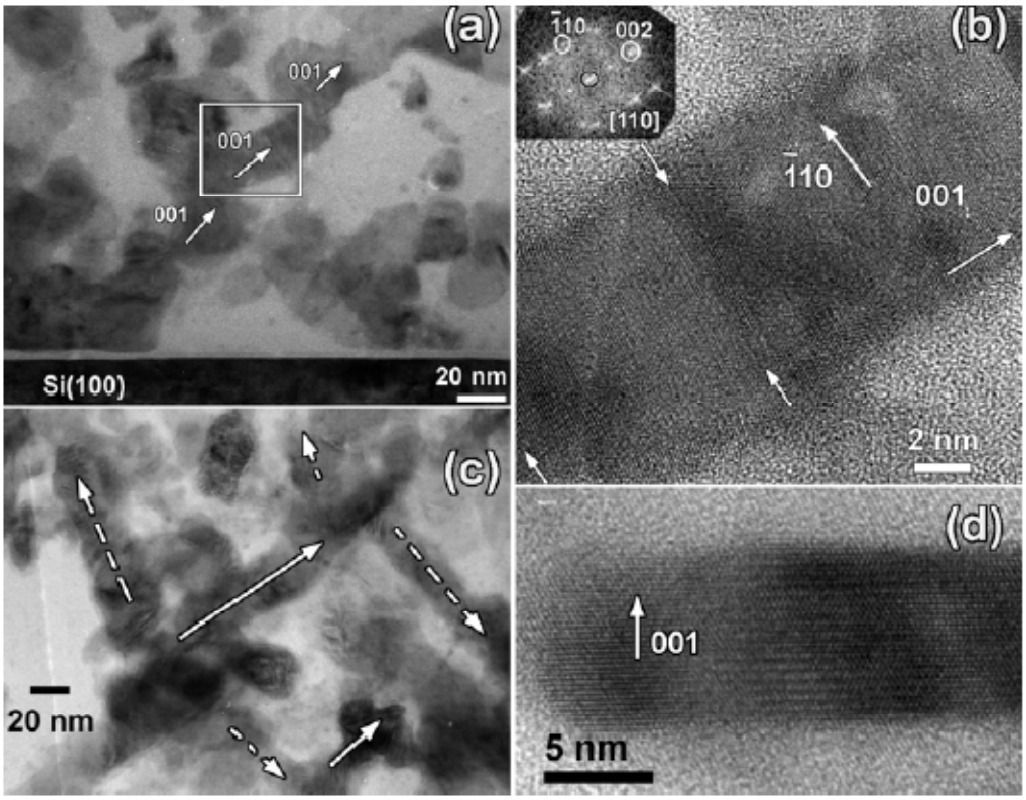

Figure 5.4: *Representative TEM images of a CuO sample deposited on Si(100) at 550°C from a dry O_2 atmosphere: (a) cross-section view of a CuO nanowire grown along the [001] direction. (b) HRTEM image of the region marked by a white rectangle in (a). Stacking faults are indicated by arrows. (c) Plane-view TEM image showing the oriented attachment mechanism. The growth direction for the main nanowire and the lateral branches are evidenced by continuous and dotted arrows, respectively. (d) HRTEM image of a single lateral branch.*

Irrespective of the specific growth mechanism, both the Cu_2O and CuO specimens reported in fig. 5.2 were characterized by an appreciably open morphology, an important pre-requisite for the above discussed functional applications. To obtain a deeper insight into the system morphology, AFM investigations were performed on both samples. In fact, since in the case of supported nanosystems surface area evaluation is a difficult task due to the low material amount, its semi-quantitative estimation can be obtained by Root Mean Square (RMS) roughness measurement.[20] In fact, the effective surface area is typically larger for a rougher surface. To this regard, fig. 5.5 displays, as a representative example, the AFM image of the specimen reported in fig. 5.2a. As can be observed, the sample texture was characterized by globular aggregates, in agreement with FESEM analyses. Interestingly, the RMS roughness for the present sample, evaluated by a $2\times2\mu m^2$ image, was as high as 83 nm. A similar AFM investigation on the sample of fig. 5.2b yielded a RMS roughness of 117 nm. This value,

appreciably higher than the previous one, was ascribed to the peculiar sample morphology characterized by the presence of entangled 1D nanowires, producing a more marked corrugation.

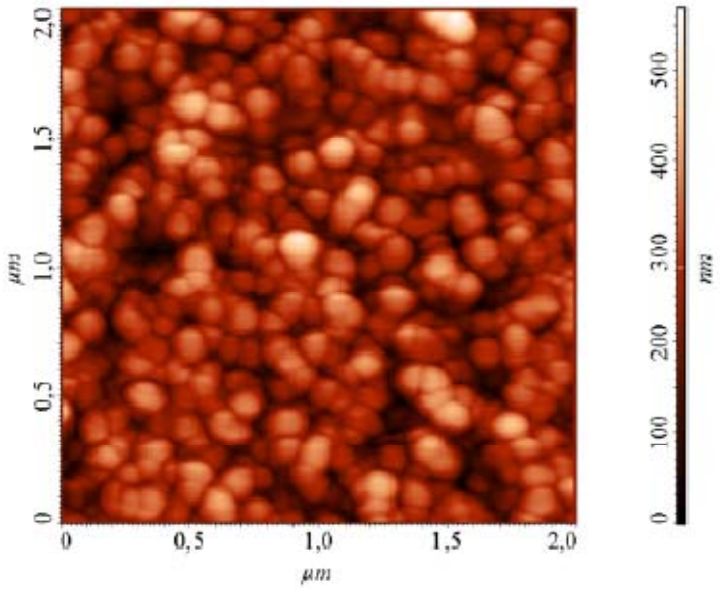

Figure 5.5: *AFM micrograph for a Cu_2O specimen on Si(100) synthesized at 350°C under a wet O_2 atmosphere.*

In the case of deposits obtained at 350°C, the absence of well detectable shake-up Cu*2p* satellites, the Cu$2p_{3/2}$ BE value (932.5 eV) and the Auger α parameter, calculated by the sum of Cu$2p_{3/2}$ BE and the CuLMM Auger peak Kinetic Energy (KE) [α=BE(Cu$2p_{3/2}$)+KE(CuLMM)=1849.5 eV], were all in agreement with the occurrence of Cu_2O as the main phase[21, 22] In a different way, for samples grown at 550°C, the Cu*2p* photoelectron peak displayed the presence of intense shake-up satellites centred at BE values ca. 9.0 eV higher than the main spin-orbit split components, whose presence is a finger-print for d^9 copper(II) species. In addition, the presence of CuO as the dominant Cu-O phase was further confirmed by the peak position [BE(Cu$2p_{3/2}$)=934.0 eV] and the Auger α parameter (α=1851.8 eV)[21, 22] These findings were consistent with GIXRD results (see above). It is worth noticing that carbon photoelectron signals disappeared after 5' Ar^+ erosion, suggesting thus that C presence was limited to the outermost regions due to atmospheric contamination and that the $Cu(hfa)_2$•TMEDA precursor had a clean decomposition pattern under the adopted conditions. After the photocatalytic tests, these compositional features were maintained and no significant variations were ever observed.

Figure 5.6 reports the rate of H_2 evolution on the obtained systems using H_2O/CH_3OH solutions. Interestingly, even by using visible light (Figure 5.6a), a constant rate of hydrogen production was observed on CuO, corresponding to a quantum efficiency of 0.6%. This unexpected reactivity, which differs from that of the homologous bulk materials or compact films (see below),[8, 11] could be ascribed to the peculiar morphology of the obtained nanosystems (Figure 5.2) Consistent with the higher band gap and the more compact structure with respect to CuO (see above and Figure 5.2), the Cu_2O nanosystem displayed a worse, although appreciable, performance. In both cases, blank experiments confirmed that no H_2 evolution was observed in the absence of catalysts upon illumination with visible light. Under irradiation with UV light (Figure 5.6b), both systems showed a considerably higher rate of H_2 production, corrected for the small amount of hydrogen generated by photolysis even in the absence of catalysts.

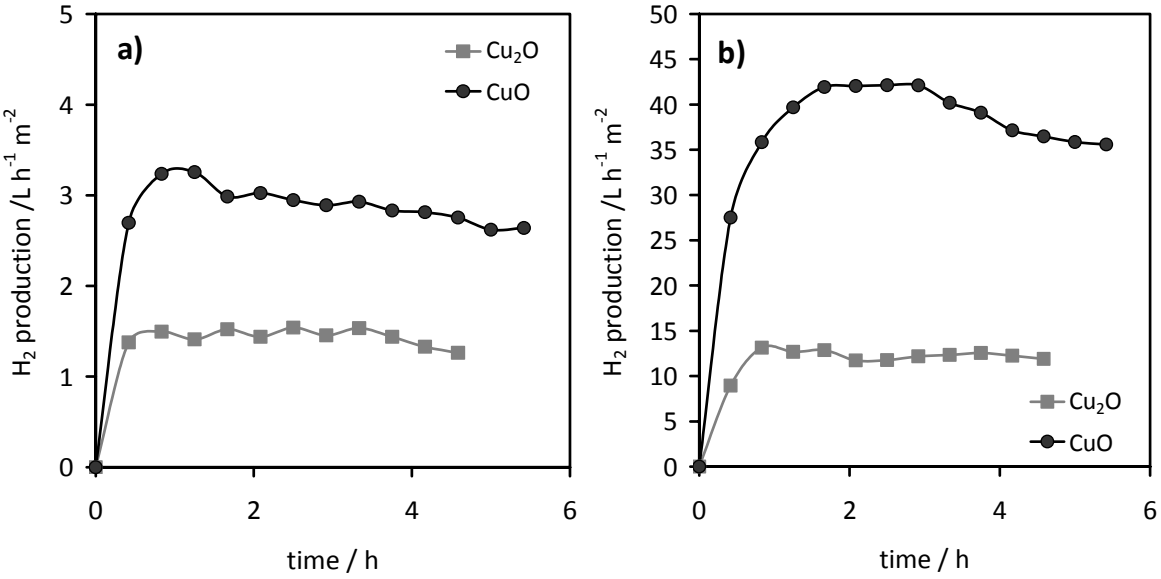

Figure 5.6: *The rate of H_2 evolution per unit area as a function of time on Cu_2O and CuO nanosystem photocatalysts from H_2O/CH_3OH solutions under irradiation with a) visible and b) UV light.*

The activity of pure copper oxides in the above process can be explained by the concurrence of different causes. In particular, in the case of CuO, the presence of size-dependent phenomena might lead to an upward shift of the conduction band, thus making feasible the water reduction process. In addition, in both cases, extensive light scattering due to the peculiar nanosystem morphologies likely enhances the absorption coefficient, thus resulting in the more efficient generation of electrons and holes.

Additionally, note that the high aspect ratio of these nanowire structures is likely beneficial to prevent electron–hole recombination phenomena.[14]

To compare the specific activity of these systems with that of the corresponding conventional oxides, we estimated the amount of Cu_xO (x=1,2) in the investigated CVD nanosystems by considering the bulk Cu_2O and CuO densities and the average sample thickness evaluated by cross-sectional FE-SEM images (see Figure 5.2). This calculation considers the specimens as compact and continuous coatings, inevitably resulting in an appreciable overestimation of the material amount, in particular in the case of CuO nanowires that are characterized by a very open structure (Figure 5.2b). The amount of Cu_xO was estimated by considering the corresponding bulk densities (6.0 and 6.4 $g \times cm^{-3}$, respectively) and the average sample thickness, as evaluated by cross-sectional FE-SEM images (Figure 5.2) and they were resulted as 1.6 and 0.12 mg for the CuO and Cu_2O nanosystems, respectively. In order to evidence the effect of the peculiar morphology on the reactivity of the CVD copper oxide samples, the catalytic performances of the synthesized specimens were compared to those of commercial Cu_2O (Alfa Aesar, 99.9%) and CuO (Aldrich, 99.99%) powders.

Under the same experimental conditions, commercial CuO and Cu_2O were used as photocatalysts in the form of pressed powders with the same geometrical area as the supported samples prepared by CVD. Notably, a significantly higher amount of Cu_xO had to be used in order to obtain a self-supported pellet. Representative FE-SEM images of the powdered samples are reported in Figure 5.7 (compare Figure 5.2). As can be observed, commercial copper(I) oxide was characterized by the presence of irregular platelet-like aggregates, with average sizes ranging from 350 nm to 6 μm. In a different way, the images for the CuO specimens evidenced the presence of particles with a mean diameter of 500 nm strongly interconnected among each other, resulting in bigger agglomerates.

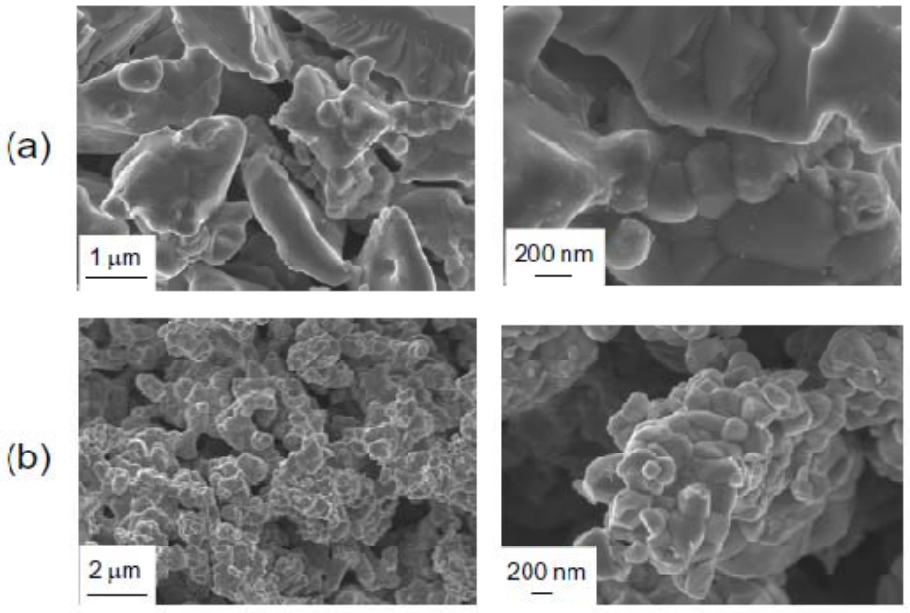

Figure 5.7: *Representative FE-SEM images of: (a) Cu_2O; (b) CuO commercial powders.*

For comparison purposes, the hydrogen production rate of the supported CVD systems and the pressed powders was normalized with respect to their geometrical area and sample weight.

With CuO (Aldrich) the H_2 production rate was evaluated to be 140 and 200 L $h^{-1}m^{-2}g^{-1}$ in the visible and UV regions, respectively, which are significantly lower than those of the nanosystem prepared by CVD (2000 and 26000 L $h^{-1}m^{-2}g^{-1}$, respectively). Similarly, bulk Cu_2O (Alfa Aesar) showed a significantly lower activity (130 and 580 L $h^{-1}m^{-2}g^{-1}$ in the visible and UV regions, respectively) with respect to the corresponding Cu_2O samples obtained by CVD (11800 and 110000 L $h^{-1}m^{-2}g^{-1}$ under visible and UV irradiation, respectively). In this context, it is worth highlighting that the rate of hydrogen production was evaluated with respect to the geometrical sample area rather than to the surface area. In fact, although the latter parameter can significantly influence the photocatalyst performance, its accurate measurement could not be performed owing to the very low amount of material in the present supported nanosystems.

Overall, these observations highlight the significant role exerted by the morphology of the present samples obtained by CVD on their photocatalytic performances.

Although the Cu_2O system showed a relatively stable H_2 evolution rate as a function of time, a decreasing rate of hydrogen production with time was observed over CuO, in particular upon UV illumination (Figure 5.6).

Cycling experiments were performed in order to evaluate the catalyst response stability vs. time by switching on and off the UV irradiation (Figure 5.8) In the absence of irradiation, after a delay of few minutes necessary to purge the residual H_2 in the reactor, no hydrogen evolution was observed, indicating thus that irradiation was essential to activate the involved catalytic process.

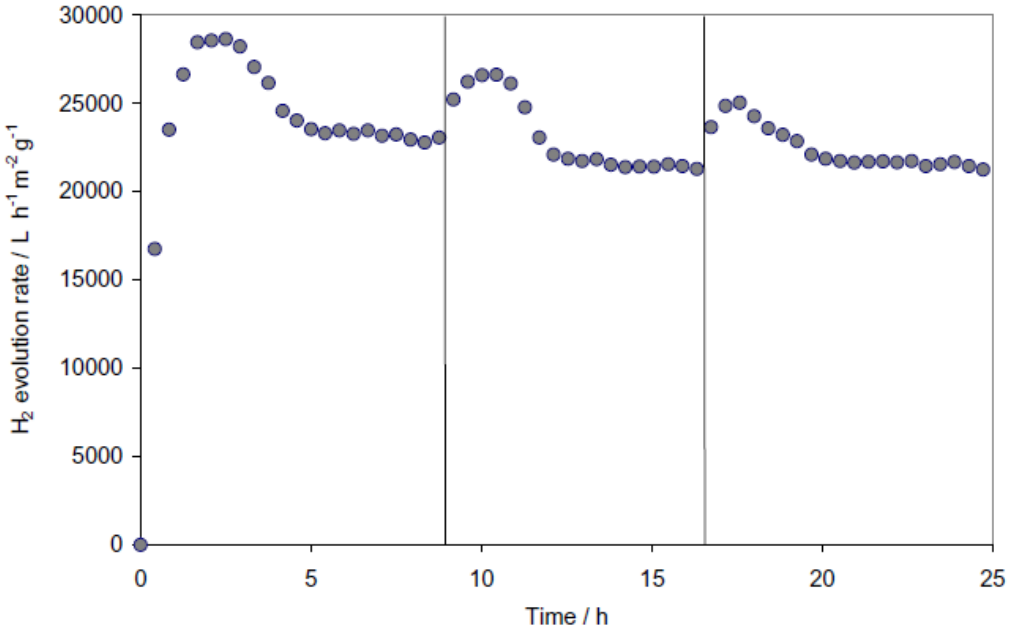

Figure 5.8: *Effect of consecutive photocatalyst recycling: the H_2 evolution rate per unit area as a function of time on a CVD CuO nanosystem from a methanol:water=1:1 solution under UV irradiation. Between two consecutive cycles (vertical bars in the figure), the irradiation was switched off for 12 h.*

These cycling experiments confirmed that the CuO catalyst prepared by CVD underwent a slow deactivation upon prolonged utilization. This phenomenon could suggest the occurrence of an in situ partial photoreduction of nanostructured CuO to Cu_2O, as confirmed by the color changes observed under irradiation. Note that the system was kept under flowing Ar throughout the activity tests and that upon exposure to air the color of the sample rapidly returned to the initial one, indicating a fast re-oxidation owing to the high reactivity that is characteristic of nanostructured systems. In agreement with this observation, data from FE-SEM, X-ray photoelectron (XPS), and X-ray excited Auger electron spectroscopy (XE-AES) studies of the aged sample indicated the absence of significant morphological and compositional modifications.

In principle, the above-discussed decrease in activity could also be the outcome of a minor photo-leaching process, leading to the release of Cu ions into solution and promoting the formation of hydroxy ions (OH^-) that, in turn, act as scavengers for H^+ ions, the precursors for H_2 formation. In addition, the release of oxygen as a consequence of leaching might further enhance the yield of OH^- ions.[23] A minor contribution of the reaction by-products, such as CO, leading to the formation of organic acids as intermediates of possible reactions involving methanol oxidation should also be taken into account. Nevertheless, note that the influence of these processes becomes particularly significant only after very long exposure times and for high conversions of the sacrificial agent into organic acids.

In an attempt to further clarify the question, we performed inductively coupled plasma mass spectrometry (ICP-MS) analyses on the final reaction medium but did not gain any direct evidence for appreciable leaching phenomena. In any case, separate independent experiments performed by intentionally introducing Cu^{II} ions into the solution did not reveal significant contributions to the observed activity. In fact, a photocatalytic experiment was carried out using 20.63 mg of $Cu(NO_3)_2 \bullet 3H_2O$ (Fluka) to evaluate possible contribution from the homogeneous reaction, but a negligible hydrogen production (0.03 L h^{-1} g^{-1} under Vis irradiation) was observed.

A further issue to be considered concerns the fact that the used sacrificial agent (methanol) could also be involved in dehydrogenation/oxidation reactions, thus partially contributing to the observed hydrogen evolution. This phenomenon was confirmed by gas chromatography (GC) analysis, which revealed the presence of small amounts of CO_2 and formaldehyde. The CO_2 evolution observed in UV photocatalytic experiments with the CuO sample prepared by CVD represented less than 30% of the stoichiometric amount expected for hydrogen production by methanol photo-oxidation. Upon irradiation with visible light, an even lower amount of CO_2 was produced. Only traces of formaldehyde were detected by GC, and accurate quantification was prevented by the high volatility of the product. Therefore, under the present experimental conditions, methanol acts both as inhibitor of the electron–hole recombination processes and partially as a hydrogen source.

The ability of these nanosystems to produce H_2 by photoreforming of water/ethanol solutions was tested. Indeed, (bio)-ethanol is considered a promising

sacrificial agent capable of enhancing the system photoresponse [24, 25]. As a representative example, fig. 5.9a shows the H_2 evolution rate for the Cu_2O sample in fig. 5.2a. Comparable results were also obtained for the CuO specimen of fig. 5.2b under the same operative conditions. As can be observed, after an initial stabilization period, an almost constant value was detected, evidencing promising photocatalytic performances. In particular, both the Cu_xO nanodeposits showed an excellent stability in terms of H_2 evolution up to 30 h of continuous utilization.

A similar behavior is in line with the H_2 production from H_2O/CH_3OH solutions. Nevertheless, in the present case a lower (≈15 times) hydrogen production rate was measured. This difference can be ascribed to the more difficult photo-activation of ethanol with respect to methanol, implying C-C bond cleavage in the former case.[25]

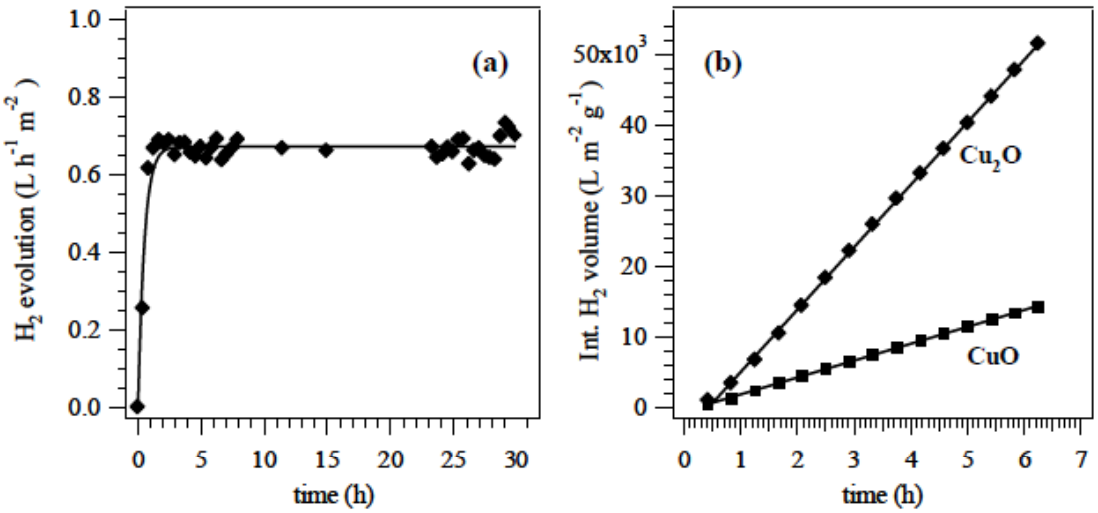

Figure 5.9: *(a) Hydrogen evolution rate per unit area over Cu_2O photocatalyst. (b) Integrated rates of H_2 evolution during the first 6 h of reaction for the Cu_2O and CuO nanodeposits, normalized with respect to the sample geometrical area and weight.*

In order to attain a deeper insight into the system performances, the produced H_2 volumes were integrated as a function of time and normalized with respect to the sample geometrical area (1×1 cm^2) and Cu_xO weight (fig. 5.9b) as, already, described for the case of methanol. In spite of this approximation, important information can be deduced from an inspection of fig. 5.9b. While the observed linear trends are in agreement with the time stability of the photocatalytic performances, the slope of the two plots can be used for a semi-quantitative estimation of the H_2 produced per unit area and per gram of catalyst. Accordingly, the volume of hydrogen generated by the

Cu_2O and CuO specimens correspond to 8.24×10^3 and 3.13×10^3 L h^{-1} m^{-2} g^{-1}, respectively, i.e. to 0.043 and 0.054 μmol min^{-1} for a 1 cm^2 sample size. The obtained values are appreciably lower (*ca.* two orders of magnitude) with respect to the most promising Pt-TiO_2 systems. Yet, it is worthwhile observing that the latter contain an expensive and rather toxic noble metal.[26] In addition, note that the present Cu_xO nanoarchitectures, despite presenting a lower activity, possess a higher time stability and do not require the use of expensive materials. As a whole, the above discussed results candidate the present Cu_xO nanosystems as promising elements for the sustainable H_2 production, especially if supported on suitable semiconductors such as TiO_2.

Supported Cu_xO-TiO_2 nanocomposites

A new CVD route towards supported Cu_xO-TiO_2 nanocomposites has been developed, consisting in the deposition of porous Cu_xO nanomatrices, followed by a controlled dispersion of TiO_2 NPs. The above-mentioned $Cu(hfa)_2$•TMEDA and $Ti(O\text{-}iPr)_2(dpm)_2$ (O-iPr = isopropoxy; dpm = 2,2,6,6–tetramethyl–3,5–heptanedionate) were used as copper and titanium precursors. The resulting composites were subsequently functionalized with Au NPs, which are of great interest as activators for photoassisted H_2 generation, even by irradiation with visible light.

In particular, Au NPs were introduced by RF-Sputtering under mild conditions, in order to minimize undesired alterations of the pristine system morphology. To the best of our knowledge, the synthesis and use of such systems in photocatalytic hydrogen generation has never been reported up to date. The morphology of the obtained Cu_2O-TiO_2 nanodeposits (Figure 5.10a,b) was characterized by cubic crystals (average dimensions ≈ 150 nm) with their apexes directed perpendicularly to the growth surface, in line with previous findings for supported Cu_2O nanosystems. The conformal coverage of such nanopyramids by smaller TiO_2 particles (≈ 15 nm) suggested the occurrence of a 3D-growth mode. Upon gold introduction (Figure 5.10c), the lateral crystal size underwent a little reduction, whereas the overall thickness was decreased by 25%. Such an effect was ascribed to a sort of "chemical annealing",[27] i.e., the combination of etching and structural compaction promoted by plasma ablation and bombardment under the adopted conditions, in agreement with previous reports for other oxide materials.[28]

The typical RMS roughness was evaluated to be 5 nm. On the other hand, supported CuO–TiO_2 nanocomposites displayed a more porous morphology, characterized by an RMS roughness of 90 nm and indicative of a significantly higher active area compared to the former case. In analogy with supported CuO–TiO_2 nanocomposites obtained by a photodeposition route,[29] the system topography (Figure 5.10d–e) was dominated by the presence of rounded nanoflowers with a mean lateral size of 400 nm, resulting from the agglomeration of ≈ 50-nm grains. This morphology was responsible for a more homogeneous TiO_2 dispersion in the CuO matrices with respect to Cu_2O ones. After introducing gold (Figure 5.10f), low sized nanoparticles with

a diameter in the range of 5–10 nm could be observed above the pristine nanoflowers, and the overall thickness of the deposit was slightly reduced due to the above-described plasma action.

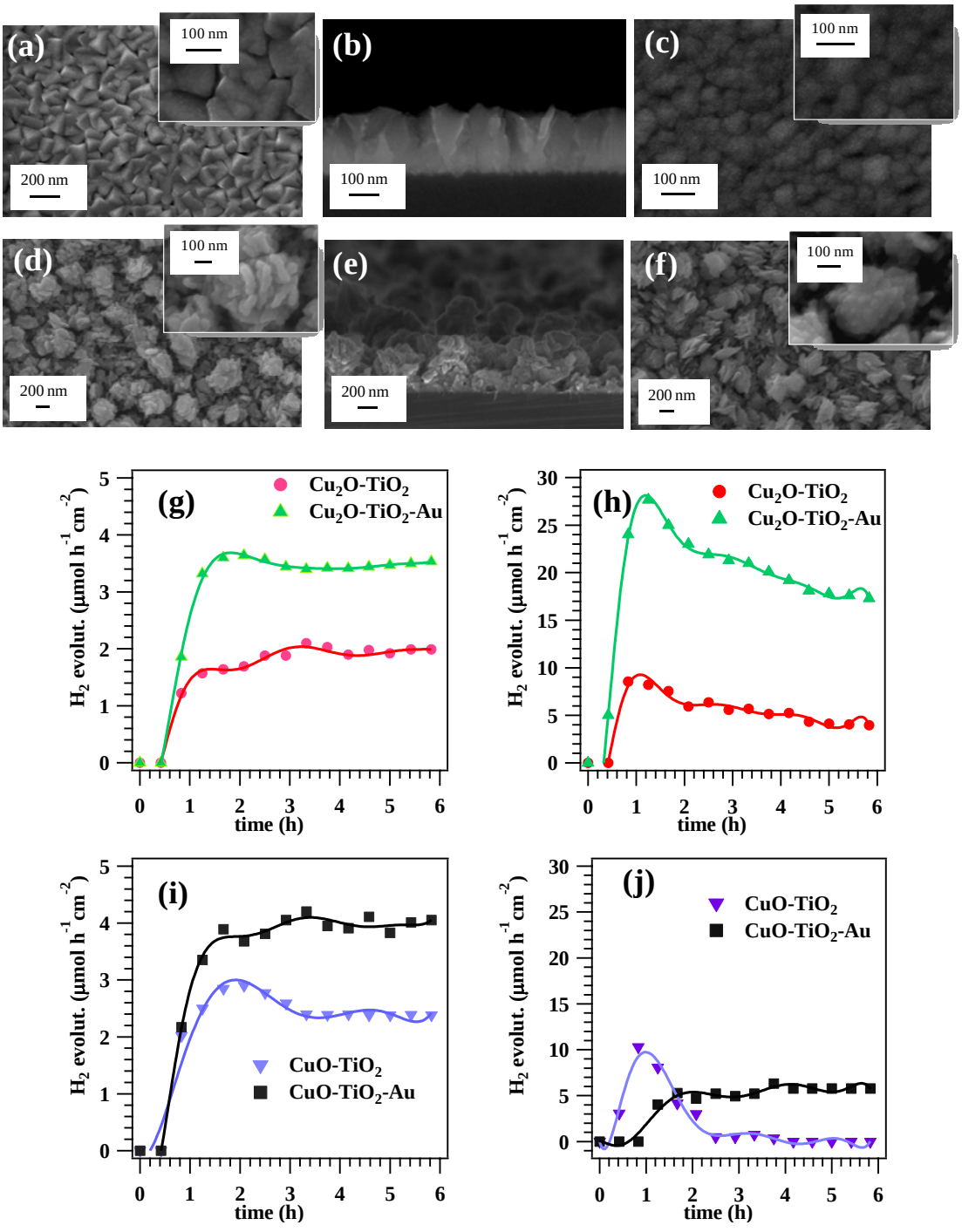

Figure 5.10: *Representative FE-SEM micrographs of composite oxide nanosystems: (a,b) Cu_2O- TiO_2; (c) Cu_2O-TiO_2-Au (d,e) CuO-TiO_2; (f) CuO-TiO_2-Au, grown by sequential thermal CVD of the single oxides. Cu_2O and CuO were deposited under O_2+H_2O atmospheres at 400°C, 3 mbar and 550°C, 10 mbar, respectively, and subjected to TiO_2 dispersion at 400°C, 10 mbar. Finally, Au NPs were deposited via RF-sputtering (60°C, 0.4 mbar). Selected H_2 evolution rates from the above nanomaterials upon: (g,i) Vis and (h,j) UV illumination.*

Similarly to the previously discussed case, hydrogen photoproduction tests were performed both upon visible and UV excitation (Figure 5.10 g–j). As a general rule, the H_2 evolution rate was directly influenced by a concurrence of factors, i.e., the system nano-organization/chemical composition and the spectral range of the incoming excitation light. As can be noticed, Cu_xO–TiO_2 nanocomposites possessed comparable performances upon visible irradiation, providing a stable H_2 production rate (≈ 2 μmol $h^{-1}cm^{-2}$) up to 6 h illumination. Interestingly, upon gold dispersion the H_2 yield was almost doubled for both kinds of composites. Such a variation, never reported to date for similar nanosystems, could be ascribed to the SPR absorption of metallic gold nanoaggregates (typically located at ≈ 550 nm for ≈ 5–10-nm Au particles), resulting in an enhanced light harvesting. In addition, the catalytic activity of smaller-sized Au NPs is expected to provide a beneficial contribution to the observed performance improvements. Although still preliminary, these indications underline the role of precise engineering of advanced composite nanosystems to achieve well-designed functional activities. On the basis of the above results, a systematic improvement of H_2 production rates could be expected upon switching to the more energetic UV irradiation, but this prediction was only partially fulfilled. In fact, Au-free samples provided maximum H_2 photoproduction rates of ≈ 7 and 10 μmol $h^{-1}cm^{-2}$ for Cu_2O– and CuO–TiO_2 composites. Nonetheless, upon UV illumination a rapid deactivation after ≈ 1 h of irradiation took place, particularly in the case of the CuO–TiO_2 nanosystem. In line with the data discussed for Figure 1, this difference, which is attributed to the concurrence of a partial CuO → Cu_2O photoreduction and a minor photoleaching process, evidenced the necessity of a suitable compromise between the nanosystem activity and the time stability of the corresponding response.

It is also worth noting that, in this case, the more compact Cu_2O structure is likely to produce a lower TiO_2 dispersion. As a consequence, the increased coverage of the outermost system layers with TiO_2 (compare Figure 5.10 a–b) is responsible for a suppression of detrimental corrosion phenomena, resulting in a more stable functional response. This effect explains the slower and less-pronounced time deactivation of Cu_2O–TiO_2 nanodeposits with respect to the homologous CuO–TiO_2 ones, which are expected to be more reactive due to their more porous structure and larger active area. In addition, during the catalyst operation, passivation of the exposed Cu_2O surface by a

thin CuO layer prevents further oxidation, contributing to the higher stability of Cu_2O–TiO_2 nanosystems under the adopted conditions.

A similar explanation is also likely to account for the stable H_2 evolution observed for CuO–TiO_2–Au nanocomposites in comparison to Au-free ones. In fact, the former are more compact due to plasma exposure (see the above comments) and thus more protected by the over dispersion of the deposited metal particles. Consequently, after an initial induction time of ≈ 1.5 h, a very stable activity is produced. For Cu_2O–TiO_2–Au, a significantly higher response upon UV excitation could be observed (Figure 5.10 h–j) due to the synergistic combination of the more compact structure, the more energetic UV irradiation, and the sensitizing action exerted by Au NPs introduction. Nevertheless, even in this case a little decrease in H_2 evolution was observed after 1 h, showing the necessity of further nanosystem engineering for a parallel improvement of the response values and their time stability upon prolonged illumination.

Conclusions

The performances of the present nanosystems prepared by CVD are very promising, especially considering that the active Cu_xO phase is deposited on an inert substrate. A direct comparison with alternative and very attractive materials from literature data is not straightforward. Nevertheless, a preliminary comparative evaluation can be performed with the widely investigated Pt/TiO_2 systems.[26] A 1.3-mm thick Pt/TiO_2 film, under optimized experimental conditions, showed a conversion efficiency of 32% (black light lamp with emission at 365 nm), whereas our CuO film showed a conversion efficiency of 11% under UV irradiation. Although the Pt loading was not reported, the huge differences in the cost of Pt and Cu, as well as the possibility to significantly enhance the performances of Cu_xO films by supporting them on TiO2, highlight the relevance of the present findings.

In conclusion, a novel and amenable CVD route, compatible with large-scale production, to prepare Cu_xO (x=1, 2) nanostructures on Si (100) was reported, enabling the resulting Cu-O phase composition and nanoscale organization to be controlled by simple variation of the growth temperature. In addition, and more interestingly, the

photocatalytic production of hydrogen on both the supported catalysts upon irradiation with UV and even visible light proved that the control of the system morphogenesis is crucial to obtain good Cu_xO performances even in the absence of TiO_2. These results represent an important step forward in the exploration of new active nanosystems for the conversion of solar light into storable chemical energy.

References

[1] Y. S. Chaudhary, A. Agrawal, R. Shrivastav, V. R. Satsangi, S. Dass. *International Journal of Hydrogen Energy* **2004**, *29*(2), 131-134.
[2] D. Chauhan, V. R. Satsangi, S. Dass, R. Shrivastav. *Bulletin of Materials Science* **2006**, *29*(7), 709-716.
[3] M. Kaur, K. P. Muthe, S. K. Despande, S. Choudhury, J. B. Singh, N. Verma, S. K. Gupta, J. V. Yakhmi. *Journal of Crystal Growth* **2006**, *289*(2), 670-675.
[4] Y. G. Zhang, L. L. Ma, J. L. Li, Y. Yu. *Environmental Science and Technology* **2007**, *41*(17), 6264-6269.
[5] C. J. Engel, T. A. Polson, J. R. Spado, J. M. Bell, A. Fillinger. *Journal of the Electrochemical Society* **2008**, *155*(3), F37-F42.
[6] *Journal of Materials Chemistry* **2008**, *18*(20), 2295-2297.
[7] W. Siripala, A. Ivanovskaya, T. F. Jaramillo, S. H. Baeck, E. W. McFarland. *Solar Energy Materials and Solar Cells* **2003**, *77*(3), 229-237.
[8] J. Bandara, C. P. K. Udawatta, C. S. K. Rajapakse. *Photochemical and Photobiological Sciences* **2005**, *4*(11), 857-861.
[9] H. J. Choi, M. Kang. *International Journal of Hydrogen Energy* **2007**, *32*(16), 3841-3848.
[10] M. Hara. *Chemical Communications* **1998**, (3), 357-358.
[11] J. P. Yasomanee, J. Bandara. *Solar Energy Materials and Solar Cells* **2008**, *92*(3), 348-352.
[12] M. K. I. Senevirathna, P. K. D. D. Pitigala, K. Tennakone. *Journal of Photochemistry and Photobiology A: Chemistry* **2005**, *171*(3), 257-259.
[13] K. H. Yoon, W. J. Choi, D. H. Kang. *Thin Solid Films* **2000**, *372*(1), 250-256.
[14] R. Van De Krol, Y. Liang, J. Schoonman. *Journal of Materials Chemistry* **2008**, *18*(20), 2311-2320.
[15] S. Delgado, A. Muñoz, M. E. Medina, C. J. Pastor. *Inorganica Chimica Acta* **2006**, *359*(1), 109-117.
[16] D. Barreca, A. Gasparotto, C. Maragno, E. Tondello, C. Sada. *Chemical Vapor Deposition* **2004**, *10*(4), 229-236.
[17] D. Barreca, A. Gasparotto, C. Maragno, E. Tondello, E. Bontempi, L. E. Depero, C. Sada. *Chemical Vapor Deposition* **2005**, *11*(10), 426-432.
[18] N. Strataki, V. Bekiari, D. I. Kondarides, P. Lianos. *Appl. Catal. B Environ.* **2007**, *77*(1-2), 184-189.
[19] D. Barreca, A. Gasparotto, C. Maccato, E. Tondello, O. I. Lebedev, G. Van Tendeloo. *Cryst. Growth Des* **2009**.
[20] D. Barreca, A. P. Ferrucci, A. Gasparotto, C. Maccato, C. Maragno, E. Tondello. *Chemical Vapor Deposition* **2007**, *13*(11), 618-625.
[21] D. Briggs, M. P. Seah. *Practical Surface Analysis,* New York, J. Wiley & Sons, **1990**.
[22] J. F. Moulder, W. F. Stickle, P. W. Sobol, K. D. Bomben. *Handbook of X-ray Photoelectron Spectroscopy,* (Ed.: J.Chastain), Perkin-Elmer Corporation (Physical Electronics), **1992**.
[23] F. L. Y. Lam, A. C. K. Yip, X. Hu. *Industrial and Engineering Chemistry Research* **2007**, *46*(10), 3328-3333.
[24] A. A. Nada, M. H. Barakat, H. A. Hamed, N. R. Mohamed, T. N. Veziroglu. *International Journal of Hydrogen Energy* **2005**, *30*(7), 687-691.
[25] A. Patsoura, D. I. Kondarides, X. E. Verykios. *Catalysis Today* **2007**, *124*(3-4), 94-102.
[26] N. Strataki, V. Bekiari, D. I. Kondarides, P. Lianos. *Applied Catalysis B: Environmental* **2007**, *77*(1-2), 184-189.
[27] M. Losurdo, M. M. Giangregorio, A. Sacchetti, P. Capezzuto, G. Bruno, G. Malandrino, I. L. Fragalá. *Journal of Materials Research* **2006**, *21*(7), 1632-1637.
[28] D. Barreca, A. Gasparotto, E. Tondello, C. Sada, S. Polizzi, A. Benedetti. *Chemical Vapor Deposition* **2003**, *9*(4), 199-206.
[29] L. Armelao, M. Pascolini, G. Bottaro, G. Bruno, M. Giangregorio, M. Losurdo, G. Malandrino, R. L. Nigro, M. E. Fragala, E. Tondello. *Journal of Physical Chemistry C* **2009**, *113*(7), 2911-2918.

Part 2:
Supported systems based on cobalt oxides

Materials based on cobalt oxides and, in particular, spinel-type Co_3O_4, have been the object of considerable attention for applications in Fischer-Tropsch syntheses,[1] hydrocracking of crude fuels,[2] oxidation reactions,[3, 4] and ethanol steam reforming.[5, 6] Recently, their photocatalytic activity has been investigated in the degradation of dyes,[7, 8] and in oxygen evolution from water under mild conditions.[9] Nevertheless, only very few studies are available on the use of powdered binary (Co_3O_4)[10, 11] and ternary (CoX_2O_4, X = Al, Ga, In)[12] spinels for light-driven hydrogen production, whereas the photo-assisted H_2 generation by supported Co_3O_4 nanosystems has never been reported. In this regard, a key step is the development of preparation routes joining the advantages of the elimination of the filtration processes required by powdered catalysts and the performances offered by nanostructured materials with tailored properties. In this context, CVD and related methods represent preferred choices for their inherent

flexibility and the possibility of controlling the nanosystem morphology by a proper choice of the process parameters, a key step to the achievement of unprecedented system performances in photo-assisted H_2 production.

Catalysts synthesis

Co_3O_4 nanopyramids were prepared using a cold-wall CVD quartz reactor equipped with a resistively heated susceptor and an external precursor reservoir. $Co(hfa)_2$•TMEDA, synthesized as recently reported,[13] was vaporized at 60°C and transported into the reaction chamber by an electronic grade O_2 flow (100 sccm), whereas an additional 100 sccm O_2 flow, bubbled through a water reservoir heated at 50°C, was supplied independently. Depositions were performed for 2 h at a total pressure of 10.0 mbar on previously cleaned 1 cm × 1 cm × 1 mm Si(100) substrates, maintained at temperatures between 400 and 500°C. Under these conditions, water partial pressure was estimated to be 1.5 mbar.

Catalysts characterization

FE-SEM measurements were carried out by means of a Field Emission Zeiss SUPRA 40VP apparatus, equipped with an Oxford INCA x-sight X-ray detector for EDXS analyses.

XPS analyses were performed by a Perkin Elmer Φ 5600ci spectrometer with a standard Al K_α source (1486.6 eV), at a working pressure lower than 10^{-9} mbar. The reported BEs were corrected for charging effects by assigning a value of 284.8 eV to the adventitious C 1*s* signal.

AFM micrographs were obtained by a NT-MDT SPM Solver P47H-PRO instrument operating in tapping mode and in air. Images were recorded on different sample areas in order to check surface homogeneity. RMS roughness values were calculated after background subtraction through plane fitting.

Photo-assisted experiments were carried out on 1:1 water/methanol mixtures in a discontinuous batch reactor directly connected to a Gas Cromatographic (GC)

apparatus for the on-line analysis of gaseous products. A 125 W low-pressure mercury lamp was used for UV-Vis irradiation, and no activity was observed in the absence of illumination. Blank tests were performed on the bare Si(100) substrates. Experiments in the absence of O_2 were carried out after de-aeration of the reaction mixture by Ar bubbling and by maintaining a controlled Ar flow throughout the irradiation time. For the experiments in the presence of O_2, a controlled flow of O_2 (5%)/Ar was used. Analysis of the liquid phase was performed using an Agilent 7890A GC coupled with a 5975C VL MSD with triple-Axis Detector.

Results and discussion

Field Emission-Scanning Electron Microscopy (FE-SEM) micrographs of systems obtained under O_2+H_2O atmospheres (Fig. 5.11) displayed the formation of pyramidal assemblies uniformly covering the Si(100) substrates. The formation of such peculiar aggregates could be associated to the preferential exposure of the [111] planes, the most stable ones in face-centered cubic structures like spinel-type Co_3O_4,[14] decreasing thus the overall system surface energy. An increase of the growth temperature from 400 to 500°C produced an increase of the aggregate mean lateral size from 270 to 550 nm (Figs. 5.11a-b). In addition, higher magnification images (Fig. 5.11b, inset) revealed the presence of a spiral-like surface texture, suggesting that the growth occurred according to a spiral dislocation mechanism.[15] The corresponding cross-sectional pictures were characterized by a well-ordered structure, with an increase of the mean nanodeposit thickness from 460±20 nm (400°C) to 630±20 nm (500°C).

The high purity of the synthesized Co_3O_4 systems was confirmed by energy dispersive X-ray spectroscopy (EDXS) analyses (see Fig. 5.11). Irrespective of the growth conditions, the patterns were characterized by the presence of the sole cobalt [Co Lα: 0.78 keV; Co Kα1: 6.92 keV] and oxygen [OKα1: 0.52 keV] signals, along with the Si Kα substrate peak at 1.74 keV, without any detectable carbon contamination. The homogeneous formation of Co_3O_4 through the whole nanodeposit thickness was investigated by means of local line-scans in several sample points. As a representative

example, typical spectra are displayed in Fig. 5.11, evidencing a uniform chemical composition from the external surface up to the substrate interface.

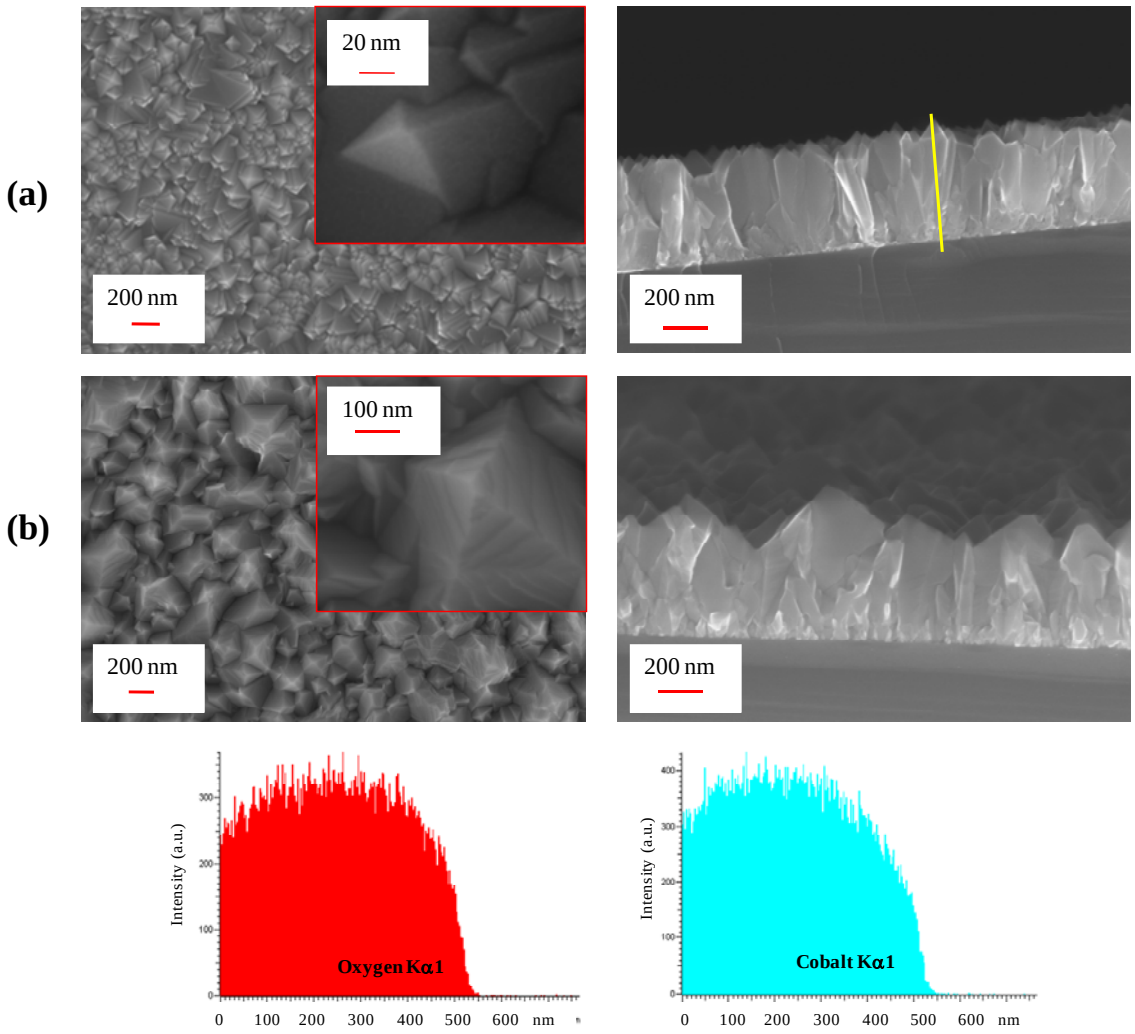

Figure 5.11: *Plane-view and cross-sectional FE-SEM images of Co_3O_4 nanopyramids synthesized at: (a) 400; (b) 500°C. In the insets of the left figures, higher magnification micrographs are also displayed. The EDXS scans for O Kα1 and Co Kα1 X-ray signals were recorded along the marked line for the 400°C-grown specimen.*

The intensity ratio between the O Kα1 and Co Kα1 X-ray signals mediated along the whole line scan provided values very close to those expected for Co_3O_4. The formation of this phase was further confirmed by X-ray Photoelectron Spectroscopy (XPS) measurements, yielding the typical Co 2*p* profile expected for Co_3O_4. The main Co 2*p* component was centered at a Binding Energy (BE) of 780.7 eV, with a mean Auger parameter of 1552.2 eV, irrespective of the adopted deposition temperature. [14]

Further insight into the system morphological features was obtained by Atomic Force Microscopy (AFM). In line with FE-SEM results, AFM analyses confirmed the

homogeneous growth of Co_3O_4 nanoaggregates on the Si(100) substrates, along with the above discussed size increase on going from 400 to 500°C.

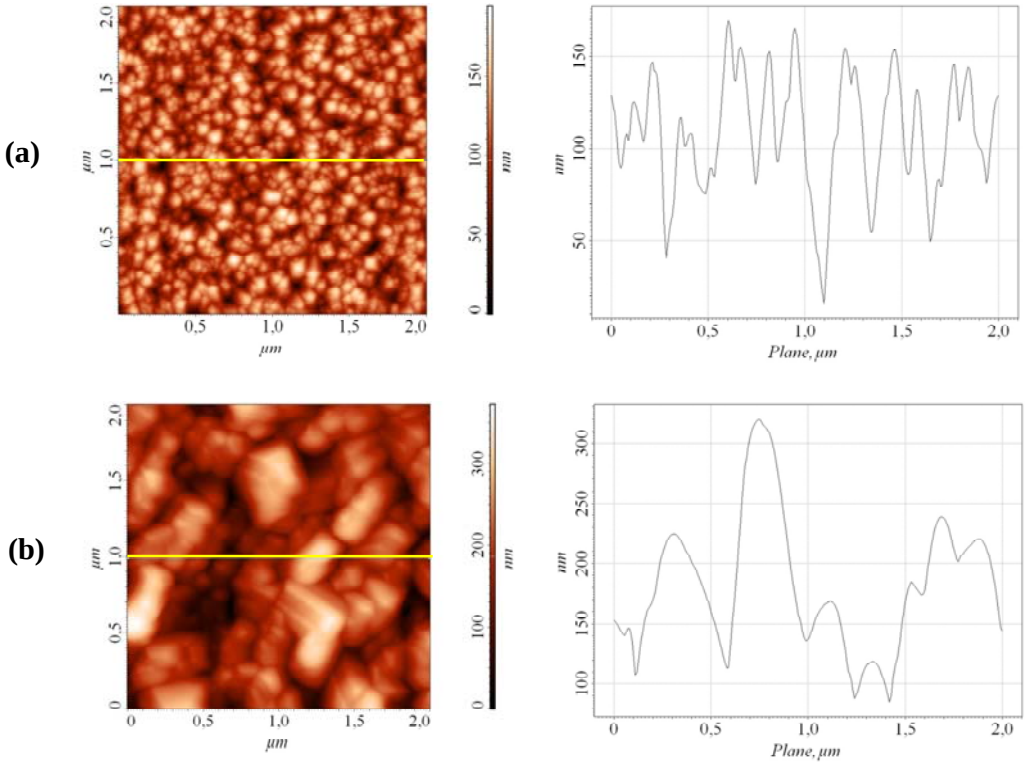

Figure 5.12: *Representative AFM surface micrographs (2 × 2 μm²) of Co_3O_4 nanopyramids synthesized at 400 (a) and 500°C (b). Height profiles along the marked lines are also reported.*

Fig. 5.12 shows the 2 μm × 2 μm AFM images for the same specimens of Fig. 5.11, along with the corresponding line profiles. The latter suggested an increase of the surface roughness with the deposition temperature. Indeed, from the 4 μm² areas, Root Mean Square (RMS) roughness values could be calculated, yielding respectively 28 nm (400°C) and 62 nm (500°C). As can be noticed, an increase of the deposition temperature resulted in a rougher texture of Co_3O_4 nanoystems, as expected on the basis of FE-SEM characterization (compare Fig. 5.11).

Photo-assisted properties of the nanodeposits towards H_2 production were evaluated using 1:1 methanol/water solutions under UV-Vis illumination, both in the presence and in the absence of O_2 (see the Experimental Section). As a prototype for the observed behaviour, Fig. 5.13 shows the gas phase products evolution as a function of irradiation time. In the absence of O_2 (Fig. 5.13a), a relatively modest and transient H_2 evolution was observed, with the concomitant formation of relatively small amounts of CO, CO_2, CH_4 and traces of formaldehyde. As can be observed, the concentrations of

hydrogen underwent a fast decrease within the first two hours. Conversely, when O_2 was present in the reaction medium (Fig. 5.13b), appreciable differences were observed in the Co_3O_4 nanodeposit reactivity. In fact, under these conditions, significant and constant hydrogen evolution was observed for at least 30 hours, indicating a promising stability of the investigated nanomaterials in view of practical applications.

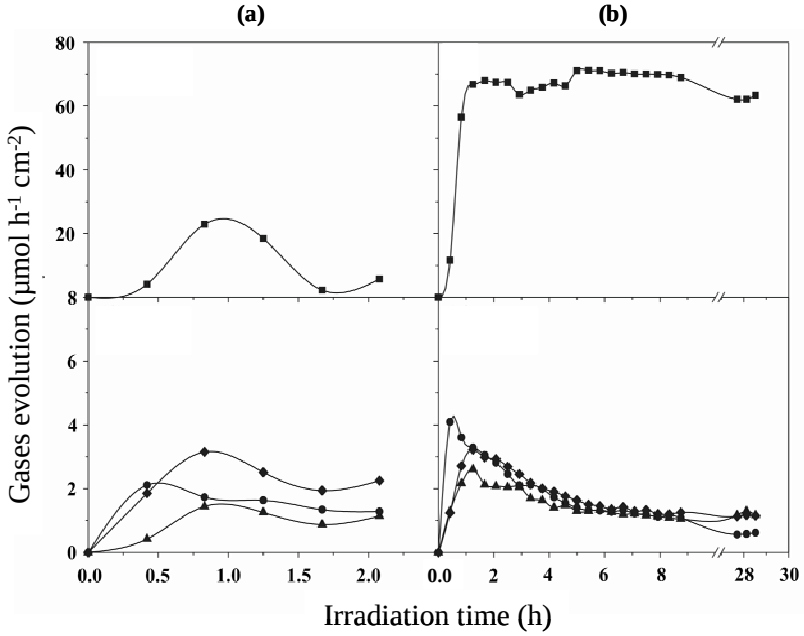

Figure 5.13: *H_2 (■), CO_2 (●), CO (◆), and CH_4 (▲) production rate per unit area vs. irradiation time for a Co_3O_4 nanodeposit: (a) in the absence of O_2; (b) in the presence of O_2.*

The evolution of CO, CO_2 and CH_4 was observed even in this case. In addition, HCHO and CH_3OCH_3 were detected in the gas phase, while traces of formic acid and methylformate were found in the liquid one. It is worth noting that O_2 addition considerably increased the evolution rate of H_2 (compare Fig. 5.13a), while the evolution of carbon-containing by-products was significantly less affected.

In order to explain the observed reactivity, it is necessary to consider not only the general photocatalysis mechanism, but also the well known capability of cobalt oxides to promote oxidation reactions and the accessibility of cobalt (II) and (III) oxidation states. Whereas the formation of methoxy species by gas-phase interaction of methanol with cobalt oxide surfaces is well documented,[5, 16] a thorough understanding of the subsequent degradation steps is a more difficult task, especially in a liquid phase containing a large amount of both water and methanol, like in the present case.

Bulk Co_3O_4 is a *p*-type semiconductor with a band gap < 2.0 eV,[12, 14] indicating the possibility of an efficient UV-Vis radiation absorption. As a consequence, Co_3O_4 illumination leads to electron excitation to the conduction band, along with the simultaneous formation of holes in the valence one.[7] Thanks to the capability of Co_3O_4 to promote the activation of O_2 and oxygen-containing species, photo-generated electrons can react with adsorbed oxygen and water molecules to produce highly oxidizing species, such as $O_2^{\bullet-}$, H_2O_2 and $OH^{\bullet}$. The latter, along with photo-produced holes, can react with methoxy species adsorbed on the surface of Co_3O_4. The photo-assisted activity improvement observed upon oxygen introduction in the reaction environment can be mainly explained taking into account that O_2 present on the surface of the photocatalyst acts as a scavenger for the photo-produced electrons, inhibiting recombination phenomena of charge carriers and extending thus their lifetime. Nevertheless, under the present conditions, additional factors have to be considered in the description of O_2 influence on the system reactivity. In fact, previous *in-situ* studies pointed out to the occurrence of an equilibrium between CoO and Co_3O_4 depending on the surrounding atmosphere, Co_3O_4 being observed as pure phase only in the presence of oxygen. In addition, the total oxidation of methanol to CO_2 and its partial oxidation to formaldehyde were suggested as preferential reaction pathways over Co_3O_4 and CoO surfaces, respectively.[5]

On this basis, when photo-assisted experiments are performed in the absence of oxygen, it is reasonable to suppose that H_2 evolution results in a partial reduction of Co_3O_4 to CoO. In this case, the nanosystem surface is likely prevalently covered by methoxy species (Scheme 1), acting as a poison for the catalyst. Dehydrogenation of these species might occur only at temperatures higher than 80°C, leading to formaldehyde and surface hydroxyls, with subsequent degradation to CO/CO_2.[12] In a different way, oxygen introduction in the reaction atmosphere is believed to have further positive effects: (i) the suppression of Co_3O_4 reduction to CoO; (ii) the reaction with adsorbed methoxy species to form adsorbed formates and hydrogen, resulting thus in a less extensive catalyst poisoning. Formates, in turn, can be further decomposed to hydrogen and CO/CO_2[17] (Scheme 5.1).

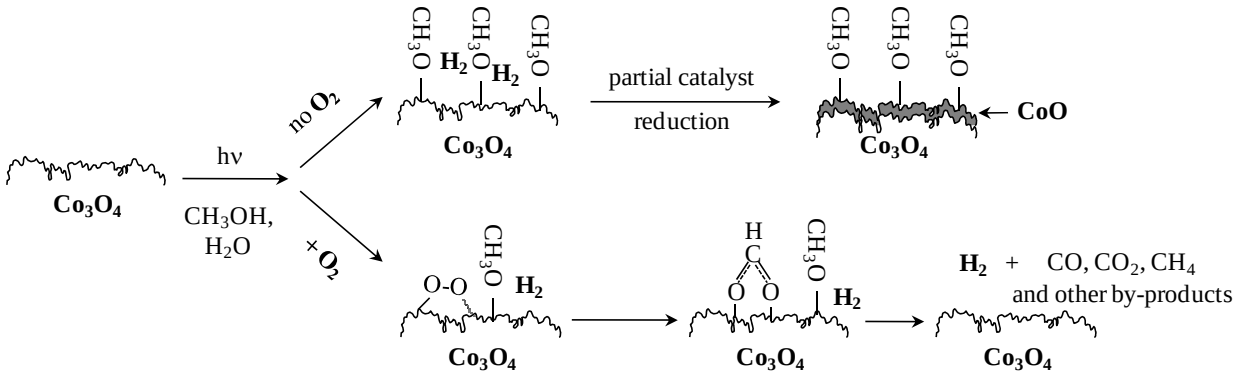

Scheme 5.1: *Simplified sketch of the main proposed reaction pathways over Co_3O_4 nanosystems in CH_3OH/H_2O media under the present photo-assisted conditions.*

F-doped Co_3O_4 supported systems

Synthesis

Co_3O_4-based systems were deposited on 1.5×2.0 cm^2 Si(100) substrates (MEMC®, Merano, Italy) and Herasil® silica slides (Heraeus, Quarzschmelze, Hanau, Germany) pre-cleaned by standard procedures[18] by a two-electrode PE-CVD apparatus powered by a Radio Frequency (RF, ν = 13.56 MHz) generator.[18, 19] Electronic grade argon and oxygen were used as plasma sources. Due to their favourable CVD properties, [18, 20] [Co(dpm)$_2$] (dpm = 2,2,6,6-tetramethyl-3,5-heptanedionate) and [Co(hfa)$_2$TMEDA] (hfa=1,1,1,5,5,5-hexafluoro-2,4-pentanedionate; TMEDA=N,N,N',N'-tetramethylethylenediamine) were used as precursors for the synthesis of undoped and F-doped Co_3O_4. To this aim, the two compounds were placed in an external vessel maintained at 60°C or 90°C respectively, and transported towards the deposition zone by a 60 sccm Ar flow. To avoid undesired condensation phenomena, the gas lines connecting the precursor vessel and reaction chamber were heated at 80°C or 120°C for [Co(dpm)$_2$] and [Co(hfa)$_2$TMEDA], respectively. Two further auxiliary gas-lines were used to introduce Ar (15 sccm) and O_2 (20 sccm) directly into the reactor. Depositions were performed for a duration of 1 h at temperatures between 200 and 400°C. The total

pressure, RF-power and electrode-to-electrode distance were fixed at 1.0 mbar, 20 W and 6 cm.

Precursor characterization

The $[Co(dpm)_2]$ and $[Co(hfa)_2TMEDA]$ precursors were characterized by electron impact-mass spectrometry (EI-MS) using a Jeol Ltd. Tokyo Japan AccuTOF GCv instrument, equipped with a 70 eV EI source and a TOF analyzer (m/z = 30-3200).

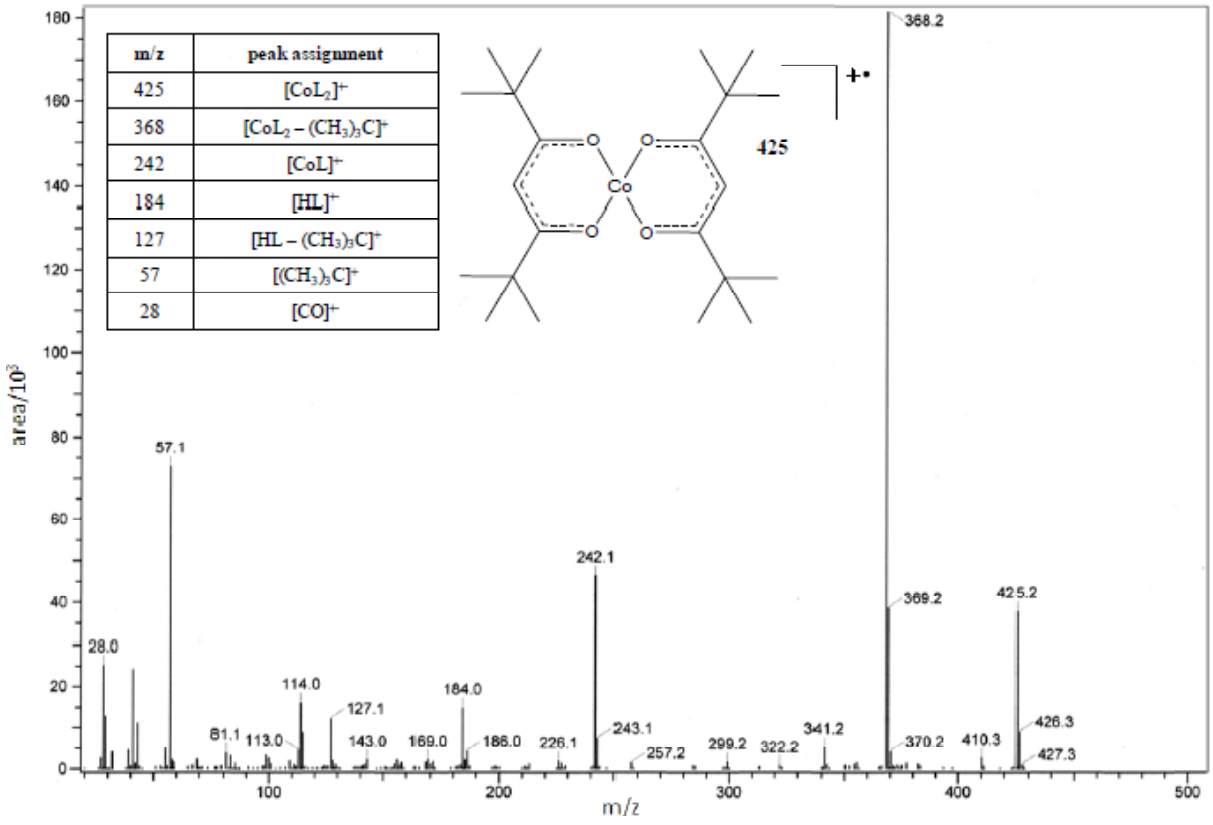

Figure 5.14: *EI-MS spectrum of precursor $[Co(dpm)_2]$. The assignment of the main peaks is reported in the table, where the symbol L indicates the dpm ligand. The structure of the molecular ion is also sketched.*

In the case of $[Co(dpm)_2]$, the EI-MS spectrum (Fig. 5.14) was dominated by several species originating from the loss of the β-diketonate ligand and of the tert-butyl group, whose presence was also directly detected. [18] For $[Co(hfa)_2TMEDA]$ (Fig. 5.15), the detachment and fragmentation of both the TMEDA and hfa moieties were revealed. In particular, ions containing the β-diketonate ligand were involved in the elimination of CF_2/CF_3 species, whose formation was in agreement with compositional data on Co_3O_4-based deposits [see X-ray Photoelectron Spectroscopy (XPS) data below]. A careful analysis of EI-MS results also revealed a mass loss of 19 a.m.u. from several ionic

species (see for instance m/z = 589 → 570; m/z = 473 → 454). These results pointed out to the formation of fluorine radicals, accounting for the efficient Co_3O_4 fluorine doping under the present PE-CVD conditions (see also comments to Figures 5.18 and 5.19).

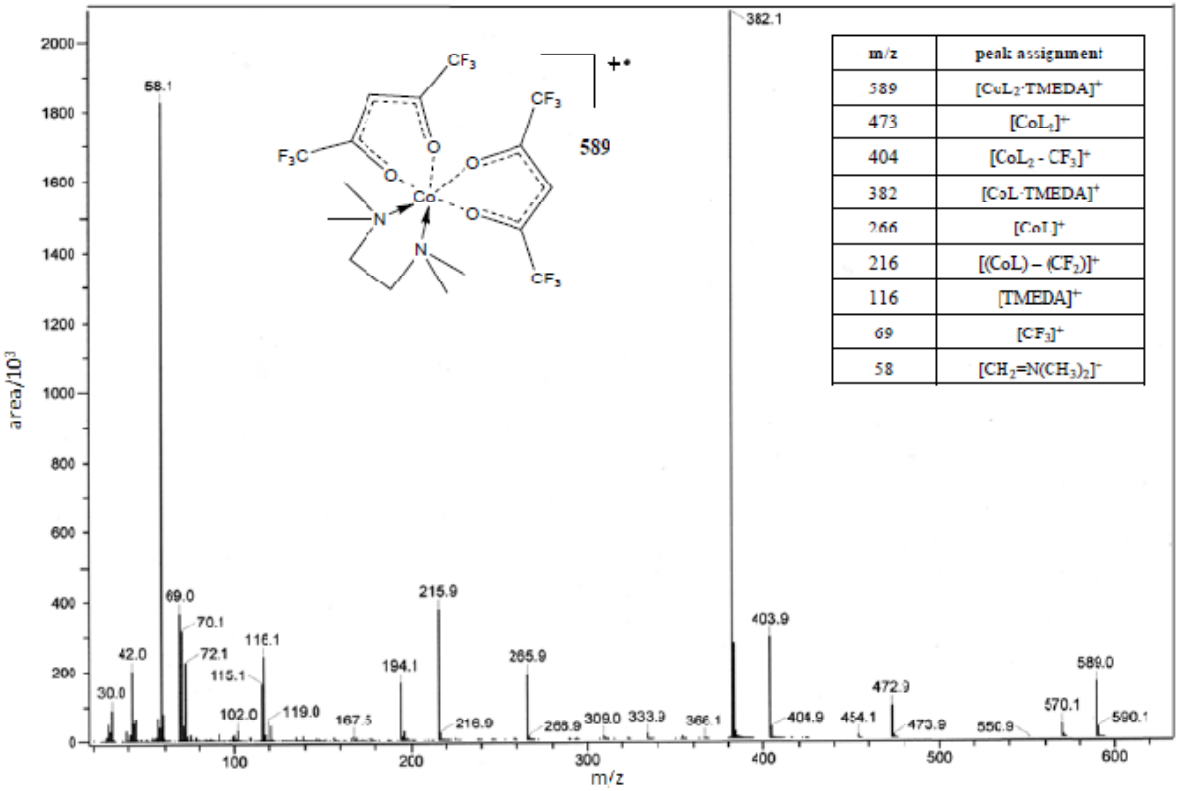

Figure 5.15: *EI-MS spectrum of precursor [Co(hfa)$_2$TMEDA]. The assignment of the main peaks is reported in the table, where the symbol L indicates the hfa ligand. The structure of the molecular ion is also sketched.*

Film characterization

Co_3O_4-based deposits were characterized by the combined use of field emission-scanning electron microscopy (FE-SEM), transmission electron microscopy (TEM) and XPS. Silica-supported samples were used for UV-Vis absorption spectroscopy and secondary ion mass spectrometry (SIMS) measurements. FE-SEM analysis were performed at a primary beam acceleration voltage of 10.0 kV by a Zeiss SUPRA 40VP instrument. TEM and high resolution TEM (HRTEM) measurements were performed on cross-section samples using a Tecnay G2 30 UT microscope, operated at 300 kV and having a 1.7 Å point resolution.

XPS measurements were run on a Perkin Elmer Φ 5600ci spectrometer at a working pressure lower than 10^{-8} mbar, using a non-monochromatized AlK_α excitation source (1486.6 eV). Binding energy (BE) correction was performed by assigning to the C1s signal of adventitious carbon a value of 284.8 eV. Ar^+ sputtering was accomplished at 4.5 kV, with an argon partial pressure of 4×10^{-8} mbar. The atomic percentages (at.%) were evaluated using sensitivity factors provided by Φ V5.4A software (Perkin-Elmer).

Optical absorption spectra were recorded by means of a Cary 5E (Varian) UV-Vis-NIR dual-beam spectrophotometer with a spectral bandwidth of 1 nm. For each spectrum, the silica substrate contribution was subtracted. Film thickness values necessary for the determination of Tauc plots (see Figure 5.18b) were determined by SIMS, that also confirmed the in-depth elemental distribution yielded by XPS (compare Figure 5.16 and Figure 5.18a). The optical band gaps were evaluated from Tauc plots $(\alpha h\nu)^2$ *vs.* $h\nu$, as reported in the literature.[18]

SIMS analyses were carried out on a IMS 4f mass spectrometer (Cameca, Padova, Italy) using a 14.5 keV Cs^+ primary beam and negative secondary ion detection. The dependence of the erosion rate on the matrix composition was taken into account by determining the former at various depths for each sample. The erosion rate was then evaluated by measuring the depth of the crater at the end of each analysis by means of a Tencor Alpha Step profilometer (maximum uncertainty of a few nanometers).

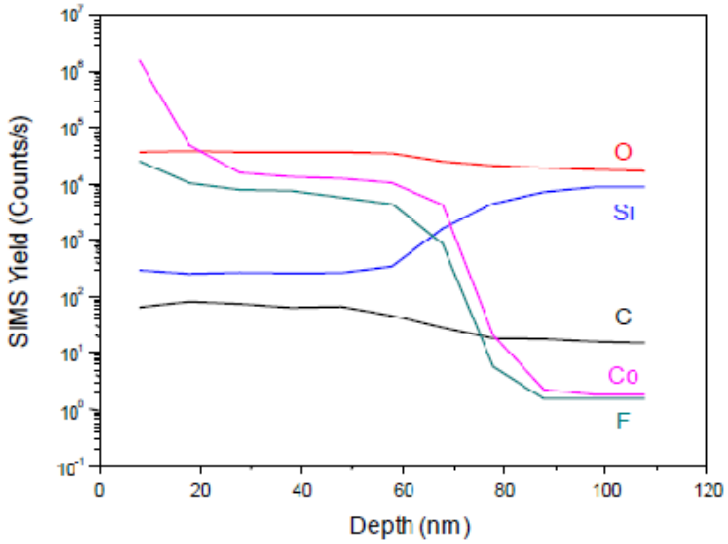

Figure 5.16: *EI SIMS profile for a representative F-doped Co_3O_4 deposit supported on SiO_2.*

As a general rule, undoped and F-doped Co_3O_4 samples presented an homogeneous composition and a sharp interface with the substrate. Moreover, carbon contamination was typically below 10 ppm, confirming the high purity of the obtained systems.

Near-UV photocatalytic experiments were carried out in a 250 mL pyrex discontinuous batch reactor maintained at 20°C, filled with a 1:1 water/ethanol mixture. Ar gas (15 mL min^{-1}) was used to collect and transfer gaseous products to the analysis system. A 125 W medium pressure mercury lamp (Helios Italquartz) with pyrex walls was used for near-UV excitation [photon flux ϕ_i = 29 mW cm^{-2} (λ = 360 nm) and 100 mW cm^{-2} (λ=400-1050 nm), determined by a DeltaOHM radiometer HD2302.0]. Experiments under simulated solar radiation were carried out in a stainless steel photoreactor, using the same temperature and reaction mixture as before. Illumination was performed using a Solar Simulator (LOT-Oriel) equipped with a 150 W Xe lamp, suitably filtered to reduce the fraction of UV photons. The light intensity for simulated solar light experiments, estimated by radiometry, was 180 mW cm^{-2}. Photocatalytic tests were repeated three times on each sample to check reproducibility. On-line detection of evolved gases was performed by an Agilent 6890 Gas Chromatographer (GC), equipped with a 10 way-two loop injection valve. A molecular sieve 5Å column connected to Thermal Conductivity Detector (TCD) was used for H_2 quantification, whereas C-containing compounds were measured by a PoraPLOTQ column connected to a methanator and to a flame ionization detector (FID). All tests were carried out in the presence of O_2, resulting from an initial air bubbling (15 mL min-1 for 10 min) in the water/ethanol solution. According to Cargill,[21] the initial concentration of oxygen was ≈ 9 mg L^{-1}. Analysis of the liquid phase was performed using an Agilent 7890A GC system (column: J&W DB-225 ms, 60 m, 0.25 mm, 0.25 mm) coupled with a 5975C VL MSD with triple-Axis Detector.

For both undoped and doped systems, the catalyst amount (ca. $1.5x10^{-4}$ g for a sample size of 3.0 cm^2) was estimated basing on film thickness (80-90 nm) and Co_3O_4 bulk density (6.1 g cm^{-3}). Blank tests performed either on the bare Si(100) substrates or on Co_3O_4-based deposits evidenced no activity in the absence of illumination. As in the case of methanol, experiments performed using fully de-areated water/ethanol solutions showed only a poor system activity and a fast catalyst deactivation.

Results and discussion

As evidenced by electron impact mass spectrometry (EI-MS) data, in the case of [Co(hfa)$_2$TMEDA] the elimination of fluorine radicals and the formation of several F-containing species took place (Fig. 5.15). Since the ionization conditions used for EI-MS analyses are analogous to those adopted in PE-CVD processes, it is reasonable to suppose that a similar fragmentation pathway also occurred during the plasma-assisted growth of Co_3O_4-based systems, thus explaining the effective fluorine incorporation into the deposited materials. This hypothesis was confirmed by X-ray photoelectron spectroscopy (XPS), evidencing a homogeneous in-depth fluorine distribution for samples synthesized from [Co(hfa)$_2$TMEDA] (see below). Figure 5.17a displays plane-view field emission scanning electron microscopy (FE-SEM) images of an undoped Co_3O_4 sample (left) and the corresponding F-doped specimen (right) synthesized under the same growth conditions. In both cases, the surface texture was dominated by pyramidal-like aggregates with a mean lateral size of 30 nm that, according to transmission electron microscopy (TEM) cross-sectional analyses (Fig. 5.17b), represented the tip of columnar structures grown perpendicular to the Si(100) substrate (deposit thickness=80-90 nm). Irrespective of the precursor used and the processing conditions adopted, electron diffraction (ED) patterns (not reported) were always characterized by the sole reflections expected for spinel type Co_3O_4. No appreciable ED variation was observed upon F-doping, a result traced back to the similar radii of fluorine and oxygen and to the substitutional fluorine doping of the spinel phase.[22, 23] High resolution TEM (HRTEM) and Fourier transform (FT) analyses (Fig. 5.17c) showed that the growth directions of the columnar structures displayed in Figure 5.17b were generally the <311> and <100> ones for undoped and doped Co_3O_4, respectively. Nevertheless, in both cases, {111} surface planes, the most stable for face-centered cubic systems such as Co_3O_4, were preferentially exposed.[24] This feature, in line with the pyramidal-like morphology of undoped and F-doped Co_3O_4 (Fig. 5.17a), highlights that their diverse photocatalytic activities (see below) cannot be related to exposure of facets with different Miller indexes.[25, 26]

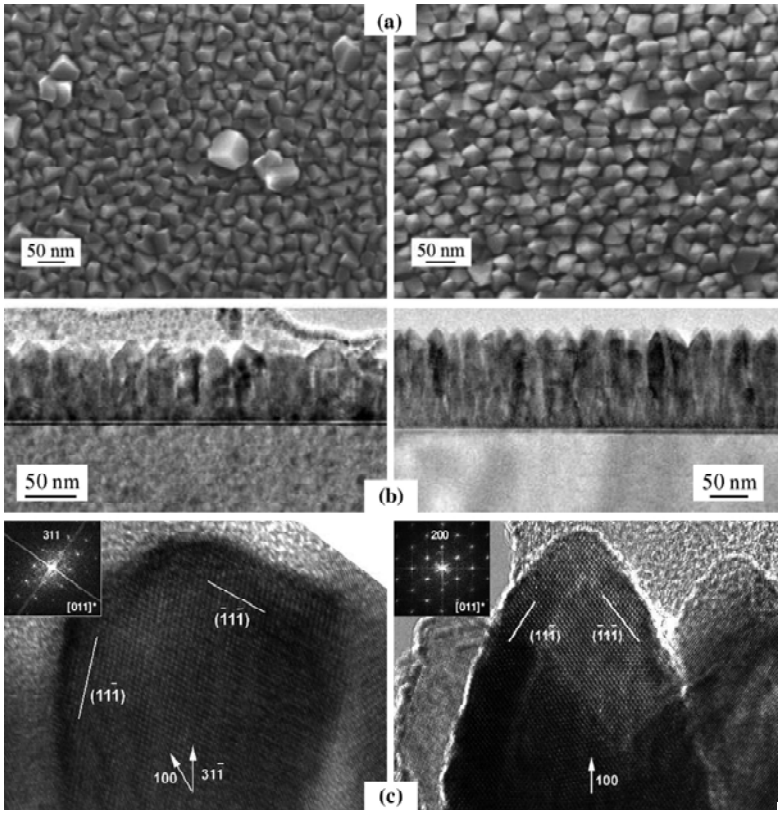

Figure 5.17: (a) Plane-view FE-SEM, (b) cross-sectional TEM, and (c) HRTEM images of undoped (left) and F-doped (right) Co_3O_4 samples. FT patterns of the HRTEM images are given as insets in (c).

In an attempt to clarify this issue, XPS analyses were performed, providing valuable compositional information. In line with literature,[24, 27] the shape and position of surface Co2p and CoLMM photopeaks (data not shown) clearly indicated the formation of Co_3O_4-based systems, irrespective of the precursor used. Nevertheless, whereas for samples synthesized from $[Co(dpm)_2]$ in-depth analyses evidenced a parallel distribution of the sole Co and O signals (Fig. 5.18a, left), the use of $[Co(hfa)_2TMEDA]$ also resulted in a constant fluorine content (~3 atom%) from the surface to the interface with the substrate (Fig. 5.18a, right).

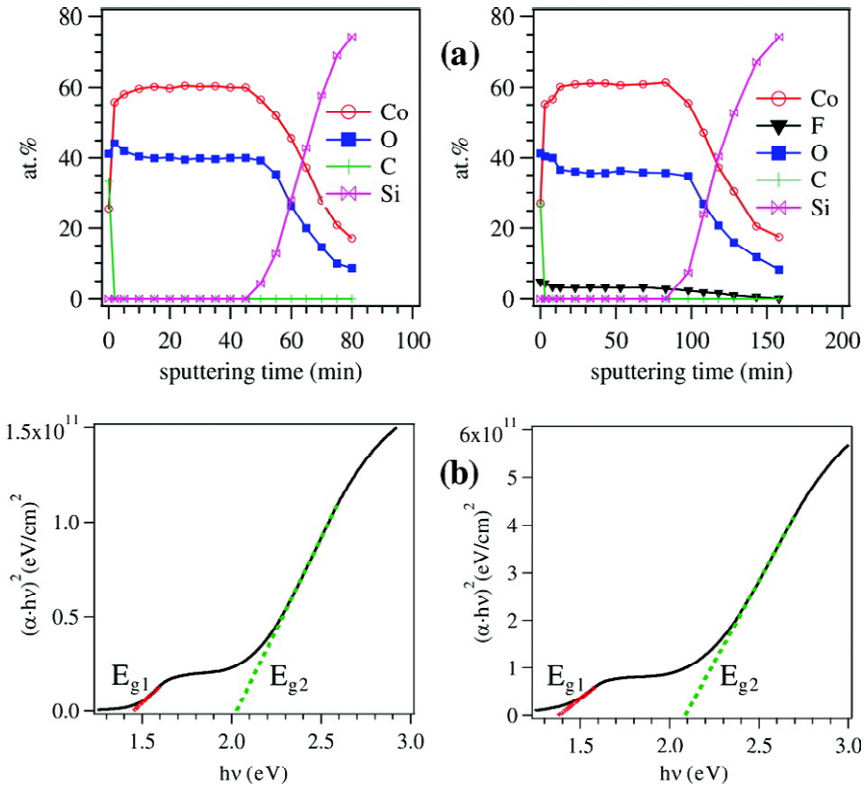

Figure 5.18: (a) XPS depth profiles and (b) Tauc plots of undoped (left) and F-doped (right) Co_3O_4 specimens.

XPS analyses were particularly useful to investigate the evolution of the F1s peak as a function of the erosion time, thus shedding light on the chemical state of fluorine in Co_3O_4. As displayed in Figure 5.19, the F1s surface signal was characterized by two well-evident components located at BE values of 684.5 (I) and 688.0 eV (II).

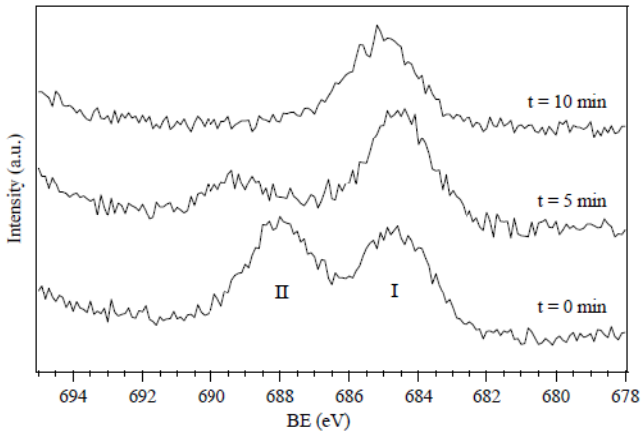

Figure 5.19. Evolution of the F1s XPS peak as a function of Ar^+ sputtering time for a F-doped Co_3O_4 specimen on Si(100).

While the former contribution was consistent with the presence of lattice fluorine in the oxide network arising from the incorporation of radical F species , the high BE one could be traced back to CF_2/CF_3 moieties. To this regard, it is interesting to note that the component (II) rapidly disappeared upon Ar^+ sputtering (Fig. 5.19), indicating that lattice fluorine was the only important species contributing to the in-depth F distribution shown in Figure 5.18a, right.

XPS investigation also highlighted the sudden disappearance of the carbon signal upon erosion, demonstrating clean precursor decomposition under the adopted PE-CVD conditions and the high purity of the obtained systems.

In order to elucidate the impact of fluorine doping on the material's optical properties, UV-vis absorption measurements were performed. Band-gap estimation from the Tauc plots of Figure 5.18b yielded values of 1.4-1.5 (E_{g1}) and 2.0-2.1 eV (E_{g2}) for both undoped and doped systems, indicating a negligible influence of fluorine doping.[24, 27] The optical absorption in the visible range demonstrated that Co_3O_4-based materials are promising SCs for the photocatalytic utilization of solar energy.[28, 29] Interestingly, a comparison of the Tauc plots reported in Figure 5.18b clearly revealed a 2-fold increase of the absorption coefficient for F-doped Co_3O_4, an important goal for efficient light harvesting and subsequent exploitation of e^-/h^+ pairs.[29, 30] In fact, since the diffusion length of charge carriers in SC oxides is small (typically a few nanometers), it is important that photons are largely absorbed in the near-surface layers, so that photogenerated e^- and h^+ species can effectively reach the catalyst surface and participate in the target chemical processes. Photoassisted H_2 generation was carried out under both near-UV (125 W Hg lamp with a photon flux of 29 mW cm^{-2} at 360 nm, 100 mW cm^{-2} in the 400-1050 nm interval) and simulated sunlight irradiation (150 W Xe lamp, 180 mW cm^{-2}), using 1:1 water/ethanol solutions. No appreciable evolution of gaseous products was observed when illumination and photocatalyst (geometrical area=3 cm^2) were not simultaneously present. Furthermore, only a weak and transient reactivity was revealed for de-aerated water/ethanol solutions, due to the surface formation of inactive CoO, as previously reported for bare Co_3O_4.[4a] Under near-UV irradiation and in the presence of O_2 (Fig. 5.20a), undoped Co_3O_4 showed an average hydrogen production of ~3 μmol h^{-1} cm^{-2}, whereas in the presence of fluorine the H_2 evolution rate was increased 5-fold. For the latter sample, an estimation of the catalyst

amount based on film thickness and Co_3O_4 bulk density led to an activity of 213 000 μmol h^{-1} g^{-1} (45 000 μmol h^{-1} g^{-1} for undoped Co_3O_4). Notably, this is one of the best values ever reported in the literature for SC-based photocatalytic hydrogen generation, also taking into account that no cocatalysts (e.g., Rh, Pd, Pt) were used in this study.[31]

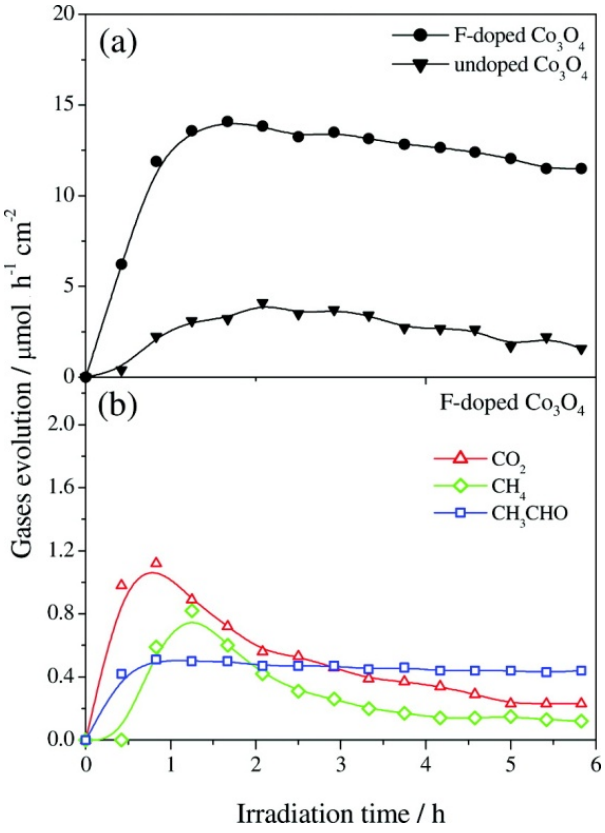

Figure 5.20: (a) H_2 evolution from a water/ethanol solution upon near-UV irradiation for undoped and fluorine-doped Co_3O_4 catalysts. (b) Evolution of C-containing gaseous products for the F-doped sample reported in (a).

The parallel evolution of CO_2 and CH_3CHO, resulting from ethanol oxidation, over F-doped Co_3O_4 (Fig. 5.20b) suggested the occurrence of two concomitant reaction pathways involving adsorbed ethanol and liquid-phase reactions between CH_3CH_2OH and free $OH^{\bullet}$, respectively.[32] The slight decrease of the H_2 yield and the net rate reduction for CO_2 and CH_4 could be associated mainly with CoO surface formation, attributed, in turn, to a progressive oxygen depletion in the reaction medium. Notably, acetaldehyde evolution was almost constant (Fig. 5.20b), suggesting thus the establishment of a gas-liquid equilibrium ensuring a buffering condition.

For liquid-phase products (see Figure 5.21), an interesting effect observed for F-doped Co_3O_4 was the photoassisted generation of 2,3-butanediol, a useful precursor for the industrial production of methyl ethyl ketone and 1,3-butadiene.[33, 34]

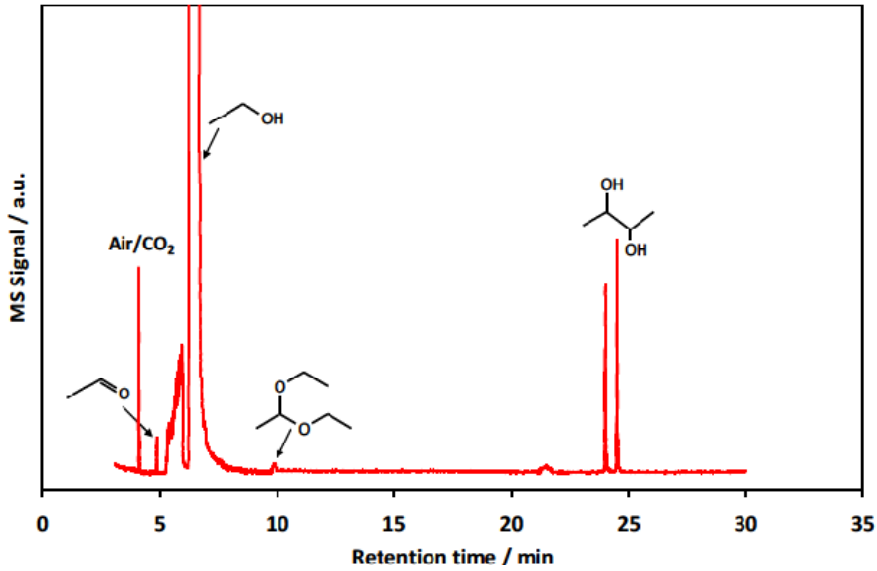

Figure 5.21. GC-MS analysis of a water/ethanol solution after the photocatalytic tests upon near-UV irradiation of F-doped Co_3O_4

Ethanol photoreforming can proceed trough ethanol dehydrogenation with the production of equimolar quantities of hydrogen and acetaldehyde. While hydrogen solubility in the liquid phase is low, the concentration of acetaldehyde is indeed remarkable, due to the establishment of a gas-liquid equilibrium. CH_3CHO could decompose to CH_4 and CO, followed by light-promoted water gas shift reaction. Although no acetic acid or its esters are detected by GC-MS analysis (Fig. 5.21), their presence cannot be completely ruled out based on the observation of strong adsorption of acetic acid on some oxides. A consequence of the presence of both ethanol, acetaldehyde and surface acidic sites of Co_3O_4 is the formation of 1,1-diethoxyethane (Fig. 5.22).

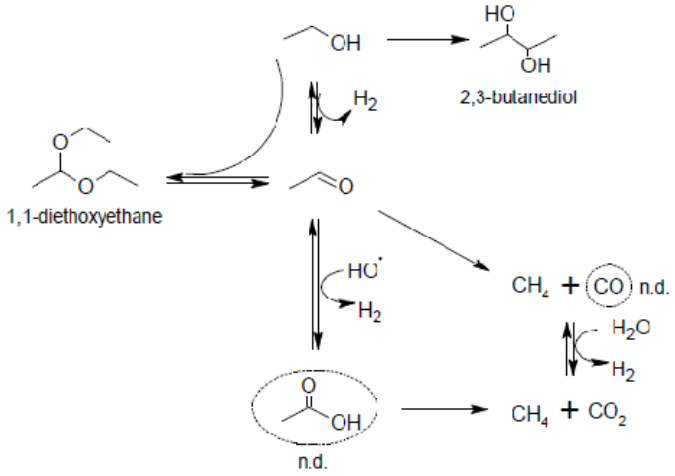

Figure 5.22:. Possible reaction pathway for H_2 formation and ethanol by-products. n.d. = not detected

Figure 5.20a also displays the presence of an initial induction period (duration~75 min) characterized by a progressive increase of the hydrogen evolution rate. This phenomenon suggests the occurrence of light-induced surface activation, followed by the establishment of an equilibrium between the byproducts adsorbed on the catalyst surface and in the liquid/gas phase. The 5-fold increase of the hydrogen yield observed for the fluorinated catalyst can be explained by the synergistic combination of various beneficial phenomena. Specifically, it has been reported that replacement of surface -OH groups by fluorine can lead to: (i) an increase of free $OH^{\bullet}$ radicals in the liquid-phase, resulting in faster ethanol oxidation and concomitant enhancement of $H^+ \rightarrow H_2$ reduction[35, 36]; (ii) inhibition of e^-/h^+ recombination[37]; and (iii) modification of absorption properties and/or tuning of band position[38, 39]. Since the presence of fluorine does not significantly change band-gap values (see above), the improved performance of F-doped Co_3O_4 could be mainly traced back to points (i) and (ii) and, in particular, to the larger availability of $OH^{\bullet}$ radicals. In addition, F-doping could induce a favorable shift of Co_3O_4 flat-band potentials, rendering photogenerated electrons more available for hydrogen production. Finally, the presence of fluorine on the catalyst surface might enhance the Lewis acidity of cobalt centers, as also observed for TiO_2-based photocatalysts, beneficially affecting the system activity.[22, 38, 40]

At variance with the case of UV illumination (Fig. 5.20), use of the less energetic simulated sunlight (Fig. 5.23) enabled us to perform photocatalytic experiments for 20h of irradiation without significantly altering the water/ethanol molar ratio. In fact, variation in the concentration of sacrificial agent could affect hydrogen production[41]. Under these more sustainable conditions, a lower, though appreciable, hydrogen evolution was still observed (Fig. 5.23). Compared to bare Co_3O_4, the fluorinated specimen showed an almost 2-fold increase in H_2 production (corresponding to 6500 $\mu mol\ h^{-1}\ g^{-1}$), along with a slightly more abundant methane evolution, as a result of acetic acid degradation or CO_2 hydrogenation (see also Figure 5.22). The relatively high initial CO_2 evolution is in line with the presence of carbonate traces on the catalyst surface[24] that are progressively decomposed under the present reaction conditions.

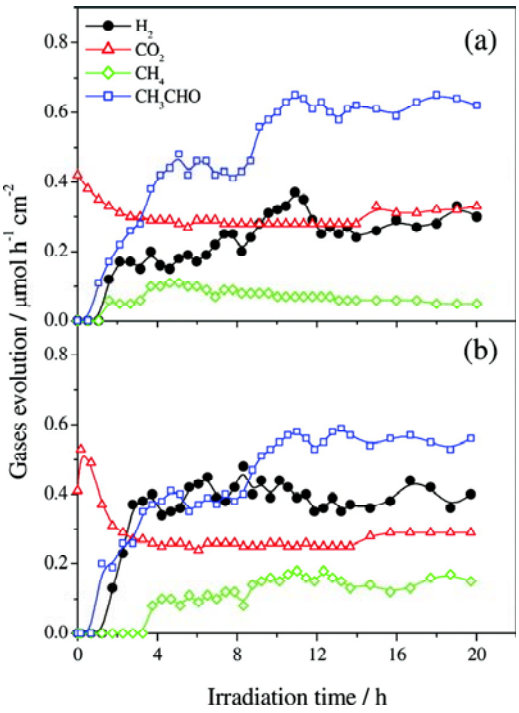

Figure 5.23: Evolution of gases from a water/ethanol solution upon simulated sunlight irradiation for undoped (a) and fluorine-doped (b) Co_3O_4 catalysts.

Nevertheless, after 2h of irradiation, constant CO_2 production was observed, indicating the occurrence of ethanol photoreforming involving a C-C bond cleavage. Notably, at variance with the case of UV light, no appreciable decrease of the hydrogen evolution rate was revealed during simulated sunlight irradiation, even after 20h of reaction. Such improved system stability was ascribed to several possible contributing effects. First, the lower conversion of ethanol into H_2 and other C-containing byproducts with respect to the case of Figure 5.20 implies lower surface coverage/poisoning by partially oxidized species. In addition, the lower H_2 yield minimizes the reaction between hydrogen and the oxygen present in solution, thus decreasing the formation of inactive CoO surface species.

Conclusions

In conclusion, a convenient CVD route to Co_3O_4 systems on Si(100) starting from $Co(hfa)_2$•TMEDA was presented, resulting in homogeneous assemblies of faceted nanopyramids. The obtained materials were tested for the first time in the photo-assisted H_2 production from methanol/water media. A remarkably stable hydrogen

evolution rate was observed over significant periods of time, provided that oxygen was present in the reaction environment. The present findings pave the way to the development of mixed cobalt oxide-containing nanocomposites for further advancements in photo-assisted hydrogen generation, with particular attention on the selectivity towards H_2 obtainment at expenses of carbon-containing gaseous by-products.

F-doping of Co_3O_4 films synthesized by PE-CVD resulted in a significant improvement of H_2 photoproduction from suitable aqueous solutions. Specifically, upon near-UV irradiation of F-doped Co_3O_4, a 5-fold hydrogen yield increase was evidenced with respect to the corresponding undoped oxide. In the case of simulated solar light, although a less marked improvement in terms of H_2 evolution was observed, the appreciable time stability of the response makes this material an attractive photocatalyst for the sustainable generation of hydrogen activated by sunlight. As a whole, the incorporation of fluorine resulted in highly photoactive Co_3O_4 materials, with H_2 yields per gram of catalyst among the best ever reported in the literature. It is also worth noting that the synthetic strategy adopted herein for the preparation of F-doped Co_3O_4 can be regarded as a general and versatile route for tailored anion doping of oxide and even non-oxide SC nanosystems. Efforts in this direction are currently underway.

References

[1] A. Y. Khodakov, W. Chu, P. Fongarland. *Chemical Reviews* **2007**, *107*(5), 1692-1744.
[2] D. G. Castner, P. R. Watson, I. Y. Chan. *Journal of Physical Chemistry* **1989**, *93*(8), 3188-3194.
[3] S. Zafeiratos, T. Dintzer, D. Teschner, R. Blume, M. Hävecker, A. Knop-Gericke, R. Schlögl. *Journal of Catalysis* **2010**, *269*(2), 309-317.
[4] J. Kirchnerova, M. Alifanti, B. Delmon. *Applied Catalysis A: General* **2002**, *231*(1-2), 65-80.
[5] J. Llorca, P. Ramírez De La Piscina, J. A. Dalmon, J. Sales, N. Homs. *Applied Catalysis B: Environmental* **2003**, *43*(4), 355-369.
[6] M. Ni, D. Y. C. Leung, M. K. H. Leung. *International Journal of Hydrogen Energy* **2007**, *32*(15 SPEC. ISS.), 3238-3247.
[7] X. Lou, J. Han, W. Chu, X. Wang, Q. Cheng. *Materials Science and Engineering B: Solid-State Materials for Advanced Technology* **2007**, *137*(1-3), 268-271.
[8] Y. Chen, L. Hu, M. Wang, Y. Min, Y. Zhang. *Colloids and Surfaces A: Physicochemical and Engineering Aspects* **2009**, *336*(1-3), 64-68.
[9] F. Jiao, H. Frei. *Angewandte Chemie - International Edition* **2009**, *48*(10), 1841-1844.
[10] S. Ikeda, T. Takata, T. Kondo, G. Hitoki, M. Hara, J. N. Kondo, K. Domen, H. Hosono, H. Kawazoe, A. Tanaka. *Chemical Communications* **1998**, (20), 2185-2186.
[11] S. Ikeda, T. Takata, M. Komoda, M. Hara, J. N. Kondo, K. Domen, A. Tanaka, H. Hosono, H. Kawazoe. *Physical Chemistry Chemical Physics* **1999**, *1*(18), 4485-4491.
[12] A. Walsh, K. S. Ahn, S. Shet, M. N. Huda, T. G. Deutsch, H. Wang, J. A. Turner, S. H. Wei, Y. Yan, M. M. Al-Jassim. *Energy and Environmental Science* **2009**, *2*(7), 774-782.
[13] G. Bandoli, D. Barreca, A. Gasparotto, C. Maccato, R. Seraglia, E. Tondello, A. Devi, R. A. Fischer, M. Winter. *Inorganic Chemistry* **2009**, *48*(1), 82-89.
[14] D. Barreca, A. Gasparotto, O. I. Lebedev, C. Maccato, A. Pozza, E. Tondello, S. Turner, G. Van Tendeloo. *CrystEngComm* **2010**, *12*(7), 2185-2197.
[15] R. A. Laudise. *Treatise on Solid State Chemistry* **1975**, *5*, 413.
[16] F. Gärtner, B. Sundararaju, A. E. Surkus, A. Boddien, B. Loges, H. Junge, P. H. Dixneuf, M. Beller. *Angewandte Chemie - International Edition* **2009**, *48*(52), 9962-9965+9771.
[17] M. M. Natile, A. Glisenti. *Chemistry of Materials* **2002**, *14*(7), 3090-3099.
[18] D. Barreca, C. Massignan, S. Daolio, M. Fabrizio, C. Piccirillo, L. Armelao, E. Tondello. *Chemistry of Materials* **2001**, *13*(2), 588-593.
[19] D. Barreca, D. Bekermann, E. Comini, A. Devi, R. A. Fischer, A. Gasparotto, C. Maccato, C. Sada, G. Sberveglieri, E. Tondello. *CrystEngComm* **2010**, *12*(11), 3419-3421.
[20] G. Bandoli, D. Barreca, A. Gasparotto, C. Maccato, R. Seraglia, E. Tondello, A. Devi, R. A. Fischer, M. Winter. *Inorganic Chemistry* **2009**, *48*(1), 82-89.
[21] R. W. Cargill. *J. Chem. Soc., Faraday Trans. 1: Physical Chemistry in Condensed Phases* **1976**, *72*, 2296-2300.
[22] D. Chen, Z. Jiang, J. Geng, J. Zhu, D. Yang. *Journal of Nanoparticle Research* **2009**, *11*(2), 303-313.
[23] J. Xu, Y. Ao, D. Fu, C. Yuan. *Applied Surface Science* **2008**, *254*(10), 3033-3038.
[24] D. Barreca, A. Gasparotto, O. I. Lebedev, C. Maccato, A. Pozza, E. Tondello, S. Turner, G. Van Tendeloo. *CrystEngComm* **2010**, *12*(7), 2185-2197.
[25] L. Hu, Q. Peng, Y. Li. *Journal of the American Chemical Society* **2008**, *130*(48), 16136-16137.
[26] C. Y. Ma, Z. Mu, J. J. Li, Y. G. Jin, J. Cheng, G. Q. Lu, Z. P. Hao, S. Z. Qiao. *J. Am. Chem. Soc.* **2010**, *132*, 2608-2613.
[27] D. Barreca, C. Massignan, S. Daolio, M. Fabrizio, C. Piccirillo, L. Armelao, E. Tondello. *Chemistry of Materials* **2001**, *13*(2), 588-593.
[28] Y. S. Hu, A. Kleiman-Shwarsctein, G. D. Stucky, E. W. McFarland. *Chemical Communications* **2009**, (19), 2652-2654.
[29] A. B. Murphy. *Solar Energy Materials and Solar Cells* **2007**, *91*(14), 1326-1337.
[30] A. Zolfagahri, K. N. Avanaki, H. Z. Jooya, H. Sayahi. *Semiconductor Science and Technology* **2007**, *22*(6), 653-658.
[31] X. Chen, S. Shen, L. Guo, S. S. Mao. *Chemical Reviews* **2010**, *110*(11), 6503-6570.
[32] J. Chen, D. F. Ollis, W. H. Rulkens, H. Bruning. *Water Research* **1999**, *33*(3), 669-676.
[33] M. J. Syu. *Applied Microbiology and Biotechnology* **2001**, *55*(1), 10-18.
[34] Z. L. Xiu, A. P. Zeng. *Applied Microbiology and Biotechnology* **2008**, *78*(6), 917-926.
[35] Y. C. Oh, W. S. Jenks. *Journal of Photochemistry and Photobiology A: Chemistry* **2004**, *162*(2-3), 323-328.
[36] C. Minero, G. Mariella, V. Maurino, D. Vione, E. Pelizzetti. *Langmuir* **2000**, *16*(23), 8964-8972.
[37] J. F. Montoya, P. Salvador. *Applied Catalysis B: Environmental* **2010**, *94*(1-2), 97-107.
[38] H. Sun, S. Wang, H. M. Ang, M. O. Tadé, Q. Li. *Chemical Engineering Journal* **2010**, *162*(2), 437-447.
[39] J. C. Yu, J. Yu, W. Ho, Z. Jiang, L. Zhang. *Chemistry of Materials* **2002**, *14*(9), 3808-3816.
[40] Y. Zhao, X. Du, X. Wang, J. He, Y. Yu, H. He. *Sensors and Actuators, B: Chemical* **2010**, *151*(1), 205-211.
[41] D. I. Kondarides, A. Patsoura, X. E. Verykios. *Journal of Advanced Oxidation Technologies* **2010**, *13*(1), 116-123.

Part 3:
Supported systems based on zinc oxide

ZnO is a *n*-type semiconductor (Eg = 3.4 eV) that can be synthesized with diverse morphologies.[1] It has been the object of several studies regarding photocatalysis and gas sensing utilization.[2] The functional properties for such applications can be improved by the synergistic combination of nanostructured ZnO with metallic NPs, which, beside their inherent catalytic activity, promote an enhancement of charge carrier separation due to the formation of a Schottky barrier at the metal/oxide interface.[3-5] Among the different metals, silver has demonstrated a great potential to improve ZnO antibacterial/pollutant degradation activity[6-9] and optical properties[10-14], whereas H_2 production and sensing from Ag/ZnO nanomaterials are still rather unexplored. In particular, whereas few reports devoted to H_2 production by methanol reforming over Ag/ZnO catalysts are available[15, 16], photoinduced reforming of aqueous solutions to yield H_2, a promising route for its clean and sustainable generation[17], has

never been attempted on such systems. In addition, only one paper on hydrogen sensing by Ag/ZnO composites is available in the literature[18].

Since Ag/ZnO features are strongly dependent on size, shape, and mutual distribution of the components, the development of controllable synthetic strategies is highly demanded to tune their functional performances. Up to date, Ag/ZnO nanosystems have been prepared both as powders and supported materials by liquid,[9, 12] vapor,[8, 13] and hybrid liquidevapor phase routes.[14] Nevertheless, in spite of various studies, a thorough understanding of Ag/ZnO interactions is still an open question, especially due to the high reactivity of silver NPs towards oxidation.[19, 20] Furthermore, beyond the use of powdered materials,[9, 21] a current challenge concerns the development of organized Ag/ZnO assemblies onto suitable substrates, enabling their direct integration into functional devices.

Catalysts synthesis and characterization

Columnar ZnO arrays were grown by PE-CVD using a Zn(II) bis(ketoiminate) precursor $Zn[(R)NC(CH_3)=C(H)C(CH_3)=O]_2$ with R = $-(CH_2)_3OCH_3$ [33]. Depositions were performed onto Si(100) substrates (MEMC®, Merano, Italy; dimensions = 2 cm x1 cm x 1mm), for hydrogen production. The substrates were suitably pre-cleaned using well established procedures.[22, 23] The precursor, placed in an external vessel heated by an oil bath, was vaporised at 150°C and transported into the reaction chamber by means of an Ar flow (60 sccm). The temperature of the lines was maintained at 170°C in order to avoid condensation phenomena. Additional Ar (15 sccm) and O_2 (20 sccm) flows were introduced into the reactor. Depositions were performed for 1 h at 300°C, at a total pressure of 1 mbar, and using an RF-power of 20 W.

A preliminary structural, morphological and compositional investigation was performed on bare ZnO matrices. FE-SEM observations (Fig. 5.24a-b) of as-prepared ZnO deposits revealed the presence of columnar structures characterized by mean length and diameter values of 180 and 20 nm, respectively.

XPS analyses of the sample surface showed the typical signals expected for ZnO (Fig. 5.24c). The presence of carbon (≈ 35 at. %) was related to surface contamination upon air exposure, since the C1s signal fell to noise level after a few minutes of Ar^+

erosion (4.5 kV, argon partial pressure = 5×10^{-8} mbar). No nitrogen contamination was observed, confirming the clean decomposition of the used precursor into ZnO under the adopted PE-CVD conditions.[22] The surface O1s photopeak (Fig. 5.24d) was fitted by two components. A first peak (I), at BE = 532.0 eV could be attributed to the presence of absorbed hydroxyl/carbonates groups arising from atmospheric contamination[22, 24], whereas a second more intense signal (II), at BE = 530.0 eV, corresponded to lattice oxygen from the ZnO matrix. [22, 24]

GIXRD patterns of as-prepared samples (Fig. 5.24e) evidenced the sole (002) ZnO reflection (JCPDS card no. 36-1451), highlighting a preferential growth along the [001] direction, as frequently observed for ZnO.[22, 25]

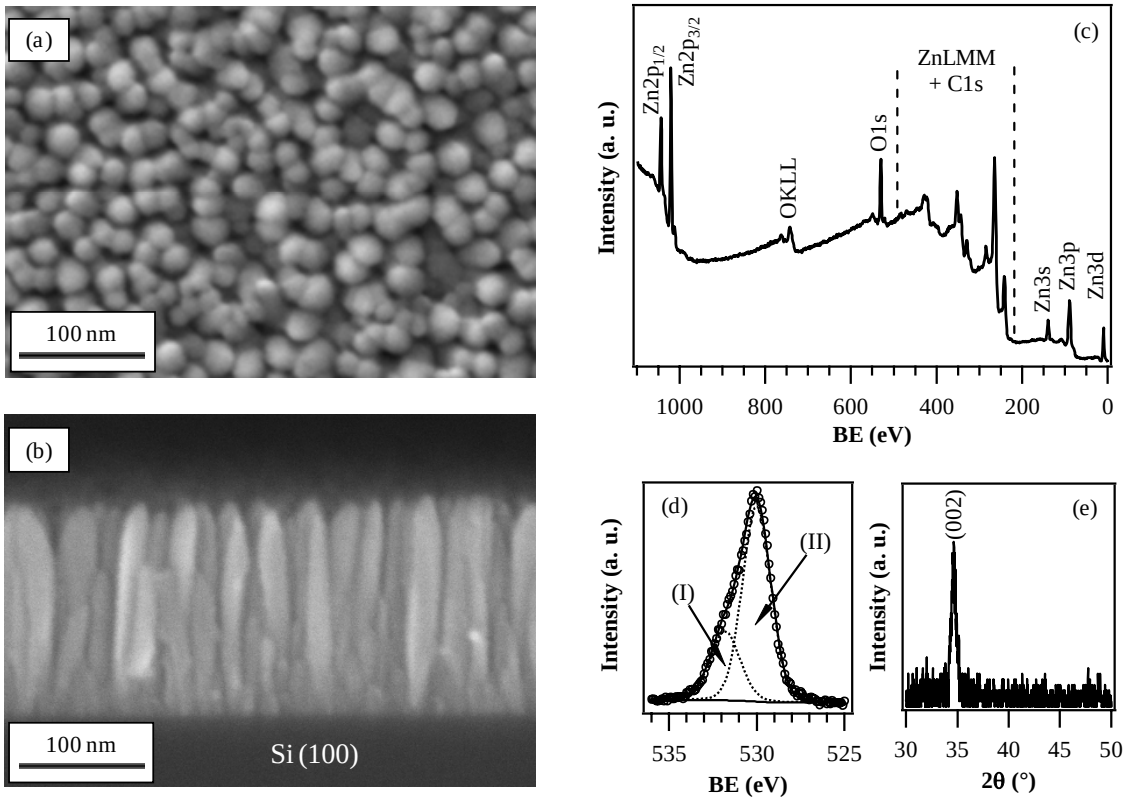

Figure 5.24. Plane-view (a) and cross-section (b) FE-SEM micrographs of an as-prepared ZnO sample. Representative XPS surface survey spectrum (c), surface O1s photopeak (d), and GIXRD pattern (e) for an as-prepared ZnO specimen.

As a matter of fact, *ex-situ* annealing at 400°C did not induce any significant structural, compositional and morphological alteration of the present systems.

Subsequently, Ag NPs were deposited on the obtained ZnO arrays by RF-sputtering from Ar plasmas, using an RF-power of 5 W and a total pressure of 0.3 mbar. The process was performed at a temperature as low as 60°C to prevent undesired

modifications of the pristine ZnO matrices. Three different sputtering times (30, 90, and 150 min, see Table 1) were used to vary the overall silver amount in the resulting composites.

The effect of ex-situ thermal treatment in air at 400°C for 1 h was also investigated. In the following, samples are denoted as X_Y, where X is the sputtering time (in min) and Y indicates as-prepared (A) or thermally treated (T) samples, respectively.

Field emission-scanning electron microscopy (FE-SEM) and energy dispersive X-ray spectroscopy (EDXS) measurements were carried out by a Zeiss SUPRA 40VP instrument, equipped with an Oxford INCA x-sight X-ray detector, at acceleration voltages between 10 and 20 kV. For cross-section EDXS linescans, OKa1, ZnKa1, and AgLa1 signals were monitored along the whole deposit thickness.

X-ray photoelectron and X-ray excited-Auger electron spectroscopies (XPS and XE-AES) analyses were performed on a Perkin-Elmer F 5600ci spectrometer at pressures lower than 10^{-8} mbar on a sample probing area of 1 mm 1 mm, using a MgK excitation source (1253.6 eV). Binding Energy (BE) values were corrected for charging by assigning to the C1s line of adventitious carbon a value of 284.8 eV. Peak fitting was performed by a least-squares procedure, using Gaussian-Lorentzian peak shapes. Zn and Ag Auger parameters were calculated as previously reported.[22, 26, 27]

Glancing incidence X-ray diffraction (GIXRD) measurements were performed by a Bruker D8 Advance diffractometer equipped with a Göbel mirror, using a CuKα source (40 kV, 40 mA), at a fixed incidence angle of 0.2°.

Conventional transmission electron microscopy (TEM) and high resolution (HRTEM) analyses were performed on cross-section samples using a Tecnai G2 30 UT microscope with a 0.17 nm point resolution, operated at 300 kV. Cross-section specimens for TEM were prepared by mechanically grinding down to the thickness of approximately 20 mm, followed by Ar^+ ion beam milling using a Balzers RES 101 GVN apparatus. High angle annular dark field-scanning transmission electron microscopy (HAADF-STEM) and spatially resolved electron energy loss spectroscopy (STEM-EELS) were performed on a FEI Titan 80-300 “cubed” microscope fitted with an aberration corrector for the probe forming lens and a GIF QUANTUM spectrometer, operated at 300 kV. The used HAADF detector inner semi-angle, the convergence semi-angle for the

EELS experiments and the collection semi-angle were 90, 21, and 90 mrad, respectively. After acquisition, the EELS data were treated using principle component analysis (PCA) to minimize the effect of random noise. Maps were generated by integrating the EELS signals over an appropriate energy window after power-law background removal.

In order to prevent the occurrence of undesired alterations upon functional testing hydrogen production measurements were performed on *ex-situ* annealed specimens. In fact, preliminary tests performed on as-prepared samples resulted in the obtainment of irreproducible responses, that were related to the occurrence of morphological alterations (system compaction) and compositional modifications (variations in the silver oxidation state).

UV-Vis photocatalytic experiments were carried out in a 250 mL pyrex discontinuous batch reactor maintained at 20°C, filled with a 1:1 water-methanol mixture.[28-31] Ar gas (15 mL min^{-1}) was used to collect and transfer gaseous products to the analysis system. A 125 W medium pressure mercury lamp (Helios Italquartz) with pyrex walls was used for UV-Vis excitation [photon flux ϕ_i = 29 mW cm^{-2} (λ = 360 nm) and 100 mW cm^{-2} (λ=400-1050 nm), determined by a DeltaOHM radiometer HD2302.0]. Experiments under simulated solar radiation were carried out in a stainless steel photoreactor, using the same temperature and reaction mixture as before. Illumination was performed using a Solar Simulator (LOT-Oriel) equipped with a 150W Xe lamp, suitably filtered to reduce the fraction of UV photons. The light intensity for simulated solar light experiments, estimated by radiometry, was 180 mW cm^{-2}. Photocatalytic tests were repeated three times on different samples to check reproducibility. On-line detection of evolved gases was performed by an Agilent 6890 Gas Chromatographer (GC), equipped with a 10 way-two loop injection valve. A molecular sieve 5Å column connected to a Thermal Conductivity Detector (TCD) was used for H_2 analysis.

Results and discussion

In this study, three different sputtering times, leading to different silver amounts, were adopted for Ag deposition onto ZnO matrices (Table 5.1).

Table 5.1: Growth conditions and silver particle sizes for as-prepared (A) and annealed (T) Ag/ZnO nanocomposites. Surface silver molar fraction, determined from XPS analyses, is defined as χ_{Ag}= [Ag/ (Ag + Zn + O)]x100

Ag sputtering time (min)	**Ag particle size** (as-prepared, **A**) (nm)	**Ag particle size** (thermally treated, **T**) (nm)	χ_{Ag} (**A**)	χ_{Ag} (**T**)
30	10	10	15.5	1.6
90	35	80	32.6	8.3
150	60	100	44.6	14.7

Cross-section FE-SEM observations showed that the zinc oxide columnar morphology did not undergo significant alteration upon silver deposition, apart from a systematic reduction of the column length from 180 to 120 nm. This effect could be ascribed to the occurrence of ablation phenomena, competitive with deposition ones in the used plasmas. Plane-view images of as-prepared Ag/ZnO nanosystems (Fig. 5.25) clearly evidenced the presence of Ag particles localized on the top of the columns, with morphological features directly dependent on the adopted sputtering time.

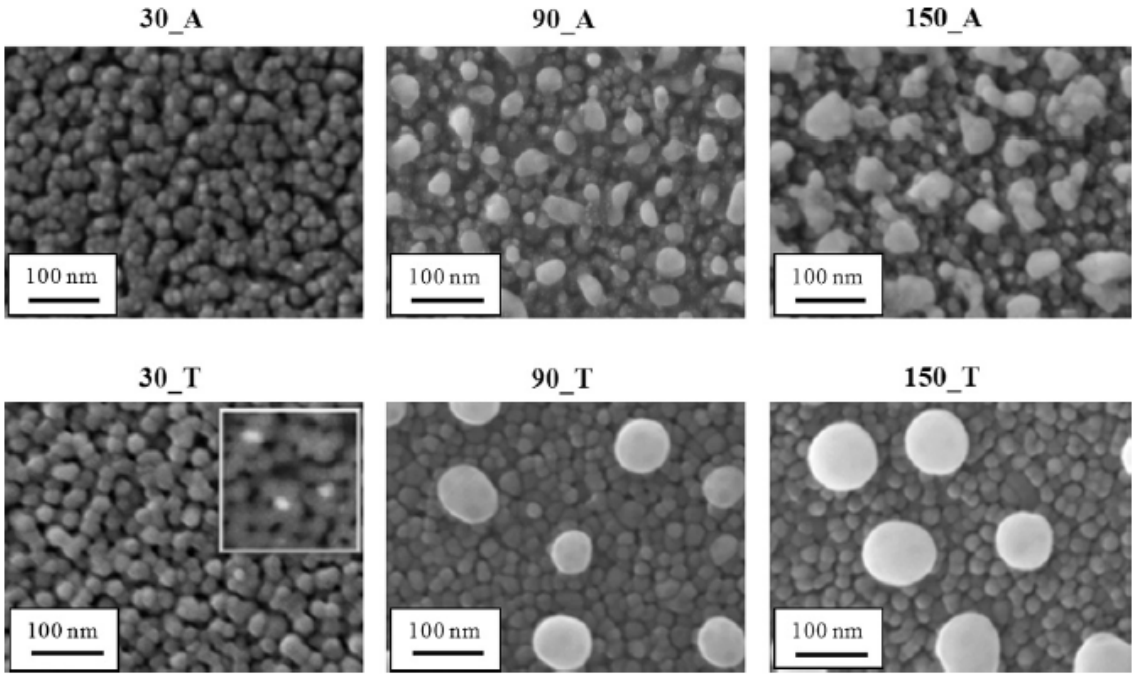

Figure 5.25: *Plane-view FE-SEM micrographs of as-prepared and annealed Ag/ZnO nanocomposites. The presence of Ag particles for sample 30_T is highlighted by a backscattered electron image (same scale bar) in the inset.*

In particular, the mean Ag NP size progressively increased on going from sample 30_A to 150_A, with a concomitant shape evolution from spherical to island-like

aggregates. Upon annealing (Fig. 5.25), the formation of large spherical Ag aggregates took place, due to thermally-induced agglomeration of the pristine NPs (see Table 1), a phenomenon particularly evident for sputtering times ≥ 90 min.

The system composition as a function of the processing conditions was investigated by EDXS along the deposit cross sections (Fig. 5.26). For all the analyzed specimens, the intensity of O and Zn X-ray signals were always overlapped throughout the sample depth, in line with the uniform and homogeneous formation of zinc(II) oxide.

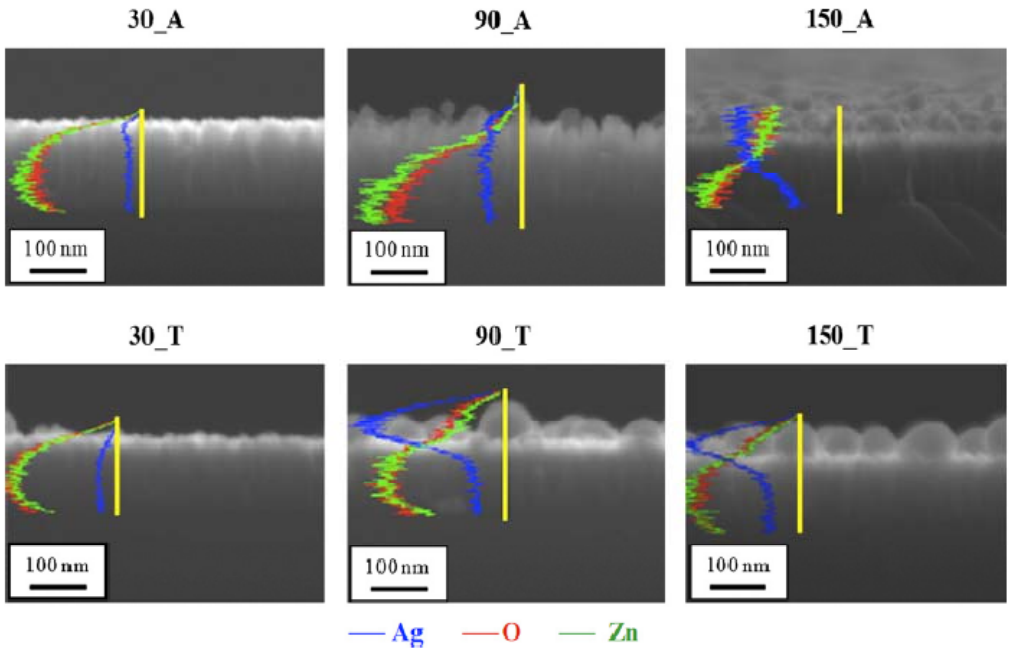

Figure 5.26: *Cross-section EDXS line-scans for as-prepared and annealed Ag/ZnO nanocomposites. The red, green and blue lines correspond to O, Zn, and Ag signals, respectively*

In as-prepared samples, silver presence was observed not only on the top of ZnO columns, but also in the sub-surface layers. Such a behavior was observed also for sample 150_A, characterized by the highest silver loading, though in this case the strong intensity of the Ag signal in the proximity of the surface suggested a metal segregation in this region. Upon annealing, two different behaviors were observed for Ag redistribution, depending on the silver content. For sample 30_T, the dominant phenomenon was an in-depth silver diffusion into ZnO. For specimens 90_T and 150_T, characterized by a progressively higher silver content, the amount of silver diffused into the inner system layers underwent an appreciable increase. In addition, excess Ag segregated in the outermost region, forming spherical particles on the sample surface.

Note that a similar behavior has also been observed upon annealing of Ag-implanted ZnO samples[32, 33].

To obtain a deeper insight into the system nanostructure, with particular regard to the spatial distribution of the Ag NPs inside the ZnO matrix, TEM analyses were carried out. Representative cross-section TEM images of specimens 30_A and 30_T are shown in Figure 13a and b, respectively.

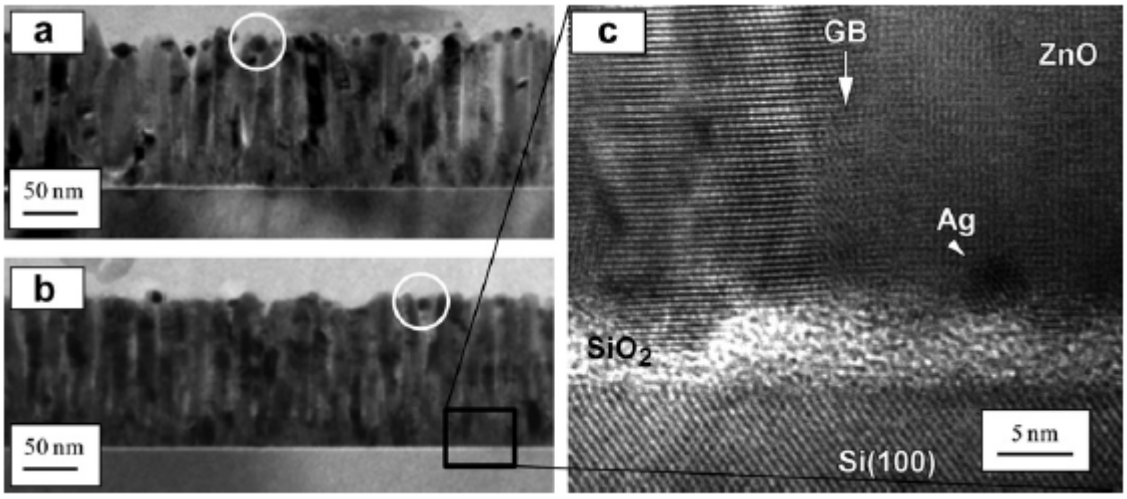

Figure 5.27: *Cross-section bright field TEM images of nanocomposites 30_A (a) and 30_T (b). White circles mark the location of Ag NPs. (c) HRTEM of the deposit/Si(100) interface region highlighted by the black rectangle in (b). Note that Ag NPs are present even at the interface with the substrate, where an amorphous SiO_2 layer is also detected.*

At variance with powdered ZnO (*zincite*), c-oriented zinc oxide systems with (001) preferential orientation were obtained, as often observed for ZnO nanostructures[1, 7, 9, 14, 16, 18]. In the present case, this [001] growth, leading to columns perpendicular to the substrate surface, was further enhanced by the sheath electric field[22, 25]. In line with FE-SEM analyses, sample 30_A showed small silver particles mainly dispersed in the outermost ZnO region (Fig. 5.27a). Conversely, for specimen 30_T (Fig. 5.27b) only a few Ag particles were present at the surface, in agreement with the Ag in-depth distribution evidenced by EDXS. Accordingly, HRTEM images of sample 30_T revealed the presence of small Ag NPs diffused through the grain boundaries (GB) of the ZnO deposit, down to the interface with the Si substrate (Fig. 5.27c). Such results unambiguously confirm the in-depth penetration of silver along the whole ZnO deposit, favoured by the porous ZnO morphology and the typical infiltration power of RF-sputtering, and further promoted by thermal treatment in air.

Figure 5.28 displays typical HRTEM (a-b) and HAADF-STEM (c) images for specimen 90_T. Beside the large silver aggregates evidenced also by FE-SEM and EDXS (compare Figs 5.25 and 5.26), even smaller Ag NPs, with typical diameters between 5 and 20 nm, could be observed. Among them, low-sized Ag NPs were single crystal and defect free, while larger ones showed the presence of {111}-type twins (marked by white arrows in Figure 5.28a). Figure 14b displays a ZnO column grown along the c-axis in contact with a silver NP. Spatially resolved EELS measurements were also performed on the region highlighted by the box in Figure 5.28c. As revealed by Figure 14d-g, elemental maps confirm the presence of large silver particles segregated in the outermost ZnO region.

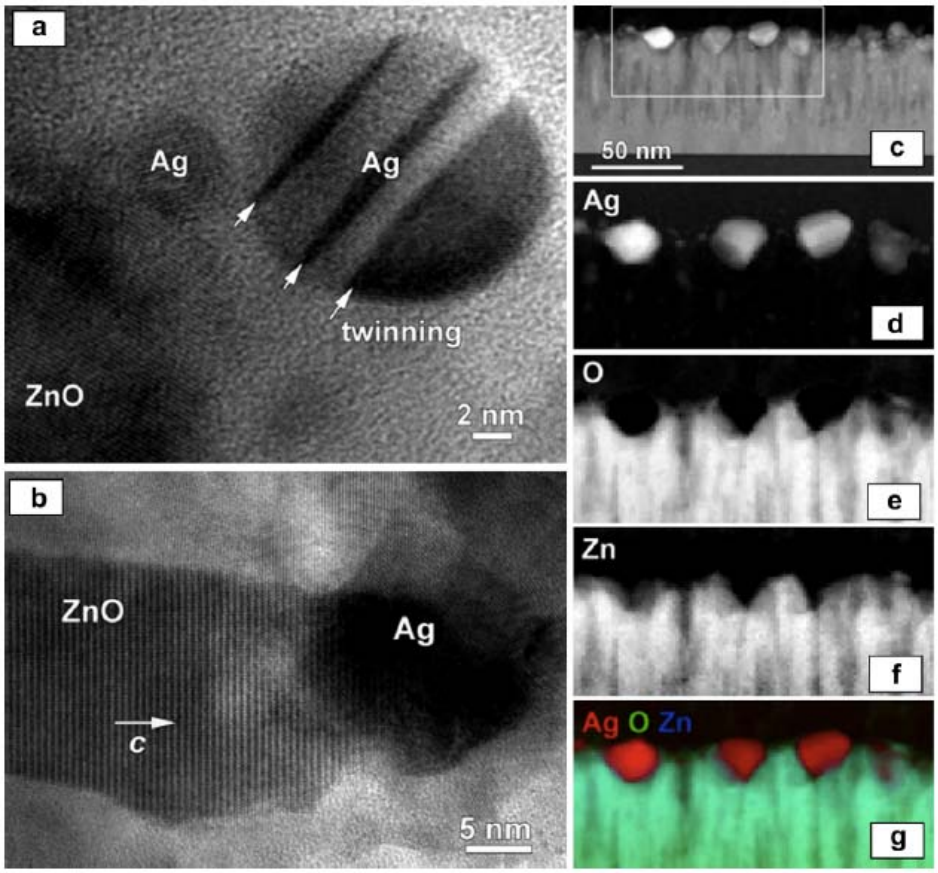

Figure 5.28: *Cross-section TEM observations of specimen 90_T: (a-b) HRTEM micrographs; (c) HAADF-STEM image and corresponding elemental maps (d-g) extracted from STEM-EELS experiments. Color codes: Ag=red, O=green, Zn=blue*

Representative GIXRD patterns of Ag/ZnO systems are displayed in Figure 5.29. As a general rule, despite no significant variation of ZnO peak positions was observed with respect to the bare oxide nanosystems, the system structural features were

influenced by both the annealing process and the Ag deposition. In fact, the appearance of additional diffraction peaks related to the presence of metallic silver (JCPDS card no. 04-0783) or silver(I) oxide (JCPDS card no. 72-2108) took place, whose intensity increased with Ag sputtering time (compare patterns for 30_A and 90_A). On going from sample 30_A to 30_T, the peak at $2\theta=38.1°$ ascribed to silver-containing phases disappeared, in line with the enhanced silver particle dispersion into the ZnO matrix evidenced by EDXS and TEM. Conversely, an appreciable intensity increase of silver-related signals was detected upon passing from specimen 90_A to 90_T, due to the previously discussed Ag segregation in the outermost system regions. Furthermore, the appearance of peaks attributed to hexagonal Ag_2O (JCPDS card no. 72-2108) highlighted the occurrence of silver oxidation during thermal treatment. At variance with the results reported by Ramesh et al. for annealed Ag_2O films[34], no evidence of the Ag_2O cubic phase was obtained.

The surface chemical composition as a function of silver content was investigated by photoelectron spectroscopies. Irrespective of Ag sputtering time and annealing process, Zn Auger parameter was always close to 2010.0 eV, the value expected for ZnO[24]. Surface quantitative data (Table 1) show that Ag content underwent a remarkable decrease after thermal treatment, due to the concurrence of two different phenomena: i) for 30_T, silver partially diffused into the inner ZnO layers (see above); ii) for 90_T and 150_T specimens, the reorganization of smaller Ag NPs into larger ones led to a higher ZnO surface exposed to XPS probing.

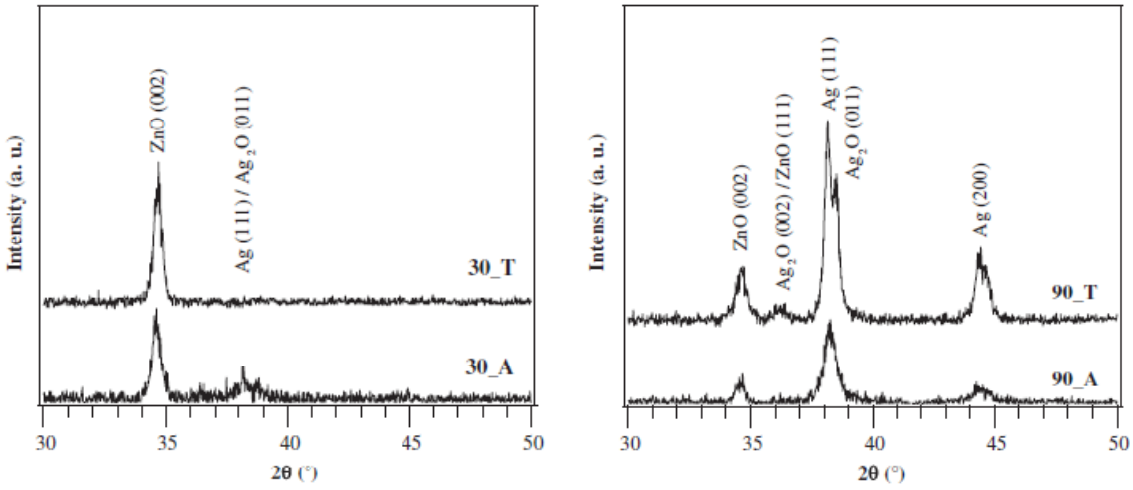

Figure 5.29: *GIXRD patterns of representative Ag/ZnO nanocomposites before and after thermal treatment.*

Surface XPS Ag3d and XE-AES AgMVV spectra of a representative Ag/ZnO nanocomposite are displayed in Figure 5.30. For all the investigated specimens, the $Ag3d_{5/2}$ photopeak was centered at a mean BE=368.0 eV. Due to the very close BE values for Ag(0) and Ag(I) species,[20, 26, 31, 35-37] silver Auger parameters were evaluated to obtain a fingerprint of silver oxidation state.[35] For as-prepared samples, the obtained values [α_1(Ag)=724.3 eV; α_2(Ag)=718.8 eV] revealed the presence of Ag(I) oxide as the main silver species.[26, 27, 35] In a different way, the increase of these values to α_1(Ag)=726.2 eV and α_2(Ag)=720.3 eV upon annealing suggested the occurrence of an Ag(I) reduction to Ag(0).[26, 35]

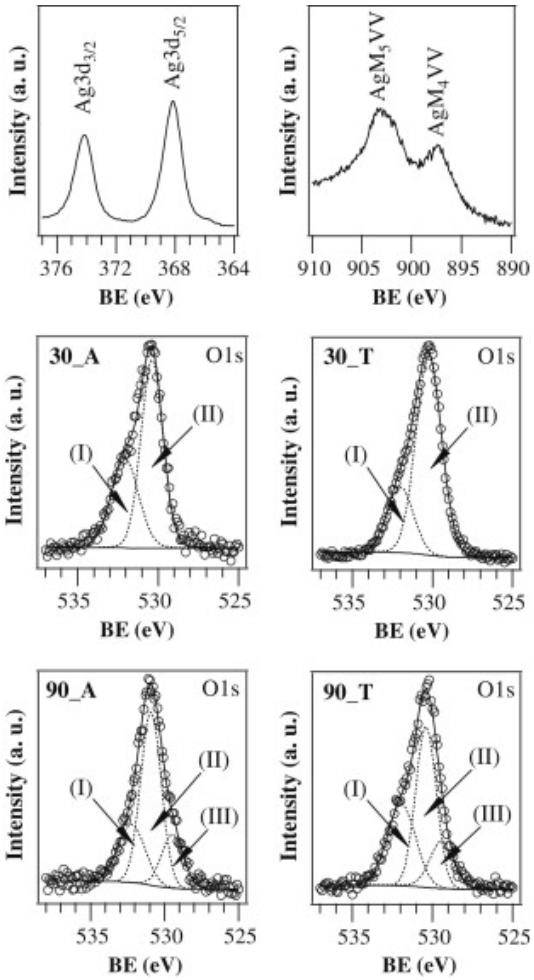

Figure 5.30: *Surface Ag3d and AgMVV signals for an asprepared Ag/ZnO nanocomposite. Surface O1s photopeaks for various Ag/ZnO nanocomposites*

This evolution could be related both to the thermal instability of Ag(I) oxide and to the morphological reorganization of silver aggregates, as highlighted by FE-SEM and EDXS observations. In fact, Ag NPs underwent a significant size increase upon

annealing. It is reasonable to suppose that the smaller Ag particles as-prepared samples had a higher contact area with both ZnO matrices and the outer atmosphere, which was responsible for a more marked silver oxidation.[19, 20] Conversely, the NP size increase and the Ag segregation in the outermost ZnO region upon thermal treatment could explain the predominance of Ag(0) at the sample surface. These results suggest that the Ag_2O phase observed in the GIXRD patterns of annealed samples (Fig. 5.29) should be mainly localized in the inner ZnO layers.

At variance with the case of pure ZnO samples, three bands contributed to the O1s signal for Ag sputtering times higher than 30 min (Fig. 5.30). The average BE of the three components were: (I) 532.0 eV, (II) 530.5 eV, and (III) 529.4 eV. Whereas peak (I) could be ascribed to surface chemisorbed carbonate and hydroxyl groups[24], the position of peak (II) was in agreement with the values reported for lattice oxygen in ZnO[22, 24]. Component (III) could be attributed to the presence of silver(I) oxide,[20, 35, 38] as its intensity increased with silver content. Interestingly, a linear increase of the surface $Zn2p_{3/2}$ BEs with Ag content took place for the as-prepared samples (Fig. 5.31), highlighting the occurrence of electronic interactions between silver and zinc oxide. Even for annealed samples, surface $Zn2p_{3/2}$ BEs were systematically higher than 1021.4 eV, the value expected for ZnO.[24]

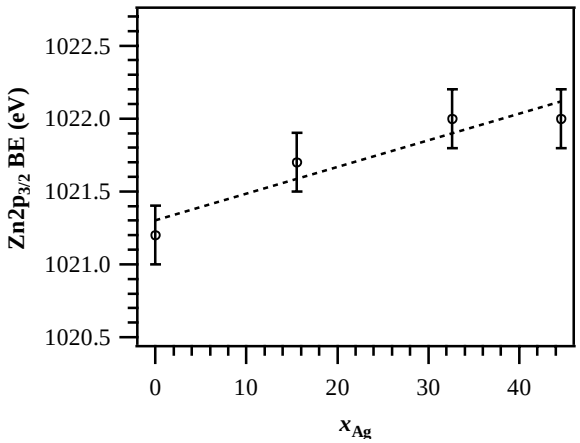

Figure 5.31: *Evolution of surface $Zn2p_{3/2}$ BE of as-prepared samples as a function of silver molar fraction (defined as in Table 1).*

The observed phenomenon could be related both to charge transfer events from ZnO to Ag/Ag_2O NPs[7, 9], and to the surface oxidation of Ag NPs to p-type Ag_2O[38], resulting in Ag_2O–ZnO p-n junctions generating a depletion layer at the interface. The obtainment of Ag_2O–ZnO and Ag–ZnO interfaces with tunable features appears very

promising for a possible improvement of the system functional properties in photocatalytic H_2 generation and gas sensing.

Figure 5.32a displays the rate of H_2 photo-production vs. UV–Vis irradiation time for Ag/ZnO nanocomposites obtained under different processing conditions. Whereas pure ZnO specimens did not show any significant activity, an appreciable H_2 evolution was measured for Ag/ZnO systems, highlighting the key role of silver NPs in promoting the photo-reforming of methanol/water solutions under UV–Vis irradiation. Under these conditions, the process is likely to proceed through the direct photoexcitation of electrons from the valence to the conduction band of ZnO, followed by their transfer to Ag NPs [31]. Subsequently, H^+ reduction on the metal particles results in H_2 generation, whereas alcohol oxidation is promoted by holes in ZnO valence band. Beside the Schottky junction between ZnO and Ag NPs, preventing electron-hole recombination[39], a further promotion of the observed process might result from the formation of Ag_2O–ZnO p-n junctions. A similar effect has recently been observed for CuO-SnO_2 nanocomposites.[40]

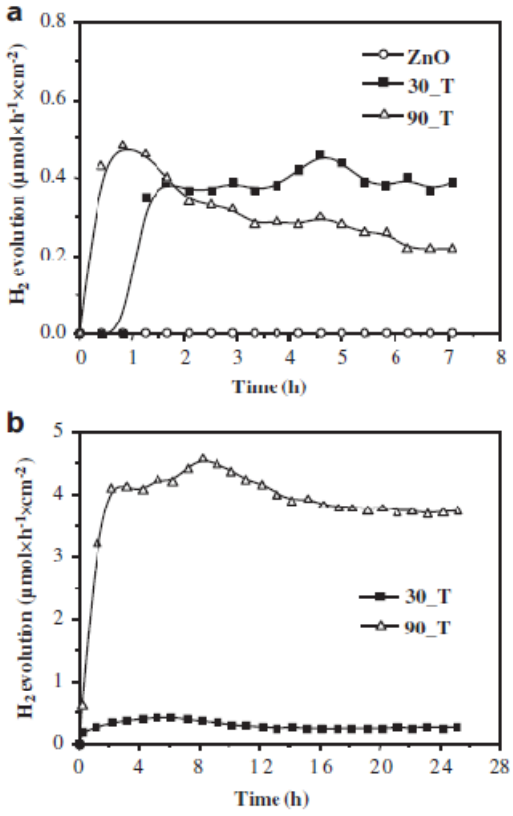

Figure 5.32: *H_2 evolution rate per unit area as a function of illumination time on Ag/ZnO nanocomposites from H_2O/CH_3OH solutions under: (a) UV-Vis light; (b) simulated solar irradiation.*

As a matter of fact, H_2 production rate was not directly proportional to silver content, and the best performances were observed for specimen 30_T. This phenomenon could be explained taking into account that, despite Ag presence is essential for the photo-assisted H_2 evolution, a sufficiently high fraction of uncovered ZnO surface must be available in order to enable an efficient radiation absorption. When Ag NP density is still limited and their size is low, such as for sample 30_T (see above and Figure 11), the good photocatalytic performances can be attributed both to an intimate contact between Ag and ZnO and to a large exposed ZnO surface. In addition, the highly dispersed Ag NPs in sample 30_T (compare SEM and TEM results, Figure 5.25, Figure 5.26 and Figure 5.27) may favorably act as electron capturing centers to generate H_2. In a different way, for specimen 90_T, the increased coverage of the ZnO matrix by larger Ag particles (compare Table 5.1 and Figure 5.25 and Figure 5.26) and the less intimate Ag–ZnO contact resulted in a lowered radiation absorption, explaining thus the observed trend. Upon increasing the silver deposition time to 150 min, a similar behavior was observed (specimen 150_T, data not shown).

The above results are consistent with those obtained for Au/TiO_2 nanosystems, whose optimal photocatalytic performances were obtained for intermediate metal loading due to a trade-off between gold NPs reactivity and their covering of titanium oxide surface[41].

A careful inspection of Figure 5.32a showed that, for the 30_T composite, a stable activity was obtained, with an average H_2 production rate of 0.4 μmol h^{-1} cm^{-2}. Conversely, specimen 90_T presented a decrease of H_2 production after 1 h of irradiation. Such an effect could be related to the reduction of Ag_2O upon illumination[42], a process which is expected to be less pronounced for smaller silver NPs, explaining thus the good stability of sample 30_T.

In this contest, it is important to highlight that the measurement of the Ag/ZnO exposed surface is a critical issue. In general, conventional N_2 or Kr physisorption methods fail, as the estimation of the mass of the active component with respect to the supporting substrate cannot be performed with accuracy. On the other hand, scratching of the deposited material from the substrate induces further uncertainties. As a consequence, we preferred to relate the activity to the geometrical surface, which has indeed a practical meaning in terms of technological applications.

A remarkable photo-reforming activity was observed under illumination with simulated solar light (Fig. 5.32b), an important result in view of practical utilization. Very interestingly, H_2 production rate over sample 90_T was more than one order of magnitude higher than that reported in Figure 5.32a, where a more energetic radiation was used. Furthermore, at variance with data obtained under UV–Vis illumination, a net performance enhancement was obtained upon passing from 30_T to 90_T. Once again, no further improvement was observed by increasing the deposition time to 150_T (data not shown). These phenomena can be interpreted basing on the combination of different effects. An increase of the metal NP content can lead a more efficient Vis light absorption due to the Surface Plasmon Resonance (SPR) of silver aggregates[26, 31, 43]. Indeed, Ag SPR band centered at $\lambda \approx 410$ nm was observed for particles with diameters in the 5–100 nm range, with a red-shift upon increasing metal NP size[44]. In addition, the presence of Ag_2O species can also positively affect the system reactivity. This observation is consistent with previous findings for TiO_2-based systems. In fact, Lalitha et al. showed that pure TiO_2 and Ag_2O, or even Ag/TiO_2 nanosystems, did not present high performances in photo-assisted H_2 production. Conversely, Ag_2O/TiO_2 nanocomposites yielded an improved efficiency, due to both a beneficial interaction between Ag(I) species and TiO_2, and an enhanced radiation absorption in the Vis range[45]. Therefore, the presence of large silver aggregates and the low accessibility of ZnO due to its high degree of coverage justify the poorer reactivity of the 150_T sample with respect to the 90_T sample.

Conclusions

This study was focused on a two-step approach to Ag/ZnO nanocomposites combining PE-CVD, for the growth of columnar ZnO arrays, and RF-sputtering, for the dispersion of Ag NPs in the oxide matrices. Various sputtering times (from 30 to 150 min) were used to tailor the overall silver amount. Depending on the adopted experimental conditions, the processes enabled a fine tuning of Ag/ZnO nanocomposite physico-chemical properties. In fact, the use of RF-sputtering technique allowed a good silver dispersion into ZnO matrices, and the simultaneous control of Ag NPs size by

variations of the sole sputtering time. In addition, silver distribution in the ZnO systems could be further controlled by thermal treatments which, in turn, governed the Ag(0)-Ag(I) inter-conversion leading to an electronic interplay between the different phases. Such an effect directly impacted the system activity in H_2 production by photo-reforming, that yielded very attractive and stable responses even upon activation with simulated solar light.

References

[1] Z. L. Wang. *Materials Today* **2004**, *7*(6), 26-33.
[2] Ü. Özgür, D. Hofstetter, H. Morkoç. *Proceedings of the IEEE* **2010**, *98*(7), 1255-1268.
[3] Q. Fu, T. Wagner. *Surface Science Reports* **2007**, *62*(11), 431-498.
[4] H. Zeng, W. Cai, P. Liu, X. Xu, H. Zhou, C. Klingshirn, H. Kalt. *ACS Nano* **2008**, *2*(8), 1661-1670.
[5] D. Barreca, A. Gasparotto, E. Tondello. *Journal of Materials Chemistry* **2011**, *21*(6), 1648-1654.
[6] M. J. Height, S. E. Pratsinis, O. Mekasuwandumrong, P. Praserthdam. *Applied Catalysis B: Environmental* **2006**, *63*(3-4), 305-312.
[7] W. Lu, G. Liu, S. Gao, S. Xing, J. Wang. *Nanotechnology* **2008**, *19*(44).
[8] T. Tan, Y. Li, Y. Liu, B. Wang, X. Song, E. Li, H. Wang, H. Yan. *Materials Chemistry and Physics* **2008**, *111*(2-3), 305-308.
[9] D. Lin, H. Wu, R. Zhang, W. Pan. *Chemistry of Materials* **2009**, *21*(15), 3479-3484.
[10] L. Irimpan, V. P. N. Nampoori, P. Radhakrishnan. *Chemical Physics Letters* **2008**, *455*(4-6), 265-269.
[11] Y. Zhang, J. Mu. *Journal of Colloid and Interface Science* **2007**, *309*(2), 478-484.
[12] R. K. Roy, S. Bandyopadhyaya, A. K. Pal. *European Physical Journal B* **2004**, *39*(4), 491-498.
[13] S. M. Prokes, O. J. Glembocki, R. W. Rendell, M. G. Ancona. *Applied Physics Letters* **2007**, *90*(9).
[14] S. Deng, H. M. Fan, X. Zhang, K. P. Loh, C. L. Cheng, C. H. Sow, Y. L. Foo. *Nanotechnology* **2009**, *20*(17).
[15] L. Mo, X. Zheng, C. T. Yeh. *Chemical Communications* **2004**, *10*(12), 1426-1427.
[16] R. Pérez-Hernández, A. Gutiérrez-Martínez, A. Mayoral, F. Leonard Deepak, M. Fernández-García, G. Mondragón-Galicia, M. Miki, M. Jose-Yacaman. *Advanced Materials Research* **2010**, *132*, 205-219.
[17] W. Yao, C. Huang, N. Muradov, A. Raissi. *International Journal of Hydrogen Energy* **2011**, *36*(8), 4710-4715.
[18] Q. Xiang, G. Meng, Y. Zhang, J. Xu, P. Xu, Q. Pan, W. Yu. *Sensors and Actuators, B: Chemical* **2010**, *143*(2), 635-640.
[19] H. Qi, D. Alexson, O. Glembocki, S. M. Prokes. *Nanotechnology* **2010**, *21*(21).
[20] L. S. Kibis, A. I. Stadnichenko, E. M. Pajetnov, S. V. Koscheev, V. I. Zaykovskii, A. I. Boronin. *Applied Surface Science* **2010**, *257*(2), 404-413.
[21] I. M. Arabatzis, T. Stergiopoulos, M. C. Bernard, D. Labou, S. G. Neophytides, P. Falaras. *Applied Catalysis B: Environmental* **2003**, *42*(2), 187-201.
[22] D. Bekermann, A. Gasparotto, D. Barreca, L. Bovo, A. Devi, R. A. Fischer, O. I. Lebedev, C. MacCato, E. Tondello, G. Van Tendeloo. *Crystal Growth and Design* **2010**, *10*(4), 2011-2018.
[23] D. Barreca, D. Bekermann, E. Comini, A. Devi, R. A. Fischer, A. Gasparotto, C. MacCato, G. Sberveglieri, E. Tondello. *Sensors and Actuators, B: Chemical* **2010**, *149*(1), 1-7.
[24] D. Barreca, A. Gasparotto, C. MacCato, C. Maragno, E. Tondello. *Surface Science Spectra* **2007**, *14*(1-4), 19-26.
[25] P. Romero-Gòmez, J. Toudert, J. R. Sánchez-Valencia, A. Borrás, A. Barranco, A. R. Gonzalez-Elipe. *Journal of Physical Chemistry C* **2010**, *114*(49), 20932-20940.
[26] D. Barreca, A. Gasparotto, C. Maragno, E. Tondello, S. Gialanella. *Journal of Applied Physics* **2005**, *97*(5), 1-8.
[27] L. Armelao, D. Barreca, G. Bottaro, A. Gasparotto, C. MacCato, E. Tondello, O. I. Lebedev, S. Turner, G. Van Tendeloo, C. Sada, U. L. Stangar. *ChemPhysChem* **2009**, *10*(18), 3249-3259.
[28] N. Alenzi, W. S. Liao, P. S. Cremer, V. Sanchez-Torres, T. K. Wood, C. Ehlig-Economides, Z. Cheng. *International Journal of Hydrogen Energy* **2010**, *35*(21), 11768-11775.
[29] T. Miwa, S. Kaneco, H. Katsumata, T. Suzuki, K. Ohta, S. Chand Verma, K. Sugihara. *International Journal of Hydrogen Energy* **2010**, *35*(13), 6554-6560.
[30] G. Wu, T. Chen, W. Su, G. Zhou, X. Zong, Z. Lei, C. Li. *International Journal of Hydrogen Energy* **2008**, *33*(4), 1243-1251.
[31] J. Liu, Y. Sun, Z. Li, S. Li, J. Zhao. *International Journal of Hydrogen Energy* **2011**, *36*(10), 5811-5816.
[32] E. Rita, U. Wahl, A. M. L. Lopes, J. P. Araújo, J. G. Correia, E. Alves, J. C. Soares. *Physica B: Condensed Matter* **2003**, *340-342*, 240-244.
[33] I. Sakaguchi, K. Watanabe, T. Ohgaki, T. Nakagawa, S. Hishita, Y. Adachi, N. Ohashi, H. Haneda. *Nippon Seramikkusu Kyokai Gakujutsu Ronbunshi/Journal of the Ceramic Society of Japan* **2010**, *118*(1375), 217-219.
[34] M. N. V. Ramesh, Y. Sundarayya, C. S. Sunandana. *Modern Physics Letters B* **2007**, *21*(28), 1933-1944.
[35] G. I. N. Waterhouse, G. A. Bowmaker, J. B. Metson. *Applied Surface Science* **2001**, *183*(3-4), 191-204.
[36] A. Michaelides, K. Reuter, M. Scheffler. *Journal of Vacuum Science and Technology A: Vacuum, Surfaces and Films* **2005**, *23*(6), 1487-1497.
[37] S. Sen, S. Mahanty, S. Roy, O. Heintz, S. Bourgeois, D. Chaumont. *Thin Solid Films* **2005**, *474*(1-2), 245-249.
[38] X. Y. Gao, H. L. Feng, J. M. Ma, Z. Y. Zhang, J. X. Lu, Y. S. Chen, S. E. Yang, J. H. Gu. *Physica B: Condensed Matter* **2010**, *405*(7), 1922-1926.
[39] A. Primo, A. Corma, H. García. *Physical Chemistry Chemical Physics* **2011**, *13*(3), 886-910.
[40] X. J. Zheng, Y. J. Wei, L. F. Wei, B. Xie, M. B. Wei. *International Journal of Hydrogen Energy* **2010**, *35*(21), 11709-11718.

[41] L. Armelao, D. Barreca, G. Bottaro, A. Gasparotto, C. MacCato, C. Maragno, E. Tondello, U. L. Štangar, M. Bergant, D. Mahne. *Nanotechnology* **2007**, *18*(37).
[42] A. Kudo, Y. Miseki. *Chemical Society Reviews* **2009**, *38*(1), 253-278.
[43] H. Y. Chuang, D. H. Chen. *International Journal of Hydrogen Energy* **2011**, *36*(16), 9487-9495.
[44] A. Zieliñska, E. Skwarek, A. Zaleska, M. Gazda, J. Hupka. *Procedia Chemistry* **2009**, *1*(2), 1560-1566.
[45] K. Lalitha, J. K. Reddy, M. V. Phanikrishna Sharma, V. D. Kumari, M. Subrahmanyam. *International Journal of Hydrogen Energy* **2010**, *35*(9), 3991-4001.

Chapter 6

CONCLUSIONS

During this PhD thesis, the syntheses and characterization of several photocatalysts for hydrogen production from renewable sources have been performed. The main focus of these studies was the preparation of active and stable photocatalysts based on metal oxides for the utilization in the photoreforming of aqueous solution of oxygenated compounds.

The study indicates appreciable advantages in preparing embedded CuO_x@TiO_2 photocatalysts for hydrogen production by photo-reforming of ethanol and glycerol water solutions with respect to conventional impregnated materials (Chapter 3). The combined presence of good dispersion of the Cu/CuO_x species, large contact area between Cu and the surrounding TiO_2 and the possibility of some Cu ion dissolution into the titania lattice during the synthesis, with some influence on band gap, are some of the positive aspects that can account for the superior performance of these systems. Stability tests under reducing conditions, i.e., argon flow and inert atmosphere, and in the presence of a sacrificial agent indicate that copper leaching is marginal, and if

operative, Cu photodeposition under UV irradiation can minimize this drawback. Vice versa, conventional Cu-TiO_2 materials suffer a dramatic Cu leaching under oxidizing conditions (exposure to air) and in the presence of acidic reaction intermediates. Therefore, the start-up and shout-down steps of a hypothetical process for hydrogen photoproduction based on CuO_x-TiO_2 should be carefully designed to prevent catalyst deactivation.

Active and cheap nanocomposites were also obtained by photodeposition of Cu on the surface of TiO_2 supports (Chapter 4). The activity of TiO_2 is strongly influenced by its structural characteristics: when a multi-phase support is used, the high number of defects (electron/hole pairs) produced results in a very high dispersion of the metal and in a high activity in H_2 production, by an increase in the oxidation rate of the sacrificial agents. Minor leaching is observed under UV irradiation, while under simulated solar irradiation a considerable fraction of Cu is oxidized and subjected to photocorrosion. After a few hours, the amount of Cu ions becomes constant suggesting the establishment of an equilibrium between the Cu photodeposition process, induced by the small fraction of UV (~ 4%), and the leaching phenomena. Remarkably, the negative effect on the hydrogen production is not dramatic. Regeneration process based on the use of short UV irradiation steps can overcome progressive and serious deactivation. Besides the production of hydrogen, the presented photocatalytic process could open the way to the synthesis of building blocks of interest for chemical industry, since the oxidation of carbonyl compounds is the limiting step of the degradation reaction occurring on the sacrificial agent.

The performances of the Cu_xO based nanosystems prepared by CVD are also very promising, especially considering that the active Cu_xO phase was deposited on an inert substrate (Chapter 5 part 1). A direct comparison with alternative and very attractive materials from literature data is not straightforward. Nevertheless, a preliminary comparative evaluation was performed with the widely investigated Pt/TiO_2 systems. A 1.3-mm thick Pt/TiO_2 film, under optimized experimental conditions, showed a conversion efficiency of 32% (black light lamp with emission at 365 nm), whereas our CuO film showed a conversion efficiency of 11% under UV irradiation. Although the Pt loading was not reported, the huge differences in the cost of Pt and Cu, as well as the possibility to significantly enhance the performances of Cu_xO films by supporting them

on TiO_2, highlight the relevance of the present findings. In conclusion, a novel and amenable CVD route, compatible with large-scale production, to prepare Cu_xO (x=1, 2) nanostructures on Si (100) was reported, enabling the resulting Cu-O phase composition and nanoscale organization to be controlled by simple variation of the growth temperature. In addition, and more interestingly, the photocatalytic production of hydrogen on both the supported catalysts upon irradiation with UV and even visible light proved that the control of the system morphogenesis is crucial to obtain good Cu_xO performances even in the absence of TiO_2. These results represent an important step forward in the exploration of new active nanosystems for the conversion of solar light into storable chemical energy.

A convenient CVD route for the preparation of Co_3O_4 systems on Si(100) starting from $Co(hfa)_2$•TMEDA, resulting in homogeneous assemblies of faceted nanopyramids, was presented (Chapter 5 part 2). The obtained materials were tested for the first time in the photo-assisted H_2 production from methanol/water media. A remarkably stable hydrogen evolution rate was observed over significant periods of time, provided that oxygen was present in the reaction environment. The present findings pave the way to the development of mixed cobalt oxide-containing nanocomposites for further advancements in photo-assisted hydrogen generation, with particular attention on the selectivity towards H_2 obtainment at expenses of carbon-containing gaseous by-products. F-doping of Co_3O_4 films synthesized by PE-CVD resulted in a significant improvement of H_2 photoproduction from suitable aqueous solutions. Specifically, upon near-UV irradiation of F-doped Co_3O_4, a 5-fold hydrogen yield increase was evidenced with respect to the corresponding undoped oxide. In the case of simulated solar light, although a less marked improvement in terms of H_2 evolution was observed, the appreciable time stability of the response makes this material an attractive photocatalyst for the sustainable generation of hydrogen activated by sunlight. As a whole, the incorporation of fluorine resulted in highly photoactive Co_3O_4 materials, with H_2 yields per gram of catalyst among the best ever reported in the literature. It is also worth noting that the synthetic strategy adopted herein for the preparation of F-doped Co_3O_4 can be regarded as a general and versatile route for tailored anion doping of oxide and even non-oxide SC nanosystems. Efforts in this direction are currently underway.

A two-step approach to Ag/ZnO nanocomposites combining PE-CVD, for the growth of columnar ZnO arrays, and RF-sputtering, for the dispersion of Ag NPs in the oxide matrices, was developed (Chapter 5 part 3). Various sputtering times (from 30 to 150 min) were used to tailor the overall silver amount. Depending on the adopted experimental conditions, the processes enabled a fine tuning of Ag/ZnO nanocomposite physico-chemical properties. In fact, the use of RF-sputtering technique allowed a good silver dispersion into ZnO matrices, and the simultaneous control of Ag NPs size by variations of the sole sputtering time. In addition, silver distribution in the ZnO systems could be further controlled by thermal treatments which, in turn, governed the Ag(0)-Ag(I) inter-conversion leading to an electronic interplay between the different phases. Such an effect directly impacted the system activity in H_2 production by photo-reforming, that yielded very attractive and stable responses even upon activation with simulated solar light.

As a final remark, it is relevant to observe that, in contrast to powdered photocatalysts, supported nanosystems allow the use of minimal amounts of material and reduce aggregation effects, thus resulting in an improved time stability.

Acknowledgements

It is a pleasure to thank those who made this thesis possible

Prof. Paolo Fornasiero for giving me the opportunity to perform the research for my PhD thesis in his group, his invaluable support and the helpful discussions.

All the present and former members of the MEE group for their individual contribution for the inspiring atmosphere and excellent working conditions by providing ideas, comments, solutions, pratical help and for making these years a pleasure rather than mere work.

I would like to express my gratitude to Dr. Davide Barreca and Dr. Alberto Gasparotto for the stimulating and costructive discussions.

A special thank to prof. Mauro Graziani for always standing at my side and being there when it counted most.